Institut für Geowissenschaften
Mathematisch-Naturwissenschaftliche Fakultät
Universität Potsdam

ANALYZING PORE SYSTEMS THROUGH COMPREHENSIVE DIGITAL IMAGE ANALYSIS (DIA)

QUANTIFYING PORE TYPE GEOMETRY, DETECTING EFFECTIVE POROSITY AND RECONSTRUCTING PORE SYSTEM EVOLUTION

Sven Maerz

Dissertation
zur Erlangung des akademischen Grades
„doctor rerum naturalium“
(Dr. rer. nat.)
In der Wissenschaftsdisziplin „Sedimentologie“

eingereicht an der

Mathematisch-Naturwissenschaftlichen Fakultät

Institut für Geowissenschaften

der Universität Potsdam

Potsdam

September 2019

Published online at the
Institutional Repository of the University of Potsdam:
https://doi.org/10.25932/publishup-44588
https://nbn-resolving.org/urn:nbn:de:kobv:517-opus4-445880

UNIVERSITY OF POTSDAM

A dissertation submitted to the Faculty of Mathematics and Natural Sciences

In partial fulfillment of the requirements for the degree Doctor rer. nat.

ANALYZING PORE SYSTEMS THROUGH COMPREHENSIVE DIGITAL IMAGE ANALYSIS (DIA): QUANTIFYING PORE TYPE GEOMETRY, DETECTING EFFECTIVE POROSITY AND RECONSTRUCTING PORE SYSTEM EVOLUTION

by

Sven Maerz

Potsdam

September 2019

Thesis Advisory Committee

First Supervisor: Prof. Dr. Maria Mutti

University of Potsdam

Institute of Geosciences

Mentor: Dr. Heiko Pingel

University of Potsdam

Institute of Geosciences

External reviewer

First Reviewer: Prof. Dr. Ida Fabricius, PhD

Technical University of Denmark

Department of Civil Engineering

Second Reviewer: Prof. Dr. Christian Betzler

University of Hamburg, Germany

Institute for Geology

Day doctorate awarded

Potsdam, March 2nd, 2020

MAERZ, SVEN (September, 2019)

Analyzing Pore Systems through comprehensive Digital Image Analysis (DIA):

Quantifying Pore Type Geometry, Detecting Effective Porosity and

Reconstructing Pore System Evolution.

Abstract of a dissertation at the Institute of Geosciences at University of Potsdam.

Dissertation supervised by Professor Dr. Maria Mutti.

No. of pages in text: 107.

ABSTRACT

Carbonates tend to have complex pore systems which are often composed of distinct assemblages of genetically and geometrically different pore types at various scales (e.g., Melim et al., 2001; Lee et al., 2009; He et al., 2014; Dernaika & Sinclair, 2017; Zhang et al., 2017). Such carbonate-typical multimodal pore systems are the result of both primary depositional processes and multiple stages of postdepositional modifications, causing small-scale heterogeneities in pore system properties and leading to the co-occurrence of both effective and ineffective pore types. These intrinsic variations in pore type effectiveness are the main reason for the often low correlation between porosity and permeability in carbonate pore systems (e.g., Mazzullo 2004; Ehrenberg & Nadeau, 2005; Hollis et al., 2010; He et al., 2014; Rashid et al., 2015; Dernaika & Sinclair, 2017), as it is also true for the marginal lacustrine carbonates studied in this thesis. However, by extracting interconnected and thus effective pore types, and simultaneously excluding isolated and ineffective pores, the understanding and prediction of permeability for given porosity can be highly enhanced (e.g., Melim et al., 2001; Zhang et al., 2017). In this thesis, a step-by-step workflow based on digital image analysis (DIA) is presented and performed on 32 facies-representative samples of marginal lacustrine carbonates from the Middle Miocene Nördlinger Ries crater lake (Southern Germany), resulting in 77 mean values of pore type effectiveness which are based on 23,508 individual pore geometry data. By using pore shape factor γ (sensu Anselmetti et al., 1998) as a parameter to quantitatively describe pore shape complexity and therefore pore interconnectivity, the potential contribution ($K_{contr.}$) of each pore type to total permeability (K_{total}) is calculated, and the most effective pore types are then identified. As a result, primary interpeloidal pores and secondary vugs are the most effective pore types in the studied marginal lacustrine succession, mainly due to their generally big size and complex shape, leading to an excellent interconnection between both pore types and consequently to the establishment of a highly effective pore network. Both pore types together compose the pore system of the peloidal grainstone facies. Therefore, this lithofacies type has been identified as the sedimentary facies with highest

porosity-permeability properties in this marginal lacustrine succession. By applying the DIA-based method to 23 additional samples from the studied outcrop which all show extensive partial to complete cementation of preexisting pores, the impact of cementation on pore geometry and therefore on porosity and permeability is quantified. This results in a cementation reduction value for each relevant parameter which can then be used to enhance precision of predicting porosity and permeability within the studied succession. Furthermore, the concept of using pore shape complexity as a proxy parameter for pore system effectiveness is tested by applying an independent method (i.e., fluid flow simulation) to the dataset. DIA is then used once again to evaluate the outcome of fluid flow simulation. The results confirm the previous findings that interpeloidal pores and vugs together build up the most effective pore system in the Ries lake carbonates. Finally, the extraction of the interconnected (i.e., effective) pore network leads to an improved correlation between porosity and permeability within the studied carbonates. The step-by-step workflow described in this thesis provides a quantitative petrographic method to identify and extract effective porosity from the pore system, which is crucial for understanding how carbonate pore systems generate permeability. This thesis also demonstrates that pore shape complexity is the most important geometrical parameter controlling pore interconnection and consequently the formation of effective porosity. It further emphasizes that pore shape factor γ (sensu Anselmetti et al. 1998) is a very robust and scale-independent proxy parameter to quantify pore type effectiveness. Additionally, DIA proves to be an ideal tool to directly link porosity and permeability to their mutual origin: the rock fabric and associated pore structure.

MAERZ, SVEN (September, 2019)

Analyzing Pore Systems through comprehensive Digital Image Analysis (DIA):

Quantifying Pore Type Geometry, Detecting Effective Porosity and

Reconstructing Pore System Evolution.

Zusammenfassung einer Dissertation am Institut für Geowissenschaften der Universität Potsdam.

Dissertation betreut durch Professor Dr. Maria Mutti.

Anzahl der Seiten im Text: 107.

ZUSAMMENFASSUNG

Der Porenraum eines Karbonatgesteins ist zumeist aus einer spezifischen Vergesellschaftung verschiedenster Porentypen aufgebaut, die eine unterschiedliche Herkunft aufweisen und zusätzlich in ihrer Form und Größe stark variieren können (e.g., Melim et al., 2001; Lee et al., 2009; He et al., 2014; Dernaika & Sinclair, 2017; Zhang et al., 2017). Diese für Karbonate typischen multimodalen Porensysteme entstehen sowohl durch primäre Ablagerungsprozesse, als auch durch mehrmalige Modifikation des Porenraumes nach Ablagerung des Sediments. Dies führt zu einer ungleichen Verteilung der Porenraumeigenschaften auf engstem Raum und das zeitgleiche Auftreten von effektiven und ineffektiven Poren. Diese immanenten Unterschiede in der Effektivität einzelner Porentypen sind der Hauptgrund für die häufig sehr niedrige Korellation zwischen Porosität und Permeabilität in Karbonaten (e.g., Mazzullo 2004; Ehrenberg & Nadeau, 2005; Hollis et al., 2010; He et al., 2014; Rashid et al., 2015; Dernaika & Sinclair, 2017). Durch die Extraktion von miteinander verbundenen und somit effektiven Porentypen jedoch kann das Verständnis und die Vorhersage der Permeabilität für einen gegeben Porositätswert stark verbessert werden (e.g., Melim et al., 2001; Zhang et al., 2017). Dazu wird in dieser Arbeit eine auf der digitalen Bildanalyse (DIA) beruhende Methode vorgestellt, mit der schrittweise die Effektivität von Poren aus den analysierten mittelmiozänen lakustrinen Karbonaten des Nördlinger Ries Kratersees (Süddeutschland) berechnet werden kann. Mithilfe des Porenformfaktors γ (sensu Anselmetti et al., 1998), der als Parameter zur Quantifizierung der Interkonnektivität zwischen Poren dient, wird der potentiellen Beitrag an Permeabilität jedes Porentyps zur Gesamtpermeabilität bestimmt. Somit können die effektivsten Porentypen innerhalb der analysierten Karbonate identifiziert werden. Desweiteren wird die digitale Bildanalyse dazu benutzt, zementierte Porenräume zu extrahieren, um den Einfluss der Zementation auf die Porenraumeigenschaften zu quantifizieren. Durch eine unabhängige Methode (Fluid-Flow-Simulation), deren Ergebnisse wiederum mit der digitalen Bildanalyse ausgewertet werden, können die vorherigen Erkentnisse bestätigt werden: Interpeloidale Poren und Lösungsporen sind die beiden effektivsten Porentypen im Porenraum der Riesseekarbonate.

Die Extraktion des miteinander verbundenen (d.h. effektiven) Porennetzwerkes führt schließlich zu einer erheblich verbesserten Korrelation zwischen Porosität und Permeabilität in den analysierten Karbonaten. Die in dieser Arbeit beschriebene Methode bietet ein quantitatives petrographisches Werkzeug, mit dessen Hilfe die effektive Porosität eines Porenraumes extrahiert werden kann. Dies führt zu einem besseren Verständnis darüber, wie Porensysteme von Karbonaten Permeabilität erzeugen. Diese Dissertation zeigt auch, dass die Formkomplexität von Poren einer der wichtigsten Parameter ist, der die Interkonnektivität zwischen einzelnen Poren und somit die Entstehung von effektiver Porosität steuert. Außerdem erweist sich die digitale Bildanalyse als ausgezeichnetes Werkzeug um die Porosität und Permeabilität direkt an ihren gemeinsamen Ursprung zu knüpfen: die Gesteinstextur und die damit assoziierte Porenstruktur.

TABLE OF CONTENT

LIST OF FIGURES ..... ***II***

LIST OF TABLES ..... ***XII***

CHAPTER ONE **1**

GENERAL INTRODUCTION 1

1.1 Porosity and Permeability in Carbonate Rocks 1

1.2 Review of Methods in Pore System Analysis 2

1.3 Motivation and Goals 5

1.4 Structure of this Thesis 5

CHAPTER TWO **6**

DATA ACQUISITION 6

2.1 Geological Setting 6

2.2 Material and Methods 8

2.3 Pore Types 12

2.4 Total Porosity and Permeability 18

CHAPTER THREE **20**

METHODOLOGY: STEP-BY-STEP WORKFLOW FOR QUANTITATIVE PORE TYPE CHARACTERIZATION 20

3.1 Introduction 20

3.2 Quantification of Pore System (Step I) 21

3.3 Pore Size versus Shape (Step II) 25

3.4 Effective Pore Types (Step III) 26

3.5 Petrophysical Facies and Pore System Evolution (Step IV) 30

3.6 Discussion of Chapter 31

3.7 Conclusions 34

CHAPTER FOUR **36**

APPLICATION I: COMPREHENSIVE PORE SYSTEM ANALYSIS OF MARGINAL LACUSTRINE CARBONATES (MIDDLE MIOCENE, SOUTHERN GERMANY) 36

4.1 Introduction 36

4.2 Pore Type Assemblages 36

4.3 Pore System Analysis of the Nördlinger Ries Carbonates 38

4.4 Effective Pore Type(s) 42
4.5 Discussion of Chapter 45
4.6 Conclusion 47

CHAPTER FIVE **49**
APPLICATION II: QUANTIFICATION OF THE IMPACT OF CEMENTATION ON PETROPHYSICAL PROPERTIES AND RECONSTRUCTION OF PORE SYSTEM EVOLUTION 49
5.1 Introduction 49
5.2 Impact of Cementation on Pore Geometry, Porosity and Permeability 50
5.3 Discussion of Chapter 56
5.4 Conclusion 61

CHAPTER SIX **63**
APPLICATION III: FLUID FLOW SIMULATION 63
6.1 Introduction 63
6.2 Methodology 63
6.3 Results 67
6.4 Discussion of Chapter 70
6.5 Conclusions 80

CHAPTER SEVEN **81**
IMPLICATION: POROSITY-PERMEABILITY RELATIONSHIP IN CARBONATES 81
7.1 Introduction 81
7.2 Porosity-Permeability Relationship 81
7.3 Discussion of Chapter 85
7.4 Conclusions 86

CHAPTER EIGHT **88**
SYNTHESIS 88
8.1 Pore Shape Complexity and Effective Porosity 88
8.2. Comprehensive Pore System Analysis of the Ries Lake Carbonates 89
8.3 Fluid Flow Simulation on 2D Thin Section Images 91
8.4 Porosity-Permeability Relationship 93

CHAPTER NINE **95**
SUMMARY 95

REFERENCES **97**
APPENDIX ..... ***i***
ACKNOWLEDGMENTS ..... ***xix***
PUBLICATIONS & PRESENTATIONS ..... ***xx***
STATUTORY DECLARATION ..... ***xxi***

LIST OF FIGURES

Figure 1.1. Co-occurrence of genetically and geometrically different pore types. 2
Figure 2.1. Overview and geological setting. 6
Figure 2.2. Marginal lacustrine carbonates of outcrop Hainsfarth. 7
Figure 2.3. Photomicrographs of typical facies types of the northern Ries lake margin. 9
Figure 2.4. Sample recovery at the outcrop in Hainsfarth, Bavaria (Southern Germany). 10
Figure 2.5. Pore types in the Nördlinger Ries carbonates I. 12
Figure 2.6. Pore types in the Nördlinger Ries carbonates II. 13
Figure 2.7. Pore types in the Nördlinger Ries carbonates III. 13
Figure 2.8. Pore types in the Nördlinger Ries carbonates IV. 14
Figure 2.9. Microporosity analysis on BSE images. 15
Figure 2.10. Micropore types in the Nördlinger Ries lake carbonates. 16
Figure 2.11. Pore types in the Nördlinger Ries lacustrine carbonates. 17
Figure 3.1. Step I: Quantification of pore system with digital image analysis (DIA). 22
Figure 3.2. Artificial neural networks (ANNs) for porosity and permeability prediction. 24
Figure 3.3. Sedimentary fabric and pore system of sample 3.16_1. 25
Figure 3.4. Pore width versus γ plot. 27
Figure 3.5. Step IIIa: Effective pore type (actual pore system). 27
Figure 3.6. Step IIIb: Effective pore type (artificial pore system). 28
Figure 3.7. Step IIIc: Effective pore type (unimodal pore systems). 29
Figure 3.8. Step IIId: Effective pore type (reassembling the actual pore system). 30
Figure 3.9. Step IV: Pore system evolution of peloidal grainstones. 32
Figure 4.1. Pore types and pore type assemblages (PTA). 37
Figure 4.2. Pore width versus γ of each individual pore and for all pore types present. 39
Figure 4.3. Pore width versus γ plot for sample 1A10_2. 41
Figure 4.4. Pore width versus γ plot for sample 3B6_9. 42
Figure 4.5. Pore system of sample 1A10_2 (PTA 2). 43
Figure 4.6. Pore system of sample 3B6_9 (PTA 3). 44
Figure 5.1. Thin section images indicating cements with different hue of color. 51
Figure 5.2. Thin section and DIA-derived images representing different stages of pore system evolution. 52
Figure 5.3. Correction of underestimation caused by preexisting but overprinted pores. 54
Figure 5.4. Pore system evolution and its impact on petrophysical properties. 56
Figure 5.5. Impact of cementation on pore geometry and petrophysical properties throughout each stage of pore system evolution. 57
Figure 5.6. Differential evolution of vugs. 60
Figure 5.7. Differential evolution of porosity in peloids. 61
Figure 6.1. Screenshot of fluid flow simulation result. 64
Figure 6.2. Digital image analysis (DIA) method to evaluate fluid flow simulation results. 66

Figure 6.3. Effective porosity versus pore shape complexity I. 68

Figure 6.4. Effective porosity versus pore shape complexity II. 69
Figure 6.5. Effective porosity versus pore shape complexity III. 70
Figure 6.6. Impact of cementation on pore geometry and fluid flow simulation. 71
Figure 6.7. Effective porosity versus pore shape complexity IV. 72
Figure 6.8. Problem of scale in intraskeletal pores of the skeletal grainstone facies. 74
Figure 6.9. Effective porosity versus pore shape complexity V. 75
Figure 6.10. 2D/3D effect in interpeloidal grainstone facies. 77
Figure 6.11. Influence of scale on fluid flow simulation and pore shape complexity. 79
Figure 7.1. Porosity-permeability relationship in the Nördlinger Ries marginal lacustrine carbonates I. 82
Figure 7.2. Porosity-permeability relationship in the Nördlinger Ries marginal lacustrine carbonates II. 84
Figure 7.3. Porosity-permeability relationship in the Nördlinger Ries marginal lacustrine carbonates III. 85

LIST OF TABLES

Table 1. Total porosity and permeability data from routine injection methods for each analyzed facies type of the Nördlinger Ries marginal lacustrine carbonates 18

Table 2. Petrophysical facies of all non-skeletal (peloidal) grainstone samples analyzed to establish the workflow 31

Table 3. Petrophysical facies of all samples examined in the Nördlinger Ries marginal lacustrine carbonates including mean values and value ranges of all relevant parameters for each pore type 40

Table 4. Impact of cementation on pore geometry and petrophysical properties throughout each stage of pore system evolution 55

CHAPTER ONE

GENERAL INTRODUCTION

1.1 Porosity and Permeability in Carbonate Rocks

Carbonate pore systems are characterized by an often low correlation between porosity and permeability. Although there is a general trend in both carbonates and siliciclastic rocks of decreased porosity with depth (Ehrenberg & Nadeau, 2005), the porosity-permeability relationships of carbonates usually show a more scattered distribution as compared to siliciclastic rocks (Melim et al., 2001; Lee et al., 2009; He et al., 2014; Dernaika & Sinclair, 2017; Zhang et al., 2017). Moreover, the correlation can differ between two formations of the same carbonate lithology and facies, caused by the formation-specific evolution of the multimodal pore system (Mazzullo, 2004; Hollis et al., 2010; Dernaika & Sinclair, 2017). As a consequence, both fundamental petrophysical parameters are not necessarily related and permeability for a given porosity can vary tremendously (e.g., Anselmetti et al., 1998; Baechle et al., 2004; Ehrenberg et al., 2006; Weger, 2006; Weger et al., 2009), depending on (i) the facies-dependent texture and composition of the sedimentary fabric, on (ii) the initial primary porosity and permeability, and on (iii) early to late stages of diagenetic modification of both the sedimentary fabric and the pore system (Mazzullo 2004; Ehrenberg & Nadeau, 2005; He et al., 2014; Rashid et al., 2015; Dernaika & Sinclair, 2017). These modifications often act locally and vary at a sub-centimeter scale. Hence, they are difficult to predict at outcrop or seismic scale, particularly if only few and local samples, for example from cores, are available. This impedes a reliable and precise prediction of the porosity-permeability distribution (Rashid et al., 2015) and results in the often typical “poroperm data cloud” in carbonates (sensu Dernaika & Sinclair, 2017). These small-scale heterogeneities are also the main cause for carbonate-typical complex pore systems, composed of genetically and geometrically different pore types. Their size and shape are confined by the depositional fabric and are commonly modified by subsequent phases of diagenetic alteration. The resulting heterogeneity within the sedimentary fabric substantially affect fabric-controlled pore geometry and thus petrophysical properties (e.g., Anselmetti et al., 1998; Anselmetti & Eberli, 1999; Eberli et al., 2003; Weger, 2006; Weger et al., 2009; Hollis et al., 2010; Verwer et al., 2010; 2011; Aliakbardoust & Rahimpour-Bonab, 2013). In fact, each pore type generally occurs either isolated and therefore is ineffective in producing permeability, or interconnects with adjacent pores via pore throats to establish an interconnected pore network, which generates effective porosity and consequently permeability. Figure 1.1 shows examples of pore systems of the studied carbonates which are composed of a co-occurrence of genetically and geometrically different pore types, producing identical porosity values but different permeability.

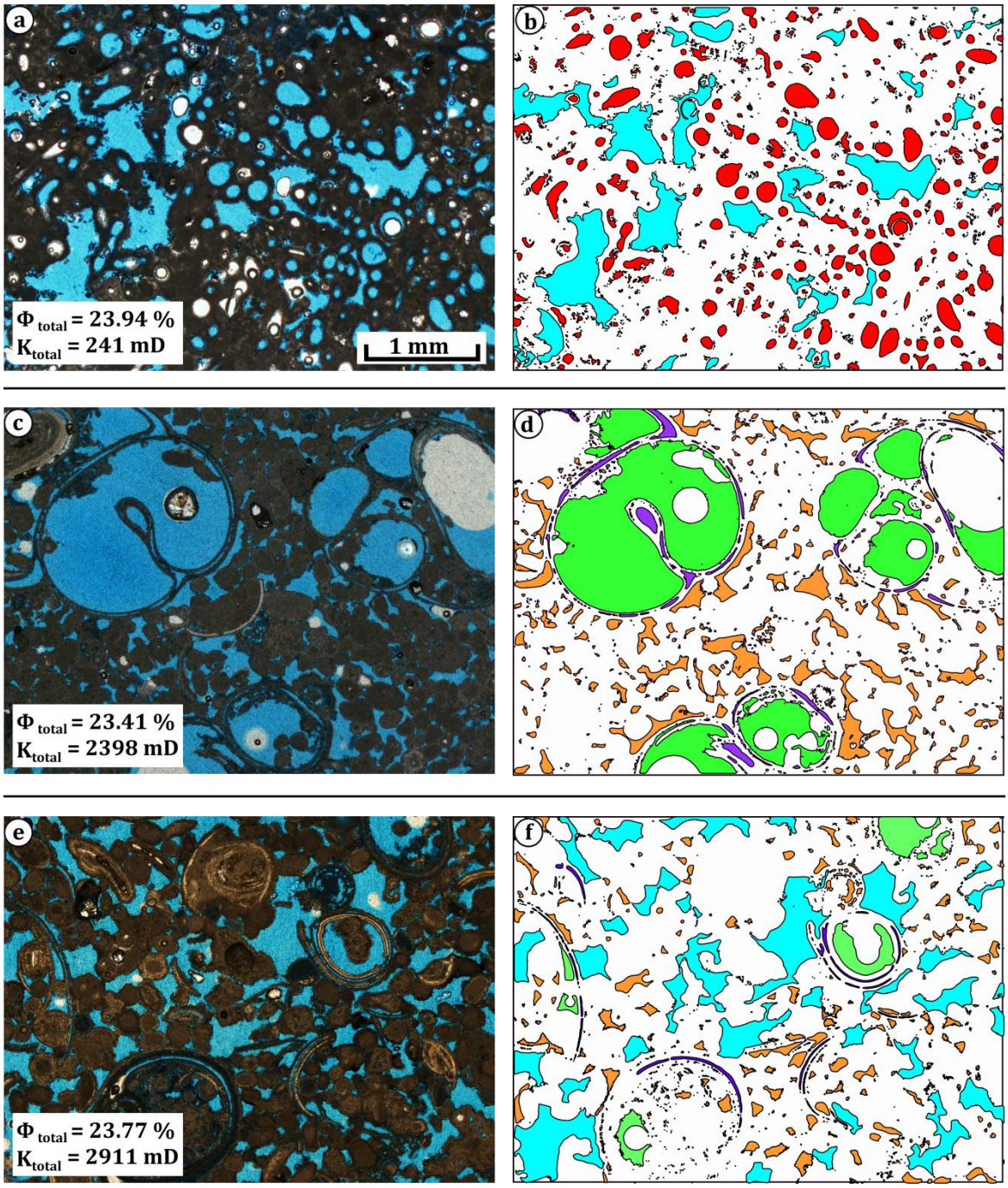

Figure 1.1. Co-occurrence of genetically and geometrically different pore types. a. Original thin section image of *Cladophorites* boundstone facies. **b.** Classified thin section image with filament molds (red) and vugs (blue). **c.** Original thin section image of gastropodal grainstone facies. **d.** Classified thin section image with intraskeletal pores (green), skeletal molds (purple) and interpeloidal pores (orange). **e.** Original thin section image of ostracodal grainstone facies. **d.** Classified thin section image with intraskeletal pores (green), skeletal molds (purple), interpeloidal pores (orange) and vugs (blue). Note the different permeability for identical porosity values. Pore type classification has been realized by using the method presented in this thesis.

1.2 Review of Methods in Pore System Analysis

The challenge in pore system analysis is the integration of multiscale data derived from different methodological approaches: Qualitative or semi-quantitative description of pore network has proven to

be a very reliant and applicable way to classify and describe porosity in a rock (Choquette & Pray, 1970; Lucia, 1983; 1995; 1999; Lønøy, 2006). However, they lack fully quantitative and consistent measurements for porosity and permeability. In contrary, total porosity of a rock can be quantitatively measured from well logs or via a proxy, such as sonic logs, neutron logs, density logs, and neutron-density cross-plots (Asquith and Gibson, 1982; Rider, 2002), or from helium- and mercury-injection porosimetry. Both methods yield numerical data which can be used to infer permeability (Rider, 2002).

Total permeability is also commonly measured directly on plugs and cores with routine gas injection permeametry. The major difference between all aforementioned methods is their effective scale and hence resolution. Porosity logs work best at reservoir scales (Ehrenberg, 2007). However, their resolution is tied to those of the well log device, with a vertical resolution in the range of centimeters (Rider, 2002). Therefore, small-scale heterogeneities within the pore system caused by differential diagenetic modification of the sedimentary fabric cannot be detected (Ehrenberg, 2007). Gas-injection provides a method to measure both total porosity and permeability, theoretically capturing all pores and representing the average value of the measured chip, plug or core. Large-scale heterogeneities and macropores bigger than core size are usually not detected (Honarpou et al., 2003). In general, log-derived porosity tends to be higher than plug porosity (Ehrenberg, 2007). A combination of both methods, where plug data are calibrated with log-derived porosity, is a routine technique for porosity calculation at a reservoir scale (Ehrenberg, 2007). However, these routine porosity and permeability measurements provide numerical data, but deliver no information about the different type of pores, including their distribution, geometry and interconnectivity. Hence, they do not provide any details about which pore types constitute the effective pore network, generating highest contribution to total permeability. This information however is required in order to assess the often inhomogeneous distribution of permeability in a sedimentary succession, especially in carbonate settings (e.g., Melim et al., 2001; Zhang et al., 2017).

Digital image analysis (DIA) provides a tool to combine both the classical methods of qualitative description of pore system and quantitative measurements of porosity and permeability. The analysis of pore systems with DIA-derived parameters avoids “descriptive bias” (sensu Anselmetti et al., 1998), especially if a large number of samples has to be processed for an increased sampling resolution. DIA is a widely used method in natural sciences and finds application in biology, medicine, geographic information systems (GIS) and remote sensing. In general, it describes the application of computer algorithms to analyze and process digital images. Over the last three decades, DIA has also gained increasing attention in geoscience as a tool to examine the sedimentary fabric and to measure the geometry of pore space (e.g., Ehrlich et al., 1991a; Anselmetti et al., 1998; Anovitz & Cole, 2015). By analyzing pore geometry, the understanding of the relationship between pore space, solid matrix and petrophysical response is enhanced, and petrophysical properties can be predicted more precisely. In contrast to the rather abstract numerical porosity and permeability values derived from routine injection methods, DIA offers a tool to simultaneously visualize and measure a pore system. The application of DIA for analyzing pore systems has been first used with the purpose of quantitatively

classify different pore systems, and relate these pore systems to porosity and permeability of a potential reservoir rock (Ehrlich et al., 1984; 1991a; 1991b). More recent studies focused on measuring the influence of DIA-derived pore geometry parameters on various petrophysical properties, such as total porosity (Anselmetti et al., 1998), permeability (Anselmetti et al., 1998; Weger et al., 2009), sonic velocity (Weger, 2006; Verwer et al., 2008; Weger et al., 2009), shear moduli (Verwer et al., 2010), electrical resistivity (Verwer et al., 2011), and water saturation (Aliakbardoust & Rahimpour-Bonab, 2013). Additionally, DIA has been used to evaluate micrometer- and nanometer-sized pores by analyzing scanning electron microscope (SEM) -derived backscattered electron (BSE) images (e.g., Loucks et al., 2009). At these pore scales, DIA is the prevalent tool for analyzing pore types and systems (Milner et al., 2010; Sondergeld et al., 2010; Loucks et al., 2012; Slatt & O´Brian, 2013). Computed tomography (CT) scans or magnetic resonance imaging (MRI) of a sedimentary rock, in combination with appropriate image analysis software, allows for measuring the geometry of a pore system in 3D. For instance, the impact of ichnofacies on petrophysical properties within a reservoir succession can be quantified (Pemberton & Gingras, 2005), or a complete three-dimensional analysis of pore system can be performed (e.g., Knackstedt et al., 2009; Hemes et al., 2015; Sun et al., 2017). DIA can also be applied to the solid matrix of a rock to measure the size, roundness, sorting and sphericity of grains or crystals (Maerz, 2012; Kasper et al., 2013), or quantify the degree of cementation and compaction (Mowers & Budd, 1996; Cook et al., 2011). By using images from thin sections with different orthogonal orientations from one sample plug, the geometry of pore system can be measured in quasi-3D, resulting in information about preferential fluid flow pathways (Maerz, 2012). Conclusively, DIA allows for analyzing the impact of sedimentary, biological and diagenetic processes on pore system geometry and therefore on petrophysical properties. Moreover, it is also widely used as a tool to evaluate pore systems and effective porosity in material sciences (e.g., Martin III et al., 2013; Renshaw et al., 2016).

Additionally, within the last decade, rock-typing has been established as an advantage method in petrophysics to improve the understanding and prediction of porosity and permeability distribution in a potential reservoir succession (Giot et al., 2000; Javaux et al., 2000; Porras & Campos, 2001; Granier, 2003; Rushing et al., 2008; Venkitadri et al., 2005; Hollis et al. 2010; Vahrenkamp & Creusen, 2010; Fournier et al., 2013; Rahimpour-Bonab & Aliakbardoust, 2014; Skalinski & Kenter, 2014). Rock types are bodies of potential reservoir rocks with similar petrophysical properties which can be predicted using core, log and seismic data as well as by sedimentological methods (e.g., Al-Habshi et al., 2003; Hollis et al., 2010; Vahrenkamp & Creusen, 2010; Skalinski & Kenter, 2014). Therefore, rock-typing also utilizes the interplay between sedimentary fabric including its associated pore structure and the resulting petrophysical response in order to understand the facies-dependent porosity-permeability generation and distribution. Hollis et al. (2010) used pore geometry of different carbonate lithofacies types as the main parameter for rock-typing of samples with similar pore system evolution and properties. This is crucial, since two samples which have identical permeability values can also have different recovery efficiencies, depending on their distinct pore geometry (Hollis et al., 2010).

1.3 Motivation and Goals

The main motivation of this thesis is to better understand the factors controlling the often heterogeneous distribution of pore system properties (i.e., porosity and permeability) in carbonates, and the relationship between porosity and permeability in general. The main goals are: (i) to develop a petrographic tool based on digital image analysis (DIA), which allows for systematically and comprehensively analyzing pore systems by measuring pore (type) geometry; (ii) to quantitatively characterize facies–specific pore systems in order to identify the most effective pore system and associated sedimentary facies, using the Middle Miocene Nördlinger Ries carbonates as a case study; (iii) to detect small-scale inhomogeneities by analyzing the effect of diagenetic modifications on pore system evolution and properties; and finally (iv) to understand how porosity and permeability are related and distributed, especially in the studied outcrop of marginal lacustrine carbonates. The key for evaluating porosity and permeability generation, particularly in carbonates, and understanding their complex mutual relationship, is the detection of effective porosity. Therefore, pore shape complexity and fluid flow simulation is used in this thesis to quantify pore interconnectivity, which then allows for identifying effective pore types.

1.4 Structure of this Thesis

Following on the introduction into porosity, permeability, pore system analysis and the method of DIA in this chapter, the database including facies description, petrographic analysis, pore type classification and routine total porosity and permeability measurements are presented in Chapter Two. The method of pore system analysis with DIA is explained as a step-by-step workflow in Chapter Three, each step providing successively more detailed information about the analyzed pore system. The method is then applied in Chapter Four to the pore systems of all selected samples, and the resulting DIA-derived information are then combined in a petrophysical facies to detect the most effective pore type, pore system and the corresponding sedimentary facies type of the Ries lake carbonates. In Chapter Five, the modification of pore system by cementation is examined, and the impact of cementation on porosity and permeability is quantified with DIA. This results in cementation reduction values for each relevant pore system parameter. In Chapter Six, the hereby presented approach is tested by using an independent method (i.e., fluid flow simulation) applied on the same dataset. Results of the DIA-based workflow and fluid flow simulation are then compared. This comparison also helps to identify potential limitations of the DIA method presented and to implement improvements. Chapter Seven addresses the general issue of the complex relationship between porosity and permeability in carbonates by evaluating if the correlation between both fundamental parameters can be improved by using DIA-derived pore system data. In Chapter Eight, the conceptual hypothesis of using pore shape complexity as a tool to asses pore type effectiveness is discussed, and the application of DIA for comprehensively analyzing pore types and systems is evaluated. The general conclusions of this thesis are summarized in Chapter Nine.

CHAPTER TWO

DATA ACQUISITION

2.1 Geological Setting

The samples used for this thesis derive from Middle Miocene marginal lacustrine carbonates, exposed at the northern paleomargin of an impact crater lake within the so-called Nördlinger Ries depression (e.g., Bayrisches Geologisches Landesamt, 1974; 1977; Hüttner & Schmidt-Kaler, 1999). Shortly (< 0.1 Ma) after the impact event which is dated at around 14.6 Ma before present (Buchner et al., 2010), a saline crater lake in a closed lacustrine system developed (e.g., Arp et al., 2013), which led to the deposition of 250 meters of basinal lacustrine mudstones in the lake center and around 50 meters of lacustrine carbonates at the lake margin (Arp, 2006, and references therein). For this thesis, the focus was on a quarry in Hainsfarth, located at the northern paleolake margin within an almost continuous belt of marginal lacustrine carbonates along the northern paleolake shore (Figure 2.1).

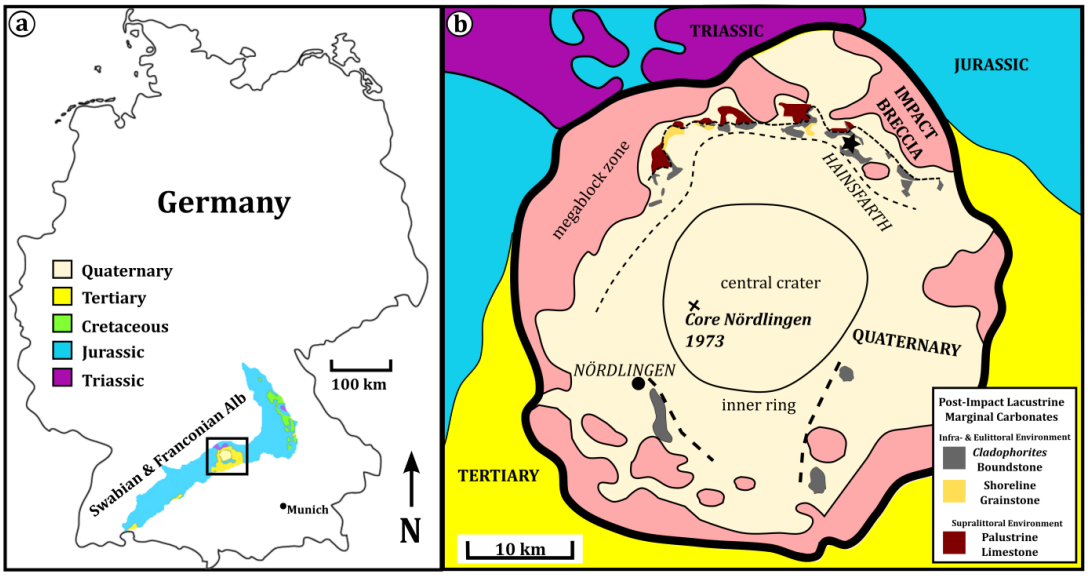

Figure 2.1. Overview and geological setting. a. Map of Germany with location of the Swabian and Franconian Alb which are separated by the Nördlinger Ries impact crater. **b.** Overview map of the Nördlinger Ries impact crater with location of outcrop Hainsfarth (indicated by black star), main structural elements of the crater and position of post-impact marginal lacustrine deposits. Map modified after Riding (1979), position of marginal lacustrine carbonates adapted from Arp (2006).

The exposed marginal lacustrine carbonates encompass individuals and groups of green algae *Cladophorites* build-ups of the infra- to eulittoral lacustrine zone (Arp, 1995b; 2006), and are separated vertically and laterally by sheets and bodies of interbuild-up skeletal and non-skeletal grainstones, which altogether define the main facies architecture (Figure 2.2).

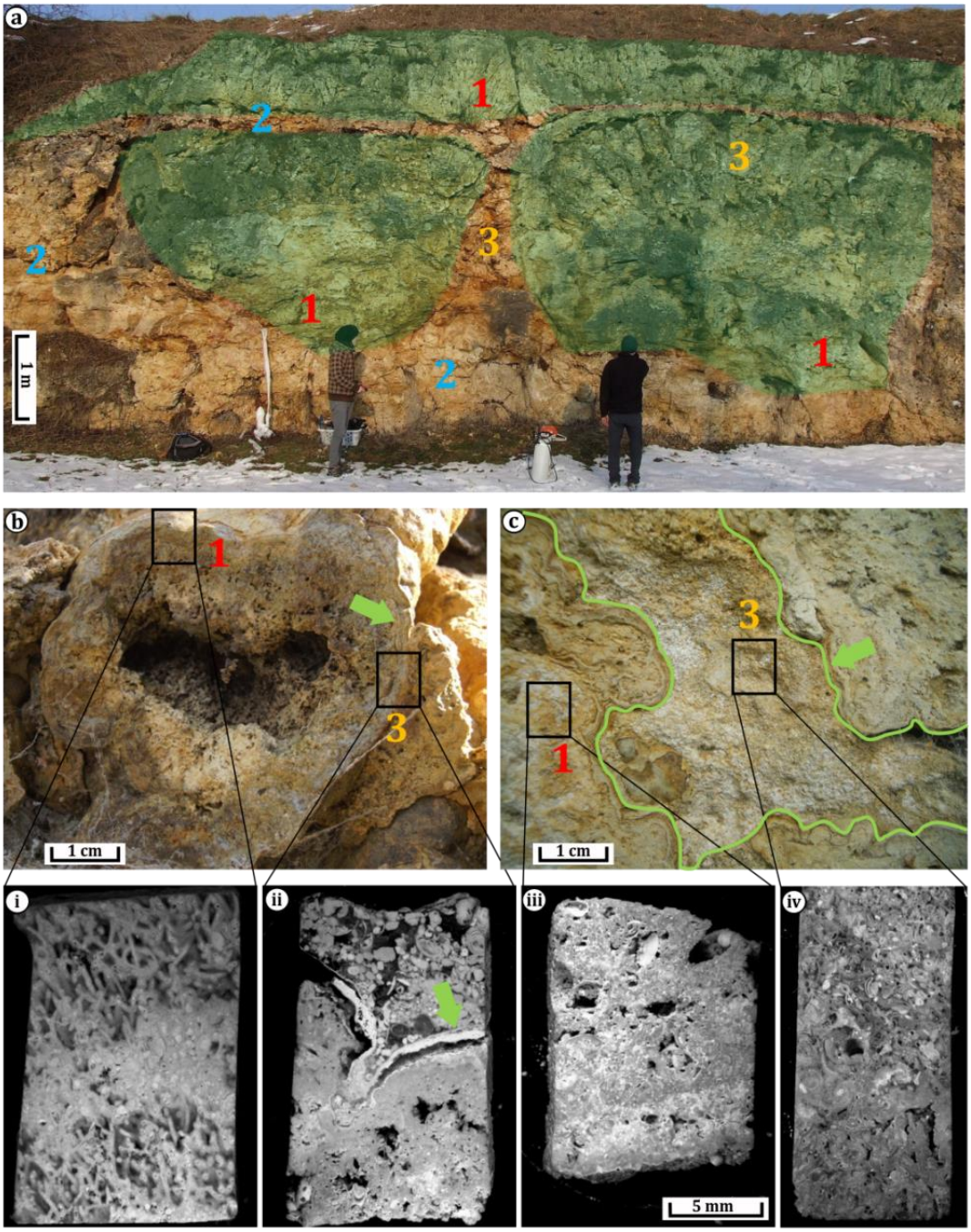

Figure 2.2. Marginal lacustrine carbonates of outcrop Hainsfarth. **a.** Field photographs representing two individual *Cladophorites* build-ups separated by sheets and bodies of grainstone in the central part, and overlain by continuous beds of *Cladophorites* cones in the uppermost part. **b.** Section through a *Cladophorites* green algae cone with original micritic matrix and *Cladophorites* filament traces (i). Conoidal *Cladophorites* framestone facies includes incorporated skeletal and non-skeletal grains, and dissolution voids. A dense and laminated crust veneers *Cladophorites* framestone (ii). **c.** Growth framework space in between veneered and individual *Cladophorites* nodules of the *Cladophorites* bafflestone facies which is in discontinuous contact and predates infilling grainstone. Peloidal grainstone serves as a substrate for *Cladophorites* growth (iii), whereas skeletal grainstone mainly occur as infillings in growth framework space (iv). Numbers indicate *Cladophorites* boundstone (1), non-skeletal grainstone (2), and skeletal grainstone (3) facies. Arrows indicate veneering crust which acts as a barrier between different facies types, preventing interconnection between their pore systems.

As minor facies types, a palustrine breccia rarely occurs as infilling in the growth framework space between individual *Cladophorites* cones and nodules within the *Cladophorites* build-ups. However, this facies type does not represent a laterally and vertically continuous facies. Even less frequently, stromatolites are present in a small area within the uppermost capping beds of the outcrop (Riding, 1979; Arp, 1995b; 2006). Their limited occurrence is mainly caused by the previous erosion of most parts of the capping beds.

Components of grainstones comprise peloids as non-skeletal constituents, and gastropod *Hydrobia trochulus* and ostracod *Strandesia risgoviensis* shells and shell fragments (Figure 2.3), indicating a species-poor but individual-rich environment (Riding, 1979; Arp, 1995b; 2006). Grainstones also occur as infillings in primary growth framework space, together with the palustrine breccia of the supralittoral zone (Arp, 1995b; 2006). There, also the very rare stromatolites have been developed. A total of five facies groups have been previously identified (Riding, 1979; Arp, 1995b; 2006, and references therein), and classified after Dunham (1962): (i) Conoidal *Cladophorites* framestone; (ii) nodular *Cladophorites* bafflestone; (iii) skeletal- and non-skeletal grainstone; (iv) palustrine breccia; and (v) stromatolites. For the purpose of this thesis, both *Cladophorites*-dominated facies types have been summarized as *Cladophorites* boundstone, since they are genetically and textural identical. Grainstones instead are further differentiated into skeletal and non-skeletal grainstones because they are genetically not related, occur independently and are textural different.

2.2 Material and Methods

For this thesis, a total of 16 stratigraphic sections have been measured at the old quarry in the village of Hainsfarth (Bavaria) in Southern Germany. They are distributed over a distance of approximately 250 meters and with a height between 3 to 6 meters. Each stratigraphic section has been described and documented by photographs, which were later used to digitally redraw the distinct macroscopic structures of each facies group, such as the size of algal nodules and cones (Christ et al., 2018). These photos have been combined into a total of four photomosaic compound images in order to trace cycle boundaries and stratigraphic relevant surfaces as well as macroscopic structures throughout the entire outcrop. 154 cylindrical samples have been recovered with a Pomeroy® portable rock drill from three reference sections (Figure 2.4), each representing areas of the outcrop with variations in the facies architectures. The northwestern area of the outcrop is characterized by an equal distribution of small (< 1.5 m) and individual *Cladophorites* build-ups and intercalated grainstones. The central part is dominated by sheets and bodies of skeletal and non-skeletal grainstones, whereas the southeastern area is mainly composed of groups of big (> 3 m) *Cladophorites* build-ups with few grainstones as interbuild-up bodies and infillings in spaces in between the growth framework of *Cladophorites* boundstone. Sampling along each reference section has been carried out systematically by using a 1 m x 1 m grid, subdivided into 16 smaller squares (each 25 cm x 25 cm). Samples have been recovered when the sedimentary facies changed within the subsquares, and when important sedimentary features, such as exposure surfaces, occurred (see Figure 2.4b).

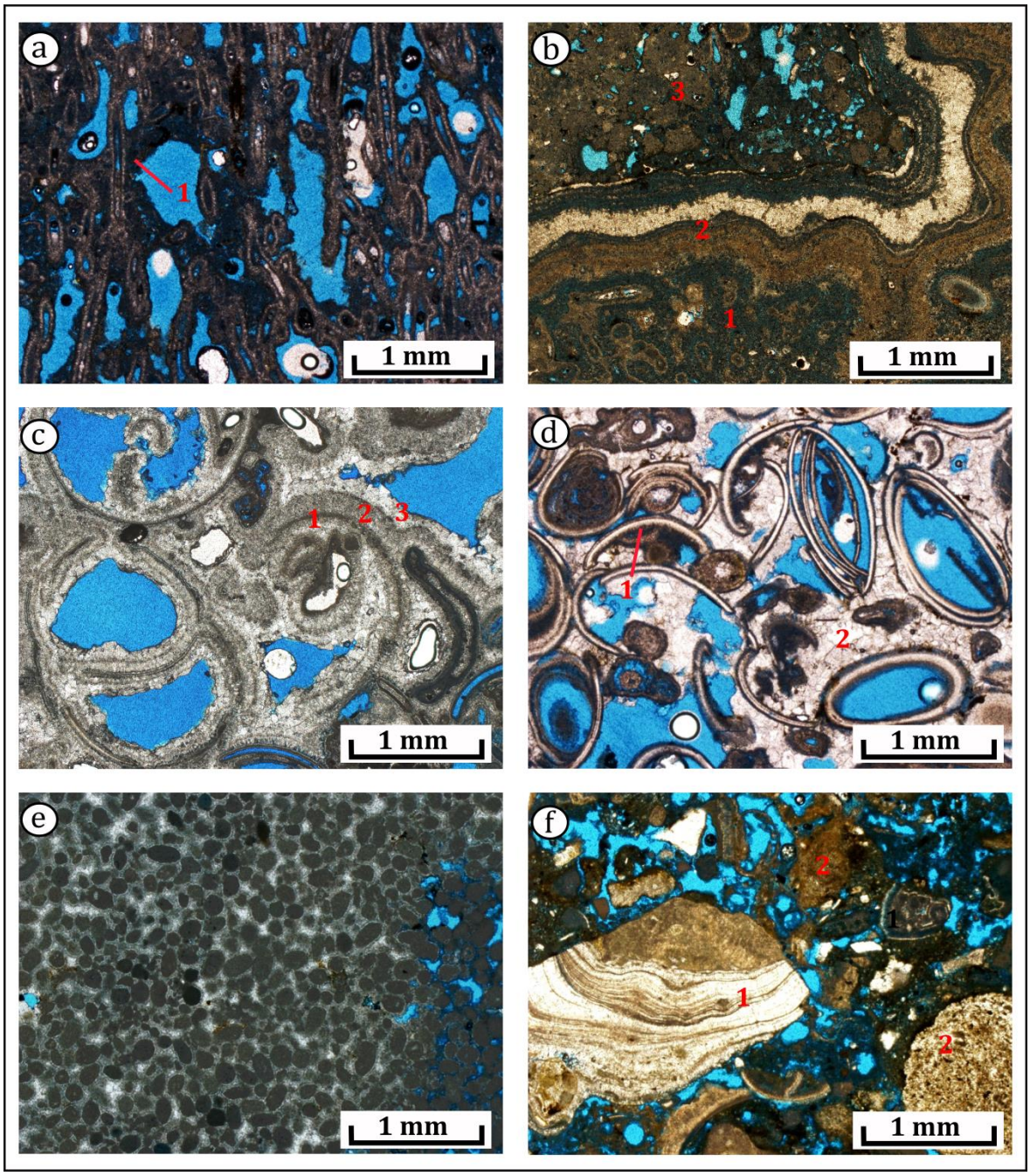

Figure 2.3. Photomicrographs of typical facies types of the northern Ries lake margin. a. Conoidal *Cladophorites* framestone with filament traces rimmed and bound by a dolomicritic rim (1). Filament tubes with preferential erect orientation distinct for *Cladophorites* cones. **b.** Nodular *Cladophorites* bafflestone with filament traces rimmed by dolomicrite (1). Nodules show generally more arbitrarily oriented filament traces and contain more incorporated skeletal grains. A thick, dense and laminated crust (2) separates nodular *Cladophorites* bafflestone from younger grainstone (3). **c.** *Hydrobia trochulus* (gastropod) grainstone with dolomicritic rim (1), inclusion-rich (2) and inclusion-poor (3) calcite cement. **d.** *Strandesia risgoviensis* (ostracod) grainstone with dolomicritic rim (1) and inclusion-poor (2) calcite cement. **e.** Peloidal grainstone with individual peloids rimmed and bound by a thin dolomicritic rim. **f.** Palustrine Breccia with intraclasts of previously eroded *Cladophorites* build-ups (1) and extraclasts (2).

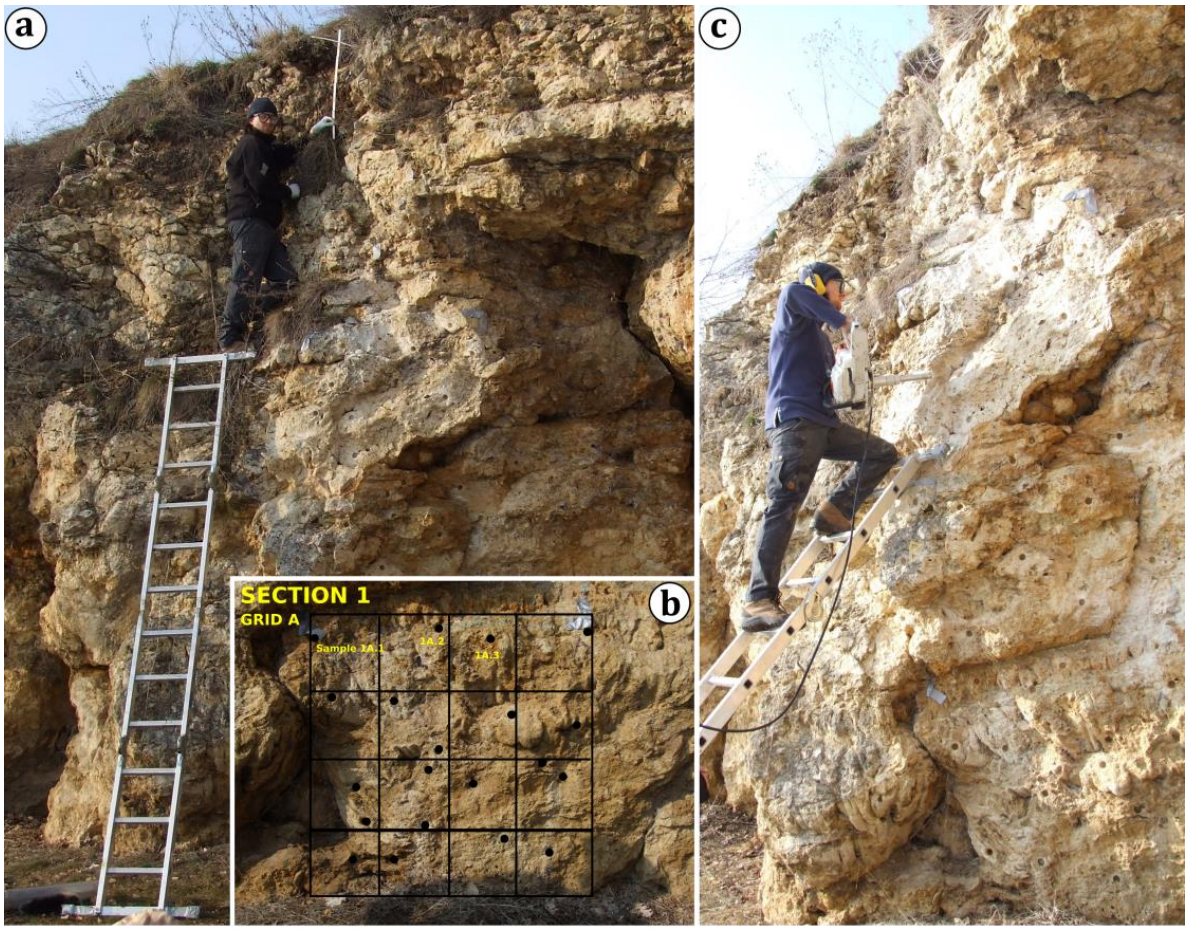

Figure 2.4. Sample recovery at the outcrop in Hainsfarth, Bavaria (Southern Germany). a. Measuring of stratigraphic logs. **b.** Subdivision of log into 1 m x 1 m grids for systematic sampling. **c.** Recovery of sample plugs with a Pomeroy® portable rock drill.

Prior to thin section analysis, total porosity and permeability of each sample plug has been measured. From the total sample suite of 154 samples, porosity and permeability values from the plug of 122 samples were successfully obtained, because some plugs were too small for porosity-permeability measurements as they partially broke during sample recovery, or they were not sufficiently consolidated to properly perform gas-injection permeability measurements, which mainly occurred in samples of the skeletal and non-skeletal grainstone facies. All 122 measured plugs have been cut horizontally into two smaller cylinders. The first cylinder has been used to determine total porosity with helium injection porosimetry. Blue-dyed thin sections of each sample have been produced from the second cylinder, which were needed to acquire microphotographs for digital image analysis (DIA) with a *DP73*© digital camera mounted on a *BX51*© polarizing microscope, both devices and the corresponding *Steam*© software from Olympus®. Petrographic characterization of each sample includes the identification of the nature of each skeletal and non-skeletal grain, point counting to quantify the amount of each component, and SEM and electron microprobe analysis to detect the distribution of dolomite and calcite. SEM analysis has been conducted with a JEOL® *JSM-6510*© microscope, including the *INCAx-act*© Energy Dispersive X-Rays Spectrometer (EDS) from Oxford Instruments® to perform quantitative element analysis. With the *INCA*© software, microporosity was quantified on site by selecting the black color hue

of each analyzed BSE image. Additionally, a JEOL® *JXA-8200*© electron microprobe has been used to generate element maps. Finally, each sample was categorized into one of the five sedimentary facies groups.

For the first part of the thesis (Chapter Three and Four), 32 samples have been selected in order to develop the workflow and analyze the pore system of the Ries lake carbonates. These samples have been selected in particular since they clearly represent an unaltered and pristine facies-specific pore system, without any major modification by cementation and without mixing of different facies types, since this would lead to unrepresentative pore system data. This allows for analyzing the facies-specific framework in which porosity and permeability is generated and also guarantees that the previously measured porosity and permeability values of these samples can be clearly assigned to a distinct sedimentary facies type and its associated pore system, which is essential for the method presented. The amount of samples chosen for each facies type also represents their relative abundance and occurrence throughout the studied outcrop. From each sample thin section, several images have been acquired, representing low, intermediate and high image analysis porosity (Φ_{DIA}). By calculating the average porosity value for each thin section with DIA from these images, an image for each sample has been selected which encompass all pore types present and which measured Φ_{DIA} value is identical to the average value of the thin section. Then, pore geometry of each individual pore in the image has been quantified which resulted in several hundreds to thousand individual pore data for each analyzed thin section image. As a result, a total of 23,508 individual pore geometry data have been obtained, which guarantees a robust statistical database and which were then summarized into 77 mean values of pore type geometry and properties.

For Chapter Five of the thesis, 52 thin section images from additional 23 facies-specific samples have been selected which all show extensive local and patchy cementation of preexisting pores, but without complete overprinting of the original texture and pore structure, which occurred in many of the measured 122 samples. These 23 samples have been excluded from detection of the most effective pore system as presented in Chapter Three and Four, since their modified pore type structure is not representative for the pore-type-specific geometry. However, their thin section images are used in Chapter Five to quantify the impact of cementation on pore system properties, since the original pore structure was still recognizable. The selection of samples which clearly represent the pore system in each facies type is crucial for this approach, because it allows for directly comparing properties of each occurring facies-dependent pore system. Since only three samples of stromatolites have been recovered due to their limited occurrence in a small area within the uppermost capping beds of the central part of the outcrop (Riding, 1979; Arp, 1995b; 2006), this specific sedimentary facies type has been excluded in advance from further analysis.

2.3 Pore Types

In all samples examined, a total of seven primary and secondary pore types have been identified and classified according to Choquette & Pray (1970). Few pore type classes have been modified and adapted to better describe the pore types of the studied lacustrine carbonates.

Interparticle pores: Primary interparticle pores mainly occur in between peloidal grains of the non-skeletal grainstone facies (Figure 2.5a). Therefore, they are described as interpeloidal pores (*Pore type 1*). These interpeloidal pores represent a primary pore space formed by the initial arrangement of peloids after deposition. Interpeloidal pores usually do not outpace the average size of surrounding peloids, but tend to have relative complex contours with numerous pore throats. In the skeletal grainstone facies, interparticle porosity in between skeletal grains is rare to absent, since interparticle space is either often reduced and filled by cement, or interparticle pores are also tied to pore space in between incorporated peloidal grains. Pore space between intra- and extraclasts within the rare palustrine facies occurs as interclastic porosity (Figure 2.5b).

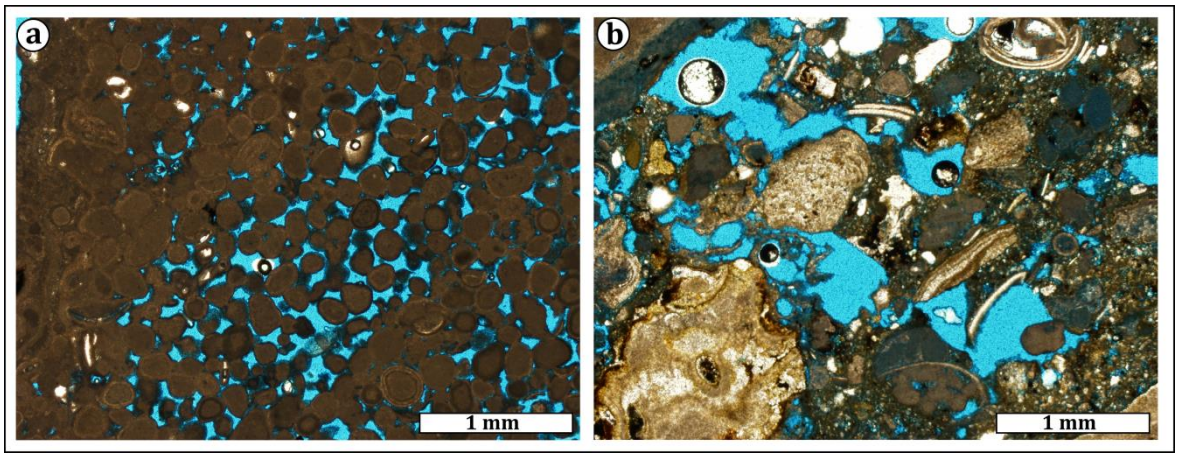

Figure 2.5. Pore types in the Nördlinger Ries carbonates I. a. Interparticle porosity in between peloidal grains. **b.** Interparticle porosity in between intra- and extraclasts of the rare palustrine breccia.

Intraparticle pores: Since interparticle pore space between skeletal grains is often closed by multiple phases of cementation, porosity in the skeletal grainstone facies is mainly tied to primary intraparticle pores (Figure 2.6a). Intraparticle pores are located within chambers of gastropod *Hydrobia trochulus* and ostracod *Strandesia risgoviensis* shells. Since both organisms produced aragonitic shells, they have been dissolved relatively soon after deposition, which also amplified early precipitation of cement in between skeletal grains in this sedimentary facies type. Their size and shape is confined by the structure of the corresponding skeletal chamber. Since only one species of both gastropod and ostracod occurs in this marginal lacustrine setting, no significant variations in size and shape caused by a different shell structure of other species types are observed. Since intraparticle pores mainly occur within skeletal grains, they are described according to the pore-hosting skeletal grain as either intraostracodal or –gastropodal pores, summarized as intraskeletal (*Pore type 2*).

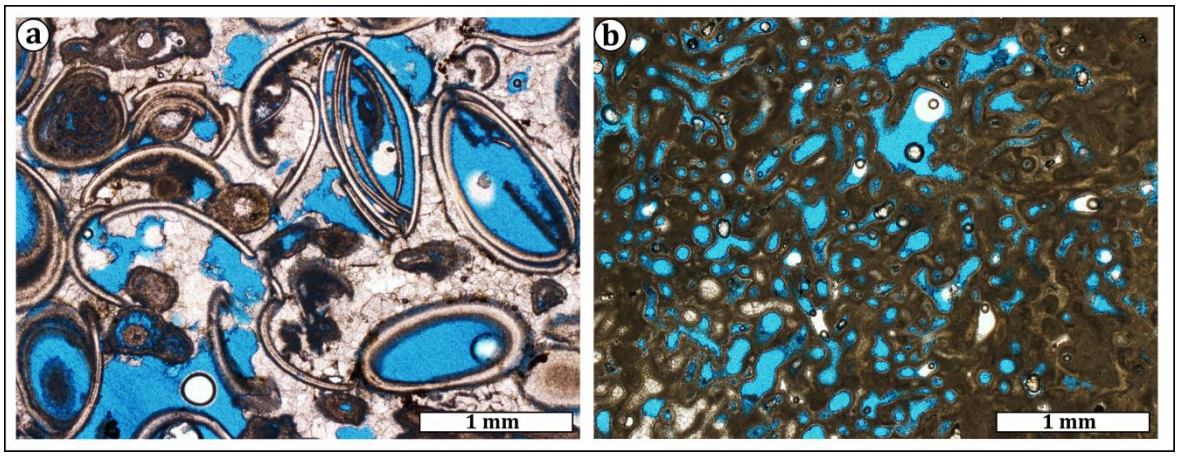

Figure 2.6. Pore types in the Nördlinger Ries carbonates II. a. Intraparticle pores within skeletal grains**. b.** Molds of *Cladophorites* filaments.

Moldic pores: In the *Cladophorites* boundstone facies, the filament traces of *Cladophorites* green algae are preserved, which left late primary to early secondary molds (see Figure 2.6b). These molds have been preserved and stabilized due to early precipitation of a rim of dolomicrite around *Cladophorites* stems (Riding, 1979; Arp 1995b; 2006). This thin dolomicritic rim is only present in primary pore types (i.e., interpeloidal pores, intraskeletal pores and filament molds) and are absent in all secondary pore types. Therefore, the timing of this rim-forming process is syndepositional to early diagenetic and consequently *Cladophorites* filament molds are classified as late primary to early secondary pores. Since this moldic pore type is exclusively tied to the filament traces of *Cladophorites* green algae, it is referred to as filament moldic pores (*Pore type 3*). In the skeletal grainstone facies, late secondary moldic pores occur as dissolved former aragonitic shells of gastropods and ostracods, and therefore pores are often elongated and relatively thin (Figure 2.7a). Their origin and timing clearly differ from filament molds because they are only present since the original shell has been rimmed by the earlier precipitated dolomicrite prior to dissolution of the shell. Hence, they are sub-categorized as gastro- and ostramoldic pores, summarized as skeletal moldic pores (*Pore type 4*).

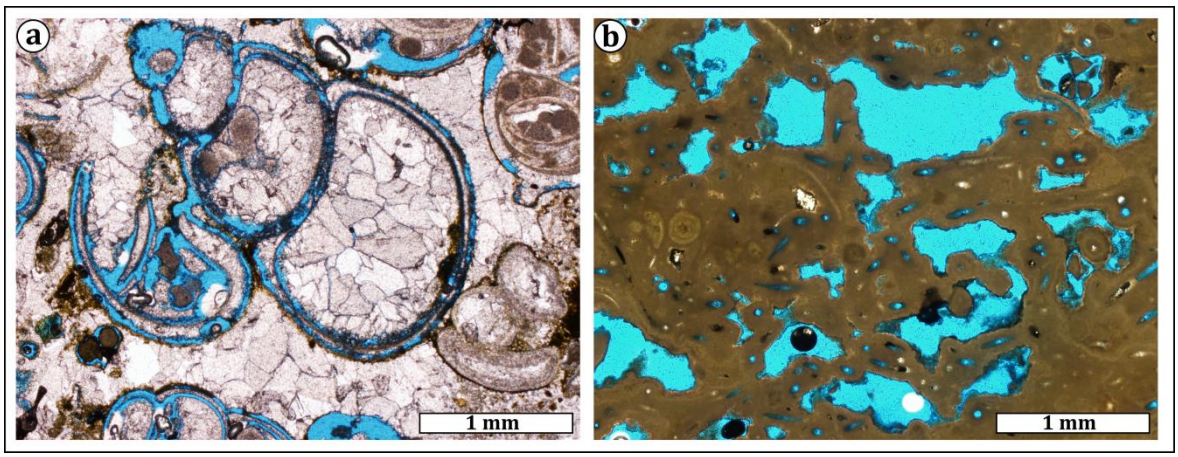

Figure 2.7. Pore types in the Nördlinger Ries carbonates III. a. Molds of skeletal grains**. b.** Vugs (with filament molds).

Vuggy pores: Late secondary vuggy pores occur in all sedimentary facies types, presumably formed by meteoric dissolution due to subaerial exposure in the eogenetic to telogenetic zone (Riding, 1979; Arp, 2006) of the marginal lacustrine build-ups (*Pore type 5*). Although their non-fabric selective nature leads to variable sizes and shape of vugs, this pore type generally occurs as big and very tortuous pores, with wide pore throats and high interconnection with adjacent pores (Figure 2.7b). The size and shape of vugs strongly depend on the extent and intensity of meteoric dissolution, which also controls if vugs are touching or not (sensu Lucia, 1983).

Laminae and fracture pores: Only few pores occur as fractures and along laminae within the *Cladophorites* boundstone facies (Figure 2.8), however they often occur together and appear to originate tertiary from mechanical weakening during thin section preparation. Due to their rareness, uncertainty in origin and little contribution to porosity and permeability, this pore type (*Pore type 6*) is not further considered for evaluation in this thesis.

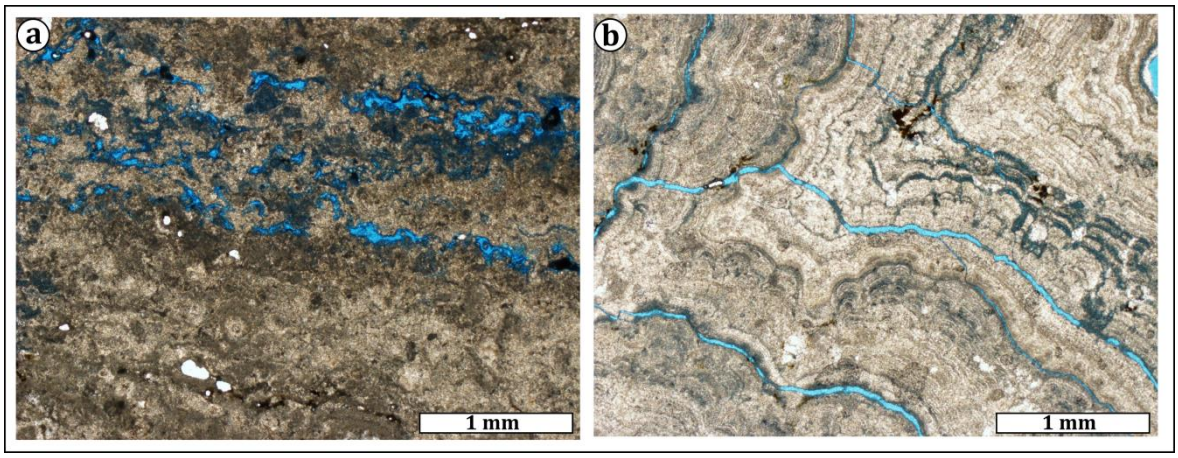

Figure 2.8. Pore types in the Nördlinger Ries carbonates IV. a. Laminae porosity**. b.** Fractures**.**

Micropores: Since microporosity (pore width < 10 µm) is usually not captured by DIA on thin section images, but can generate a highly effective pore system, for example in chalks (e.g., Fabricius, 2003; 2007), the types of micropores have been examined by using SEM-derived backscattered (BSE) images from eight rock chips covering each facies type, which then allows for quantifying microporosity (Figure 2.9). Additionally, by visualizing the micropore system, each occurring type of micropore (*Pore type 7*) is described in order to complete the pore type classification of the studied lacustrine carbonates (Figure 2.10). The contribution of microporosity to total porosity has been calculated by using digital image analysis directly applied during SEM examination to each microporous area of the analyzed chip (e.g., Anselmetti et al., 1998; Anovitz & Cole, 2015, Buckmann et al., 2018). Figure 2.9a shows an image of an area with highest microporosity measured in all samples analyzed for microporosity. There, microporosity encompasses 9.12 % of the total image porosity of 20.48 %. This image represents a rare matrix-related micropore system within an ostracodal grain which has been incorporated into the

Cladophorites boundstone facies and filled with micrite. Microporosity occurs as microintercrystalline porosity and as few micromolds in the micritic matrix within the ostracod shell.

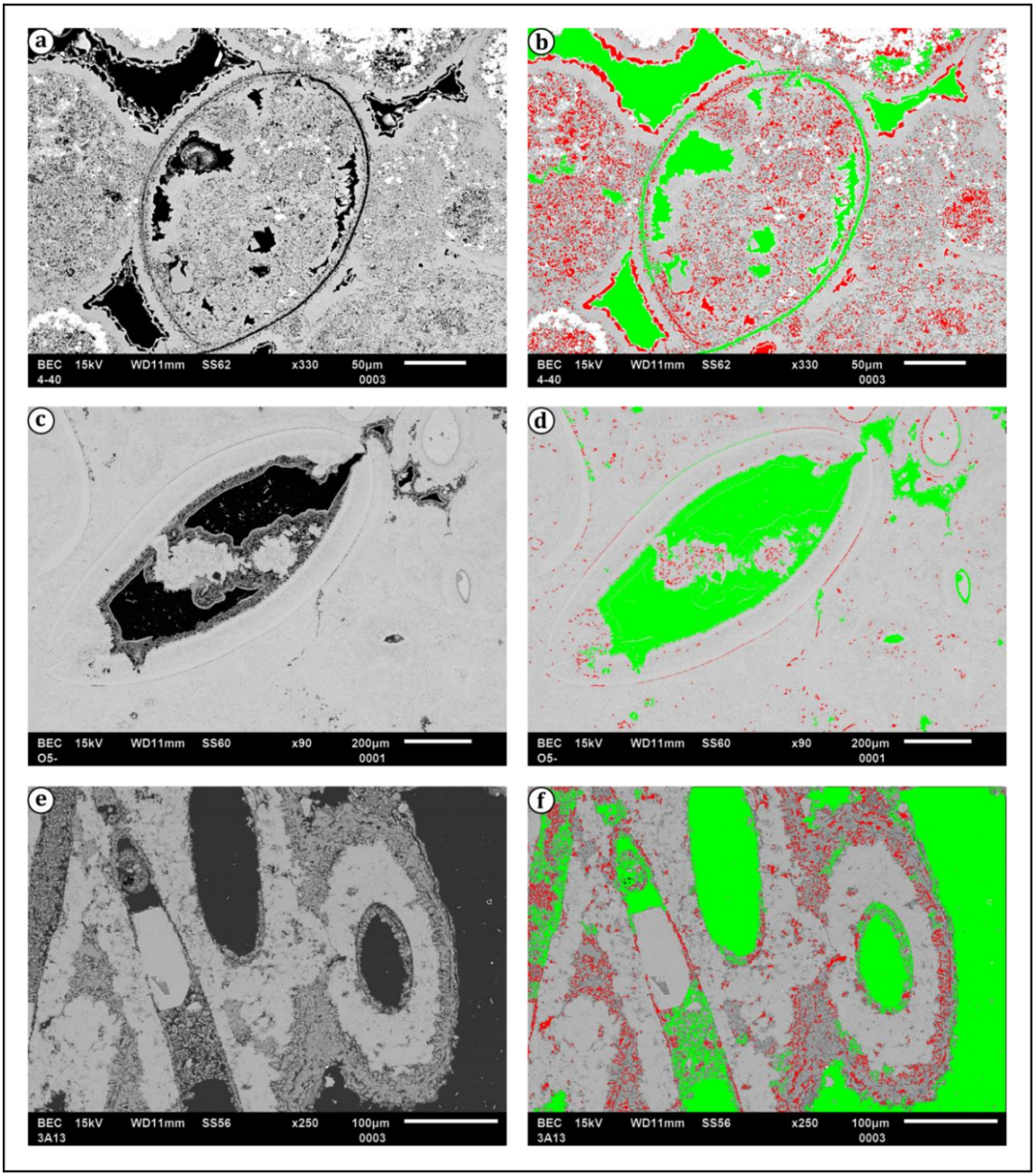

Figure 2.9. Microporosity analysis on BSE images. a. Micropore system within an incorporated ostracod within the *Cladophorites* boundstone facies. **b.** There, highest microporosity (red color) detected (9.12 %) is related to the micrite within the skeletal grain. **c.** Micropore system in the cemented skeletal grainstone facies. **d.** Lowest microporosity detected (0.98 %) has been measured in the cemented intergranular space. **e.** Micropore system in the *Cladophorites* boundstone facies with open meso- and macropore system. **f.** Microporosity is tied to the dolomicritic rim (3.83 %). Green areas represent mesopores (> 10 µm).

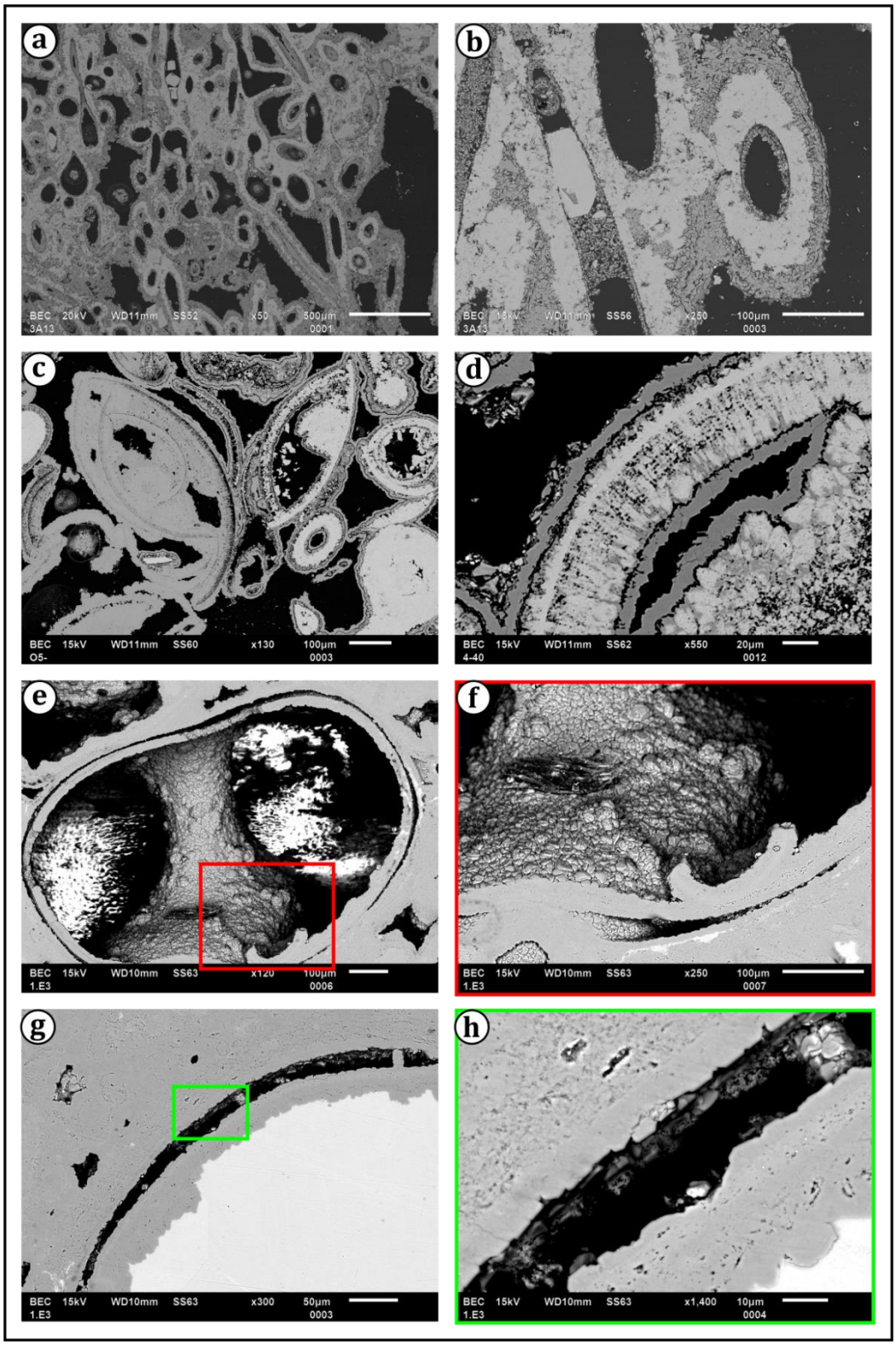

Figure 2.10. Micropore types in the Nördlinger Ries lake carbonates. a. *Cladophorites* framestone with filament moldic porosity (black color). **b.** Microintercrystalline porosity (black color) in surrounding dolomicritic rim (dark grey color). **c.** Intraskeletal pore and skeletal mold of *Strandesia risgoviensis* ostracod. **d.** Microintercrystalline porosity (black color) in surrounding dolomicrite (dark grey color). **e.** Intraskeletal pore and skeletal mold of one *Hydrobia trochulus* gastropod. **f.** Microporosity is present as few micromolds and as microintercrystalline porosity between cement crystals **g.** Mold of one ostracod shell (center) and interpeloidal pores (left). **h.** Microporosity is represented as microintercrystalline porosity within the micritic matrix (top left) and by micromoldic porosity (bottom right).

In the non-skeletal grainstone facies, microporosity is also present as few microintercrystalline pores and micromolds within the micritic peloidal grains. If the intergranular pore space is partially or completely closed by cement, microporosity occurs as few micropores along the boundaries of the calcite cement crystals, and rarely as micromolds. In Figure 2.9c, microporosity within the cemented intergranular space encompasses only 0.98 % of the total image analysis porosity of 15.63 %. In most samples analyzed, both micritic matrix and cement between components are totally absent and space between each grain and component is open, generating meso- to macropores. Microporosity is then tied to the boundaries of dolomite cement crystals of the thin dolomicritic rim (Figure 2.9e). There, micropores produce an image analysis porosity of 3.83 % in respect to total porosity of 30.56 %. As a result, microporosity is less than 5 % on average in all SEM-derived images analyzed. Consequently, all pore systems of the studied marginal lacustrine succession are dominated by meso- to macropores, and micropores are not further evaluated for their effectiveness. Conclusively, the majority of all pore systems analyzed for this thesis is composed of assemblages of five main pore types (i.e., *Pore type 1 - 5*), and therefore only these pore types are considered for evaluating pore type effectiveness with DIA (Figure 2.11).

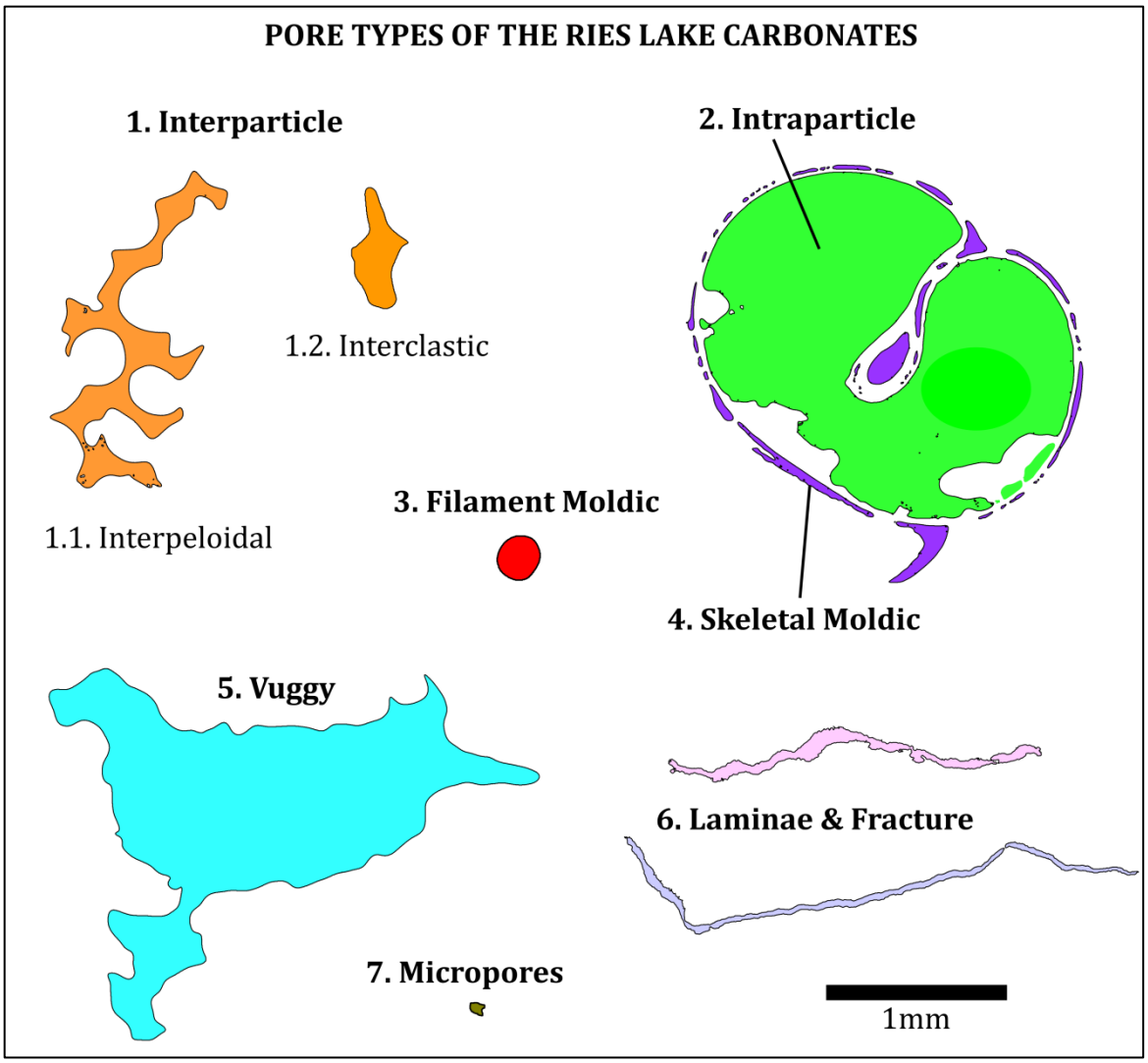

Figure 2.11. Pore types in the Nördlinger Ries lacustrine carbonates. For evaluation of pore type effectiveness, micropores has been excluded due to their insignificance as well as laminae pores and fractures due to their rare occurrence.

2.4 Total Porosity and Permeability

Total porosity (Φ_{total}) has been measured by using a combination of helium-injection with the *AccuPyc 1330*© pycnometer which results in the absolute density of the sample, and measurements of the bulk (or envelope) density with the *GeoPyc 1360*©, both devices from Micromeritics®. The density difference between both values can then be used to calculate the volume of pore space, if the weight of the sample is known. Total permeability (K_{total}) measurements have been conducted by nitrogen-injection with the *Digital Probe Permeameter*© from Corex®, performed on top of each plug which has also been used for thin section preparation, ensuring that the images represent the area of the sample where permeability has been measured.

The petrophysical measurements revealed a wide range of Φ_{total} and K_{total} in all sedimentary facies types analyzed. Φ_{total} ranges between 3.88 % and 46.03 %, whereas K_{total} shows values between 1.20 mD and 3543.50 mD (Table 1). This high variation is further marked by a very low correlation coefficient R^2 of 0.09 between total porosity and permeability measured with routine injection methods. There is also no clear tendency of one distinct sedimentary facies type to exhibit exceptional high petrophysical properties as compared to all other facies types. However, the mean value and the range of K_{total} values of the non-skeletal grainstone facies indicate that its pore system is capable of producing highest permeability.

Sedimentary Facies	Mean Φ_{total} [%]	Range Φ_{total} [%]	Mean K_{total} [mD]	Range K_{total} [mD]
***Cladophorites* Boundstone** (32 samples)	**18.60**	5.64 – 35.82	**422.87**	2.10 – 2265.02
Skeletal Grainstone (34 samples)	**21.02**	6.97 – 42.89	**397.96**	1.32 – 1867.00
Non-Skeletal Grainstone (49 samples)	**19.62**	3.88 – 40.39	**442.54**	1.20 – 3543.50
Palustrine Breccia (7 samples)	**23.70**	12.72 – 46.03	**201.92**	1.60 – 655.00
All Samples (122 samples)	**19.98**	3.88 – 46.03	**411.15**	1.20 – 3543.50

Table 1. Total porosity and permeability data from routine injection methods for each analyzed facies type of the Nördlinger Ries marginal lacustrine carbonates

The wide range of Φ_{total} and K_{total} values results from inhomogeneous, mixed (or multimodal) and facies-specific pore systems, each formed by an assemblage of at least two different pore types with variable

effectiveness. Some of the 122 measured samples which have not been used for the DIA method include two different facies-specific pore systems, for example infillings of grainstones or of the palustrine breccia within the growth framework of the *Cladophorites* boundstone facies, or peloidal grainstones as a substrate on which *Cladophorites* grew. Additionally, as previously noted, many samples show extensive local and patchy cementation of pore system up to an complete overprinting of the original sedimentary texture and pore structure, which also leads to a high variation in porosity and permeability within each sedimentary facies type.

CHAPTER THREE

METHODOLOGY: STEP-BY-STEP WORKFLOW FOR QUANTITATIVE PORE TYPE CHARACTERIZATION

3.1 Introduction

In this chapter of the thesis, a step-by-step workflow is presented which uses quantitative information on the geometry of pores derived from digital image analysis (DIA) to evaluate the effectiveness of each relevant pore type. It builds on the previous work by Anselmetti et al. (1998) and Weger (2006) in utilizing the fundamental implications of their conceptual studies on the relationship between pore geometry and petrophysical properties (i.e., porosity and permeability), with the purpose of performing a detailed and comprehensive analysis of a carbonate-typical mixed pore system composed of an assemblage of geometrically and genetically different pore types. In fact, the two distinct pore geometry parameters pore width and pore shape factor γ (sensu Anselmetti et al., 1998) are used to calculate the contribution of each individual pore type to total porosity and permeability, respectively, which results in the characterization of pore interconnectivity and quantification of effective porosity produced by each pore type present. A combination of both pore geometry and petrophysical parameters allows for establishing a petrophysical facies for each pore type which is then used to identify the most effective pore type(s) in these multimodal carbonate pore systems. Additionally, by analyzing each pore type individually, the evolution of the entire pore system can be reconstructed.

For this workflow, *JMicroVision*© has been used as image analysis software to visualize the pore system, quantify pore geometry and detect the effective pore type(s). It is a toolbox to describe, measure and quantify components of all kinds of images within a very intuitive working interface (Roduit, 2018). The software is ideal to analyze thin section images for various applications in geoscience. Both pores and sedimentary fabric components such as grains and cements can be detected and classified, and their geometry can be quantified. At first, the methodological approach presented in this chapter has been developed and tested on thin section images of 11 selected peloidal grainstone samples with the purpose to demonstrate the workflow. This facies type has been chosen in particular since it represents the most abundant sedimentary facies type in the studied outcrop, and encompasses a generally open and interconnected pore network composed of a co-occurrence of two different pore types, which are primary interpeloidal pores and secondary vugs. Both pore types are very abundant in the pore system and provide the largest number of individual pore geometry data for one sedimentary facies type with over 12,941 values, which also guarantees a statistically robust dataset to develop the method.

The methodological workflow is subdivided into four main steps:

Step I: Pore System Quantification

Requirements: Thin section and/or BSE images

Outcome: Pore geometry data, pore type classification, DIA porosity (Φ_{DIA})

Step II: Pore Size versus Shape

Requirements: Pore width, pore shape factor γ (sensu Anselmetti et al., 1998)

Outcome: Pore size, shape, abundance, efficiency

Step III: Effective Pore Type

Requirements: γ, total permeability, proportion of pore type

Outcome: Permeability contribution ($K_{contr.}$)

Step IV: Petrophysical Facies and Pore System Evolution

Requirements: Pore type class, pore width, abundance, efficiency, γ, Φ_{DIA}, $K_{contr.}$, proportion of pore type

Outcome: Petrophysical facies and pore system evolution

3.2 Quantification of Pore System (Step I)

During Step I, a thin section image is transferred into quantitative pore geometry data by using IHS-thresholding binarization, based on the method described by Anselmetti et al. (1998) and Weger (2006). Pores are detected by setting threshold values for the intensity, hue and saturation spectra of the image. Blue-impregnated pores are segmented by selecting values confining the blue color range of the hue spectra. Occasionally, the rims of pores appear darker than their interior part. Therefore, threshold values of intensity and saturation must be adapted to limit a spectral range which allows for precisely capturing the entire pore (Figure 3.1a). Once all pores are detected properly, Φ_{DIA} is determined. Additionally, the number of all captured pores is calculated and their geometric attributes are measured. A combination of single parameter classification and manual classification has been applied to differentiate between various pore types (Figure 3.1b). By selecting different value ranges for a specific pore geometry parameter which allows for clearly distinguishing between different pore types, all detected pores are assigned to pore type classes depending on the selected range of values. For instance, pore size parameters area or width can both be used to distinguish between vuggy macropores and interpeloidal mesopores. Manual classification has only been used if a previously classified pore was not assigned to the correct pore type class. This only occurs if the primary parameter used for automatic classification partly overlap between two different pore types. As an example, the minimum size of vugs can be equal or lower as the maximum size of interpeloidal pores. As a result of the classification, Φ_{DIA} and number of pores (or abundance) of each pore type class are obtained (Figure 3.1c), and numerous pore geometry parameters such as area, perimeter, length, width and elongation are quantified for each detected pore.

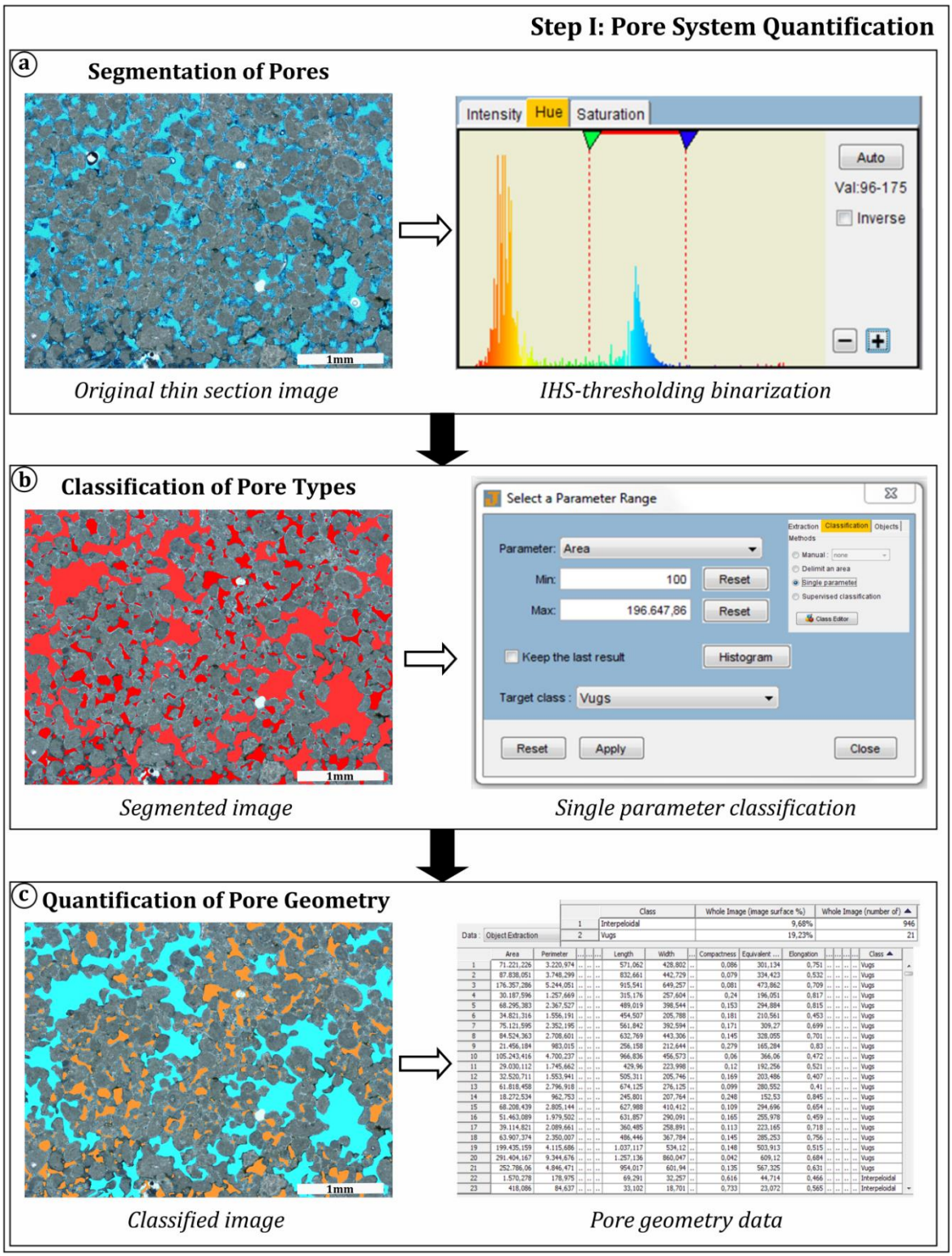

Figure 3.1. Step I: Quantification of pore system with digital image analysis (DIA). a. Pores are segmented from the surrounding solid matrix by using IHS-thresholding binarization. **b.** Pores are classified into pore types by using single parameter classification. **c.** Pore geometry of each pore type is quantified, resulting in numerical data for each parameter. *JMicroVision*© (Roduit, 2018) has been used as DIA software.

The geometry of pores has proven to be one of the most important factor controlling petrophysical properties of a sedimentary rock (e.g., Ehrlich et al., 1991b; Lucia, 1995; Anselmetti et al., 1998;

Anselmetti and Eberli, 1999, 2001; Eberli et al., 2003; Baechle et al., 2004; Ehrenberg et al., 2006; Weger, 2006; Weger et al., 2009; Verwer et al., 2010; Verwer et al., 2011). For this thesis, artificial neural networks (ANN) have been generated with the free available software *JustANN*© from Neural Planner Software® in order to test the influence of different petrophysical and pore geometry parameters on porosity and permeability.

For ANN performance, at least two input parameters and one output parameter are needed (e.g., Fausett, 1994). By training combinations of all different input parameters, the weight of each parameter on the output parameter (i.e., porosity or permeability) is calculated. As a result, the parameters which are most important to predict the output parameter are identified. Five parameters have been selected to predict Φ_{total} and K_{total}: Pore width, pore shape factor γ (sensu Anselmetti et al., 1998), Φ_{DIA}, equivalent (circular) diameter (or ED, sensu Weger, 2006) and perimeter over area (or PoA, sensu Weger et al., 2004). All parameters are described in detail by Anselmetti et al. (1998), Weger et al. (2004) and Weger (2006), respectively. Additionally, K_{total} has been used as input parameter for prediction of Φ_{total}, and vice versa.

ANN outcome is in accordance with the results of previous studies (e.g., Anselmetti et al., 1998; Weger 2006; Weger et al., 2009). Pore size, here represented as pore width, is the most important pore geometry parameter describing total porosity, together with Φ_{DIA} (Figure 3.2a). Individual pores within a pore system generate high porosity when their sizes are generally big. Therefore, size parameter pore width can be used as a proxy parameter to estimate porosity. Permeability instead is mainly controlled by the complexity of pore shape. Pore shape factor γ is the most robust pore geometry parameter to predict permeability (Figure 3.2b). This can be explained by the fact that the more complex the contour of a pore is, the higher is its chance to interconnect with other pores (Anselmetti et al., 1998). Complex-contoured, tortuous and branching pore types with high γ values tend to interconnect with adjacent pores more easily to form an interconnected network, since they have more pore throats. Hence, pore types with high γ values represent pores with high interconnectivity and therefore create effective porosity (Anselmetti et al., 1998; Weger, 2006; Weger et al. 2009). This positive correlation between the amount of interconnected and thus effective pores with permeability has been also reported by He et al. (2014). Consequently, γ is used in this thesis to quantify pore interconnectivity and as a proxy parameter to represent the effectiveness of each pore type present.

The dimensionless parameter γ is calculated by using DIA-derived area (A) and perimeter (P) of a pore (sensu Anselmetti et al., 1998):

$$\gamma = \frac{P}{2\sqrt{\pi A}} \qquad [-]$$

It describes how close the shape of a pore is in respect to a perfect circle (in 2D) or a sphere (in 3D). If γ is 1, the corresponding pore has a perfectly spherical shape and therefore the simplest contour possible.

The second most important parameter for permeability prediction is pore width, since big pores also have a higher capability to interconnect with adjacent pores and generally provide a wider and more open pore network as compared to smaller pores. Pore width is directly calculated after the segmentation and classification of pores with DIA.

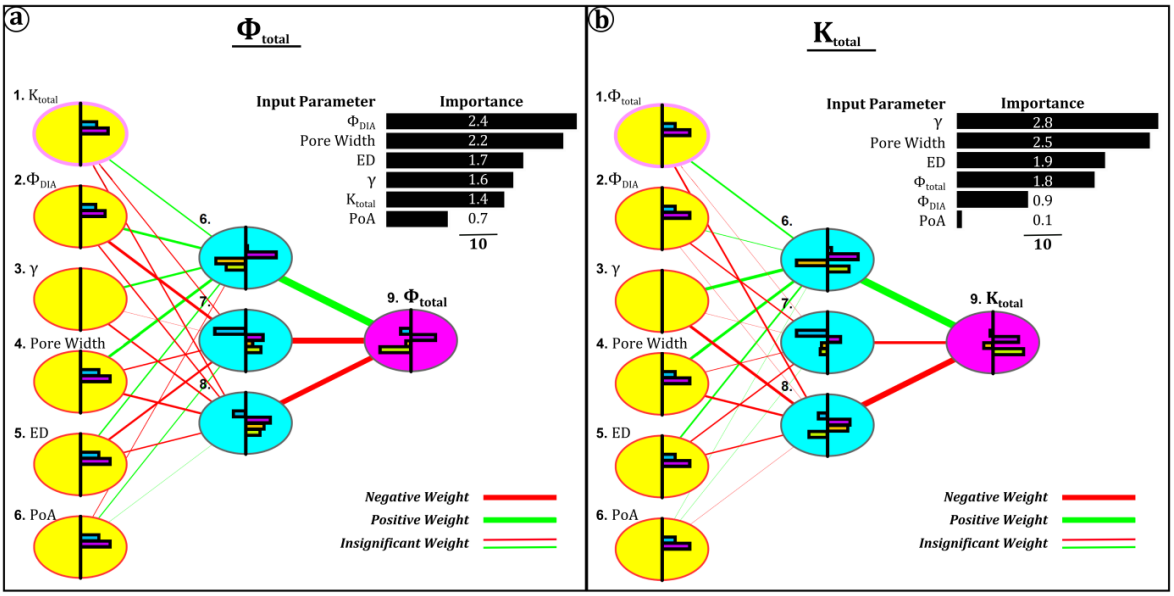

Figure 3.2. Artificial neural networks (ANNs) for porosity and permeability prediction. a. ANN for prediction of Φ_{total}. The higher the importance of one input parameter, the more positive is its weight on the output parameter. **b.** ANN for prediction of K_{total}. For explanation of pore shape factor γ, ED (equivalent circular diameter) and PoA (perimeter over area), see Anselmetti et al. (1998), Weger (2006) and Weger et al. (2004), respectively.

An increase in γ value is equal to an increase in shape complexity of a pore. Additionally, elongation of pores such as molds of shells also result in high γ values. As Anselmetti et al. (1998) noted, γ values < 1 occur in practice due to the digital properties of the thin section image. In a pore system with a high number of insignificant small pores and only few big but more significant pores, the average γ value of the pore system is not representative for its complexity (Anselmetti et al., 1998). Therefore, average γ is calculated by weighting the γ value of each pore by its pore size (i.e., $\overline{\gamma}$, sensu Anselmetti et al., 1998):

$$\overline{\gamma} = \frac{\sum_i (A_i \times \gamma_i)}{\sum_i (A_i)} \qquad [-]$$

Both proxy parameters pore width and γ can be calculated for each individual pore, for each different pore type, and for the entire pore system, and are the base for the next steps of the method.

3.3 Pore Size versus Shape (Step II)

After classifying all pores into different pore types and quantifying pore geometry during Step I, a pore width versus γ plot is generated (Step II). Each individual pore is plotted in respect to its size (i.e., pore width) and shape complexity (i.e., γ), and color-coded according to the pore type classification with DIA. As inferred from artificial neural networks (ANN), both parameters can be used as proxy parameters to estimate porosity and permeability, respectively. The plot displays all different pore types within a pore system, the number of pores within one pore type class, and the size and shape complexity of each single pore. The five fundamental parameters recognized in this plot are pore type, pore width, pore shape factor γ, abundance (i.e., number of pores), which all can be directly determined by using the pore width versus γ plot, and efficiency. This latter dimensionless parameter is calculated by measuring the relationship between the numbers of pores within one pore type class in respect to the porosity these pores generate, and is not to be confused with pore effectiveness. High values of efficiency represent a pore type which produces high porosity with only a small number of pores:

$$\text{Efficiency} = \frac{\Phi_{\text{PoreType}}}{\#_{\text{Pores}}} \times 100 \qquad [-]$$

Figure 3.3 illustrates the example of sample 3.16_1, which is used to visualize the step-by-step workflow in this chapter of the thesis. There, vugs encompass 19.23 % of the DIA-derived porosity (Φ_{DIA}) of 28.91 %. Their average pore width is 386.89 µm (range: 205.75 to 860.05 µm). Vug shape complexity is described by an average γ value of 3.23 (range: 1.89 to 4.88).

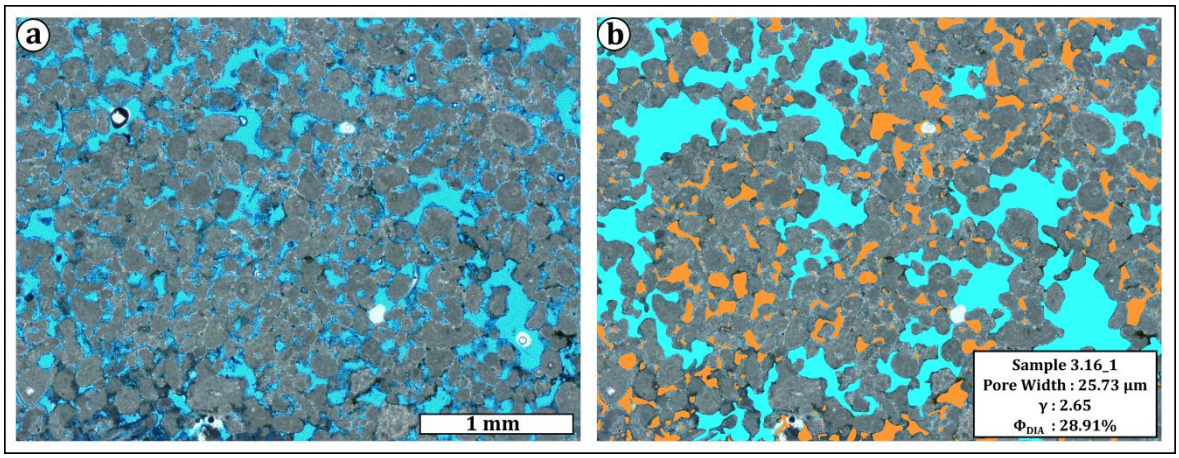

Figure 3.3. Sedimentary fabric and pore system of sample 3.16_1. This sample is used to demonstrate the methodological workflow of pore system quantification with digital image analysis (DIA). **a.** Original thin section image. **b.** Classified thin section image.

Although only 21 vugs occur in this thin section image of the sample, they have a high efficiency value of 91.57 due to their general big size. In contrast, interpeloidal pores provide a Φ_{DIA} of 9.68 % in sample 3.16_1. They are much smaller with an average pore width of 17.71 µm (range: 0.93 to 37.65 µm) and less complex in shape with a γ value of 1.56 (range: 0.76 to 1.64). Interpeloidal pores are very abundant

(n = 946), but due to their small sizes less efficient than vugs, with an efficiency value of 1.02. The entire pore system of sample 3.16_1 shows an average pore width of 25.73 µm, and a γ value of 2.65. A total of 967 pores in the image produce a Φ_{DIA} of 28.91 % and therefore have an efficiency of 2.99 (Figure 3.4).

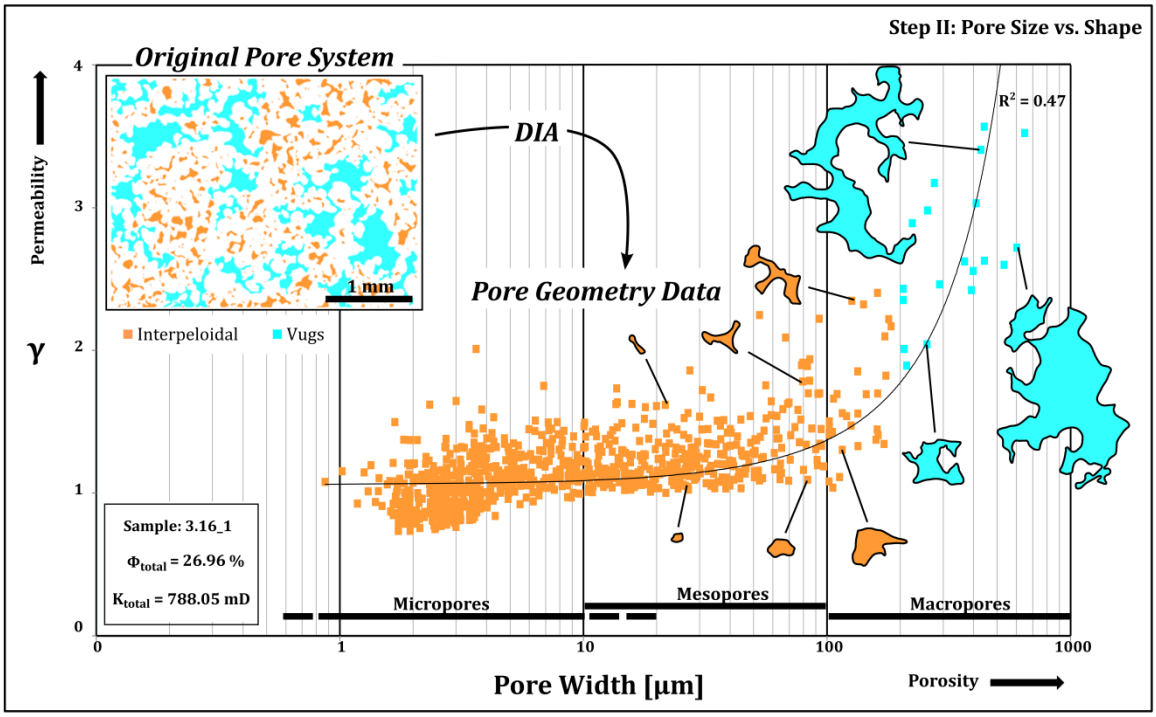

Figure 3.4. Pore width versus γ plot. It represents the pore system of sample 3.16_1, composed of primary interpeloidal pores and secondary vuggy pores. Pore width and γ changes with increasing pore size and complexity, respectively. Individual pores are displayed and their pore geometry values are indicated.

3.4 Effective Pore Types (Step III)

As a next step, the potential permeability contribution ($K_{contr.}$) of each pore type to total permeability (K_{total}) is calculated, resulting in the detection of effective pore types. One or more effective pore types create an interconnected pore network and therefore generate effective porosity in a pore system, making a sedimentary rock permeable. The step of extracting the effective pore network is also usually required prior to performing fluid flow modeling and permeability simulations (e.g., Kayser et al., 2006; Youssef et al., 2007). With this method, the framework (i.e., the sedimentary fabric and its associated pore structure) of which effective porosity originates from is evaluated in regard to its potential to contribute to total measured permeability (K_{total}). Thus, the permeability contribution ($K_{contr.}$) of each individual pore type is calculated in order to quantify pore type effectiveness. Since permeability can be estimated by using the proxy parameter γ (see Figure 3.2), the average γ value for each pore type and for the entire pore system is linked to the total permeability value in order to calculate pore-type-specific $K_{contr.}$ by using a K_{total} versus γ plot. Therefore, it is crucial for this approach to use only samples and corresponding thin section images of which the measured plug also contains only one facies-specific pore system.

In the example of sample 3.16_1 (see Figure 3.4), pore system effectiveness is controlled by either one or both occurring pore types (i.e., interpeloidal pores and vugs). This multimodal pore system produces a K_{total} of 788.05 mD and a Φ_{DIA} of 28.91 %, and has an average γ value of 2.65 (Figure 3.5). It is composed of 33.48 % primary interpeloidal pores with an average γ value of 1.56, and 66.51 % secondary vuggy pores with an average γ value of 3.23 (see Figure 3.5).

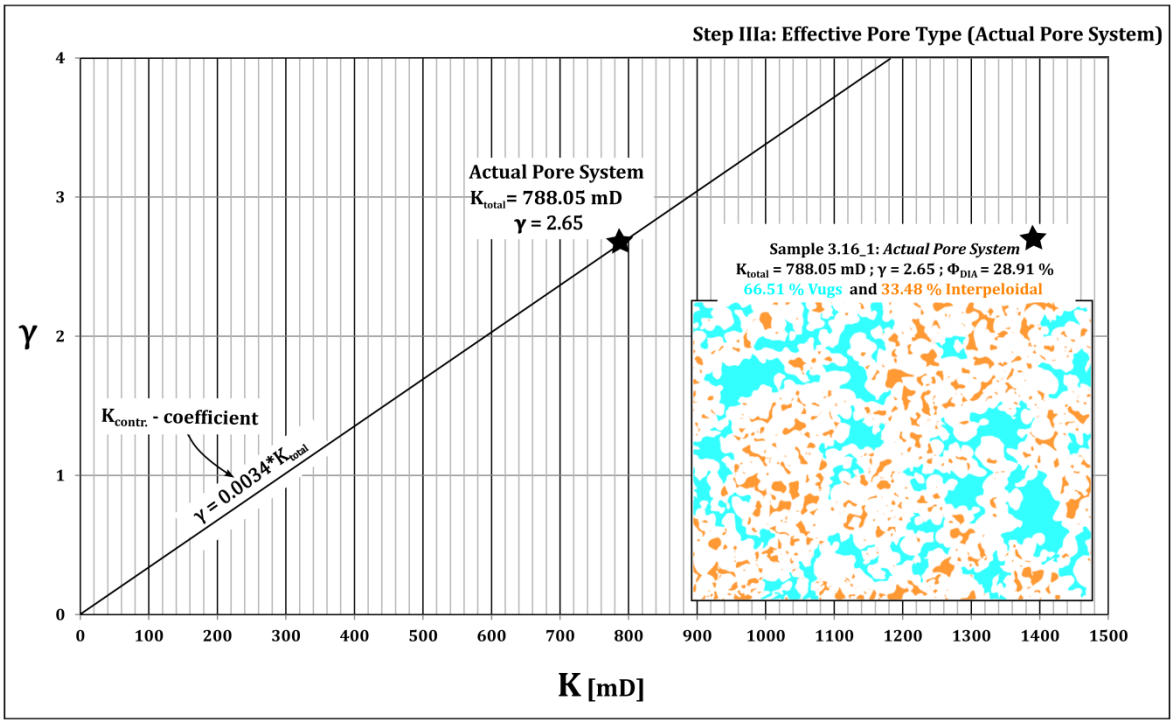

Figure 3.5. Step IIIa: Effective pore type (actual pore system). In order to detect the effective pore type(s), the permeability contribution ($K_{contr.}$) of each pore type to total permeability (K_{total}) must be calculated. First, the actual pore system is plotted in a K_{total} versus γ plot, and the "$K_{contr.}$ – coefficient" can be calculated.

Thus, in a K_{total} versus γ plot, the actual pore system plots at a given point in the graph (K_{total} = 788.05 mD; γ = 2.65). By drawing a line from the coordinate origin to this point of the plot, γ can then be theoretically calculated from permeability (and vice versa) for this sample by using the equation of the resulting linear regression including a "$K_{contr.}$ – coefficient", which varies for each individual sample (here: 0.0034):

$$\gamma_{total} = K_{total} \times \text{"}K_{contr.} - \text{coefficient"} \qquad [-]$$

As a next step, the two occurring pore types in sample 3.16_1 are extracted from the actual mixed pore system, and two artificial unimodal pore systems are generated (Figure 3.6).

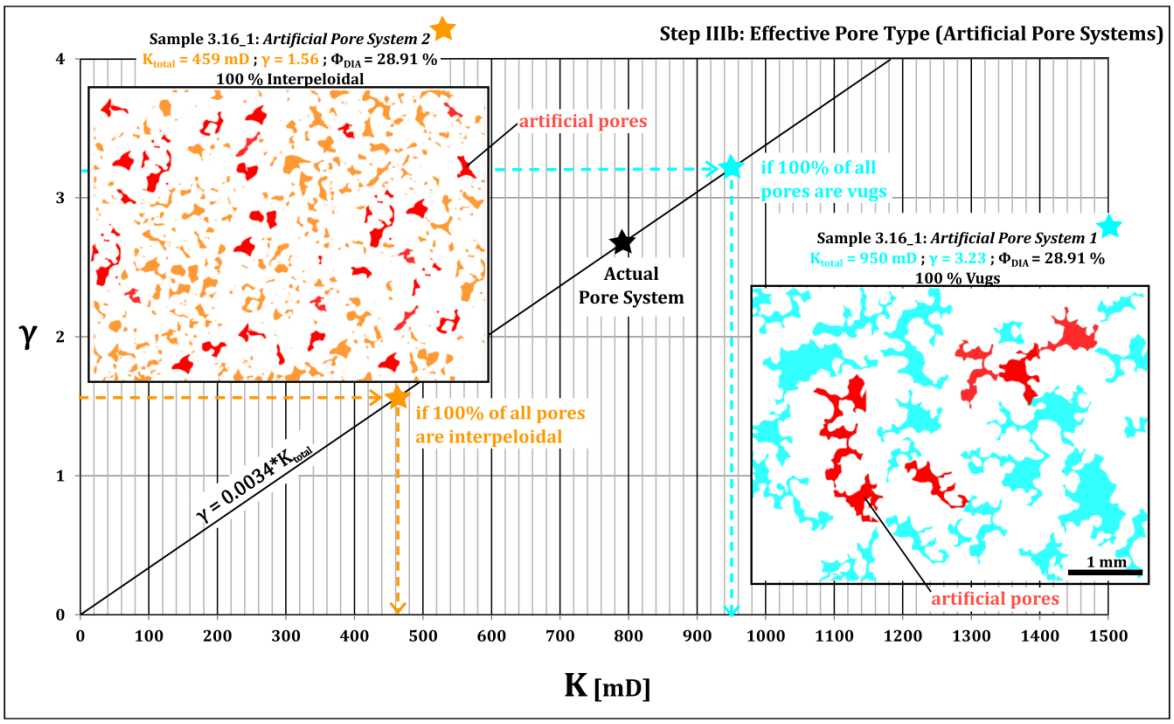

Figure 3.6. Step IIIb: Effective pore type (artificial pore system). Two artificial pore systems are created which have identical Φ_{DIA} value as the original actual system, but consist 100 % of only one pore type. K_{total} of both systems is then calculated by using the pore-type-specific γ value.

In order to maintain the Φ_{DIA} of 28.91 % of the actual pore system, each artificial pore system is virtually filled with artificial interpeloidal pores or vugs, leading to the creation of two pore systems which are composed of 100 % of interpeloidal pores and 100 % of vuggy pores, respectively. Since the average γ value of both artificial unimodal pore systems must be identical with the average γ value of both individual pore types in the actual multimodal system, the resulting linear regression of the K_{total} versus γ plot can then be used to calculate K_{total} for each of the two artificial systems:

$$K_{total} = \frac{\gamma_{total}}{"K_{contr.}-\text{ coefficient}"} \qquad [mD]$$

For the artificial pore system with 100 % interpeloidal pores, K_{total} decreases to 459 mD in respect to the total permeability value of the original actual system, whereas in the artificial pore system with 100 % vuggy pores an increase in K_{total} to 950 mD is calculated (see Figure 3.6). The potential permeability contribution ($K_{contr.}$) of each pore type to measured K_{total} of 788.05 mD must then be calculated by using the γ value of each pore type and the "$K_{contr.}$ – coefficient", calibrated with the pore-type-specific porosity proportion ($\%_{PoreType}$) in respect to the total Φ_{DIA} of the actual pore system (Figure 3.7):

$$K_{contr.} = \left(\frac{\gamma_{PoreType}}{"K_{contr.}-\text{ coefficient}"}\right) \times \%_{PoreType} \qquad [mD]$$

Proportion of porosity ($\%_{PoreType}$) in respect to total Φ_{DIA} strongly depends on the size (i.e., pore width) and abundance of each pore type.

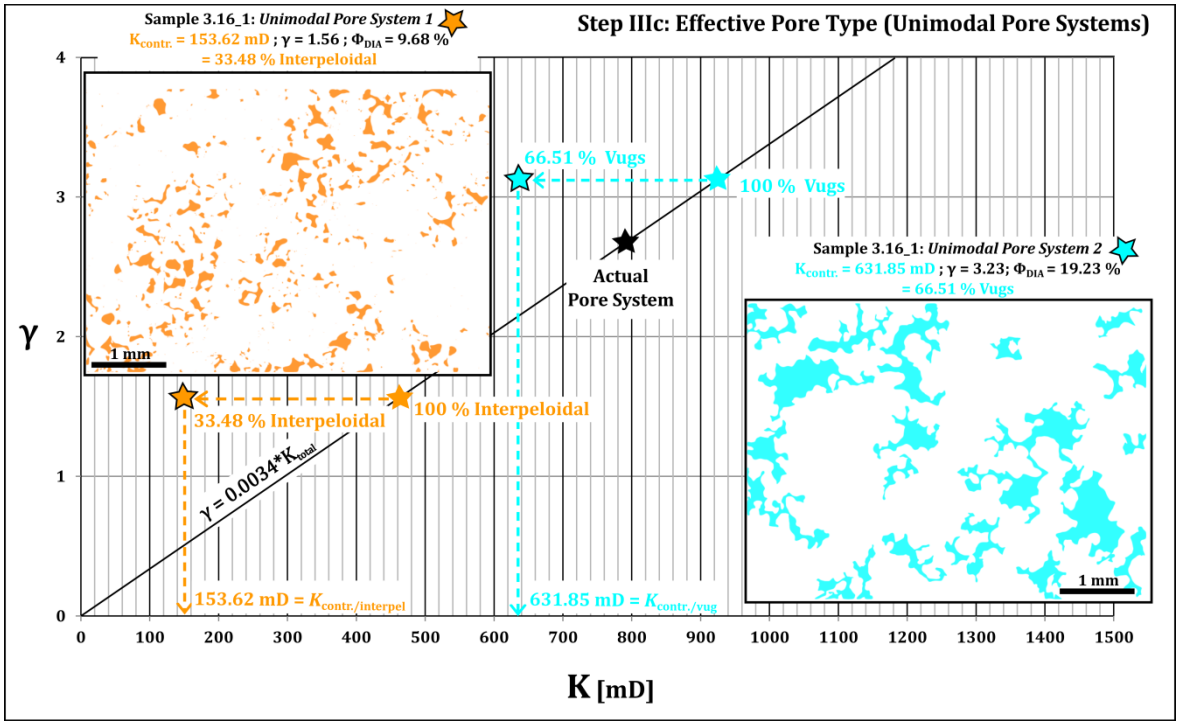

Figure 3.7. Step IIIc: Effective pore type (unimodal pore systems). The actual proportion of each pore type in respect to both previously created artificial pore systems is used in order to calculate the $K_{contr.}$ for each pore type present.

In sample 3.16_1, a $K_{contr.}$ of 631.85 mD (66.51 % of 950 mD) has been calculated for the vuggy pore type. This corresponds to a potential contribution of 80 % to K_{total} of 788.05 mD. For the interpeloidal pore type, $K_{contr.}$ is 153.62 mD (33.48 % of 459 mD), and therefore interpeloidal pores potentially generate 20 % of the total permeability (K_{total}) in this pore system. Addition of both results, which means virtually reassembling both artificial pore systems into the original actual system, yields a total permeability contribution value $\sum K_{contr.}$ of 785.47 mD (Figure 3.8). This value is identical to the K_{total} value of 788.05 mD measured with routine injection methods, and represents the maximum permeability which can be generated by this specific pore system as inferred from pore geometry measured on the thin section image of sample 3.16_1.

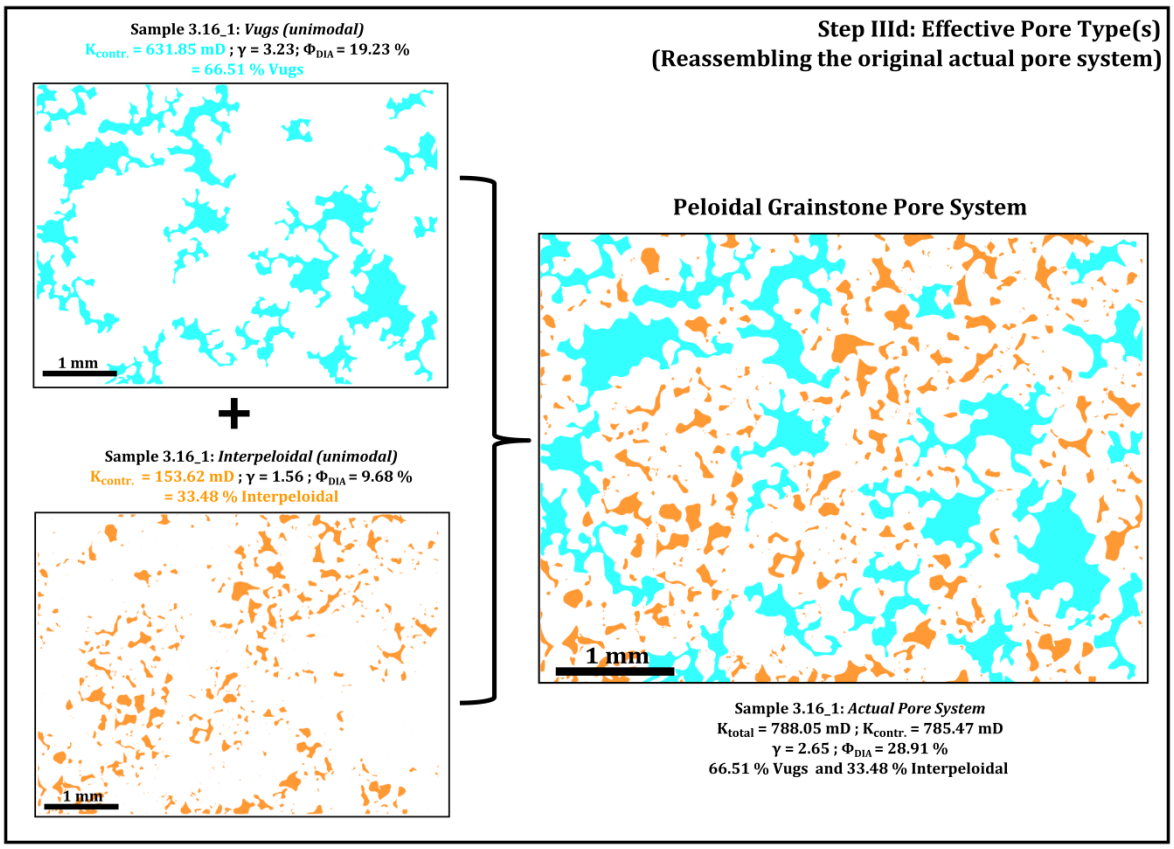

Figure 3.8. Step IIId: Effective pore type (reassembling the actual pore system). Finally, the two individual pore systems are reassembled into the original actual pore system, resulting in all parameters required to establish a petrophysical facies during Step IV of the workflow.

3.5 Petrophysical Facies and Pore System Evolution (Step IV)

By combining all data obtained during Step II and III, which are pore type class, pore width, pore shape factor γ, abundance, efficiency, Φ_{DIA}, $K_{contr.}$ and proportion of porosity ($\%_{PoreType}$), a petrophysical facies for all analyzed peloidal grainstones samples used in this chapter is established (Step IV). It comprises information about pore geometry and petrophysical properties of each occurring pore type. Hence, the petrophysical facies provides a framework to directly integrate information about porosity and permeability with the sedimentary fabric and its associated pore structure. Table 2 represents the seven key petrophysical facies parameters for all peloidal grainstone samples analyzed for this chapter and the occurring pore type classes.

Figure 3.9 illustrates the variations in porosity and permeability in respect to pore system geometry of the peloidal grainstone pore systems analyzed. As seen in the thin section image 2C4_6 (see Figure 3.9), a pore system which resembles an initial system with 100 % primary interpeloidal pores has moderate porosity and permeability values (Φ_{DIA} = 17.30 %; K_{total} = 385 mD). Pore width and γ values of this specific sample are identical to the average values of interpeloidal pores of all samples examined (see Table 2). If secondary vugs are introduced into the initial primary pore system, Φ_{DIA} generally increases due to the big size of vugs (pore width = 317.68 µm on average). The addition of vugs also increases permeability

due to a generally increased average pore size, but moreover due to the more complex shape of vugs (γ = 2.73 on average). Both factors lead to an enhanced probability of pores to interconnect with adjacent pores and therefore forming effective porosity. Maximum Φ_{DIA} and K_{total} measured are produced by a pore system which is composed of 94.72 % of predominantly touching vugs (sensu Lucia, 1983), and 5.28 % of primary interpeloidal pores in between vuggy pores, as demonstrated in sample 1B11_5 (see Figure 3.9). There, vugs contribute to K_{total} of 3543.5 mD with over 97 %. Since both interpeloidal pores and vugs show averagely moderate to high pore shape complexity values, no pore systems with high Φ_{DIA} and low K_{total} have been developed (see Figure 3.9). In contrary, since porosity and permeability increases simultaneously with increasing number of vugs, no low Φ_{DIA} and high K_{total} pore systems occur.

All Non-Skeletal Grainstones	Pore Geometry				Petrophysical Properties		
Pore Type	**Pore Width [µm]**	**γ [-]**	**Abundance [-]**	**Efficiency [-]**	**Φ_{DIA} [%]**	**$K_{contr.}$ [mD]**	**Proportion [%]**
1. Interpeloidal	**20.48** 6.69 – 39.91	**1.84** 1.48 – 2.74	**1159** 258 – 2750	**1.08** 0.19 – 3.68	**9.74** 1.83 – 27.54	**256.82** 98.23 – 560.32	**52.34** 5.28 – 100
2. Vug	**317.68** 205.75 – 860.05	**2.73** 1.89 – 4.88	**15** 1 – 40	**112.92** 46.63 – 218.80	**13.05** 1.70 – 32.82	**1000.32** 25.38 – 3605.10	**57.94** 5.81 – 94.72
Average Pore System	**152.23**	**2.24**	**644**	**51.41**	**20.99**	**591.40**	-

Table 2. Petrophysical facies of all non-skeletal (peloidal) grainstone samples analyzed to establish the workflow

Conclusively, the more pronounced the vug-forming process of dissolution has acted, the higher are the values for pore width and shape complexity of the sample. Consequently, pore width and γ of a pore system successively increase with increasing abundance of vugs. As a result, it can be stated that the vug-forming process of dissolution highly enhanced petrophysical properties during this stage of pore system evolution in the analyzed non-skeletal grainstones samples. Although this positive effect of vug formation on petrophysical properties is well-known (e.g., Lucia, 1983; 1995), the method presented in this chapter allows for precisely quantifying this effect by calculating the different contributions of co-occurring pore types to permeability and evaluate their interconnectivity (i.e., effectiveness) with pore shape complexity.

3.6 Discussion of Chapter

There are several errors which can occur during the application of the DIA method to determine pore geometry. The most important step of this method relies on the careful selection of samples (i.e., rock chip, cylindrical plug or a core) to be prepared as thin sections which guarantees that the measured total porosity and permeability values derive from an absolutely facies-representative pore system.

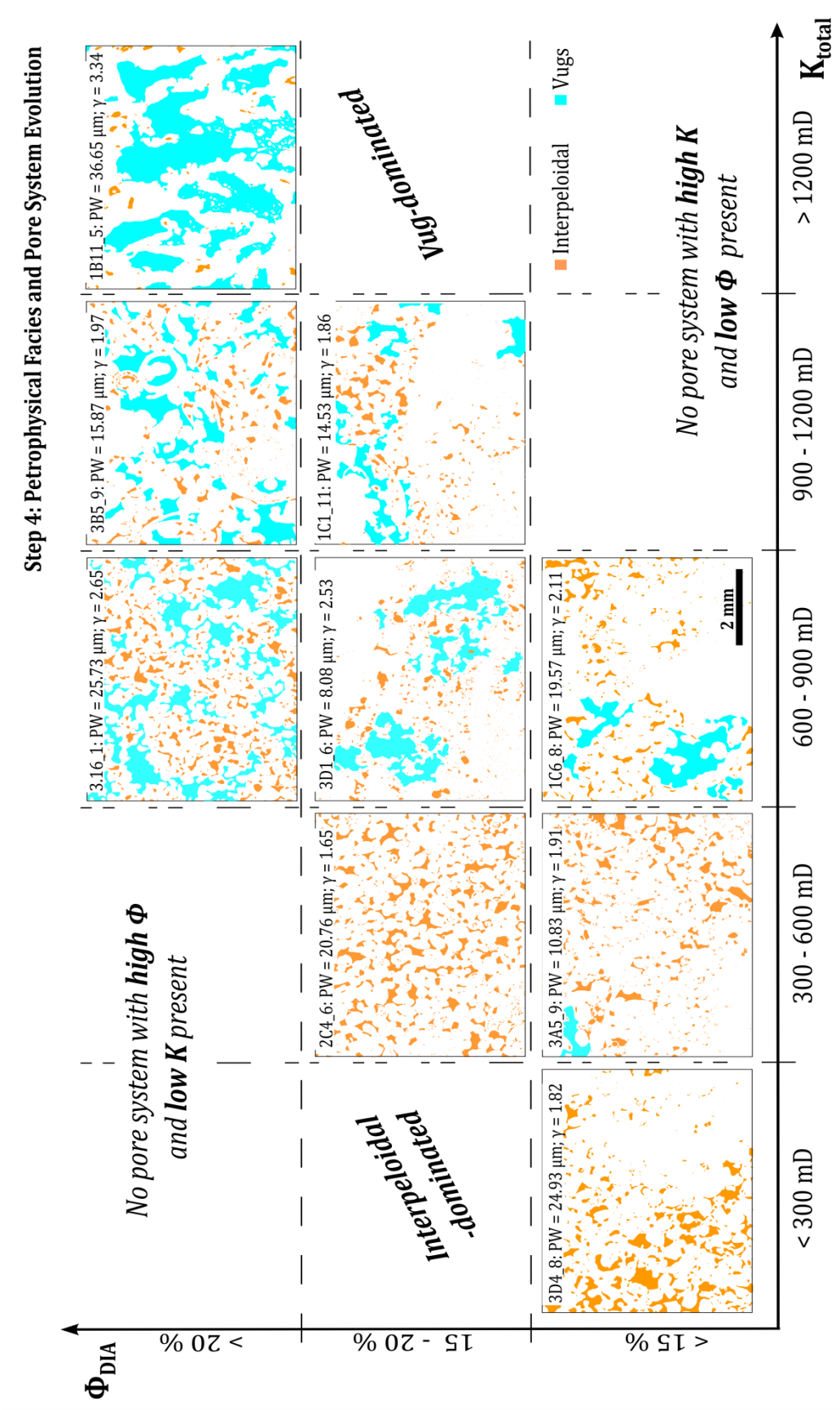

Figure 3.9. Step IV: Pore system evolution of peloidal grainstones. The evolution of pore system onsets with the initial pore system with 100 % primary interpeloidal pores (see sample 2C4_6), which has moderate porosity and permeability values. Then, pore system properties successively increase by introduction of secondary vuggy pores.

Routine petrophysical measurements bear sources of errors as well. Temperature, humidity and sampling performance can vary between each measurement and therefore causing relative errors in resulting K_{total} values and porosity estimations. The second important step of this method depends on a precise and accurate acquisition of the thin section images used for DIA processing. Since usually one individual image of the whole thin section has a magnification which is too low to precisely capture all meso- to macropores, either several higher-magnified images have to be processed with the DIA software, or one representative image has to be selected. An image is representative if its Φ_{DIA} value is identical to the average value derived from several images representing minimum, intermediate and maximum Φ_{DIA}, and to measured total porosity (Φ_{total}) if microporosity is not the dominant pore type. Additionally, all pore types present should be captured by the image. Another source of error is the application of IHS-thresholding binarization to segment pores from the solid matrix. Color ranges have to be selected precisely to capture the entire pore outline. If not, pore size and pore shape complexity as well as Φ_{DIA} are over- or underestimated. The use of the same IHS-threshold values for one set of samples can ensure that pore geometry data are consistent. Gas bubbles (caused by thin section preparation) often partly fill pores and occur predominantly in big pores. They can be deleted by using crossed polarized light (XPL) at the microscope (see Anselmetti et al., 1998). Furthermore, the usage of 2D images to analyze a 3D object is a fundamental problem of the DIA method. Again, a representative image from a facies-specific sample is required to avoid or at least reduce this potential error. Alternatively, the analysis can be performed on three thin section images, each derived from different orthogonal orientations of a rock chip or plug in order to obtain a quasi-3D pore system representation (Maerz, 2012). Although the aforementioned potential errors can be avoided by using three-dimensional computed tomography (CT) images and corresponding DIA software, this 3D analysis of pore system is usually very time-consuming and cost-expensive which only allows for processing a low amount of samples.

In the pore width versus γ plot which has been used to extract all different pore types from a pore system (see Figure 3.4), it has been observed that the higher the correlation coefficient between pore width and γ, the more homogenous is a pore system, and the less different pore types are present. This is mainly caused by the fact that pore systems which are dominated by one pore type (> 90 %) contain pores which have pore geometries and sizes of the same magnitude. Thus, the individual pore geometry values are identical to the average values of the entire pore system. Hence, the R^2 value of the correlation between pore width and γ can be used as a quantitative measure for the homogeneity of a pore system. Furthermore, the calculation of $K_{contr.}$ is performed by using a correlation between γ and K_{total}. The resulting linear relationship is needed to determine the permeability contribution ($K_{contr.}$) for each pore type. In sample 3.16_1 for instance, this relationship is expressed in the formula $\gamma = 0.0034 \times K_{total}$, whereas 0.0034 is the "$K_{contr.}$ – coefficient". Although this coefficient varies between different types of pore systems, it has been measured in all samples examined that the lower this coefficient is, the higher K_{total}. A correlation between K_{total} and the "$K_{contr.}$ – coefficient" values of all peloidal grainstone samples used for this chapter yield a high correlation coefficient $R^2 = 0.84$. Therefore, permeability of samples

with identical pore systems but unknown permeability (K_{total}) values can be predicted by using the "$K_{contr.}$ – coefficient".

Moreover, the method of detection of $K_{contr.}$ is based on the assumption that there is a high correlation between γ and K_{total}. In this thesis, correlation between γ and K_{total} results in a maximum correlation coefficient R^2 of 0.38. Previous studies showed that correlation coefficients increase towards $R^2 > 0.90$ if several pore geometry and petrophysical parameters are combined (Anselmetti et al., 1998; Baechle et al. 2004; Weger, 2006; Weger et al., 2009). Although γ does not correlate perfectly with K_{total}, the relative proportion however with which each individual pore type is potentially contributing to K_{total} in respect to all other pore types present within one individual pore system is consistent, and $\sum K_{contr.} \cong K_{total}$. Therefore, γ can be used to calculate $K_{contr.}$ of each individual pore type within one system, if the measured K_{total} value represents a facies-specific pore system. If $K_{contr.}$ of one pore type is determined by calculating the pore-type-specific proportion from K_{total} alone, then $K_{contr.}$ is overestimated from pore types with a low γ value, and underestimated from pore types with a high γ value. Instead, $K_{contr.}$ must be calculated by using the γ value of each pore type present and the pore-type-specific porosity proportion in respect to total Φ_{DIA}, as presented in Step III of the method (see Figure 3.7). In sample 3B6_9 for instance, interpeloidal pores encompass a proportion of 11.88 % of the multimodal pore system, producing a $K_{contr.}$ of 79.76 mD when calculated with γ = 1.41. Without γ, $K_{contr.}$ would be 115.43 mD. Considering that samples which are dominated (> 90 %) by interpeloidal pores produce a maximum K_{total} of 401 mD, this $K_{contr.}$ value would represent a proportion of minimum 28.76 % of interpeloidal pores in the mixed pore system of sample 3B6_9. Consequently, the contribution of interpeloidal pores to K_{total} would be overestimated. Therefore, the pore-type-specific pore shape complexity is crucial for calculating $K_{contr.}$ due to the fact that although the average γ value of a pore system represents the mean of all γ values from each individual pore type, complex pore types with high γ values contribute more to K_{total} as inferred from their relative proportion.

3.7 Conclusions

The workflow presented in this chapter offers a novel approach to quantitatively characterize each pore type present and identify the most effective pore type(s) of a mixed pore system from thin section images. Previous studies focused on analyzing the most dominant (> 50 %) pore type within a mixed carbonate pore system, solely (Anselmetti et al., 1998; Weger, 2006; Weger et al., 2009). As Weger et al. (2009) noted, this may cause complications in quantifying the impact of each individual pore type on total porosity and permeability, which strongly depends on its pore geometry rather than on its abundance. Therefore, by providing a workflow which allows for analyzing each occurring pore type individually, previous methods of quantifying pore system geometry with DIA have been improved. It has been also demonstrated that the application of pore geometry parameters (i.e., pore size and pore shape complexity) is a very useful tool to quantitatively characterize a mixed pore system and evaluate the effectiveness of each occurring pore type contributing to total permeability. As a result, the pore systems of all peloidal grainstone samples analyzed are composed of an assemblage of two moderately

to highly effective pore types (i.e., primary interpeloidal pores and secondary vugs, respectively), both forming a very well-interconnected pore system. The workflow presented delivers a more detailed quantitative description of pore system as compared to routine petrophysical measurements, and complements qualitative or semi-quantitative pore type descriptions. These quantitative data and the extracted effective pore network can be integrated into further petrophysical modeling processes.

Further application of this method, with the purpose of evaluating all relevant types of pore system in the marginal lacustrine carbonates from the Nördlinger Ries crater lake is presented in Chapter Four. Although each sedimentary facies type is composed of assemblages of several different and interacting pore types, each type of pore can be characterized individually with the workflow presented in this chapter. Hence, there are no limitations in respect to the number of pore types present. The petrophysical facies parameters of all pore types are then used to identify the most effective pore system and corresponding sedimentary facies type. Moreover, pores of unknown type can be identified based on their petrophysical facies parameters. If the pore-forming processes are known, the evolution of pore system can be reconstructed and the impact of primary (depositional) and secondary (diagenetic) processes on petrophysical properties can be quantified as presented in Chapter Five. This applies in particular to the processes which led to the creation of effective pore types. Reconstructing their evolution contributes to a better understanding of how effective porosity is distributed throughout the different sedimentary facies types in this marginal lacustrine succession.

CHAPTER FOUR

APPLICATION I: COMPREHENSIVE PORE SYSTEM ANALYSIS OF MARGINAL LACUSTRINE CARBONATES (MIDDLE MIOCENE, SOUTHERN GERMANY)

4.1 Introduction

Pore systems in carbonates are often composed of assemblages of at least two different primary and/or secondary pore types which together form a multimodal pore system, here now referred to as pore type assemblage (PTA). This is in consensus with He et al. (2014) who showed that petrophysical properties of carbonates mostly depend on distinct "combination patterns" of various pore types. Since each pore type is formed and modified by sedimentary and diagenetic processes, not only the evolution of pore system can be reconstructed. Moreover, the depositional and postdepositional history of the entire host rock can be traced back by understanding the origin of each pore type present. Therefore, the method demonstrated in Chapter Three has been applied to the pore system of several facies types of the case study area to test and unravel the relationship between the co-occurrence of genetically and geometrically different pore types, and porosity and permeability. The goal of this chapter is to establish a petrophysical facies for each individual pore type of the analyzed facies types based on the seven key parameters calculated with the workflow presented in Chapter Three, which then allows for detecting the most effective pore type(s). Finally, the pore type assemblage (i.e., PTA) and its corresponding sedimentary facies, which potentially generates most effective porosity and thus permeability, can be identified.

4.2 Pore Type Assemblages

In the marginal lacustrine carbonates of the Nördlinger Ries crater lake, four pore type assemblages have been identified, each typical for one distinct sedimentary facies type (Figure 4.1):

PTA 1: As shown in the previous chapter, the pore system of the non-skeletal grainstone facies is mainly composed of an assemblage of primary interpeloidal and secondary vuggy pores (see Figure 4.1a). Both occurring pore types usually have numerous pore throats, leading to a high interconnection between pores. The size of primary and fabric-selective interpeloidal pores strongly depends on the size, arrangement and sorting of peloidal grains. However, even if their pore size is small, interconnection to adjacent secondary and non-fabric-selective vugs is still governed by their complex pore throats. Rarely, incorporated skeletal grains are present and additional intraskeletal and skeletal moldic pore types occur.

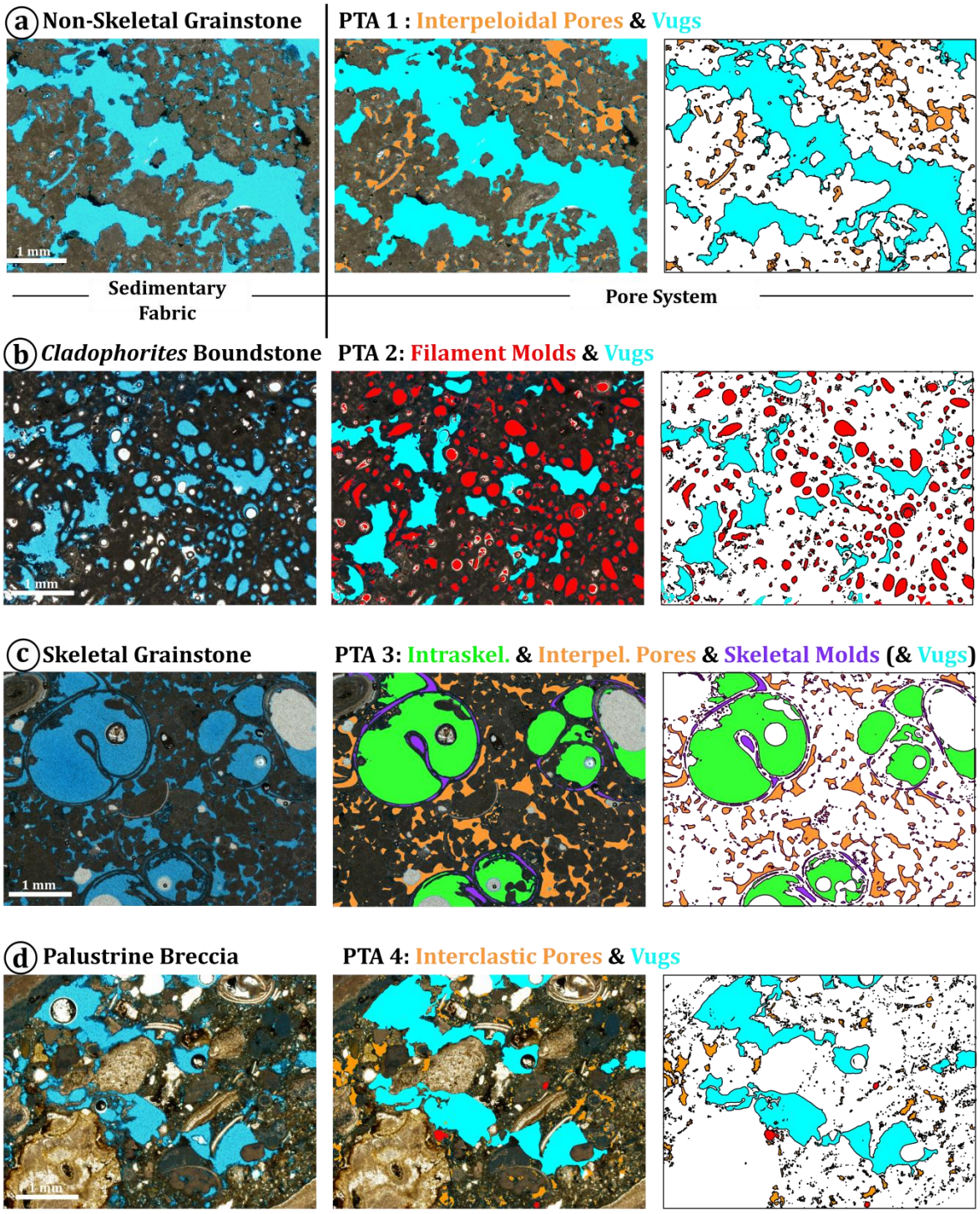

Figure 4.1. Pore types and pore type assemblages (PTA). a. PTA 1 with interpeloidal pores and vugs as occurring in the peloidal grainstone facies. **b.** PTA 2 with filament molds and vugs as occurring in the *Cladophorites* boundstone facies. **c.** PTA 3 with intraskeletal and interpeloidal pores as well as skeletal molds and vugs as occurring in the skeletal grainstone facies. **d.** PTA 4 with interclastic pores and vugs as occurring in the palustrine breccia.

PTA 2: Porosity and permeability in the *Cladophorites* boundstone facies are tied to late primary to early secondary molds of *Cladophorites* filament traces and late secondary vugs. In contrast to PTA 1, vugs are less abundant and show lower interconnection with the generally isolated and simple-shaped

subspherical filament molds (see Figure 4.1b). Occasionally, incorporated skeletal grains occur. However, they are then filled by micrite and provide no additionally meso- to macropore space. Since only individual peloidal grains have been trapped by *Cladophorites* green algae, they also do not produce interpeloidal pore space in PTA 2.

PTA 3: The skeletal grainstone facies comprises at least four different pore types, including primary intraskeletal and interpeloidal pores, and secondary skeletal moldic and vuggy pores. In this facies type, vugs are rare, and interpeloidal pore space is restricted to peloids which have been deposited in between skeletal grains (see Figure 4.1c). Usually, this type of pore system shows highest degree of partial cementation by low-magnesium calcite around and within skeletal grains. Therefore, primary intraskeletal pore are usually isolated and not connected to adjacent pores. This can be explained by the fact that the primary pore system of the skeletal grainstone facies initially must have been very porous due to the big size and resulting open arrangement of the skeletal grains. Secondary skeletal molds often occur together with intraskeletal pores, however they are genetically not related, and have been formed in a later stage of pore system evolution. Due to their elongated shape, skeletal molds often interconnect with adjacent pores.

PTA 4: In the palustrine facies, mainly primary interparticle (i.e., interclastic) pores between and within intra- and extraclasts dominate, together with few secondary vugs. Porosity mainly depends on the size of intra- and extraclasts, which shows a very high and variable range (see Figure 4.1d). However, due to the low abundance and confinement as infilling in the growth framework space of the *Cladophorites* boundstone facies, and the generally rare occurrence and limited spatial distribution of the palustrine breccia in the outcrop, PTA 4 is not further evaluated in this thesis, and only the pore systems of the three major facies types (i.e., *Cladophorites* boundstone, non-skeletal grainstone and skeletal grainstone) are analyzed. Therefore, for the purpose of detecting the most effective pore system and their corresponding sedimentary facies in the studied marginal lacustrine carbonates, three different types of pore systems (i.e., PTA 1, PTA 2 and PTA 3) have been evaluated.

4.3 Pore System Analysis of the Nördlinger Ries Carbonates

For this chapter, thin sections of all 32 selected samples have been analyzed with the methodological workflow presented in Chapter Three. They encompass the pore type assemblages of the three major facies types in the studied marginal lacustrine succession. These samples include facies-representative pore systems without any extensive diagenetic modifications and mixing of different pore systems which allows for linking the total permeability value measured on the sample plug directly to the corresponding thin section image. As previously mentioned, the selection of appropriate samples is essential for the method presented. All samples selected show pore systems dominated by meso- and macropores. Only a few samples show single-porosity systems, however the majority of pore systems analyzed have multiple-porosity systems. All pores of the selected samples have first been analyzed by using the pore width versus γ plot (Figure 4.2).

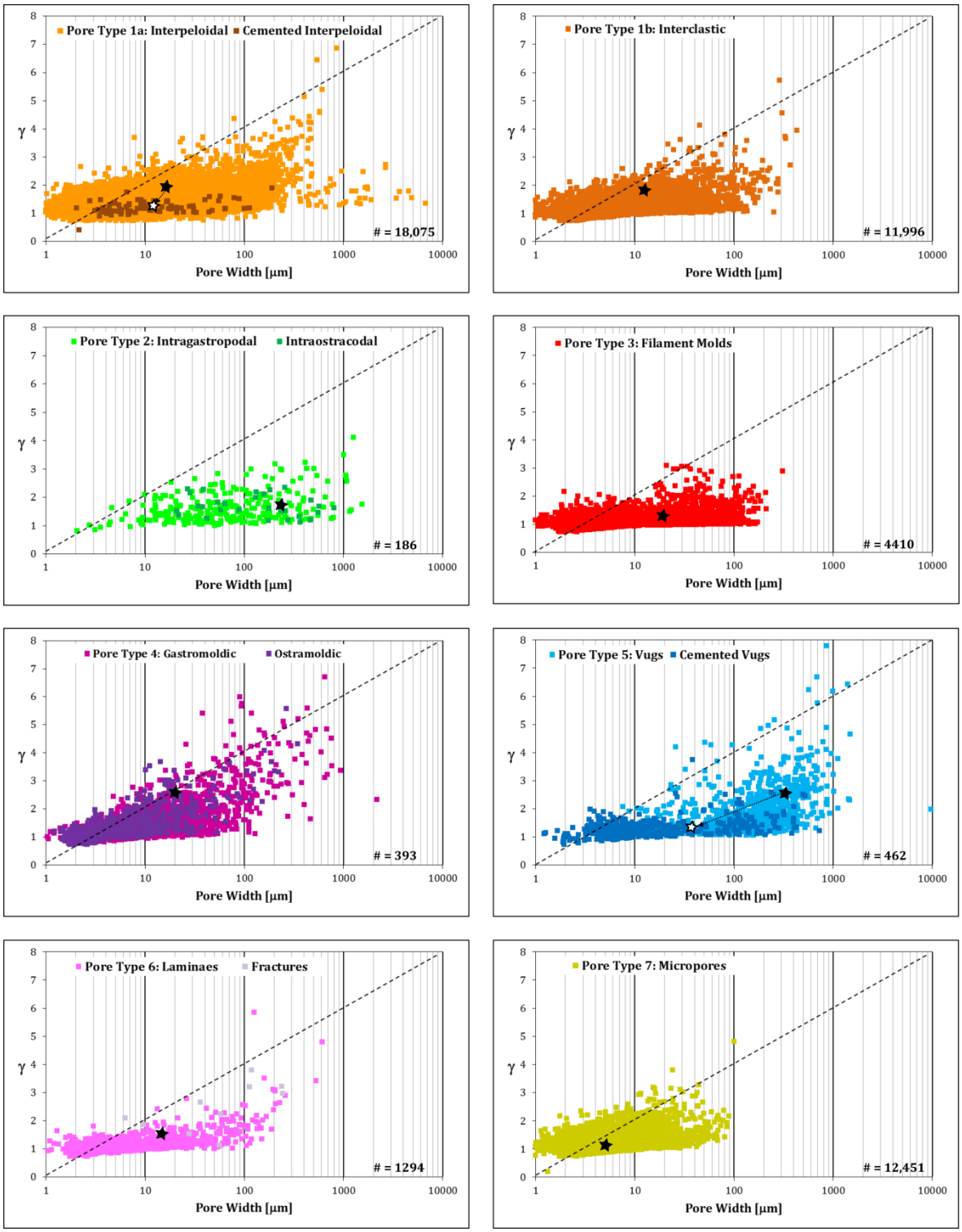

Figure 4.2. Pore width versus γ of each individual pore and for all pore types present. Black stars indicate mean values for pore width and γ (sensu Anselmetti et al., 1998) of uncemented pores, white stars indicate mean values of pores showing minor cementation at the pore rim. Numbers of analyzed pores are labelled. Micropores are abundant, but insignificant in producing porosity and permeability. For quantification of pore type effectiveness, fractures and laminae have not been considered due to their low abundance and uncertain origin, as well as all PTA 4 pore systems including all interclastic pores and some vugs which are tied to the rare and only locally occurring palustrine breccia.

Figure 4.2 also demonstrates the high number of individual pore geometry data obtained from the DIA method presented in this thesis, resulting in distinct mean values and value ranges for all seven key parameters used to establish a petrophysical facies which describes the most relevant pore type properties (Table 3).

All samples	Pore Geometry				Petrophysical Properties		
Pore Type	**Pore Width [µm]**	**γ [-]**	**Abundance [-]**	**Efficiency [-]**	**Φ_{DIA} [%]**	**$K_{contr.}$ [mD]**	**Proportion [%]**
1. Interpeloidal *PTA 1, 3*	**17.86** 6.69 - 37.01	**1.71** 1.24 - 2.74	**904** 31 - 2750	**1.22** 0.19 - 4.58	**7.53** 0.46 - 27.54	**195.82** 22.81 - 560.32	**39.36** 3.84 - 100
2. Intraskeletal *PTA 3*	**248.15** 51.34 - 468.19	**1.74** 1.55 - 2.08	**21** 1 - 51	**74.51** 18.61 - 190	**7.38** 1.90 - 12.90	**185.88** 50.54 - 535.65	**32.48** 11.63 - 50.78
3. Fil. Moldic *PTA 2*	**17.82** 7.84 - 26.44	**1.21** 1.11 - 1.51	**441** 68 - 2150	**2.25** 0.24 - 8.07	**4.43** 0.68 - 12.01	**74.46** 3.86 - 219.04	**39.22** 8.25 - 100
4. Skel. Moldic *PTA 3*	**21.18** 7.42 - 38.19	**2.45** 1.66 - 3.96	**33** 8 - 59	**7.93** 0.73 - 73.52	**2.04** 0.08 - 16.91	**63.62** 1.10 - 176.10	**12.39** 0.35 - 100
5. Vug *PTA 1, 2, 3*	**307.34** 134.81 - 667.26	**2.27** 1.40 - 3.34	**17** 1 - 57	**100.76** 22.96 - 294.00	**11.55** 1.70 - 32.82	**649.72** 22.79 - 3605.10	**59.71** 5.81 - 94.72

Table 3. Petrophysical facies of all samples examined in the Nördlinger Ries marginal lacustrine carbonates including mean values and value ranges of all relevant parameters for each pore type

Primary interpeloidal pores are most abundant in PTA 1 and, less frequently, in PTA 3, where they cover 39.36 % of the entire pore system. They usually occur in large numbers (n = 904), and have small pore sizes and moderate shape complexity (pore width = 17.86 µm; $\gamma = 1.71$). They produce a Φ_{DIA} of 7.53 % on average. The range of pore shape complexity values is very high due to variable size and shape of peloidal grains, but they tend to form a fairly well-interconnected pore network. Due to their high abundance but only moderate porosity production, their efficiency value of 1.22 is very low.

Late primary to early secondary filament moldic pores occur exclusively in PTA 2 (Figure 4.3), often together with secondary vugs. They are equally small as interpeloidal pores (pore width = 17.82 µm), but have much simpler pore contours ($\gamma = 1.21$). They also occur very abundant (n = 441), but contribute to total porosity with only 4.43 % of Φ_{DIA}, and with a proportion in respect to the entire pore system of 39.22 % on average. Therefore, their efficiency of producing porosity is also very low (2.25). In the nodular *Cladophorites* bafflestone facies, the orientation of filaments of *Cladophorites* green algae is arbitrary due to an increase in skeletal and non-skeletal grains in the depositional realm which have been incorporated in between *Cladophorites* stems (Riding, 1979). As a consequence, the shape of filament molds can be more variable as compared to the conoidal framestone facies which leads to a higher range in γ values.

As seen in PTA 3 (Figure 4.4) both primary intraskeletal and secondary skeletal moldic pore types are tied to the skeletal grainstone facies, where shells of ostracods and gastropods are the main constituents. Although they usually occur together in close proximity within the same shell or shell fragment, they are temporally asynchronous and genetically not related. Primary intraskeletal pores have been formed syndepositionally within the empty chambers of the shells. On average, 21 big and simple-contoured intraskeletal pores (pore width = 248.15 µm; γ = 1.74) contribute with an average proportion of 32.48 % and a Φ_{DIA} = 7.38 % to total porosity, resulting in a high efficiency value of 74.51. In contrary, secondary skeletal moldic pores have been formed after shells have been rimmed by dolomicrite and later dissolved during diagenetic modification. They are confined by the thickness of the shell and its elongated shape (pore width = 21.18 µm; γ = 2.45), producing Φ_{DIA} values of 2.04 % from 33 pores on average per thin section image. This results in a moderate efficiency in producing porosity of 7.93. Therefore, the size and shape complexity of both pore types strongly depend on the original size, mineralogy and inherent morphology of the pore-hosting shell.

Vuggy pores which occur in PTA 1, 2 and 3 encompass averagely 59.71 % of the pore system, generated by only a small number (n = 17 pores per thin section on average) of big and complex pores (pore width = 307.34 µm; γ = 2.27). They generate the highest amount of porosity (Φ_{DIA} = 11.55 %), and inferred from their complex shape have a high potential to form a very well-interconnected pore network. Consequently, vugs also show a high average efficiency of 100.76.

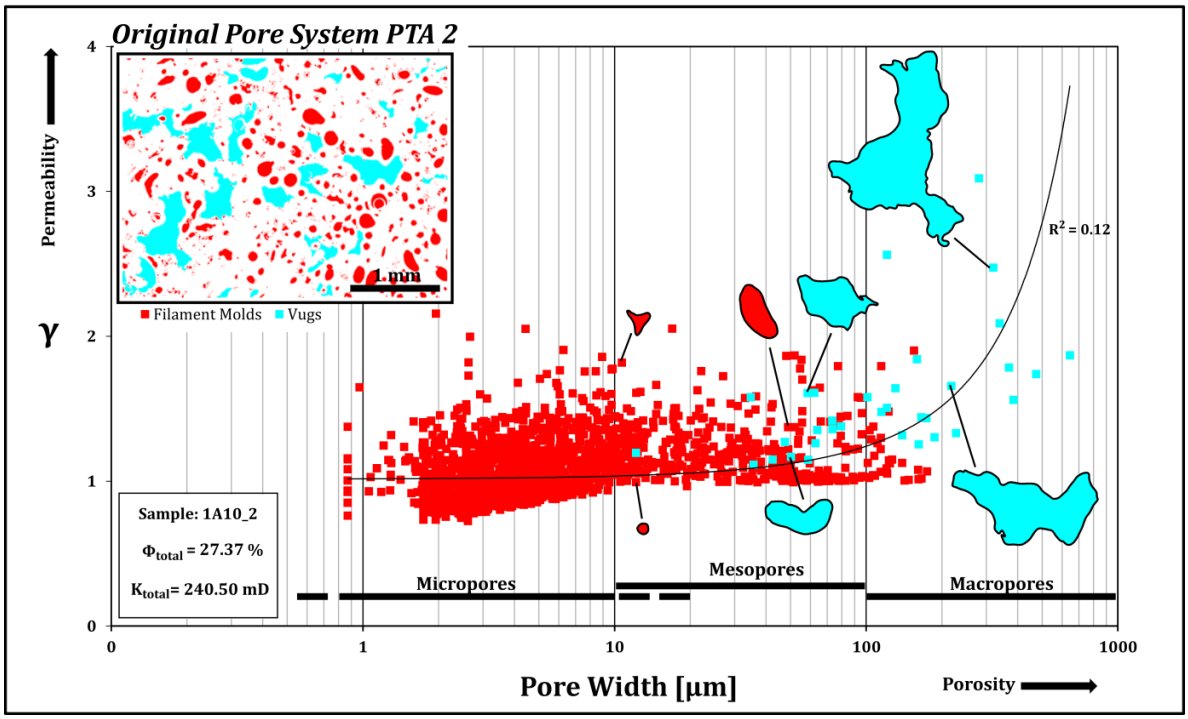

Figure 4.3. Pore width versus γ plot for sample 1A10_2. It represents a pore system composed of late primary to early secondary filament molds and secondary vuggy pores (PTA 2). Pore width and γ changes with increasing pore size and complexity, respectively. Individual pores are displayed and their pore geometry values are indicated.

In summary, vugs have been identified as the biggest and most complex pore type. On the contrary, filament molds are generally relatively small with a very simple pore contour. Although interpeloidal pores are equally small as filament molds and also inefficient in producing porosity, their shape complexity and resulting interconnectivity is much higher. Both intraskeletal and skeletal moldic pores are tied to the skeletal grainstone facies, but show completely opposite pore geometry properties: Primary intraskeletal pores within empty chambers of gastropod or ostracod shells generally have simple contours but big pore sizes due to the original big size of the chambers. Secondary skeletal molds instead are usually very thin and constrained by the thickness of the original but now dissolved shell or shell fragment. However, their γ values are usually very high due to their elongated shape. Since both pore types usually occur together, their opposite pore geometries are balanced out, leading to a moderately interconnected and open pore system as seen in the PTA 3 pore system of the skeletal grainstone facies.

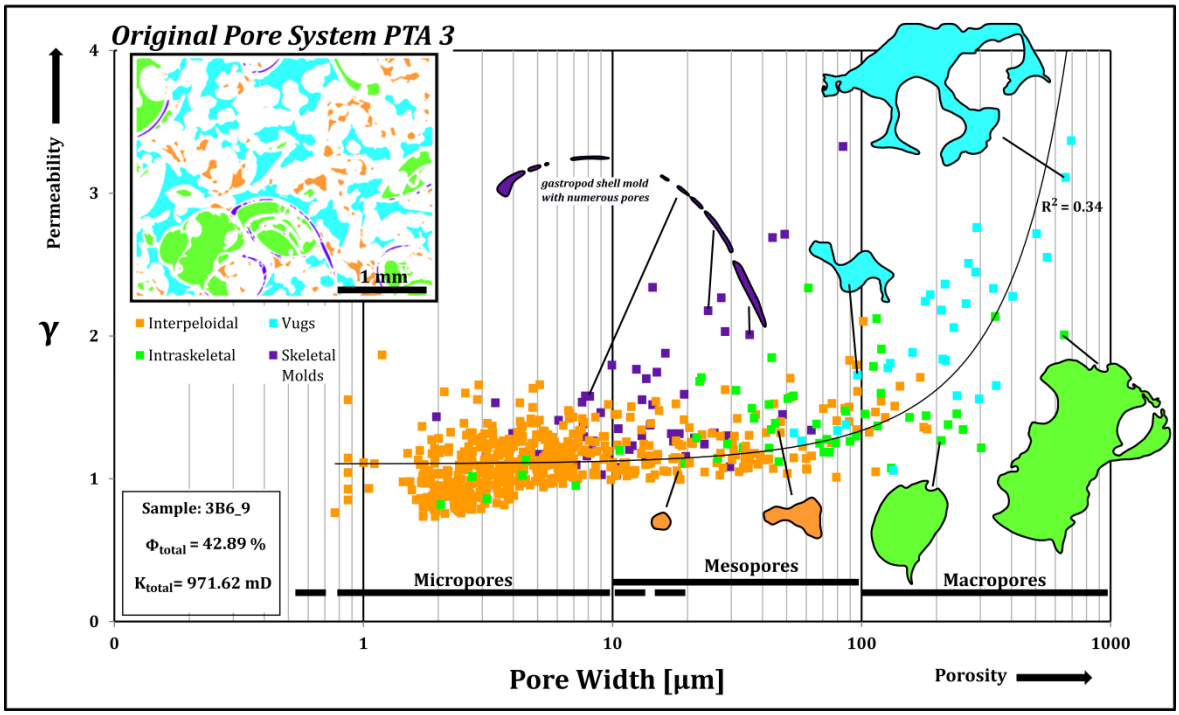

Figure 4.4. Pore width versus γ plot for sample 3B6_9. It represents a pore system composed of primary interpeloidal and intraskeletal pores, and secondary skeletal molds and vuggy pores (PTA 3). Pore width and γ changes with increasing pore size and complexity, respectively. Individual pores are displayed and their pore geometry values are indicated.

4.4 Effective Pore Type(s)

By extracting each individual pore type from all PTAs, pore-type-specific permeability contribution ($K_{contr.}$) can be calculated. In order to detect the type of pore which contributes most to total permeability (K_{total}), the γ versus K_{total} plot has been used (see Chapter Three). As a result, all vuggy pores, which occur in PTA 1, 2 and 3 with a proportion of averagely 59.71 % in respect to the entire pore system and as

measured on a thin section image, contribute to K_{total} with a $K_{contr.}$ of 649.72 mD (range: 22.79 to 3605.10 mD) on average (see Table 3). This high permeability contribution is also reflected in total permeability of pore systems dominated by vugs (> 90 %) which produce the highest K_{total} value of 3543.50 mD measured. Interpeloidal pores produce an average $K_{contr.}$ of 195.82 mD in PTA 1 and PTA 3 (range: 22.81 to 560.32 mD), with a proportion of 39.36 % on average. Pore systems dominated by interpeloidal pores (> 90 %) produce a moderate maximum total permeability K_{total} of 401 mD.

Due to their simple shape and small sizes, filament moldic pores (as occurring in PTA 2) contribute to K_{total} with a $K_{contr.}$ of 74.46 mD (range: 3.86 to 219.04 mD). As a consequence, a pore system dominated by filament molds (> 90 %) produce a low maximum permeability (maximum K_{total} = 187.05 mD). They usually occur with a high proportion of 39.22 % due to their large number (Figure 4.5). Accordingly, porosity in such pore systems is moderate.

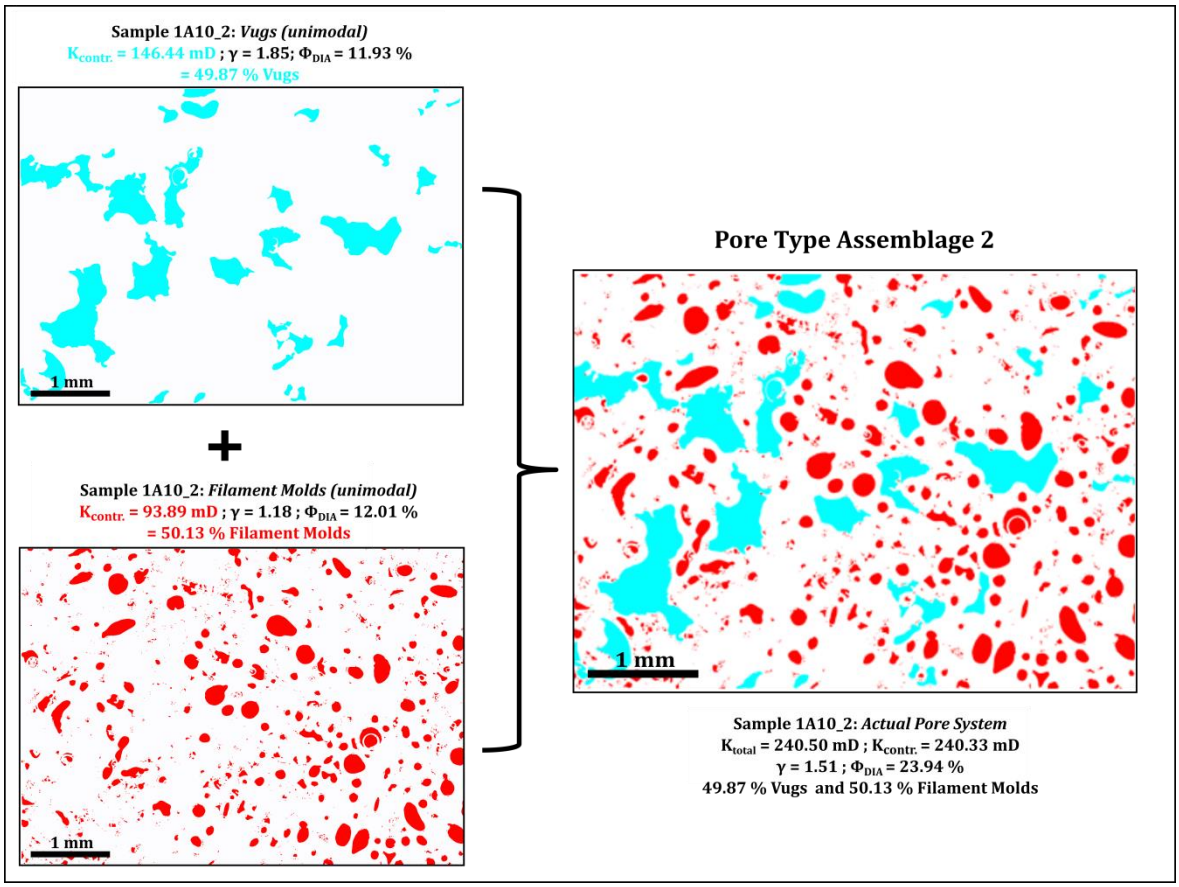

Figure 4.5. Pore system of sample 1A10_2 (PTA 2). It is composed of filament molds and vugs. The permeability contribution of vugs to total permeability is higher as compared to filament molds, although they both occur with the same proportion. This can be attributed to the generally big size and complex shape of vuggy pores.

As seen in PTA 3 (Figure 4.6), intraskeletal and skeletal moldic pores show different pore sizes and shape complexity values, and therefore contribute differently to K_{total}. Big, but simple-contoured intraskeletal pores produce an average $K_{contr.}$ of 185.88 mD (range: 50.54 to 535.65 mD), with a proportion of 32.48

% on average. Due to their big sizes in respect to the thin section image, they produce relatively high porosity values and proportion of porosity in the pore system, which also leads to an increase in $K_{contr.}$ although they generally have low γ values. Skeletal molds are relatively thin but complex pores and therefore generating a $K_{contr.}$ of 63.62 mD (range: 1.10 to 176.10 mD) despite a low average proportion of only 12.39 %. The maximum K_{total} in a skeletal grainstone pore system, where both skeletal-bound pore types (which exclusively occur together) dominate, reaches 1867 mD.

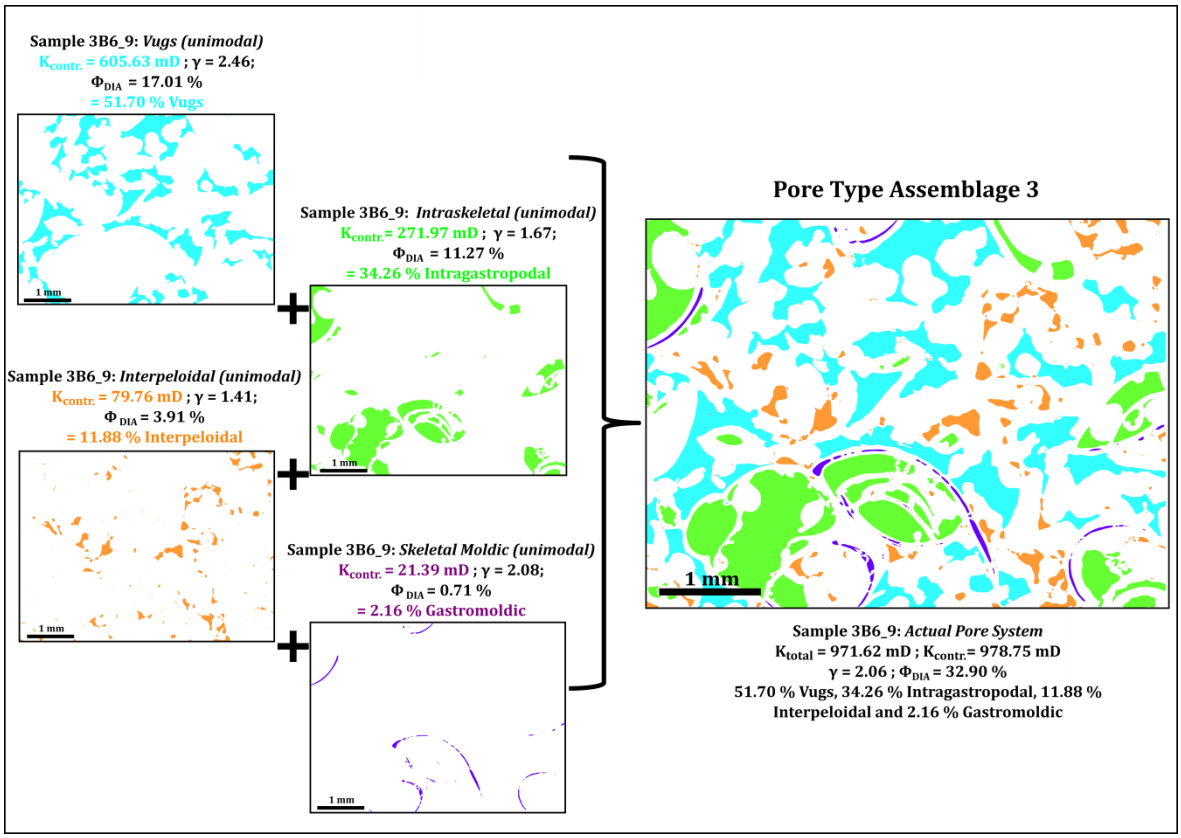

Figure 4.6. Pore system of sample 3B6_9 (PTA 3). It is composed of interpeloidal, intraskeletal, gastromoldic and vuggy pore type. The permeability contribution of vugs to total permeability is highest. Although occurring with a high proportion and having big pore sizes, intraskeletal pores show a relatively moderate contribution to total permeability due to their simple pore contour and low shape complexity. In contrary, both interpeloidal and gastromoldic pores contribute with a relatively high amount to total permeability due to their high shape complexity and in respect to their lower proportion.

In conclusion, it can be stated that based on all seven key parameters, vugs are the most effective pore type, contributing in most part to total permeability if present, followed by interpeloidal pores. Skeletal molds are identified as the third most effective pore type because although they usually occur in small numbers and are usually very thin, they produce a moderate average efficiency value and a fairly high amount of $K_{contr.}$ in respect to their small size and low abundance. This is caused by their elongated shape which increases the probability of interconnection with adjacent pores and therefore the formation of an effective pore network, which is also reflected in the highest average γ value measured. Intraskeletal pores instead are very efficient in producing porosity and have moderate permeability contribution

values if analyzed at a thin section scale. However, their average $K_{contr.}$ in respect to their high proportion and moderate range of shape complexity values point to a more isolated and low interconnectivity attribute of this pore types as compare to the previous effective pore types. Therefore, based on all seven petrophysical facies parameters, this pore type is interpreted to be ineffective. Filament molds instead show lowest shape complexity, efficiency and $K_{contr.}$ values in respect to their very high abundance and proportion. Therefore, they are the most ineffective pore type present. As a result, by establishing a petrophysical facies for each occurring pore type, distinct pore-type-specific attributes can be assigned which then allows for classifying each type as either effective or ineffective.

4.5 Discussion of Chapter

In the studied lacustrine succession, PTA 1 which encompass both interpeloidal and vuggy pores proves to be the most effective type of pore system, since both occurring pore types potentially contribute with a high amount to total permeability (see Figure 3.9). Since PTA 1 is tied to the peloidal grainstone facies, this sedimentary facies type contains the most effective type of pore system in the studied lacustrine carbonates. Moreover, peloidal grainstones occur as continuous sheets and amalgamated interbuild-up bodies, which are both very abundant and spatially extensive in this marginal lacustrine succession. Consequently, this sedimentary facies type is able to generate highest porosity and permeability throughout large areas of the studied succession.

PTA 2 includes filament molds and vugs which both have contrary pore geometries (see Figure 4.3). An increase in porosity and permeability values strongly depends on the abundance of big and complex vugs and therefore on the extent of diagenetic modification by dissolution. Hence, pore system effectiveness of PTA 2 as occurring in the *Cladophorites* boundstone facies can vary slightly, but generally is moderately effective.

PTA 3 commonly encompasses a hierarchy of four genetically different pore types (see Figure 4.4). Vugs are rare due to the limited space for vug formation. However, both skeletal-bound pore types together produce fairly high porosity and permeability values, respectively. Interpeloidal pores are less abundant in PTA 3, and contribute to a lower degree to pore system effectiveness in this type of pore system. PTA 3 is present in the skeletal grainstone facies, which is very sensitive for diagenetic alterations due to its high primary porosity generated by big intraskeletal pores. Thus, even relatively open PTA 3 pore spaces often show cementation at the pore rim, and most of the samples which were not used for evaluation of pore type effectiveness in this chapter due to complete closure by cementation can be found in the skeletal grainstone facies. Consequently, PTA 3 also shows a wide range of pore system effectiveness.

The benefit of linking DIA-derived pore type properties to the corresponding pore-forming processes can best be shown in the example of vugs: Since vugs have been identified as the most effective pore type, it can be implied that pore system effectiveness and therefore porosity-permeability properties of this marginal lacustrine succession enhance with increasing abundance of vugs. The presence,

distribution and abundance of vugs formed by meteoric diagenesis generally depend on the duration, amplitude and frequency of subaerial exposure. In a hypothetical analogue, the vug-forming process of dissolution might have acted with a different amplitude and frequency which would results in varying distribution and abundance of vuggy pores, respectively. Moreover, this would lead to variations in pore size and shape complexity of vugs which differ from the studied marginal lacustrine carbonates. If the duration of subaerial exposure is shorter, vugs are smaller and less abundant which causes lower interconnectivity and therefore a reduced effectiveness of the pore system. Finally, the vug-forming process of dissolution by meteoric diagenesis can be totally absent if subaerial exposure was too brief, and the marginal carbonates have been buried soon after deposition. Further processes may also decrease effectiveness in a potential analogue, for example by several phases of cementation of vugs, or enhance porosity, for example by generating additional secondary pore types. However, it must be noted that within the different pore systems of the same succession, the vug-forming process of dissolution has acted with identical amplitude and frequency.

The role of subaerial exposure in the formation of vugs and the modification of pore system have been studied in detail for marine shallow-water carbonates (e.g., Esteban & Wilson, 1993; Saller et al., 1994a; Saller et al., 1999). Saller et al. (1999) defined four successive stages of pore system modifications based on the duration of subaerial exposure. After the first stage with brief exposure and minor to absent modifications, most preexisting primary pores are partially or completely filled with cement during the second stage. In the third stage of moderately long exposure, secondary moldic pores and vugs are formed which are then filled with cement during the fourth stage with longest duration of subaerial exposure. In the studied lacustrine carbonates, all petrographic evidences for a stage 4 (sensu Saller et al., 1999) modification of pore system are observed. Both primary and secondary pores are present, and partially or completely filled by calcite cement. However, the duration of exposure required for such advanced modification of pore system is estimated to be more than 130,000 years in marine systems (Saller et al., 1999). Considering that the entire marginal lacustrine succession of the Nördlinger Ries with a thickness of 50 meters has been deposited within approximately 0.3 to 2 Ma years (Bolten, 1977; Pohl, 1977; Jankovski, 1981) which results in a cycle duration between 12,000 and 800,000 with an average cycle thickness of 2 meters, and a calculated build-up growth duration based on the rhythmic growth pattern of *Cladophorites* of 775 years (Arp, 1995b) which is approximately one half of a cycle, it is unlikely that vugs have been formed by subaerial exposure during each individual internal "bioherm cycle" (sensu Arp, 2006) in the eogenetic zone as compared to marine shallow-water carbonates. Additionally, vugs in the studied lacustrine carbonates do not show the veneering laminated crust and infilling with skeletal grains and palustrine sediment as found in the growth framework space, which previously has been interpreted as an indication for brief subaerial exposure during each internal cycle (Riding, 1979; Arp, 1995b; Arp, 2006). Therefore, vugs in the studied carbonates must have been formed in the telogenetic zone after deposition of this lacustrine marginal succession has ceased. In this zone, the formation of vugs is also typical in marine carbonates (Mazzullo, 2004). However, the extent of pore system modifications through subaerial exposure in marine systems depends on numerous intrinsic factors such as the chemical composition and the residence time of the percolating freshwater, the

porosity and permeability within the affected carbonates, and their texture and chemical composition (Saller et al. 1994; Mazzullo, 2004). Due to the scarcity of equivalent studies in lacustrine system, and a non-correlation between the stable isotope signal and the internal sedimentary cycles of the studied outcrop (Christ et al., 2018), it remains unclear whether these factors and processes act differently in marginal lacustrine carbonates, and especially in the studied succession.

It can be further observed how a hierarchy of different pore types interact with each other throughout pore system evolution, and in respect to porosity and permeability generation within one sample: Only few (average proportion of 12.39 %) but elongated (γ = 2.45) skeletal moldic pores with a very low Φ_{DIA} of 2.04 % usually contribute to K_{total} with a relatively high $K_{contr.}$ of 63.62 mD in respect to their size and abundance. In contrast, simple-contoured (γ = 1.74) but big intraskeletal pores which usually encompass 32.48 % of the pore space on average and thus generating a high Φ_{DIA} of 7.38 %, only produce relatively moderate $K_{contr.}$ values of 185.88 mD in respect to their proportion. Therefore, in an initial pore system of the skeletal grainstone facies (i.e., PTA 3), primary intraskeletal pores represent a stage in the pore system evolution where porosity exceeds permeability. In contrast, no high primary porosity and permeability can be expected in matrix-dominated facies types, such as the *Cladophorites* boundstone facies. However, porosity and permeability in both the *Cladophorites* boundstone and skeletal grainstone facies can be extensively modified by the introduction of vugs or by the formation of skeletal molds. Both secondary pore types which have been formed by dissolution are responsible for main permeability contribution to K_{total}. Thus, their formation represents a "permeability stage" of pore system evolution. A pore system dominated by primary interpeloidal pores (> 90 %; see sample 3A5_9 in Figure 3.9) with a Φ_{DIA} of 12.92 % generates a K_{total} of 356 mD. It contains only one single secondary vug which has been added during the "permeability stage", and original interpeloidal pores at the site of dissolution are overprinted and replaced by this new vug. As a consequence, Φ_{DIA} only changes slightly. However, since vugs are much more complex (i.e., have a higher average γ value) than interpeloidal pores, K_{total} increases noticeable. This single vug contributes to total permeability with 69.50 mD, which is 19.52 % of the K_{total} value of 356 mD.

4.6 Conclusion

Based on all petrophysical facies parameters, vugs have been identified as most effective, contributing to K_{total} with averagely $K_{contr.}$ = 649.72 mD, and with an average porosity of Φ_{DIA} = 11.55 %. This pore type predominantly occurs in PTA 1 and 2, which can be found in the peloidal grainstone and the *Cladophorites* boundstone facies, respectively, and less frequently in the PTA 3 pore system of the skeletal grainstone facies. Vuggy pores are marked by their large sizes and very complex shape. Although interpeloidal pores are relatively small and less complex as vugs, they represent the second most effective pore type ($K_{contr.}$ = 195.82 mD; Φ_{DIA} = 7.53 %). They mainly occur together with vugs in the interpeloidal grainstone facies and associated PTA 1, which consequently has the potential to generate highest effective porosity and therefore permeability in this marginal lacustrine succession. Furthermore, this sedimentary facies type is most abundant in the marginal lacustrine succession of the

Nördlinger Ries crater lake, occurring as lateral continuous and extensive sheets and amalgamated bodies in between *Cladophorites* build-ups. Skeletal molds are the third most effective pore type, because apart from their very small size and low abundance, they tend to interconnect with adjacent pores due to their elongated shape and high shape complexity, which is also reflected in a relatively high $K_{contr.}$ and efficiency values in respect to their proportion. Intraskeletal pores and filament molds occur predominantly isolated, and due to their simple shape contour rarely interconnect with other pores. Based on all seven petrophysical facies parameters, they are therefore identified as ineffective pore types in the studied pore systems.

In this chapter, all obtained quantitative information about pore size (pore width), shape complexity (γ, sensu Anselmetti et al., 1998), abundance (number of pores), efficiency (ratio between number of pores and porosity they produce), porosity (Φ_{DIA}), permeability contribution ($K_{contr.}$) and proportion ($\%_{PoreType}$) of each pore type are summarized in a petrophysical facies which is the base for evaluating the effectiveness of all PTAs present. Since each PTA can be assigned to a distinct sedimentary facies, this approach can be used to perform quantitative rock-typing for petrophysical characterization of each sedimentary facies type examined. Resulting numerical data can also be integrated into a geological map or model which can then be transferred into a porosity-permeability equivalent.

CHAPTER FIVE

APPLICATION II: QUANTIFICATION OF THE IMPACT OF CEMENTATION ON PETROPHYSICAL PROPERTIES AND RECONSTRUCTION OF PORE SYSTEM EVOLUTION

5.1 Introduction

Pore system evolution of the marginal lacustrine carbonates of the Nördlinger Ries have experienced an additional stage of cementation of preexisting pores after introduction of secondary vugs into the pore system (see Chapter Four). In 23 facies-specific samples of the total sample suite of 122 samples, an extensive partial or complete cementation of pore space by at least one generation of low-magnesium calcite cement has been observed. However, their original texture and pore structure can still be recognized. This mainly occurs in the *Cladophorites* boundstone facies and to a lower degree in the non-skeletal grainstone facies. The skeletal grainstone facies instead often shows a complete overprinting of the sedimentary fabric by cementation and the original pore structure cannot be recognized. Cementation with low-magnesium calcite occurs patchily, varies at a sub-centimeter scale and shows no facies-dependency. Additionally, it has affected both primary and secondary pores, and therefore must have acted after the formation of each pore type present. The previously presented workflow of extracting pores from the surrounding sedimentary fabric (see Chapter Three and Four) has been modified in order to detect the cement, and in a later stage to graphically remove this extracted cement to obtain a pore space representation of the pore system prior to cementation. Consequently, the evolution of pore system is further reconstructed and the effect of diagenetic modifications on porosity, pore geometry and therefore pore system effectiveness is quantified for each stage of pore system evolution.

Mowers and Budd (1996) also assign the problem of heterogeneity in carbonate pore system to the variable distribution of cements causing heterogeneities at a millimeter scale. However, they emphasize the possibility to locate this heterogeneity by using DIA which further helps to understand the distribution of cemented intervals. Additionally, the authors recommend to analyze each occurring pore type individually and throughout the entire postdepositional history of the sedimentary rock. By analyzing each different stage of postdepositional modifications of pore system with the method presented in this chapter, the approach presented by Mowers and Budd (1996) is therefore further developed. The goal is to find a specific measure or cementation reduction value which quantitatively describes the impact of cementation on pore system properties in the studied carbonates. The resulting information can then be used to further improve the complex prediction of petrophysical properties, using this marginal lacustrine succession as a case study. Additionally, the effect of the formation of late secondary vuggy pores on porosity and permeability is quantified.

5.2 Impact of Cementation on Pore Geometry, Porosity and Permeability

The local postdepositional history of pore system evolution of the Nördlinger Ries carbonates can be summarized into three main chronological stages: (i) an initial stage encompassing primary (i.e., interparticle and intraparticle) and late primary to early secondary (i.e., filament moldic) pores; (ii) a second stage of dissolution resulting in the formation of late secondary vuggy and skeletal moldic pores; and (iii) a third stage of partial or complete cementation of preexisting pores with low-magnesium calcite.

The initial stage is marked by a pore system which includes primary and fabric-selective (sensu Choquette & Pray, 1970) interparticle pores, which occur mainly as pore space in between peloids and skeletal grains, and as intraparticle pores within the shells of gastropod *Hydrobia trochulus* and ostracod *Strandesia risgoviensis*. These primary pore types are tied to the peloidal and skeletal grainstone facies, and consequently their size and shape complexity depend on the original arrangement of peloids and skeletal grains, and on the size and shape of skeletal chambers. In the *Cladophorites* boundstone facies, these early primary meso- to macropores are absent. Instead, early primary porosity occurs as few micropores in the micritic matrix of the boundstone facies. However, as noted before, this microporosity is inefficient in producing porosity and permeability. In a late primary to early secondary stage, each grain has been rimmed by a phreatic dolomicritic cement during early and shallow burial within the eogenetic zone (Riding, 1979; Arp, 2006; Christ et al., 2018), which also helped to stabilize the filaments of *Cladophorites* green algae prior to their dissolution. This led to the generation of spherical to elliptical moldic pores with a very simple contour which is confined by the original green algae filament shape. The dolomicrite clearly predates all secondary pores and can only be found as a thin cement (< 40 µm) rimming each original grain and primary pore. Due to its very small size and low microporosity (see Chapter Two), its effect on porosity and permeability is insignificant.

The second stage is characterized by the introduction of vugs into the pore system. They have been formed by chemical weathering due to subaerial exposure and meteoritic dissolution in the vadose and eogenetic to telogenetic zone. Vugs are not fabric-selective and tend to cross-cut both the sedimentary fabric and preexisting pores. They have very irregular shapes and generally much bigger pore sizes as compared to all other pores types. Vugs usually cover large areas of the pore system and show a high interconnectivity as touching vugs (sensu Lucia, 1983).

The third stage of pore system evolution encompasses the extensive partial or complete cementation of preexisting pores formed during both earlier stages with a vadose low-magnesium calcite (Riding, 1979; Arp, 2006; Christ et al., 2018), which very often also led to a complete overprinting of the original sedimentary texture. Cementation occurs patchily and shows no dependency towards a distinct sedimentary facies or towards any pore type. In only two thin sections examined, this vadose low-magnesium calcite appears to have been precipitated within two successive stages, indicated by an inclusion-rich and an inclusion-free phase of cement (Figure 5.1). It is also observed that small pores (e.g., filament molds) show a higher tendency to become entirely cemented as opposed to bigger pores

(e.g., vugs). However, even partial cementation of vugs does not only decrease porosity to the same extent as the volume of precipitated cement but moreover can close interconnected pore throats between adjacent pores. Then, this newly precipitated cement acts as a barrier which decreases effective porosity and therefore permeability, tremendously. In fact, the decrease of porosity caused by cementation correlates with the volume of pore space area closed by newly precipitated low-magnesium calcite. Therefore, porosity is mainly altered by the decrease in area of pore space and simultaneous gain in solid sedimentary fabric produced by the process of cementation. In contrast, permeability does not decrease simultaneously with the degree of cementation and the area of newly precipitated cement. Instead, permeability decrease is mainly controlled by a change in pore shape complexity initiated by partial cementation. It leads to a progressive occlusion of pores and pore throats with cement, and results in the modification of pore shape complexity. Therefore, cementation literally transforms a complex, big and touching vug of high interconnectivity into a more isolated and simpler pore with lower interconnection to adjacent pores. Finally, if cementation proceeds, this pore is closed entirely by cement.

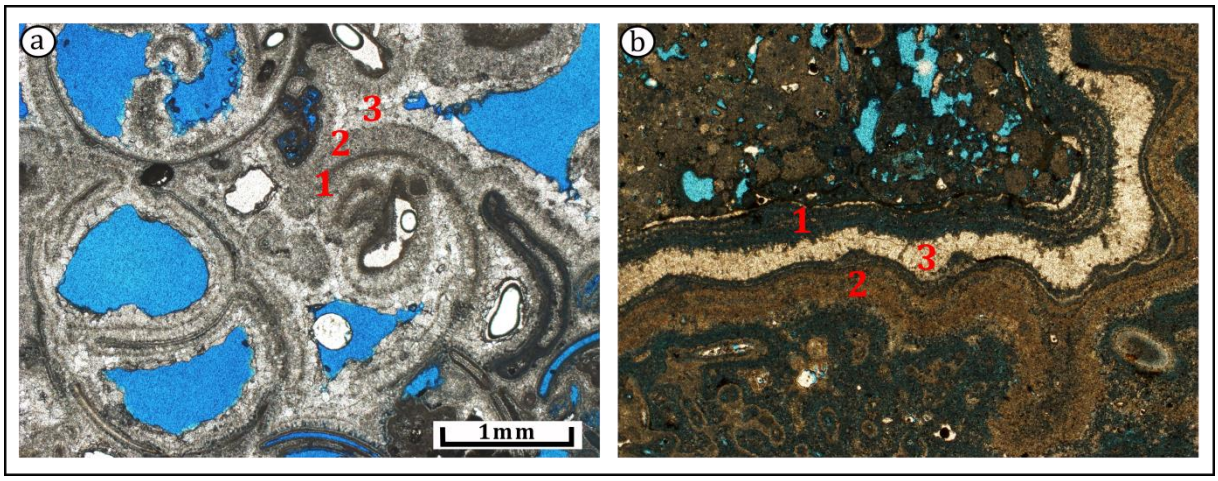

Figure 5.1. Thin section images indicating cements with different hue of color. a. Skeletal grainstone. **b.** *Cladophorites* boundstone. Dark grey to black dolomicritic rim (1), medium grey to brown, inclusion-rich sparry calcite cement (2), and light grey to white inclusion-free sparry to blocky calcite cement (3).

In order to detect and extract the pore-filling cement with DIA, the previously presented workflow of pore system analysis (Chapter Three and Four) has been applied on 52 thin section images derived from the 23 cemented samples. In the following, the method is presented on the examples of three different thin section images of sample 3_60, representing three areas of the thin section with lowest, intermediate and highest degree of cementation, respectively (Figure 5.2). During the first step, both pore space and cement are segmented from the actual pore system by using their distinct color spectra, as presented in Step I of the methodological workflow. Since the low-magnesium calcite cement has a very bright and whitish to greyish hue, it can be clearly distinguished and differentiated from the surrounding micritic matrix which has a darker and brownish hue, and from the blue-dyed pore space where the cement has precipitated (Figure 5.2a). After segmentation, each detected component is

classified with the single parameter classification (see Chapter Three) into a regular pore type where cementation is absent, or into a partially or fully cemented pore type.

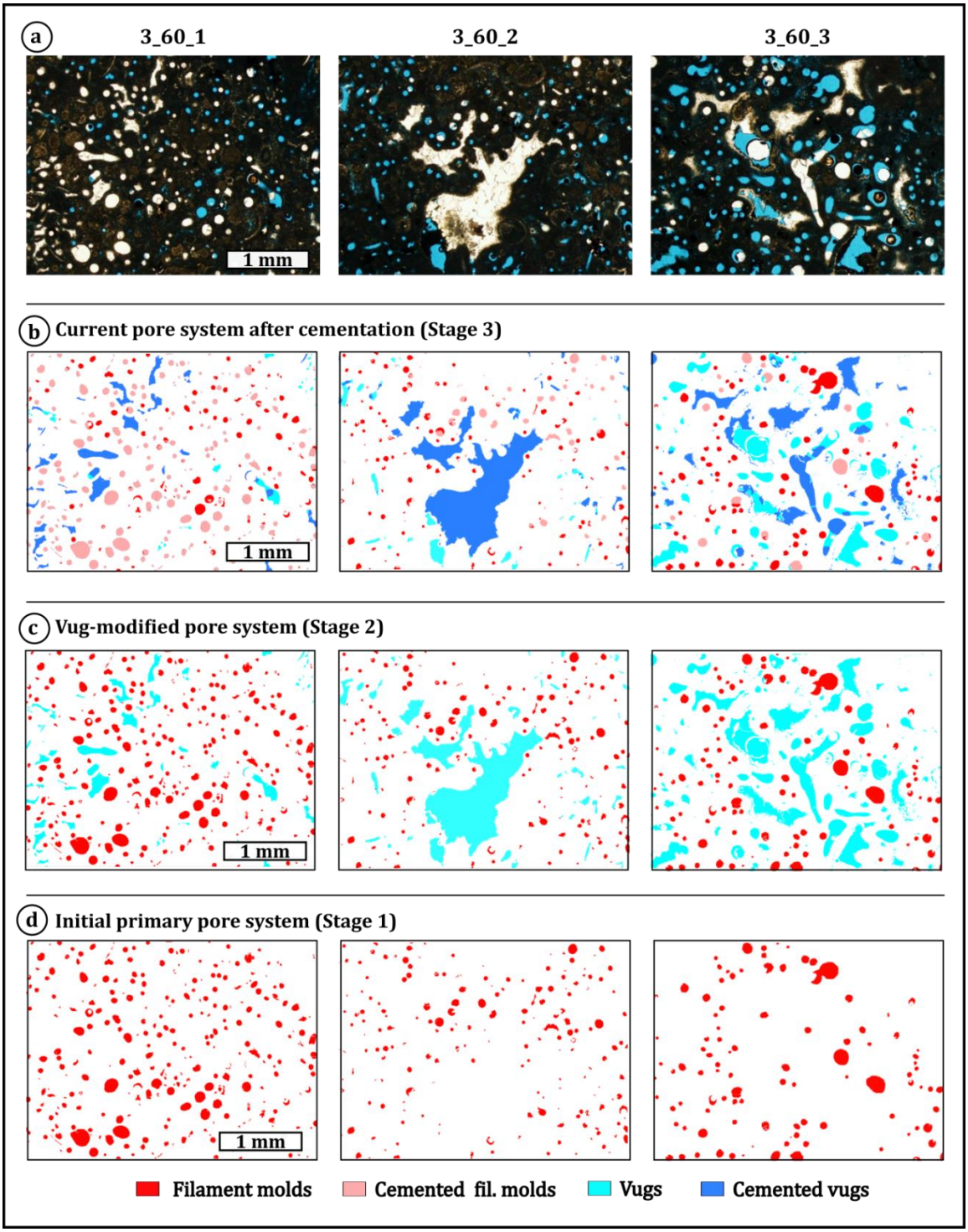

Figure 5.2. Thin section and DIA-derived images representing different stages of pore system evolution. a. Three different images of sample 3.60 representing low (3.60_1), intermediate (3.60_2) and high degree (3.60_3) of cementation. **b.** The original thin section images are classified into regular and cemented pore types with DIA. **c.** Then, the cement within each pore is graphically classified into the corresponding regular pore type to obtain a pore system prior to cementation. **d.** In order to reconstruct the initial primary pore system prior to vug-forming dissolution, all secondary vugs must be graphically removed.

is classified as either vug or filament mold, whereas the cemented area is classified as either cemented vug or filament mold. As a result, an image of the segmented and classified pore system is obtained, with each class highlighted in different colors. This classification is key to measure the change in pore geometry between the current stage of pore system evolution and the stage prior to cementation.

The classified image of the actual pore system is then integrated into a graphic software which supports scalable vector graphic files (e.g., *Adobe Illustrator*©, *Inkscape*©). This allows for manipulating the entire segmented pore system, each class of components, and each individual pore. Consequently, the class color of cemented vugs and filament molds are then modified and adapted to the class color of the corresponding open regular pore type (Figure 5.2c). As a result, a new image is created which closely resembles the pore system prior to cementation. This newly created pore system image is then integrated into the DIA software, where both porosity and pore geometry are measured again (see Chapter Three). Finally, the resulting quantitative pore geometry data are compared with previously obtained values from the original unmodified image of the actual pore system. This results in distinct values describing the difference in pore geometry of each pore type class between the current stage of pore system evolution and the second stage prior to cementation. Therefore, the impact of cementation on porosity and permeability between both stages is quantified.

As a next step, the pore system is further reconstructed to the first stage, representing the initial primary pore system. All secondary pores have to be removed graphically since they clearly postdate both the early primary interparticle and intraparticle pores as well as the late primary to early secondary filament molds, indicated by the absence of the dolomicritic rim. The newly created image of the uncemented pore system is integrated into the graphic software again, and by selecting the pore type class of secondary pores, they are removed from the image. This yields a pore system image which resembles the first initial stage of pore system evolution and includes primary pores, solely (Figure 5.2d). By uploading this image into the DIA software, both pore geometry and porosity are quantified, and results are compared in order to calculate the change in pore geometry between the first initial stage and the second stage of vug formation. However, in order to reconstruct the pore system of the initial stage, it must be considered that primary (e.g., interpeloidal and intraskeletal pores) to early secondary pores (e.g., filament molds) might have been enlarged and thus overprinted by the formation of secondary vugs (Figure 5.3). However, this only applies to non-fabric-selective vugs, since secondary skeletal molds are fabric-selective and do not overprint preexisting pores. Therefore, a statistical estimation has been applied to predict potential preexisting but overprinted pores and to avoid underestimation of porosity produced by the initial pore system. This correction is based on the statistical distribution of both open and cemented primary pores and secondary vugs. The original primary porosity of the initial stage of pore system evolution is estimated by using following equation:

$$\Phi_{\mathrm{DIA}}\ (\mathrm{Stage1}) = \frac{(\Phi_m + A_m) \times 100}{100 - (\Phi_v + A_v)} \qquad [\%]$$

Φ_m : primary porosity

A_m : area covered by cemented primary pores

Φ_v : vuggy porosity

A_v : area covered by cemented vuggy pores

In this formula, all vuggy pores and their cemented equivalents are considered as regular sedimentary fabric, since they did not exist during the first stage of pore system evolution. Therefore, their proportion is subtracted from the actual sedimentary fabric. Then, the amount of cemented area of the initial pore system dominated by primary pores is measured and added to their porosity value. Finally, the percentage of potentially overprinted pores is calculated with the newly obtained Φ_{DIA} value of stage 1.

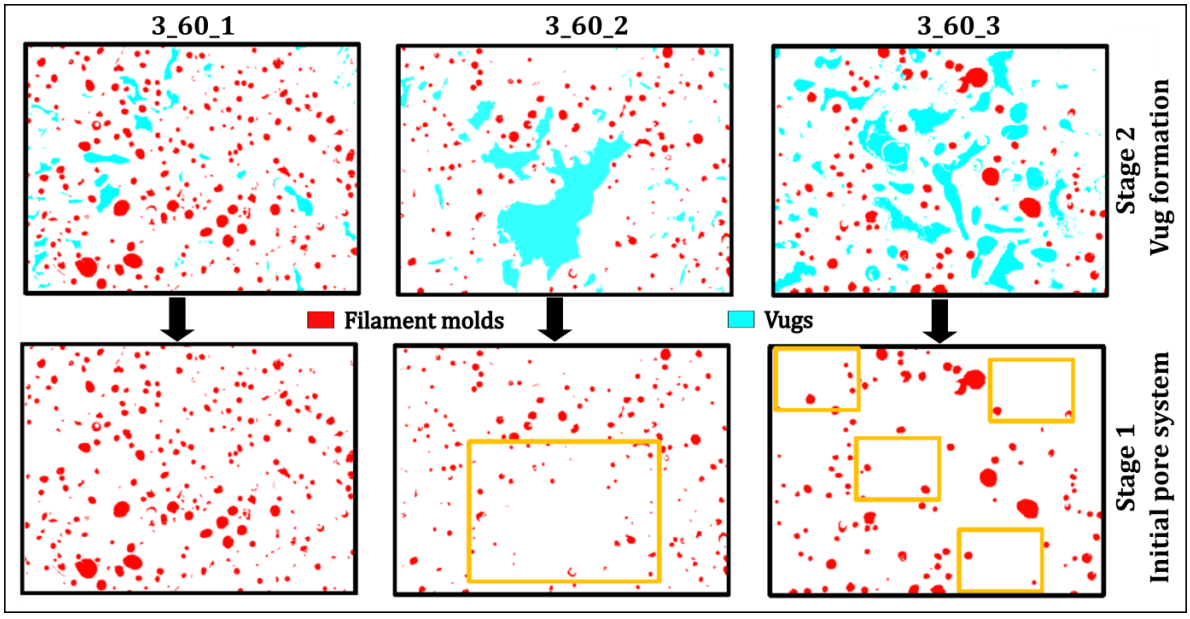

Figure 5.3. Correction of underestimation caused by preexisting but overprinted pores. DIA-derived images of sample 3_60, representing the change in pore system between Stage 2 (vug-modified pore system) and Stage 1 (initial primary pore system). Boxes indicate areas of potential overprinting of preexisting filament molds by vugs. This potential underestimation is corrected by using the statistical distribution of each pore type.

The correction of the initial porosity of all 52 thin section images examined in this chapter yields an average underestimation of less than 0.5 % of porosity in respect to the calculated meso- and macroporosity with DIA. This very low value of underestimation can be attributed to the small size and resulting low amount of porosity produced by most initial pores (i.e., filament molds). However, it is worth noting that if the majority of preexisting initial pore types were generally more effective in generating porosity and permeability, the correction would result in a more significant underestimation. Therefore, this adjustment is important for a precise reconstruction of pore system evolution.

In order to analyze the change in permeability throughout each stage of pore system evolution, the method of quantifying permeability contribution ($K_{contr.}$) of each pore type to total permeability (K_{total}) has been applied, as presented in Chapter Three in Step III of the methodological workflow. Based on the proportion of each pore type and calibration of the total permeability value with the pore-type-specific γ value, a permeability contribution can be assigned to each pore type and consequently also to each pore system throughout each stage of pore system evolution. Table 4 shows the average values of pore geometry, here represented by pore width and pore shape factor γ, DIA-derived and corrected meso- and macroporosity (Φ_{DIA}), as well as permeability contribution ($K_{contr.}$) for all 52 images examined for this chapter.

Stage of Pore System Evolution	**Pore Width [µm]**	**Φ_{DIA} [%]**	**γ [-]**	**$K_{contr.}$ [mD]**
Stage 1 (Initial pore system)	20.57	1.92	1.46	138.26
Stage 2 (Vug-forming dissolution)	23.70 *+ 15.21 %*	**14.42** *+ 651.04 %*	**2.39** *+ 63.69 %*	**227.07** *+ 64.30 %*
Stage 3 (Cementation, actual pore system)	**33.85** *+ 42.82 %*	8.44 *- 41.47 %*	1.63 *- 31.79 %*	154.53 *- 31.94 %*

Table 4. Impact of cementation on pore geometry and petrophysical properties throughout each stage of pore system evolution

As a result, the impact of cementation on pore geometry and thus porosity and permeability is quantified, and a distinct percentage of average decrease in value for each parameter (i.e., cementation reduction value) can be assigned. Based on all 52 thin section images examined, it has been calculated that porosity generally increased between the initial stage and the second stage of vug-forming dissolution by 14.42 % on average, whereas permeability increases averagely towards 227.07 mD (see Table 4). As previously noted, the differential porosity and permeability increase is mainly caused by the ineffectiveness of initial filament molds and intraskeletal pores in producing permeability, since they have a much lower interconnectivity as compared to vugs. Between the second stage of vug formation and the third and current stage of pore system evolution which is marked by a profound cementation of pore space, porosity decreases to an average value of 8.44 %, whereas permeability decreases to 154.53 mD on average (Figure 5.4). The percentage of change in porosity (- 41.47 %) and permeability (- 31.94 %) as well as for pore width (+ 42.82 %) and γ (- 31.79 %) values can then be used as a measure to quantify the impact of cementation on pore geometry, porosity and permeability. Since cementation occurs patchily, varies at a sub-centimeter scale and can therefore not be detected easily in the subsurface and at outcrop or reservoir scale, these values serve as distinct error bars or as lower threshold values for porosity and permeability predictions.

This potential decrease in pore system properties caused by cementation can be further refined by considering the total volume of cements in this marginal lacustrine succession. Riding (1979) calculated that the volume of postdepositional cements in respect to the depositional stages of *Cladophorites* bioherm evolution is around 1/3 of the entire volume of the carbonate host rock. Since this value also includes the thin dolomicritic rim which has been precipitated around each component but which does fill preexisting pores only to a very low degree, it can be assumed that the volume of low-magnesium calcite is slightly less than 1/3 of the total volume. As a consequence, if the total volume of a succession is known, the previously quantified porosity and permeability reduction value can be used to further refine possible error bars in porosity and permeability predictions. If cementation is facies-dependent and tied to a distinct type of pore system, these possible errors can be reduced even more, since only the volume of the sedimentary facies type modified by cementation must be known. Accordingly, the values of increase in pore system properties by the formation of vugs can be used to quantify their role in enhancing porosity and permeability throughout a succession.

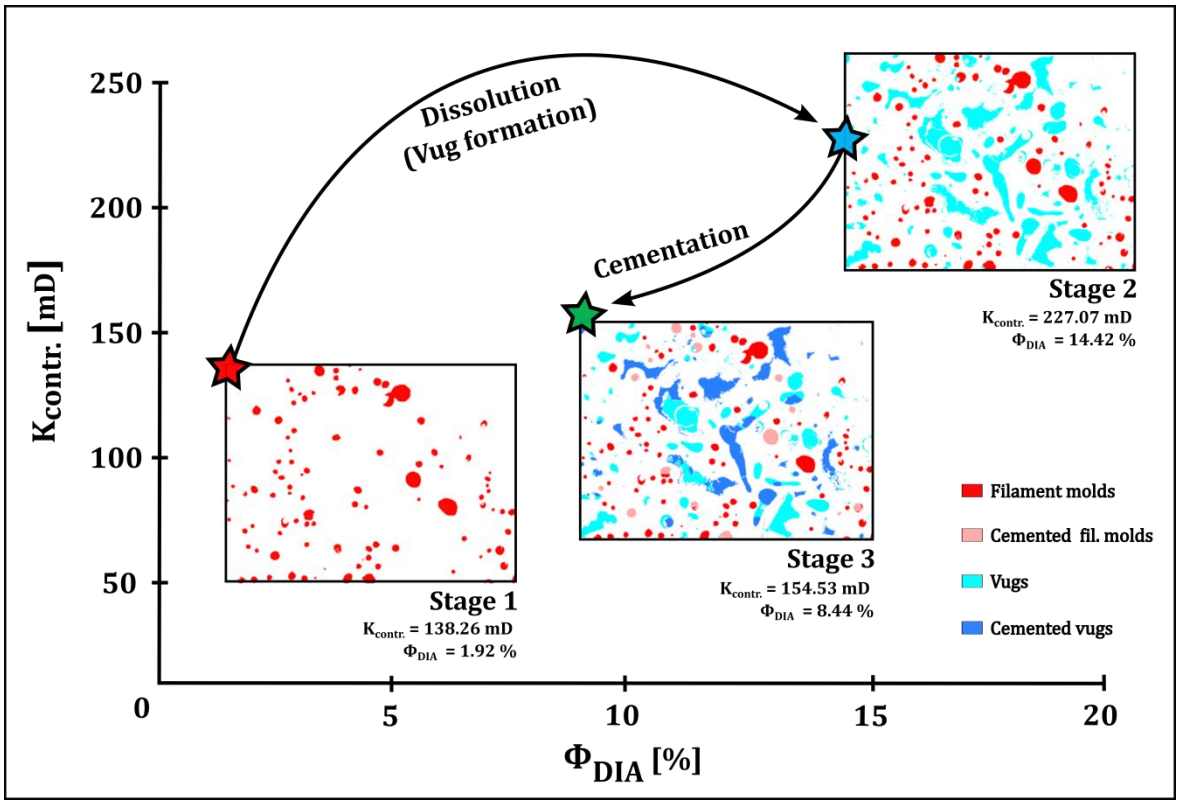

Figure 5.4. Pore system evolution and its impact on petrophysical properties. Stars indicate mean values of all samples analyzed for this chapter.

5.3 Discussion of Chapter

In this chapter, it has been shown that the evolution of pore system is marked by a first initial stage including early primary interparticle and intraparticle pore types, and late primary to early secondary filament molds. These initial pore types are then modified by the vug-forming process of dissolution, when late secondary vugs are introduced into the pore system which is the main factor enhancing

porosity and permeability during this stage. These enhanced pore systems are then filled by a vadose low-magnesium calcite cement which leads to a reduction of pore system properties.

All pore systems analyzed experienced pronounced changes throughout each stage of pore system evolution (Figure 5.5). Pore width shows lowest value (20.57 µm) in the initial primary pore system (Stage 1), caused by the presence of relatively small filament molds and interparticle pores (see Figure 5.5a). This is also reflected in a low average Φ_{DIA} value of 1.92 (see Figure 5.5b) and an average pore shape factor γ value of 1.46 (see Figure 5.5c), indicating small and generally simple-contoured pores. In consequence, this leads to a low permeability contribution of 138.26 mD on average (see Figure 5.5d).

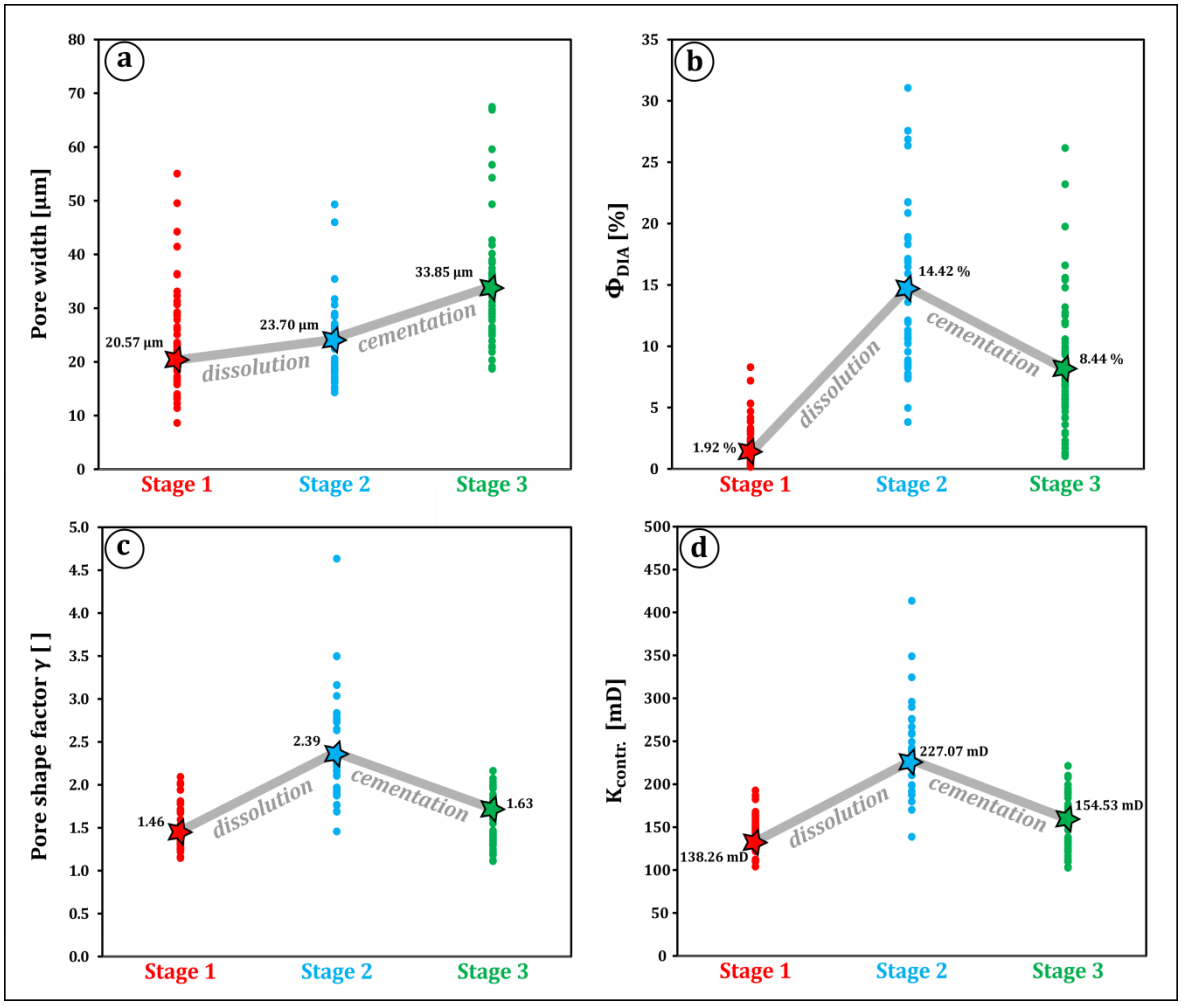

Figure 5.5. Impact of cementation on pore geometry and petrophysical properties throughout each stage of pore system evolution. a. Pore width. **b.** Φ_{DIA}. **c.** Pore shape factor γ. **d.** $K_{contr.}$. Mean values are labelled and indicated by stars.

The range of both porosity and γ values in the first initial stage is very narrow, which lies in the fabric-selective nature of all initial pore types present. They are bound by the original size and shape of *Cladophorites* filament traces or by the size and arrangement of skeletal and non-skeletal grains. As a consequence, no high variation in porosity and shape complexity, and therefore in permeability, occurs. During the next stage of dissolution (Stage 2), porosity produced by the pore system is strongly

enhanced mainly due to the introduction of vugs. This increase in porosity towards 14.42 % can be attributed to the bigger pore size of vugs, which is reflected in a general increase in average pore width towards 23.70 µm. Pore shape factor γ increases towards 2.39, indicating the higher shape complexity of vugs. Simultaneously, the average $K_{contr.}$ value increases towards 227.07 mD. Additionally, the range of porosity and pore geometry values is significantly higher than during the initial stage. Non-fabric-selective vugs can be highly variable in size and shape, and they are generally much bigger and more complex than initial pores, leading to a higher variance in values for both parameters.

In the third and current stage of pore system evolution, preexisting primary and secondary pores are partially or completely filled by cement. This is reflected in a decrease of DIA-derived meso- to macroporosity (Φ_{DIA}) towards 8.44 %, because cementation reduces the area of available pore space. Additionally, cementation decreases the pore shape complexity of vugs, since even if a vug is only partially cemented, it loses its tortuosity. This can be explained by the fact that cement, which grows from the pore walls towards the center of the pore, first fills the branching of a complex vug and therefore reducing its tortuosity and consequently its pore shape complexity. This is reflected in a lower pore shape factor γ value of 1.63 and results in a decrease in permeability contribution towards 154.53 mD.

The wide range of both porosity and pore shape factor γ values during this stage is identical to the value ranges in the previous second stage, since both pore systems are multimodal as opposed to the generally unimodal initial pore systems. Additionally, the differential degree of cementation of each pore also leads to a higher scatter of values. Interestingly, although it can be expected that partial or complete closure of pore system by cementation reduces the average pore width fundamentally, the average pore width increases towards 33.85 µm instead. This is caused by the fact that small pores usually experience full closure of pore space with cement, and the average pore size of the entire pore system increases because big and only partially cemented vuggy pores remain. This is observed in some of the analyzed samples, where all filament molds are completely filled by cement, and the original multimodal pore system including small filament molds and bigger vugs turns into a unimodal system with only partially cemented vugs in the current stage. Then, the average pore width and pore shape complexity values are determined by partially cemented vugs, solely. In few samples of the *Cladophorites* boundstone, it is observed that if the initial pore system is dominated by filament molds and the vug-forming process of dissolution has acted to a lower degree as compared to other samples and therefore vugs are rare to absent, the change in pore geometry between both stages is not as pronounced as compared to samples which show a pore system clearly modified by vugs (see Figure 5.2; thin section image 30_6_1). The main difference is that in samples where vugs are rare and filament molds are the dominant pore type during all three stages, porosity highly decreases during the last stage of cementation. As previously noted, this is caused by the fact that filament molds and other initial pore types are usually much smaller and less complex than vugs and are therefore much more prone to become completely filled by cement. Thus, these pore systems dominated by filament molds which lack a profound modification of pore system by vugs do not show a high increase in pore shape complexity values because of the scarcity of complex

vuggy pores and the general simple contoured shape of filament molds. Consequently, no increase in effective porosity and thus permeability throughout pore system evolution can be expected. Hence, cementation of the small and simple-contoured filament molds decreases permeability contribution only to a low degree, since filament molds are generally ineffective in producing permeability, whether they are completely, partially or not cemented (see Chapter Four).

In contrast, pore systems which experienced pronounced vug-forming modification generally have increased pore shape complexity and therefore permeability contribution values (see Figures 5.4c and 5.4d). This also indicates a more open and interconnected pore system where vugs dominate and provide the effective pore network. Such enhanced pore systems are ideal for diagenetic fluids to circulate, which further amplifies cementation. As a consequence, the impact of cementation on vug geometry and therefore on their permeability contribution is much more severe than cementation of filament molds. This aspect validates the previous findings in Chapter Three and Four about the importance of vugs in creating highly effective pore systems. It further highlights the important role of extracting each effective pore type from the entire pore system in order to understand porosity and permeability distributions and variations, and to generally unravel the petrophysical heterogeneity in carbonates.

A pioneering study about using image analysis for detecting cements and quantifying the impact of cementation on petrophysical properties have been conducted by Mowers & Budd (1996). They quantified the amount of pore space covered by cement to reconstruct porosity and permeability reduction caused by calcite cementation on two different dolomite reservoirs. Porosity and specific surface have been calculated by the authors with DIA in order to solve the Kozeny-Carman equation (Mowers & Budd, 1996, and references therein), and consequently obtain permeability estimates. Specific surface is the ratio of pore perimeter to pore area; therefore it also describes pore complexity identical to pore shape factor γ (sensu Anselmetti et al., 1998) as used in this thesis. However, their analytical results represent the complexity of the entire pore system, but do not include differentiation between (effective and ineffective) pore types. Mowers & Budd (1996) point out that pore throat distribution and thus pore type interconnection and pore system complexity is highly controlled by the variety of different pore types. Therefore, they suggest integrating analysis of each individual pore type into their method, especially for complex multimodal pore systems. For the purpose of this thesis, the effect of cementation on the entire pore system has been calculated to infer the impact of cementation on pore system properties, since all occurring pore types have been affected by cementation synchronously during the same stage of pore system evolution. However, since each cemented pore has been classified individually with the method presented in this chapter, the pore-type-specific effect of cementation can also be quantified. By using the pore type classification of the three thin section images in Figure 5.2 for instance, the degree of cementation of each occurring pore type (i.e., filament molds and vugs) can be quantified. Filament molds are filled with an average proportion of 2.76 % with cement in respect to the whole thin section image, whereas all occurring vugs are covered by 7.02 % of cement on average. Additionally, quantifying the effect of cementation on all relevant parameters (i.e., pore width,

γ, Φ_{DIA} and $K_{contr.}$) for each individual pore type can be realized. This pore-type-specific analysis of cementation is useful if one pore type has been affected predominantly by cementation, or if the effect of cementation on pore type properties of one distinct pore type, for example the most effective pore type, needs to be analyzed. Furthermore, the general understanding of the pore-type-specific evolution and modification is important since each pore type can experience differential diagenetic modifications throughout pore system evolution. Vugs, for instance, can develop from enhanced laminae pores with moderate interconnectivity over channel porosity with higher interconnection into either non-touching or touching vugs (Figure 5.6).

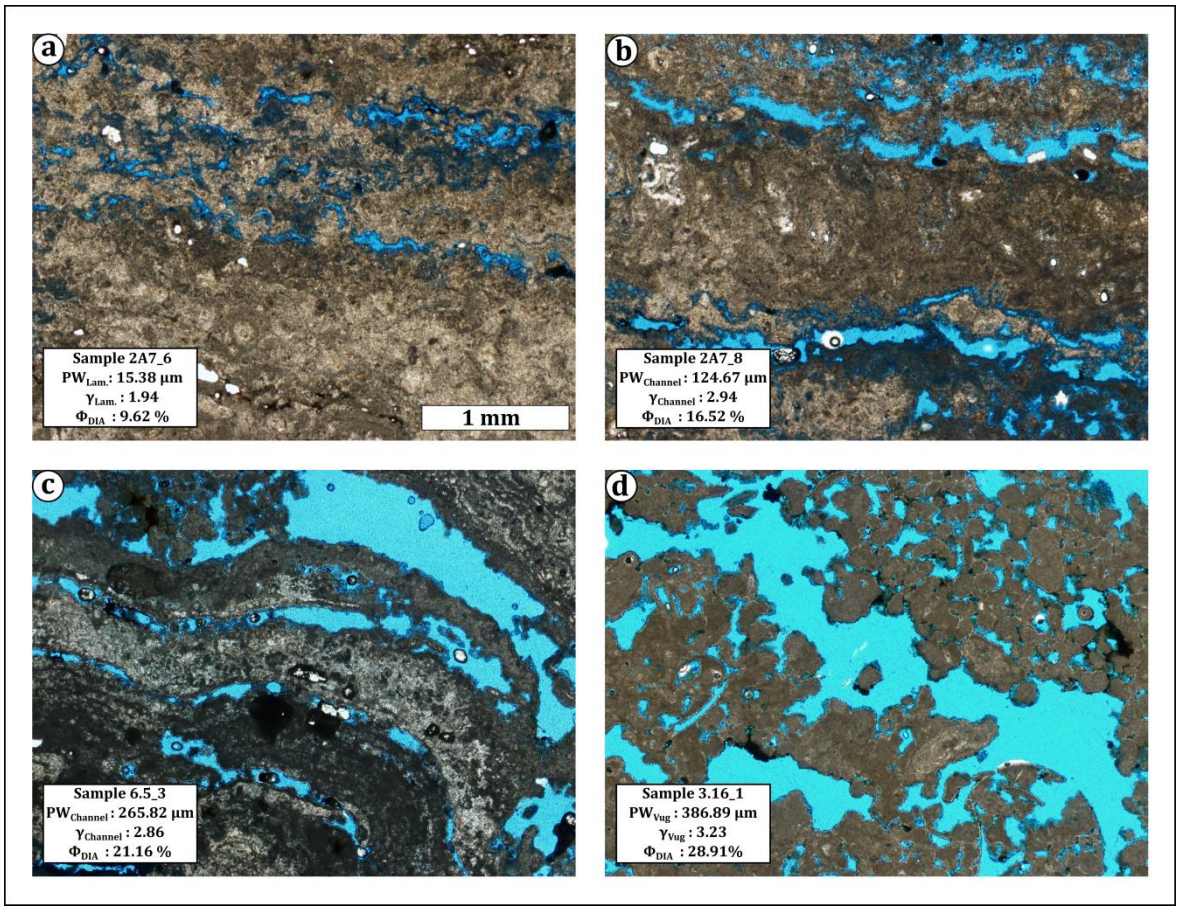

Figure 5.6. Differential evolution of vugs. a. Laminae porosity in the *Cladophorites* boundstone facies which can be enlarged and transformed into channel porosity by onset of dissolution with higher interconnectivity (**b.**). **c.** Channel porosity of enlarged former laminae in the *Cladophorites* boundstone facies, indicating ongoing dissolution and showing reduced fabric-selective character. **d.** Vuggy pores in the peloidal grainstone facies producing a big and open pore system with highest interconnection and thus effectiveness. This is indicated by highest pore width (PW) and γ values.

Additionally, the modification of preexisting components such as peloids also does not occur simultaneously and the degree of dissolution is variable. Figure 5.7 shows the differential dissolution of some peloidal grains captured on SEM-derived images. There, each peloid shows a different abundance of micromolds, indicating variable degrees of dissolution, ranging from low grade dissolution to pervasive micromold formation of adjacent peloidal grains.

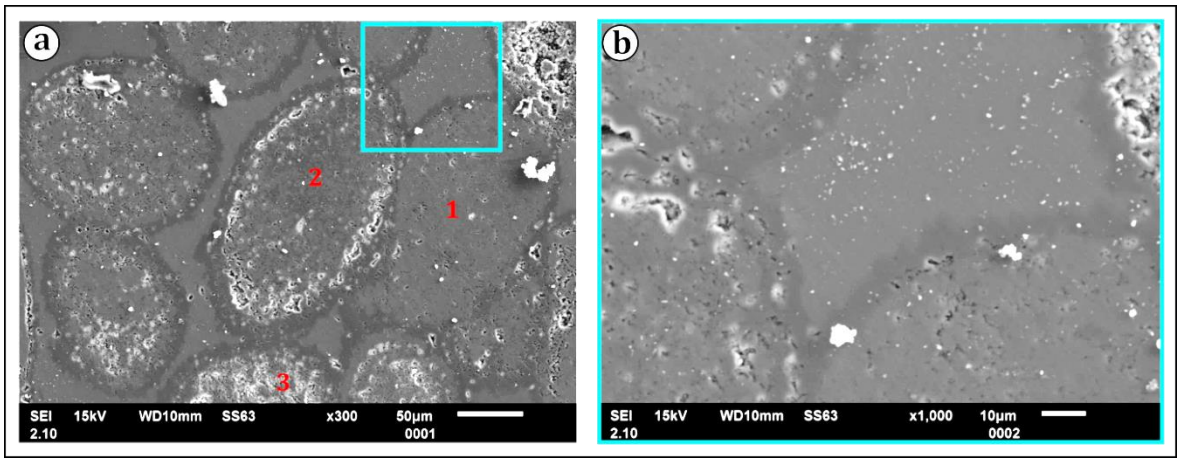

Figure 5.7. Differential evolution of porosity in peloids. SEM images of peloidal grainstone facies. **a.** Note the different abundance of micromolds and therefore the different degree of dissolution of each peloid, from low degree of micromold formation within the entire peloidal grain (1), to partially dissolved peloids with micromold formation concentrated at the rims of each peloidal grain (2), and pervasively micromold-modified peloids (3), representing the highest degree of dissolution. **b**. Close-up image (indicated by box in a.) show few micromolds along the rim of one partially dissolved peloidal grain (left), and smaller microintercrystalline pores within the matrix of peloids.

As previously noted, it has been observed that the low-magnesium calcite precipitated shows at least two phases of cementation, with a first inclusion-rich cement followed by an inclusion-free cement (see Figure 5.1). Since the DIA software is capable of differentiating between both types of cement due to their difference in hue, their distribution and volume in the pore space can be quantified individually. However, this inclusion-rich cement was only observed in two thin sections and is therefore not further differentiated from the associated inclusion-free cement since both usually occur together as pore-filling cement. Moreover, not only blue-dyed thin section images can be processed with DIA, but also images of thin sections stained with Alizarin red S (ARS; Dickson 1965; 1966; Evamy 1963; 1969) to differentiate between calcite and dolomite, or images derived from a cathodoluminescence (CL) microscope to quantitatively describe calcite and dolomite cements of different origin and composition.

5.4 Conclusion

For this chapter, 52 thin section images of 23 samples which show extensive cementation of individual pores have been selected in order to quantify the impact of cementation on pore geometry, porosity and permeability. The goal was to find a quantitative cementation reduction value to characterize the possible variation of pore system properties throughout the marginal lacustrine succession of the Nördlinger Ries, caused by locally and patchily distributed and facies-independent cementation. This third stage of pore system evolution represents the current state of pore system. After the preceding second stage of dissolution which highly enhanced pore system properties, pores became partially or completely filled by low-magnesium calcite cement, leading to a reduction of porosity and permeability. By integrating DIA-derived pore system images into a graphic software, the pore system can be reconstructed throughout each stage of pore system evolution until the initial primary pore system.

Adjustments based on the statistically distribution of pores have been made in order to avoid underestimation of porosity and permeability caused by overprinting of initial pores by late secondary vugs.

The methodological workflow as presented in Chapter Three has been applied to first calculate the differences in pore geometry and porosity between each stage of pore system evolution and then to infer permeability by using the pore shape factor γ. As a result, porosity and permeability both increase between the first initial stage and the second stage which is marked by the formation of vugs. After the introduction of vugs, both porosity and permeability values highly increase which can be assigned to the generally much bigger size of late secondary vugs and to their complex shape and tortuosity. Due to the cementation process, both parameters are reduced between the second stage and the current stage of pore system evolution. The decrease in permeability is also represented as low average values of pore shape factor γ. However, pore width further increases which can be attributed to the full closure of most small initial pores and the presence of partially cemented but still big vuggy pores. Furthermore, the cementation of vugs is more severe than cementation of initial primary pore types in respect to pore system effectiveness, since partial cementation decreases the tortuosity of the highly effective vugs by closing their branching and therefore reducing interconnections by occluding pore throats.

All obtained values can be used to calculate distinct cementation reduction values which quantitatively describe the impact of cementation on each relevant parameter of the analyzed pore systems. The resulting quantitative data are ideal for integration into forward- and reservoir-modeling processes, which further refine the prediction of porosity and permeability distribution within a carbonate succession. The previously calculated cementation reduction values for porosity and permeability can then be used as distinct corrections or error bars for prediction of both parameters in order to consider local and patchy cementation which are unpredictable at a larger scale. Additionally, reconstructing the pore system evolution with the quantitative method presented in this chapter complements diagenetic studies of this marginal lacustrine outcrop, and yields detailed information about postdepositional processes and their effect on porosity and permeability which are not detectable by using routine petrophysical measurements.

CHAPTER SIX

APPLICATION III: FLUID FLOW SIMULATION

6.1 Introduction

The key conceptual approach of this thesis is that pore shape complexity can be used as a proxy parameter for quantification of pore type effectiveness. This subsequently allows for assessing the potential of a specific pore to generate permeability. In this chapter, results of the previously presented methodological workflow (see Chapter Three and Four) are tested by using a different and independent method of analyzing the effectiveness of pores applied to the same dataset. 2D fluid flow simulation is used as a tool to determine whether a pore is effective and therefore generates flow, or if it is ineffective and no flow establishes. The aim of this simulation is to test which pore types are most effective according to this approach and then to compare results with those derived from the DIA method as presented in Chapter Four. Possible similarities or deviations from previous results help to evaluate and discuss both methods of quantifying pore type effectiveness. Fluid flow simulation on thin section images as presented in this chapter therefore provides an additional DIA-based tool of pore system analysis and detection of effective porosity.

6.2 Methodology

Fluid flow simulation has been performed with the free available software *Flow Illustrator*© (Chernyshenko, 2018) on 30 thin section images, resulting in 69 mean values of pore type effectiveness which are then compared to their corresponding pore shape complexity values as calculated in Chapter Four. The software requires a bitmap image in which the void space where flow can be simulated is colored in white. The object which is used in the simulation as a boundary for fluid flow can be colored in any other hue. Therefore, the original thin section image has to be binarized with DIA, resulting in pore space being colored in white and the surrounding solid sedimentary fabric colored in black (Figure 6.1). Finally, the software transforms the uploaded bitmap image into numbers on a Cartesian grid, which are then solved by the Navier-Stokes equation which in turn determines the flow at any transformed pixel point in the grid (Chernyshenko, 2018). The Navier-Stokes equation generally provides a mathematical model describing the motion of Newtonian fluids and are one of the most established and widely used numerical algorithms for modeling fluid flow (e.g., Nakayama & Boucher, 1998; Tiab & Donaldson, 2004; Johnson, 2016; Chernyshenko, 2018). Then, the numerical data are transformed back into a graphic and a video of the fluid flow simulation for the selected time interval is created.

The flow is represented as fluid particles which follow the fluid motion in the velocity field and then disappear. Based on their movement and in particular on their change in motion throughout the grid,

the fluid flow behavior for each time step of the selected time interval is determined with the Navier-Stokes solver applied on the grid (Chernyshenko, 2018). The corresponding velocity vectors of each fluid particle are then graphically linked in a curve, representing the streamlines of the flow. Figure 6.1 represents a snapshot of the video resulting from fluid flow simulation and shows that the flow is either colored in blue, green or red.

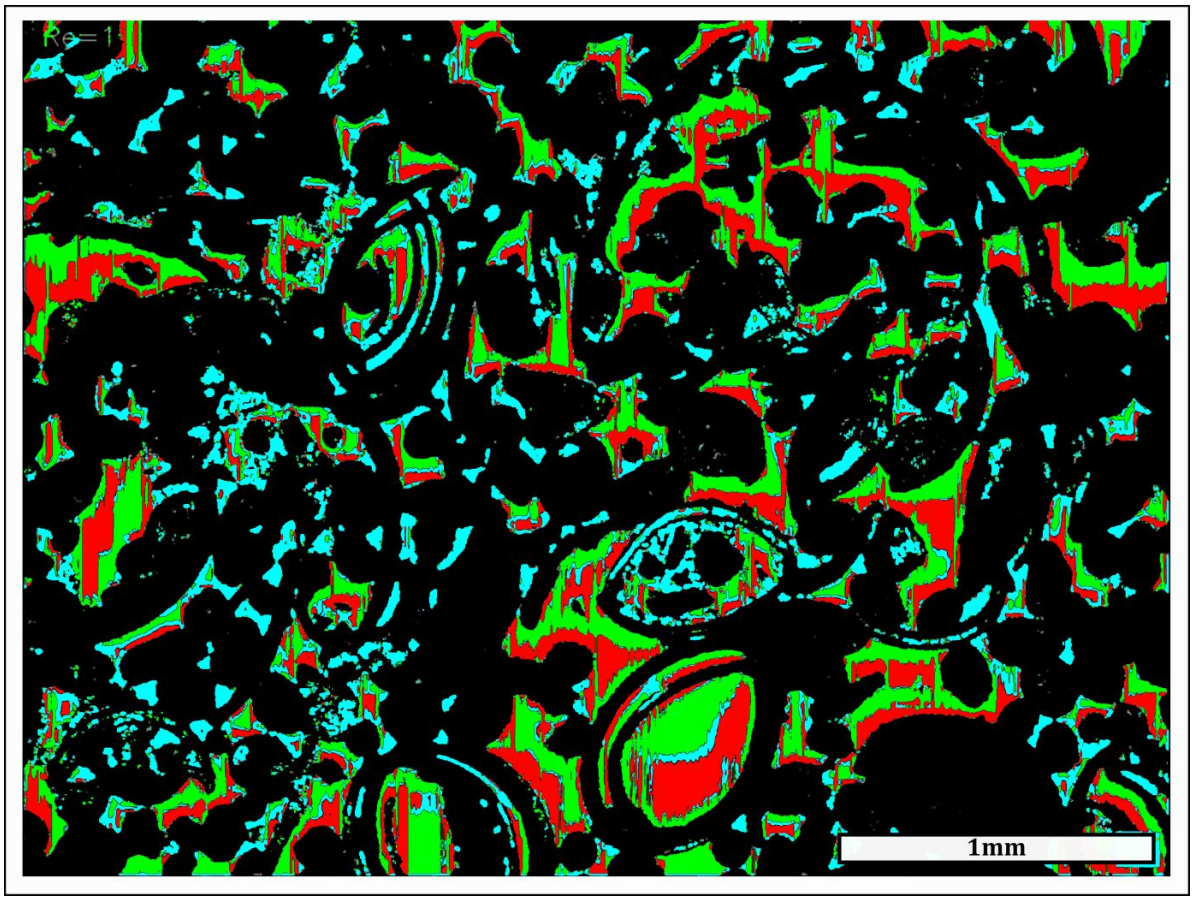

Figure 6.1. Screenshot of fluid flow simulation result. Simulation has been performed on a previously binarized thin section image of sample 3B3_4. Colors represent the change in velocity vector (vorticity), indicating low (blue), intermediate (green) and high (red) fluid flow. Big and interconnected pores generally allow for establishing high flow regimes (green and red) and are therefore effective pore types, whereas isolated pores prevent fluids to flow. Thus, no flow is established in these ineffective pores (blue).

These colors represent the rotation velocity (or vorticity), and form the vorticity field. Vorticity describes the rotation of particles. If a fluid particle moves constantly without any change of velocity vectors, its vorticity is zero, indicated by a blue color in the simulation. If a fluid particle touches other particles or the boundary of an object where due to friction velocity is zero, it has to rotate. High particle rotation results in high vorticity (Nakayama & Boucher, 1998; Chernyshenko, 2018). In the simulation, green and red colors indicate intermediate and high vorticity values, respectively.

As most important input parameter for creating the simulation, a specific Reynolds number (Re) has to be selected. The Reynolds number can be interpreted as the ratio of inertial forces and viscous friction forces, and depends on the fluid velocity, the kinematic viscosity of the fluid and the characteristic dimension which in this case is the distance between the top and bottom of the image (Tiab & Donaldson, 2004; Chernyshenko, 2018). Mathematically, the non-dimensionalized Navier-Stokes equation used in this software only depends on the Reynolds number as the most important input parameter (Nakayama & Boucher, 1998; Johnson, 2016). For this simulation, a Reynolds number of 1 has been selected due to several considerations:

Firstly, the object is modelled using the immersed-boundaries method (Chernyshenko, 2018). This method implies that an object, in this case the sedimentary fabric, is infinite porous and fluid flow particles are able to constantly flow through the object. This would lead to a false simulation, since in isolated pores where realistically no flow can be established, a high fluid flow will be shown, indicated by intermediate to high vorticity. However, by using a Reynolds number of 1, the steady flow of particles becomes quasistatic (Johnson, 2016). As a consequence, fluid particles which move nearly static will disappear in isolated pores because they do not change their velocity vectors and therefore show zero vorticity (indicated by blue color). Instead, simulation results will only indicate establishing of fluid flow in pores which are interconnected and where fluid particles can move and interact. Thus, they change their velocity vectors to variable degrees which results in intermediate to high vorticity (indicated by green and red color, respectively). Therefore, by using a Reynolds number of 1, pores where no fluid flow is established can be clearly separated from pores where fluids are able to flow, which consequently represents effective porosity. Additionally, since the applied numerical algorithm is very robust but less accurate with increasing Reynolds number, a Re = 1 maintains accuracy of the simulation results (Chernyshenko, 2018).

Finally, since only the effectiveness of pores is modelled which is determined by their size, shape, arrangement and interconnection, the Reynolds number of the fluid itself must not be considered. Instead, in this fluid flow simulation, it is analyzed whether a pore allows for fluids to migrate easily in an open and effective pore network via pore throats causing high fluid flow, or to remain in isolated pores or “dead ends” of pore throats of an ineffective pore network, resulting in low to no flow. Hence, this approach will provide data about the effectiveness of each individual pore which can be directly compared with the results of quantifying the effectiveness of pores with pore shape factor γ. Consequently, although both methods do not predict absolute permeability, they both deliver a tool to analyze pore type effectiveness on a thin section image.

In order to perform fluid flow simulation and to quantify its results, each original pore system image (Figure 6.2a) has been transformed into a binary image (Figure 6.2b). In a next step, snapshots of each simulation videos at the final stage of the simulation have been acquired, as seen in Figure 6.2c. These images have then been graphically overlaid by the corresponding image of pore type classification (Figure 6.2d) used for the DIA method of quantifying pore geometry in the previous chapters. This

results in information about the establishment of fluid flow within each individual pore and therefore within each pore type.

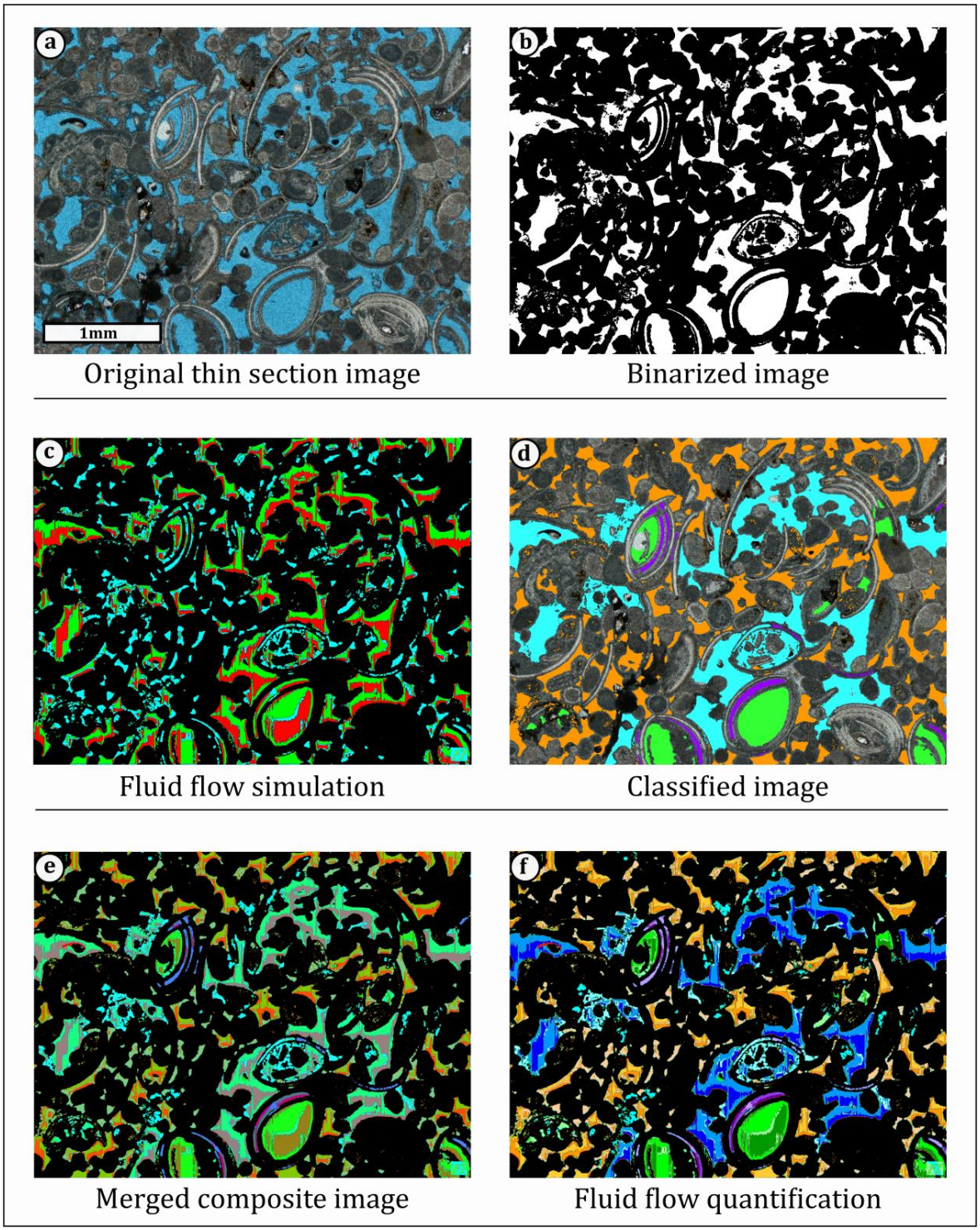

Figure 6.2. Digital image analysis (DIA) method to evaluate fluid flow simulation results. a. Original thin section image. **b.** Binarized thin section image with pore space (white) and sedimentary fabric (black) as simulation constraints. **c.** Screenshot of fluid flow simulation video. **d.** Classified DIA-derived image used in previous chapters to evaluate pore type effectiveness. **e.** Composite image with classified image overlaid onto image of fluid flow simulation results and then merged together. **f.** Result of quantification of fluid flow simulation for each pore type with DIA. The darker the color of each pore type class, the higher fluid flow.

By reducing the opacity of the classified image, each pore type obtains a distinct hue of color caused by mixing of colors of both images (Figure 6.2e). These colors represent the pore-type-specific low, intermediate and high potential fluid flow and therefore effectiveness. Finally, by analyzing these new compound images with the DIA software, the specific colors can be precisely selected with the method described in Chapter Three, and the amount of low, intermediate and high effectiveness for each pore type as derived from fluid flow simulation of each sample is quantified (Figure 6.2f).

6.3 Results

As a result, intermediate and high flow regimes in the simulation usually occur together in interconnected pores. Intermediate flow occurs at the boundary between pores and the sedimentary fabric, and high flow in the central parts of the pores, both resembling the flow behavior of a river stream (see Figure 6.1). This is caused by the fact that in the central part of interconnected pores, the interaction between fluid particles is highest and thus their velocity vector changes more frequently, resulting in higher vorticity values. Additionally, both intermediate and high flows are mostly absent in isolated pores. Therefore, since both flow regimes indicate the establishment of a certain flow, they are grouped together to represent areas of the pore network which are effective. On the contrary, the low flow regime in the pore network represents areas where no flow occurs; therefore these areas of the pore system represent ineffective porosity. In order to compare the fluid flow simulation results with the results of pore geometry quantification with DIA, the percentage of area of each pore type covered by intermediate plus high flow (or effective porosity) has been used. These percentage values of effective porosity are then compared with the corresponding γ values of each pore type. Since both presented methods of quantifying pore type effectiveness are independent but have been applied on the same dataset, results are ideal for comparison.

Figure 6.3 shows a cross-plot of average γ values for each pore type derived from the previously presented DIA method of all individual pores in Chapter Four versus the percentage of average pore area covered by effective porosity in respect to total porosity for each pore type resulting from fluid flow simulation. Apart from one single outlier (i.e., skeletal moldic pore type), the plot shows a distinct upper threshold in the high pore shape complexity regime of the dataset (Figure 6.4). Since both results are mathematically not related, yet derived from two independent methods which yield comparable results, this upper methodological threshold indicates a strong relationship between pore geometry and effective porosity. No unusually low or high effective porosity values derived from fluid flow simulation for given γ are present, and vice versa. This threshold also demonstrates that both methods of pore system analysis work best on pore systems which show an open, well-interconnected and highly porous pore space.

The linear correlation between γ and effective porosity values yields a correlation coefficient $R^2 = 0.35$. However, by calculating the mean values of γ and effective porosity for each pore type, a linear correlation between both parameters is apparent with a correlation coefficient $R^2 = 0.81$. Additionally,

an exponential regression yields a correlation coefficient of R^2 = 0.83, indicating a slight exponential trend in the dataset. The difference in correlation coefficient between each individual pore type and the mean values indicates that some data points deviate from the trend. These deviations are examined in the discussion of this chapter.

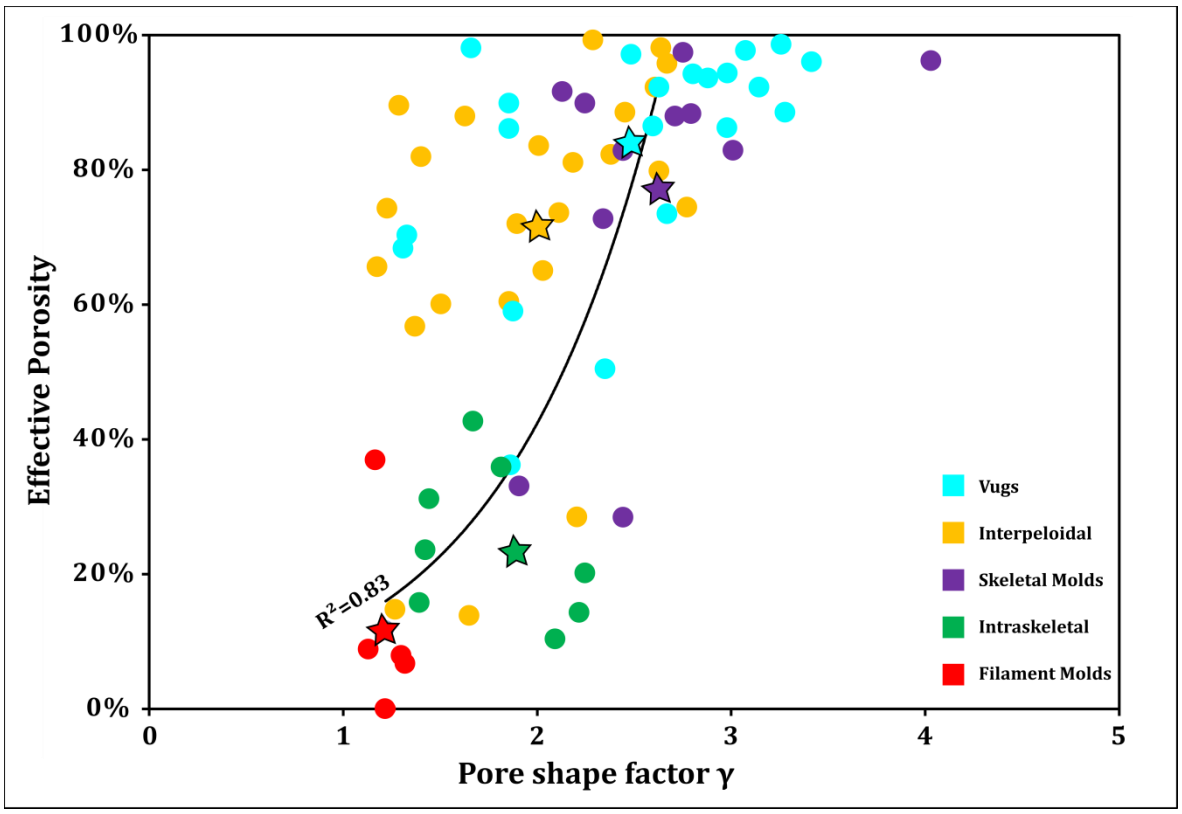

Figure 6.3. Effective porosity versus pore shape complexity I. Pore shape factor γ calculated with the DIA workflow presented in previous chapters versus effective porosity (i.e., percentage of intermediate and high flow) obtained from fluid flow simulation. Stars indicate mean values of each pore type. R^2 represents the correlation coefficient of mean values of each pore type.

Furthermore, it can be observed that all pore types group into two different fields in the plot: The upper field contains mainly vuggy pores, interpeloidal pores and skeletal moldic pores, whereas the lower field is mainly composed of intraparticle pores and *Cladophorites* filament molds (Figure 6.5). Since both fields are clearly separated from each other, they can be regarded as two different classes of pore type effectiveness. The upper field or class has a lower threshold value of 60 % of effective porosity in respect to total porosity of each sample analyzed, representing pores which predominantly produce effective porosity. Consequently, this class can be considered as the effective pore type class, since more than half of the porosity produced by these pore types is effective.

This upper class is separated from the lower class by an area between 40 % and 60 % of effective porosity where only one data point plots in the center (i.e., vuggy pore type). Below 40 %, mainly intraskeletal pores and filament molds group together and form the lower class. Its upper threshold

value of 40 % of effective porosity indicates that only a maximum of 40 % of effective porosity is generated by these pore types in respect to total porosity and therefore more than half of the porosity produced is ineffective. Hence, they generate predominantly ineffective porosity and are consequently considered as the ineffective pore type class.

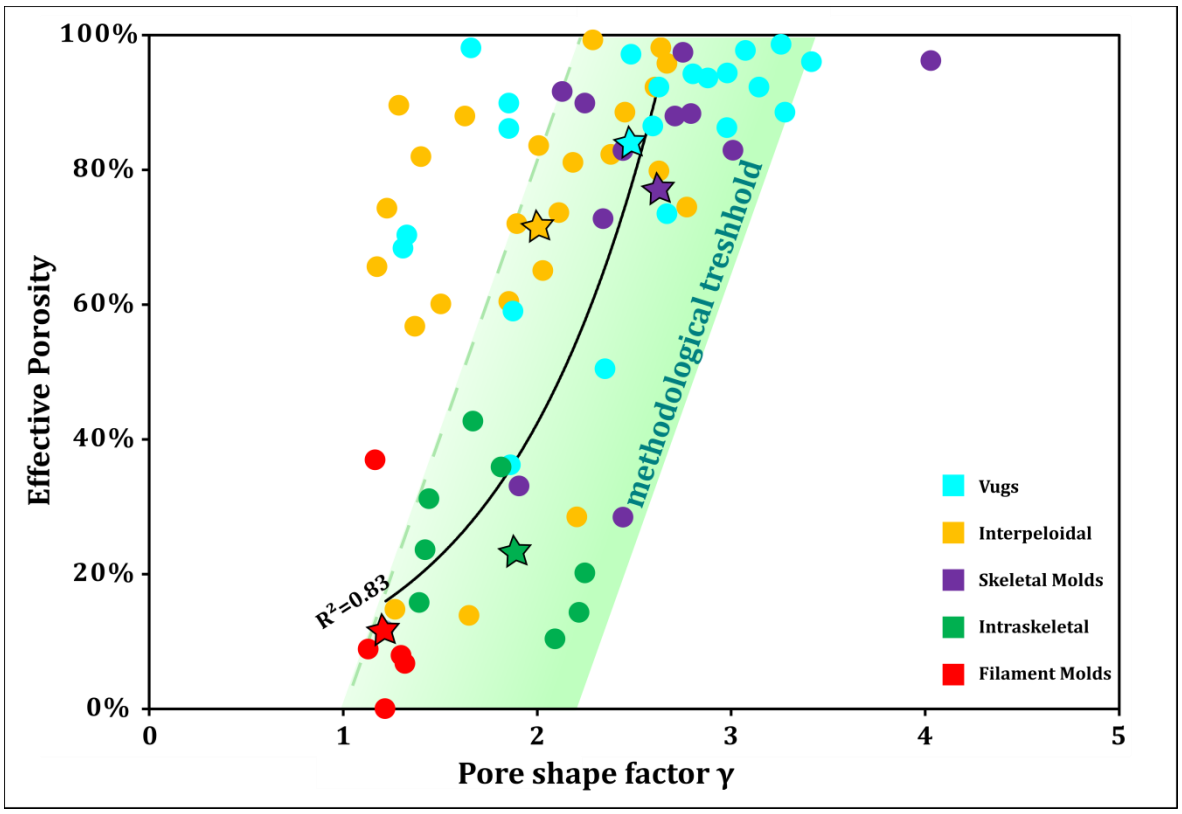

Figure 6.4. Effective porosity versus pore shape complexity II. Comparison between the results of both independent methods shows an upper methodological threshold in the dataset.

As a result, vugs are identified as the most effective pore type followed by skeletal moldic pores and then interpeloidal pores in the upper (i.e., effective) pore type class. The mean values of intraskeletal pores and filament molds plot in the lower (i.e., ineffective) pore type class, with filament molds showing the lowest percentage of effective porosity. Although interpeloidal pores have been previously identified as the second most effective pore type based on the petrophysical facies established in Chapter Four, the classification of all evaluated pore types into effective and ineffective types are in accordance with the outcome of fluid flow simulation performed in this chapter. It confirms the previous predictions that vugs, interpeloidal pores and skeletal molds mostly generate effective porosity and are therefore effective pore types, whereas intraskeletal pores and filament molds represent pore types which generate predominantly ineffective porosity. Consequently, PTA 1 of the non-skeletal grainstone facies which includes primary interpeloidal pores and secondary vugs is also identified as most effective by fluid flow simulation.

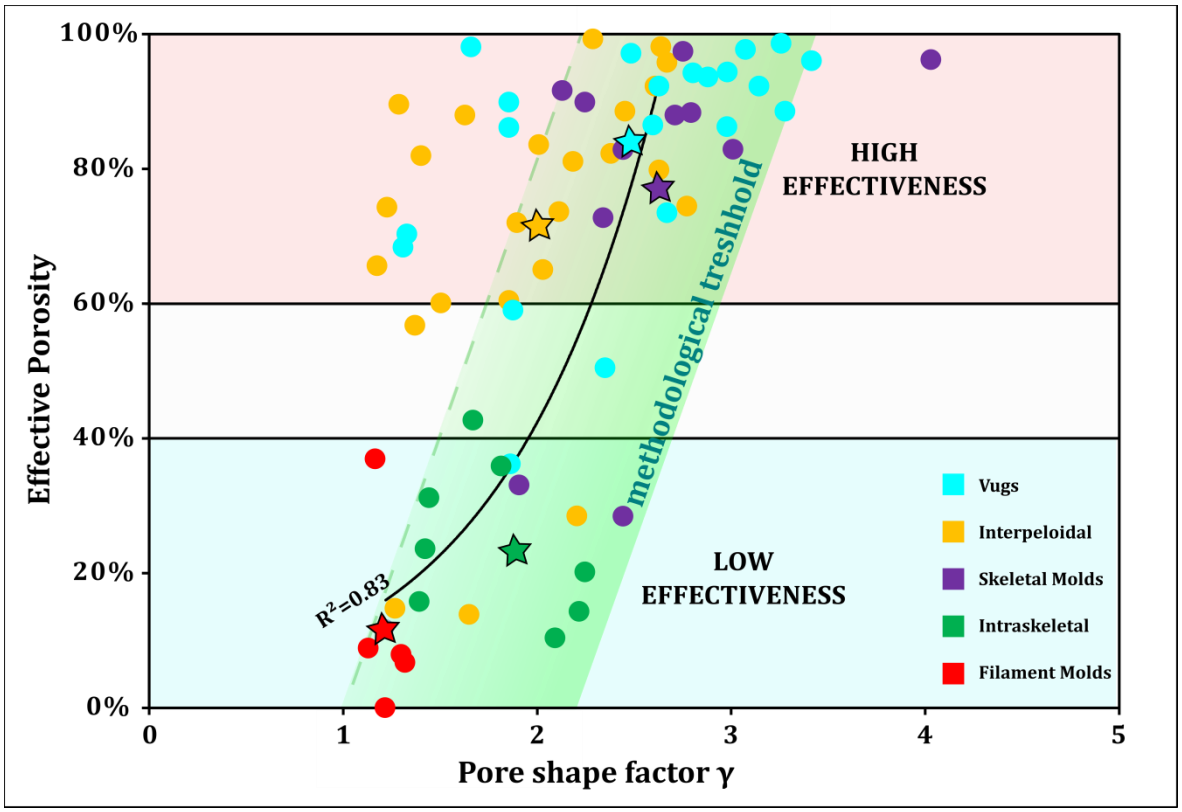

Figure 6.5. Effective porosity versus pore shape complexity III. The dataset plots in two separated fields: An upper field of high (> 60 %) and a lower field of low (< 40 %) effective porosity. The mean values (indicated by stars) which show an exponential correlation of R^2 = 0.83 confirm the previous findings that vugs, skeletal molds and interpeloidal pores are the most effective pore types. Filament molds and intraskeletal pores instead are ineffective pore types.

6.4 Discussion of Chapter

Considering the upper methodological threshold in the high pore shape complexity regime (see Figure 6.5), which is dominated by highly porous and permeable pore systems, and the exponential correlation between the mean values of all pore types, deviations from this trend can be observed in the lower pore shape complexity regime and in both effective porosity classes. In the high effective porosity class, some data points of vuggy and interpeloidal pore type tend towards lower γ values in respect to their effective porosity and relative to the upper threshold and their mean values. In the lower ineffective class, few intraparticle pores show higher percentage values of effective porosity as derived from fluid flow simulation in respect to the mean value for this pore type (see Figure 6.5). Since the DIA based method has the advantage to directly cross-check all obtained data with the thin section image they derive from, the cause for such deviations can be directly detected in the corresponding image: At first, six samples (i.e., two vuggy and four interpeloidal pore types) which have the lowest γ value for their given percentage of effective porosity show all partial cementation with calcite cement along the rims of their pores (Figure 6.6).

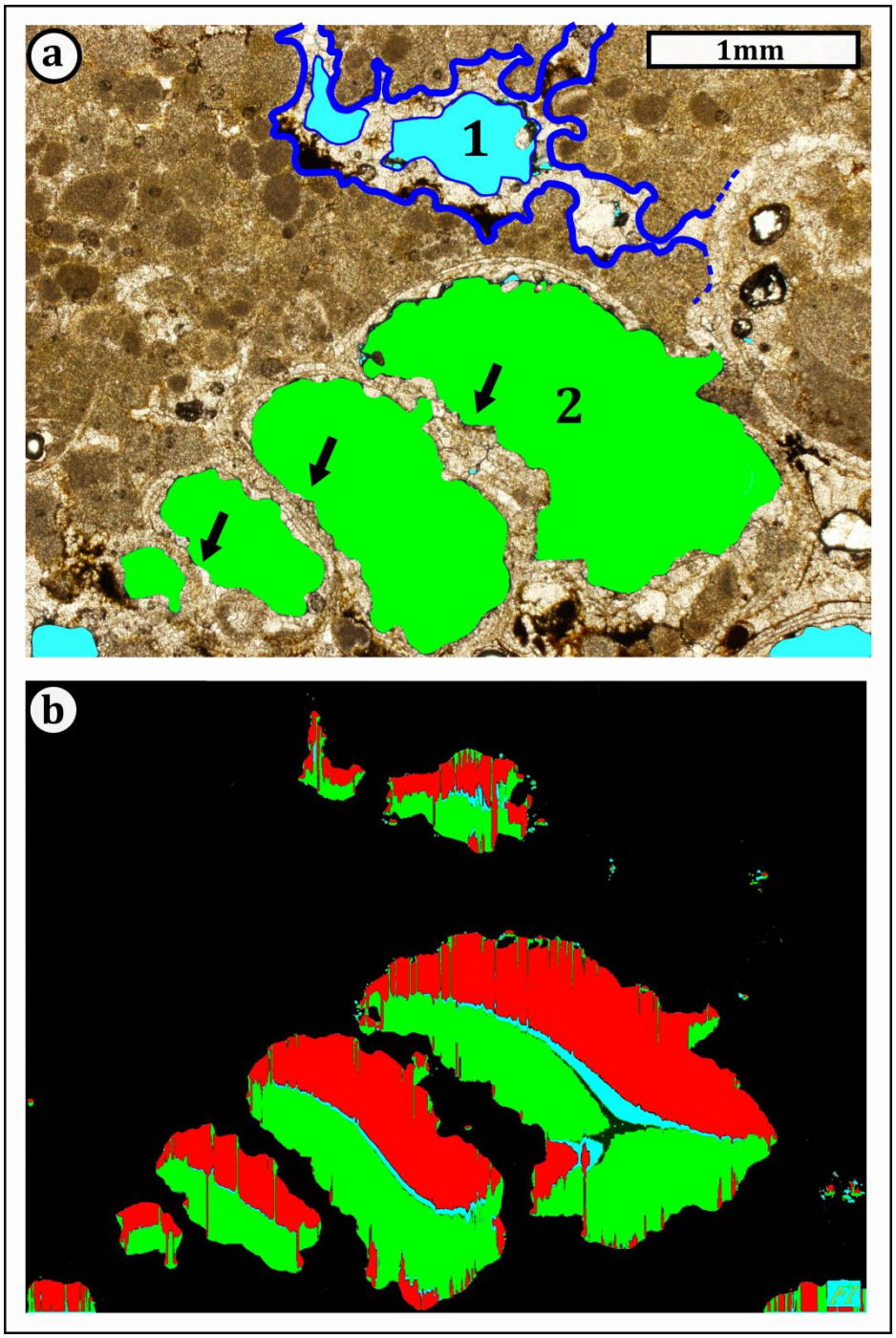

Figure 6.6. Impact of cementation on pore geometry and fluid flow simulation. a. Both the size and shape complexity of the partially cemented vug (1) and intraskeletal pore (2) are decreased by cementation. Note the previously complex contour of the vuggy pore wall prior to partial cementation (top, bold blue contour line) and its actual less complex shape. This is reflected in a decrease in pore shape factor γ values. **b.** However, fluid flow simulation yields high effective porosity values of both pores due to their big size.

Due to the edgy nature of the blocky cement crystals, the original smooth and tortuous contour of the pore will highly decrease in complexity, represented by a profound decrease in its γ value. In Figure 6.6, both vuggy pore types present in the previously uncemented single vug produce γ values of 1.39 and

1.54, respectively. By using the method presented in Chapter Five, the shape complexity of the uncemented single vug can be reconstructed by removing the cement, resulting in a γ value of 2.51 which indicates a much higher effectiveness of this previously uncemented vug. Moreover, it can be observed that this vug had more complex pore throats prior to cementation and was even interconnected with an adjacent skeletal moldic pore which is now also cemented (see Figure 6.6a). However, since both the vuggy and intraskeletal pore type are usually relatively big and very well interconnected, this rim of cement does not affect the potential of establishing a flow in the simulation to the same extent (see Figure 6.6b). Therefore, fluid flow simulation performed on this thin section image results in higher values in respect to the lower γ values caused by the simpler-contoured pore walls.

By applying the cementation reduction value of 31.79 % of decrease for pore shape factor γ previously calculated in Chapter Five on all deviated samples which show minor cementation, new γ values are obtained which represent an uncemented pore system for each of these deviated samples (Figure 6.7). As a result, all partially cemented pore type values are located closer to the trend of mean values in the dataset, which also causes an increased correlation coefficient of mean values towards R^2 = 0.85. However, it must be emphasized that this first deviation points to a major limitation of fluid flow simulation and also helps to explain the second deviation in the lower ineffective porosity class.

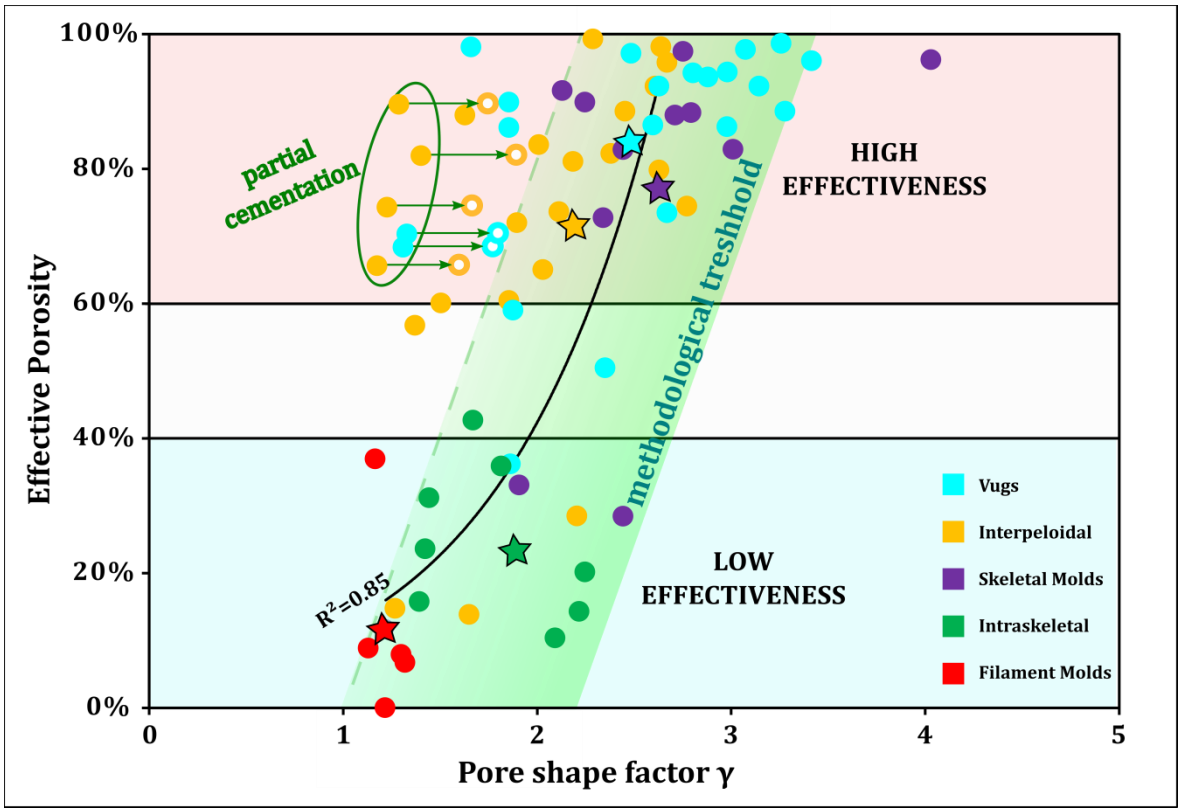

Figure 6.7. Effective porosity versus pore shape complexity IV. Few interpeloidal pores and vugs show partial cementation which leads to decreased pore geometry values. This can be corrected by applying the previously calculated cementation reduction value for γ of 31.79 % (green arrows).

This second deviation from the trend of mean values is tied to the intraskeletal pore type. As noted above, intraskeletal pores are primary fabric-selective pores which are confined by the shell and skeletal chambers of gastropods and ostracods. Although they are generally big pores, they have low γ values due to their simple contour. Considering intraskeletal pores in 3D, it is inferred that their simple contour is nearly identical in all space directions due to the confinement of these pores by the shell, and only their size slightly changes. Moreover, these pores are usually isolated from other pores and do not interconnect, although they might occur very abundant in proximity to each other and therefore producing high porosity values. Hence, they have been previously classified as ineffective pores with the DIA method as presented in Chapter Four. However, results of fluid flow simulation performed in this chapter show increased effective porosity values in three thin section images dominated by big intragastropodal pores (Figure 6.8a). In these samples, the pore space is represented by one or only few big intraskeletal pores within a gastropod which cover a large area of the thin section image. As a consequence, by performing fluid flow simulation on the corresponding 2D image, the software models the establishment of a certain fluid flow in these big pores only due to the fact that they span over a large distance on the thin section image (Figure 6.8b). This leads to unrealistic results because as stated above, the shape complexity and consequently the effectiveness of an intraskeletal pore is generally identically low in all space directions, and pores are usually simple-contoured and isolated from each other. Moreover, although a certain internal flow can be established within big gastropod shells at a thin section scale, they do not interconnect and therefore no flow will realistically be governed by these isolated pores at a larger scale (i.e., chip, plug or core scale). In Figure 6.8b for instance, both intraskeletal pores are partly effective at a thin section scale due to their big size and a flow is established during simulation. However, both pores will not contribute to permeability when analyzed at a larger scale due to their isolation. Thus, pore systems containing similar big pores should be analyzed with fluid flow simulation either with a lower magnification of the thin section image or at a different scale, for example derived from 2D scans of rock chips, plugs or slabs.

Furthermore, it can be observed that the relatively high fluid flow in some intragastropodal pores shows extreme turbulent behavior as compared to the more stream-like flow behavior of interconnected vugs and interpeloidal pores (see Figure 6.8b), which have highest flow in the central part and intermediate flow at the boundaries between pore system and sedimentary fabric. This latter flow behavior is considered to represent the most effective pore network since a steady flow is established. In contrast, the high flow with a very turbulent behavior in some big intragastropodal pores can be attributed to their big size in relation to the thin section image, because no steady flow throughout the entire pore system will be realistically governed by this pore type. Additionally, since a low Reynolds number of 1 has been used for the simulation, the visualized flow should be laminar (Chernyshenko, 2018), and the establishment of a turbulent flow behavior is not realistic. Therefore, these pore systems dominated by intragastropodal pores are clearly less effective in nature as indicated by fluid flow simulation. Pore shape factor γ (sensu Anselmetti et al., 1998) instead is a scale-independent parameter, and its pore-type-specific values are identical at every scale.

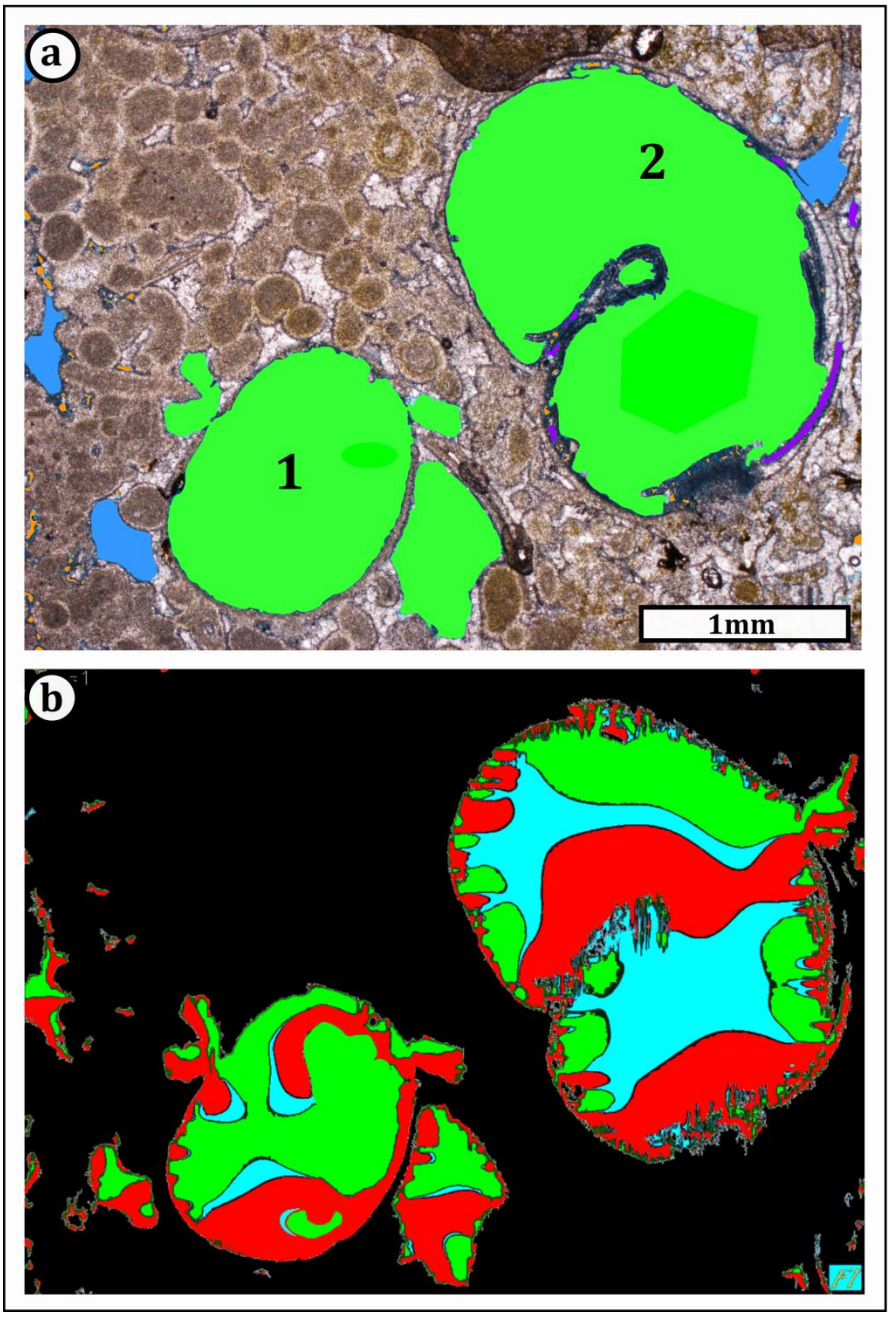

Figure 6.8. Problem of scale in intraskeletal pores of the skeletal grainstone facies. a. Two (1, 2) relatively big but simple contoured intragastropodal pores are confined by their own shell and a fully cemented peloidal grainstone fabric. Therefore, these pores are isolated and do not interconnect with adjacent pores. **b.** Fluid flow simulation results in unrealistically high and turbulent fluid flow within these intragastropodal pores.

As a result, the deviation towards higher effective porosity values as derived from fluid flow simulation in few big but isolated and simple-contoured intraskeletal pores can be assigned to the limitation of the dataset scale (i.e., thin section scale), and the general problem of (up-) scaling. Additionally, as previously observed (see Figure 6.6), isolation of pores can also occur due to partial cementation of previously well-interconnected and complex pores such as vugs, and is therefore not only tied to intraskeletal pores.

Consequently, partial cementation also leads to an overestimated fluid flow simulation result, and both observed deviations can be assigned to the problem of (up-) scaling.

Although applying the cementation reduction value to all cemented samples which hypothetically decreases the first deviation in the dataset, it can be observed that still some vuggy and interpeloidal pore type data points cluster in a more narrow field which deviates from the exponential trend with lower γ values as compared to their high effective porosity (Figure 6.9). This third deviation in the upper effective porosity class can be assigned to the general problem of analyzing a three-dimensional object (i.e., the pore system of each sample) with a two-dimensional method. Although the 2D information of pore shape complexity delivers a very good approximation for describing pore type interconnectivity, the 3D nature of each pore type must always be considered.

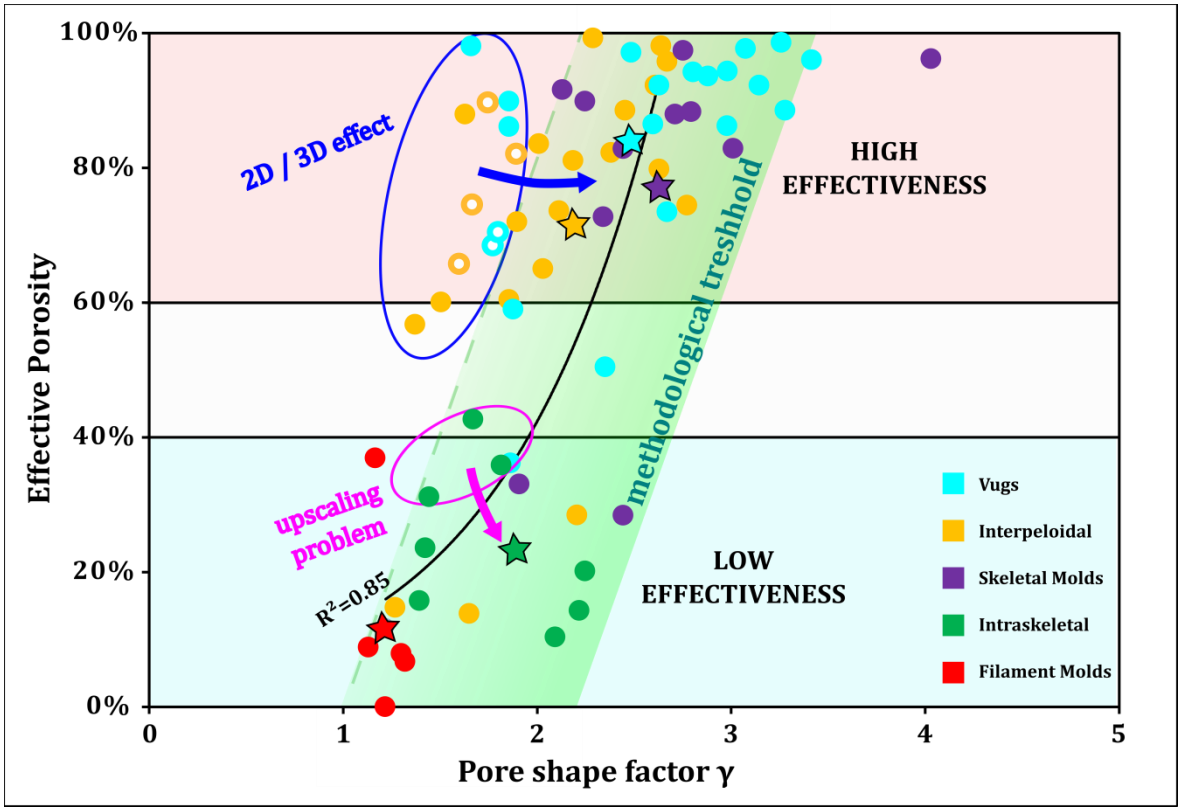

Figure 6.9. Effective porosity versus pore shape complexity V. Finally, further deviation from the correlation occurs in the upper field due to the 2D/3D effect of the DIA method, and in the lower field due to the general problem of (up-) scaling pore system information.

In intraskeletal pores for instance, which are confined by simple contoured ostracod and gastropod shells, it is obvious that their low γ values calculated on a 2D thin section image will show identical values as if measured in three dimensions. Independent from the orientation of the thin section image in respect to the gastropod or ostracod shell, its associated intraskeletal pores will show simple shape contours in all space directions, and only the size of the pore can slightly vary. Consequently, γ is independent from the orientation of the section represented in the thin section image and an

identical γ value can be assumed for these intraskeletal pore types in all directions if measured fully in 3D. Vugs and interpeloidal pores instead show the highest γ values of all pore types, since they have very complex contours and form pore throats which interconnect with adjacent pores. Interpeloidal pores are confined by the original arrangement, the size and the shape of peloids. Thus, if the peloidal grainstone facies show distinct depositional patterns such as grading, differential sorting or preferential orientation of peloids, the complexity and tortuosity of the interpeloidal pore space can vary at a sub-centimeter scale if viewed and analyzed in 3D.

In Figure 6.10a, areas of the thin section image (see area 1 and 3 in Figure 6.10a) show peloids which are mostly elongated and therefore have been cut in parallel to their long axis which obviously leads to a more open pore system due to the bigger size of the grains and to a more open packing of peloidal grains. In contrast, peloids which have been cut perpendicular to their long axis appear to have a more densely packed and therefore less open pore system (see area 2 in Figure 6.10a). This consequently leads to variations in γ values when measured in 2D, depending on the orientation of the thin section in respect to the pore system analyzed. Fluid flow simulation instead yield identical results regardless of these variations within one thin section image, because interpeloidal pores are generally very well-interconnected with numerous pore throats and usually allow for establishing a flow throughout the image in the simulation (Figure 6.10b). Therefore, interpeloidal pores obtain much lower values of γ when analyzed in 2D as compared to their realistic γ values when analyzed in 3D and in respect to their fluid flow generation.

Vugs instead show highest γ values of all pore types. This can be explained by the fact that a vug is a secondary non-fabric-selective pore type and therefore is not or only to a very low degree confined by the sedimentary fabric as compared to interpeloidal pores. Thus, vugs usually cross-cut the solid sedimentary fabric and form very complex pores with high effectiveness. Although it is not possible to predict their three-dimensional extent, size and geometry from 2D thin section image, it can be assumed that analyzing the complexity of a vug in 3D would yield much higher γ values as measured in 2D, only because of the non-fabric-selective and high-tortuosity nature of vuggy pores with numerous pore throats which could then be detected and analyzed in each (pore) space direction. This is also true for interpeloidal pores, because even if they have different pore sizes in 2D depending on the packing, sorting and size of peloids, they have amplified γ values due to an increased abundance of pore throats of this usually complex and tortuous pore type when analyzed in 3D. However, it would affect interpeloidal pores not to the same extent as vugs due to the fabric-selective nature of interpeloidal pores which confines their shape.

As previously stated, the γ value of simple contoured pores such as intraskeletal pores or filament molds show only minor differences between 2D and 3D analysis of pore shape complexity, since both pore types are highly confined by the sedimentary fabric (i.e., by shells and filaments traces), which results in identical pore shape complexity properties in every space direction.

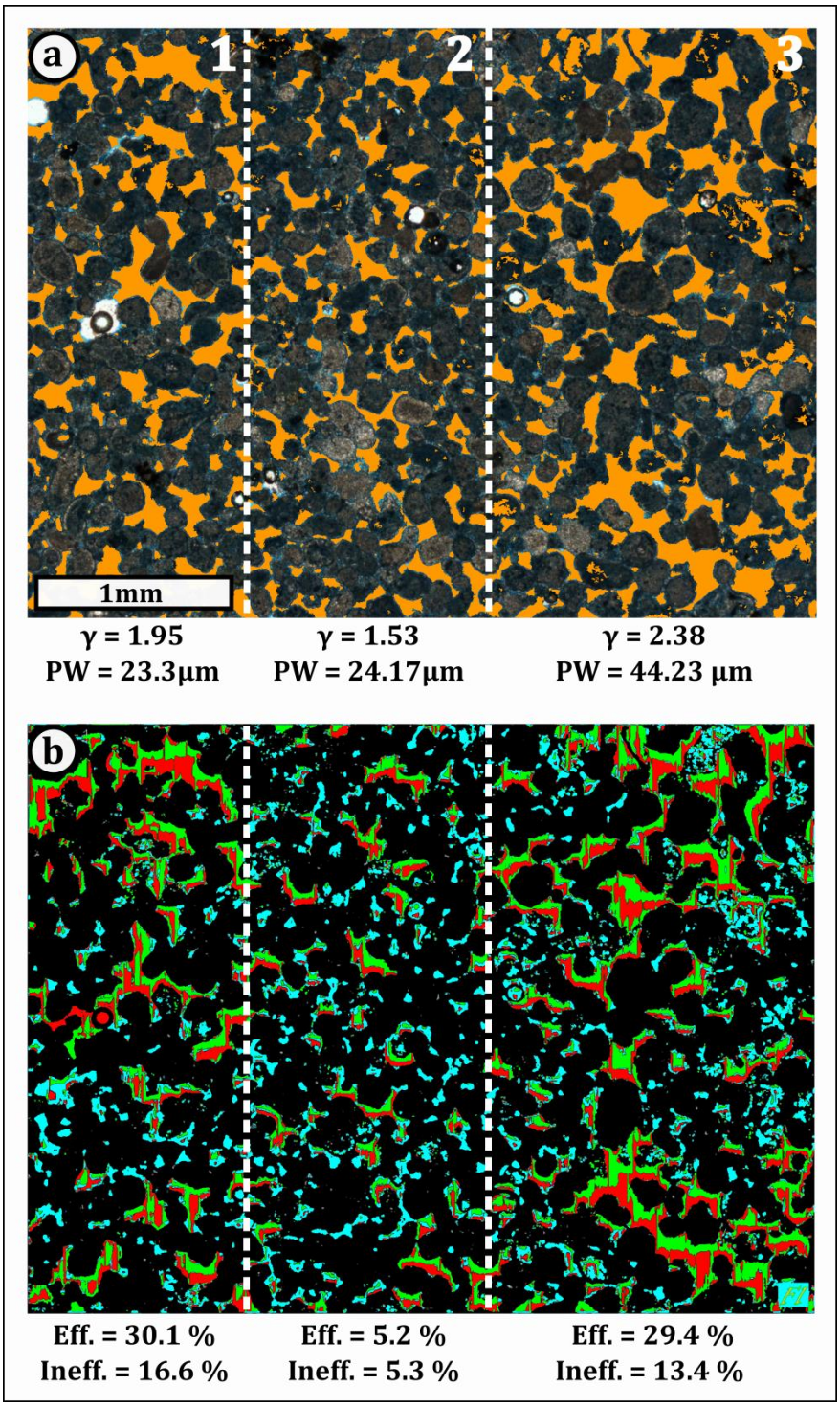

Figure 6.10. 2D/3D effect in interpeloidal grainstone facies. a. Variations in pore type geometry, here represented as pore shape factor γ and pore width (PW), occur at a millimeter scale, depending on the size, sorting, texture and arrangement of peloids and on the relative orientation of the thin section. Sample 2A3_7 shows an area (1) with intermediate pore system properties (i.e., γ and pore width). The central part (2) is dominated by smaller peloids with poorer sorting and lowest pore system properties. In the third area (3), peloids are biggest and thus show a more openly packed arrangement. Therefore, γ and pore width show highest values. **b.** Fluid flow simulation results confirm pore geometry quantification results. Effective porosity (Eff.) is lowest in the central part whereas it reaches highest values in area 1 and 3, with lowest amount of ineffective porosity (Ineff.) in area 3.

Therefore, if all pores are analyzed in 3D, the differences in γ values between simple-contoured and complex pore types would be amplified, with simple pores showing similar values as derived from 2D measurements, whereas the γ value of complex pore types would highly increase depending on their complexity in three dimensions. Hence, this deviation of some data points in the effective porosity class towards lower γ values can be clearly assigned to the 2D/3D effect, as discussed above. Consequently, all three deviations from the upper methodological threshold in the high pore shape complexity regime and the exponential trend of mean values of the dataset represent the two major limitations not only of the method presented in this thesis, but in pore system analysis in general: (i); the problem of (up-) scaling, and (ii) the problem of analyzing a 3D object in 2D (i.e., 2D/3D effect). How can these limitations be improved?

The problem of (up-) scaling pore system information to larger scales is one of the biggest challenges in reservoir characterization (e.g., Qi et al., 2001; Farmer, 2002; Durlofsky, 2003; Qi & Hesketh, 2005; Qi & Zhang, 2009; Vahrencamp & Creusen, 2010; Hollis et al., 2010; Li & Durlofsky, 2015; Peng et al., 2015). As seen in intraskeletal pores, fluid flow simulation performed on thin section images can yield results which are unrealistically high as compared to different scales, which is mainly caused by limitations of the dataset scale of the method applied. However, if γ is used as a proxy parameter for pore type effectiveness, results can be transferred to larger scales, because in contrast to scale-dependent fluid flow simulation, γ is scale-independent (Figure 6.11). In Figure 6.11 for instance, three images of the same gastropod including intraskeletal and skeletal moldic pores captured with three successively higher magnifications (i.e., 1x, 2.5x, and 4x) yield identical γ values, but increasing effective porosity values as derived from fluid flow simulation. Consequently, the γ value of a pore type measured on rock chip scale is identical to the γ value measured for the same pore type at a plug or core scale. If the abundance and distribution of pores are known, information derived from a rock chip can be successively upscaled to larger scales, for example to plug and core scale. By using 2D computer scans of plugs, slabs or cores, or even 3D CT and µCT scan images, models of pore system for each scale can be generated (e.g., Knackstedt et al., 2009; Iassonov et al., 2009; Matrecano, 2011, and references therein; Wildenschild & Sheppard, 2013; Buckman et al., 2018). Once a core scale has been reached, this information can then be transferred to outcrop scale. The studied outcrop in Hainsfarth for instance has a width of approximately 250 m in length and a height of 5 m. There, core scale pore system information could be integrated into each measured section and the pore system properties between all sections can be simulated in order to obtain a pore system properties model for the entire outcrop. At this outcrop scale, precision and accuracy of the model which is based on previously integrated pore system information can be tested by recovering random "checkpoint" samples in between each section and compare their realistic pore system properties with the corresponding values obtained from the model. From this sub-reservoir scale, results can further be upscaled to reservoir scale. Therefore, by using the scale-independent pore shape factor γ and by successively upscaling the obtained pore system information to larger scales, the problem of (up-) scaling and the limitations caused by the dataset scale can be overcome.

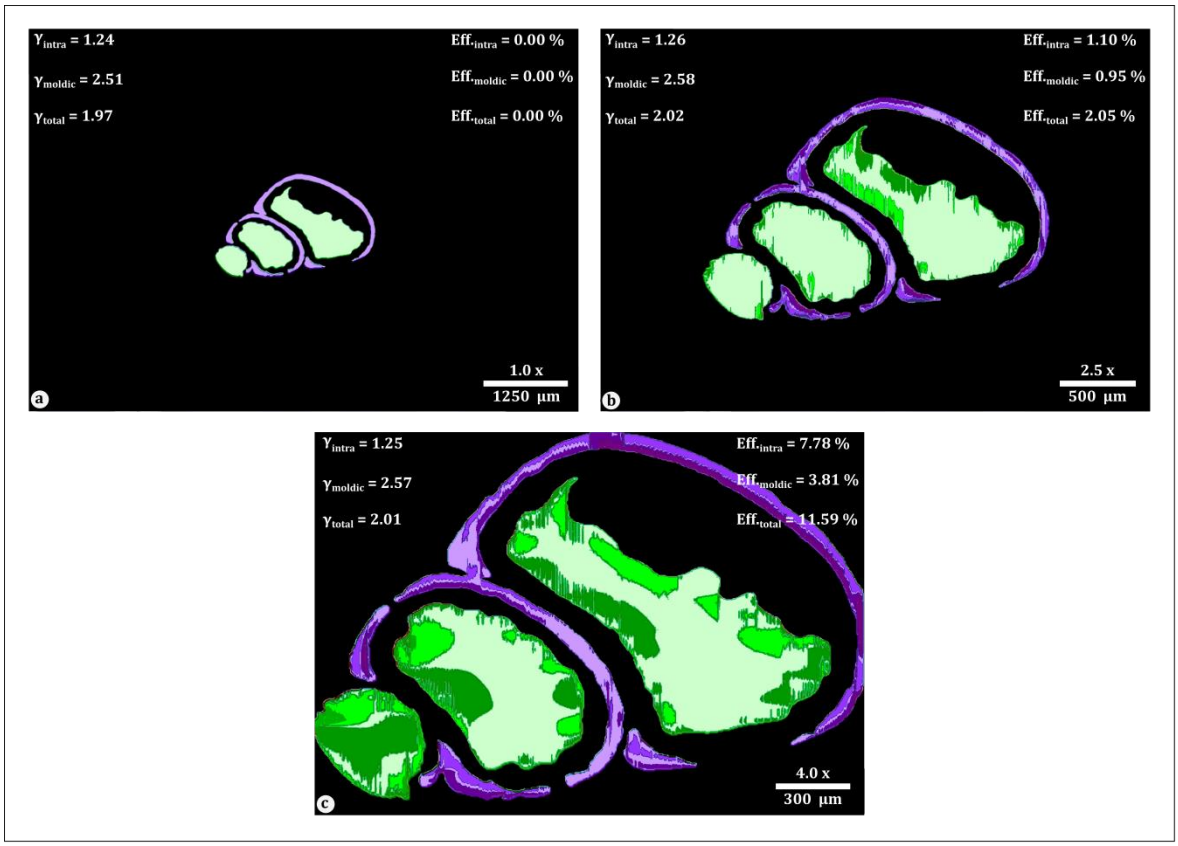

Figure 6.11. Influence of scale on fluid flow simulation and pore shape complexity. a. Gastropod with intraparticle pores (green) and skeletal molds (purple) captured with a magnification of 1x. Fluid flow simulation yield no effective pore areas **b.** Fluid flow simulation of the same gastropod captured with a magnification of 2.5x results in increased effective porosity values (darker colors), but identical γ values. **c.** By using a magnification of 4x, fluid flow simulation yield even higher effective porosity values. However, pore shape factor γ is identical to both lower magnified images.

In order to solve the second problem of the 2D/3D effect, the method presented in this thesis must be transferred into 3D. This can be also realized by using CT scan images of a rock sample to create a three-dimensional model, a widely used method which gained increasing popularity throughout the last decade (e.g., Anovitz & Cole, 2015; Hemes et al., 2015; Ranachowski et al., 2015; Archilha et al., 2016; Kaufhold et al., 2016; Mukunoki et al., 2016; Andriamihaja et al., 2016; Xiong et al., 2016; Kang et al., 2017; Sun et al., 2017; Ma et al., 2017; Buckmann et al., 2018). The implementation of the presented method into 3D analysis will highly improve existing methods of analyzing CT-derived 3D models. Pore type classification, quantification of pore geometry and detection of effective pore type(s) can potentially be performed identically as with the 2D software used in this thesis, and the workflow presented can therefore be translated into three dimensions by using CT models and appropriate image analysis software. This would result in even more precise and realistic pore geometry data as previously discussed on the example of interpeloidal pores and vugs in the effective pore type class and intraskeletal pores in the ineffective class. Moreover, since each 3D computer model consists of several thousands of 2D images, these individual images can be preprocessed with a 2D image analysis software. This allows for creating already classified images which can then be stacked to create a more detailed

3D model. However, this approach would require an automatized 2D analysis with an image analysis software due to the large amount of images needed to build the 3D model.

6.5 Conclusions

The comparison between the results of fluid flow simulation performed in this chapter and the pore geometry data as derived from the method presented in the previous chapters yields identical results of pore type effectiveness. Apart from an upper methodological threshold in the dataset, the different pore types are also grouped into two classes: an upper effective class encompassing the effective pore types vugs, skeletal molds and interpeloidal pores, whereas a lower ineffective class contains intraskeletal pores and filament molds. The mean values for each pore type also confirm the previous findings that vugs are the most effective pore type in the studied carbonates. Hence, it can be stated that pore shape factor γ (sensu Anselmetti et al., 1998) can be utilized as a proxy parameter to quantify pore (type) effectiveness. Since γ describes the complexity and therefore the possibility of interconnection between pores and the resulting formation of a pore network, high γ values indicate effectiveness and the potential establishment of a flow. In contrast, low γ values indicate simple-contoured pores with a lower potential to interconnect with adjacent pores. Thus, they are ineffective and no flow can be established. It has been observed that few vugs and interpeloidal pores show a deviation towards lower γ values in respect to the exponential trend. This can be assigned to the effect of partial cementation on pore geometry which has been improved by using the cementation reduction value as calculated with the method presented in Chapter Five.

A further deviation in the dataset of few intraskeletal pores towards higher percentage values of effective porosity in respect to their γ values can be explained by the limitation of the scale used for analysis. Additionally, the third deviation of few effective pore types can be explained by a limitation which originates from the 2D nature of the presented methods used to analyze a three-dimensional object (i.e., 2D/3D effect). In order to improve both latter limitations, the method must be implemented into analysis of three-dimensional pore system models which will further enhance the precision and accuracy of pore geometry quantification and generally improve 3D pore system analysis. Furthermore, by using the scale-independent pore shape factor γ and transferring the method presented in this thesis into 3D, not only the problem of the 2D/3D effect can be solved, but additionally a tool to successively transfer and upscale pore system information to larger scales is provided. In summary, not only the main results of quantifying pore type effectiveness over pore shape complexity as previously analyzed with DIA in Chapter Three and Four have been verified by fluid flow simulation, but additionally the observed deviations clearly point at the limitations of the methods presented. This offers the chance to implement improvements into the approach in order to overcome the fundamental problems in pore system analysis of the 2D/3D effect and of (up-) scaling pore system information to different scales.

CHAPTER SEVEN

IMPLICATION: POROSITY-PERMEABILITY RELATIONSHIP IN CARBONATES

7.1 Introduction

What can be implied from the previously gained results of each chapter in respect to the complex relationship between porosity and permeability in carbonates? The often low correlation of both parameters can be assigned to (i) the facies-dependent texture and composition of the sedimentary fabric, to (ii) the initial primary porosity and permeability, and to (iii) early to late stages of diagenetic modifications of both the sedimentary fabric and the pore system (Mazzullo 2004; Ehrenberg & Nadeau, 2005; He et al., 2014; Rashid et al., 2015; Dernaika & Sinclair, 2017). This leads to a heterogeneous distribution of pore system properties, even at sub-centimeter scale. The main reasons for these small-scale heterogeneities in carbonate pore systems can be assigned to (i) the high chemical reactivity of carbonates (Mazzullo 2004; Ehrenberg & Nadeau, 2005; Hollis et al., 2010; He et al., 2014; Rashid et al., 2015; Dernaika & Sinclair, 2017), and to (ii) the mostly autochthonous and biogenic character of carbonate deposition (Ehrenberg & Nadeau, 2005, and references therein). Both reasons strongly contrast with siliciclastic rocks and their often homogeneous pore systems (e.g., Ehrenberg & Nadeau, 2005). The high reactivity of carbonates can lead to early lithification by (chemical) compaction and cementation, and to diagenetic modifications of pore system throughout the entire postdepositional history. These modifications encompass the partial or complete occlusion of pores by cement, transformation of calcite into dolomite and dissolution of the sedimentary fabric up to a complete inversion of texture. One of the main controls on pore system modification (with increasing burial and thermal exposure) is its primary porosity since it provides pathways for diagenetic fluids to flow, and initial pores can be either enhanced by dissolution or closed by cement precipitation (e.g., Purser, 1978).

7.2 Porosity-Permeability Relationship

In the case of the lacustrine marginal carbonates of the Nördlinger Ries crater lake, the correlation between total porosity and total permeability is very low (R^2 = 0.09; see Chapter Two), whereas the correlation between DIA-derived total porosity and permeability measured with routine methods of each sample used for DIA analysis in Chapter Four is only slightly higher, with a correlation coefficient R^2 = 0.17 (Figure 7.1). This indicates a non-relationship between both fundamental petrophysical parameters. Each facies type in the studied marginal lacustrine succession contains a facies-specific pore system, formed by an association of different primary and/or secondary pore types (i.e., pore type assemblages (PTA), see Chapter Four). As presented in Chapter Five of this thesis, the evolution of each PTA is marked by one stage of dissolution resulting in the formation of vugs and at least one stage of extensive partial or complete cementation of preexisting pores. Depending on the initial primary pore

types and the surrounding sedimentary fabric, which is either grain- or mud-supported, vug-forming dissolution has acted differentially and is variably pronounced, with facies types dominated by micrite being more prone to become modified by the formation of vugs. The cementation of preexisting pores also has a differential effect on each pore type present: Small and spherical late primary to early secondary filament molds are often completely close by cement, whereas late secondary vugs mostly show partial cementation and their interconnectivity with other pores is often maintained if the pore throats are not completely cemented. The effect of cementation on primary interpeloidal pores instead is twofold: if the initial interpeloidal pore space is relatively open due to a general big size and resulting arrangement of the peloidal grains, then cementation must not necessarily close all interpeloidal pores. In contrast, pore systems of peloidal grainstones with smaller peloids tend to have a less opened initial pore system, and pores and their throats are occluded more easily by cementation.

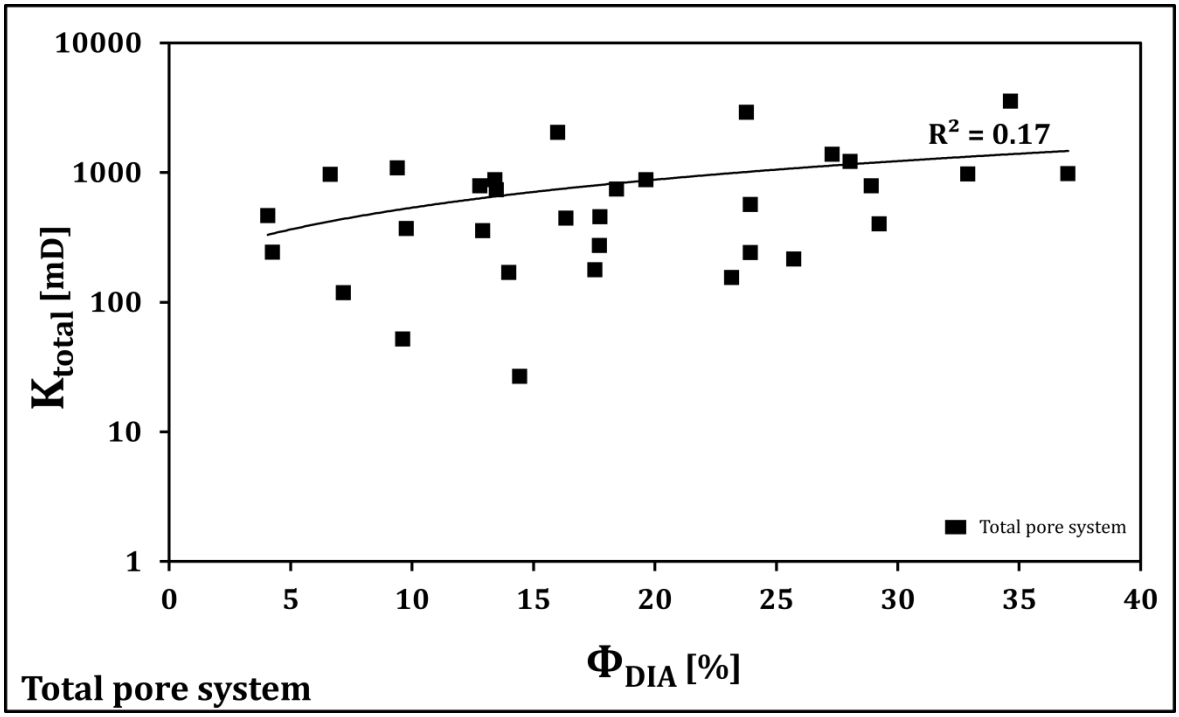

Figure 7.1. Porosity-permeability relationship in the Nördlinger Ries marginal lacustrine carbonates I. DIA-derived porosity (Φ_{DIA}) versus total permeability (K_{total}) of all 32 samples analyzed in Chapter Four.

Therefore, the weak correlation in the studied lacustrine carbonates is mainly caused by three factors: (i) the sedimentary facies-dependent differences in texture, primary pore types and chemical composition; (ii) the individual evolution and modification of each facies-specific pore type assemblage throughout its postdepositional history; and (iii) the general inhomogeneity of pore system caused by differential diagenetic modifications acting at sub-centimeter scale.

The influence of differential modification of pore types on the porosity-permeability relationship can be demonstrated on the example of the usually effective vuggy pore type in this marginal lacustrine

succession. A vug can experience three different possible scenarios throughout its evolution: (i) if a vug, which usually has large sizes and high shape complexity, is not affected by cementation, it maintains its high porosity and interconnectivity and therefore remains a highly effective pore; (ii) if cementation partially closes the vug, its pore space and therefore porosity decreases simultaneously by the same volume as newly precipitated cement (see Chapter Five). Additionally, partial cementation at the rim of this vug decreases its pore shape complexity and resulting interconnectivity. However, if pore throats are not fully occluded, vugs can still maintain interconnection and generate permeability. If pore throats are completely closed by cement, interconnection is blocked and no permeability is produced, although the vug itself can still generate a certain amount of porosity due to its big size and only partial closure by cement; (iii) if cementation fully occludes the entire vuggy pore, all pore space and pore throats are destroyed. Therefore, since this pore is now closed, it does not generate any porosity and permeability at all. In strong contrast to these three destructive scenarios, size and shape complexity of a vug can be highly enhanced by further dissolution. Hence, its contribution to porosity and permeability also increases. Therefore, in the case of an initial effective vuggy pore, it can be demonstrated that differential modification of this pore by cementation or dissolution has a major effect on both pore size and shape complexity, and therefore on porosity and permeability produced by this vug. However, the change of porosity and permeability of such effective pore types is generally correlative throughout pore system evolution.

In contrast, it has been observed that the change in porosity and permeability of initially isolated and ineffective pores such as filament molds and intraskeletal pores is more asynchronous as compared to effective pore types. Since filament molds have a simple shape complexity and hence does not interconnect with adjacent pores over pore throats, porosity and permeability produced by this pore does not change simultaneously to the same extent throughout pore system modification. Considering the aforementioned three possible scenarios, an ineffective but open and uncemented filament mold usually generates a certain amount of porosity, but produces a low permeability due to its shape simplicity and resulting low interconnection. If this isolated pore is partly filled by cement, porosity also changes by the same volume as newly precipitated cement. Permeability instead is still as low as prior to cementation due to the lack of pore throats. Finally, if this pore is closed entirely by cement, it stops contributing to both porosity and permeability. In contrast, if the pore-filling cement is partially or fully dissolved during a later stage, porosity would increase. However, due to lack of pore throats, the increase in permeability is not correlative with the porosity increase. As a result, porosity and permeability evolution of this pore during its evolution is not consistent. Considering that each pore in a pore system experiences its intrinsic postdepositional evolution and is modified to a variable extent, it can be stated that this differential and asynchronous change of porosity and permeability by diagenetic modification of initially ineffective pores is the main factor causing a reduced porosity-permeability correlation in carbonates. Therefore, in order to better understand their porosity-permeability relationship, it is crucial to extract all interconnected pores and effective pore types from the entire pore system, and simultaneously exclude isolated and ineffective pores. This enhanced correlation between porosity and permeability by extracting effective pore types is demonstrated in Figure 7.2. There, the correlation

coefficient between porosity measured with DIA (Φ_{DIA}) and the permeability contribution ($K_{contr.}$) of the two most effective pore types (i.e., vugs and interpeloidal pores), extracted from the total pore system of all samples used for Figure 7.1, is improved to $R^2 = 0.45$. Since both pore types build up the PTA 1 pore system which is found exclusively in the peloidal grainstone facies and which has been previously identified as the most effective pore type assemblage (see Chapter Four), the prediction of total permeability for given porosity for this effective sedimentary facies type is improved by using the method presented.

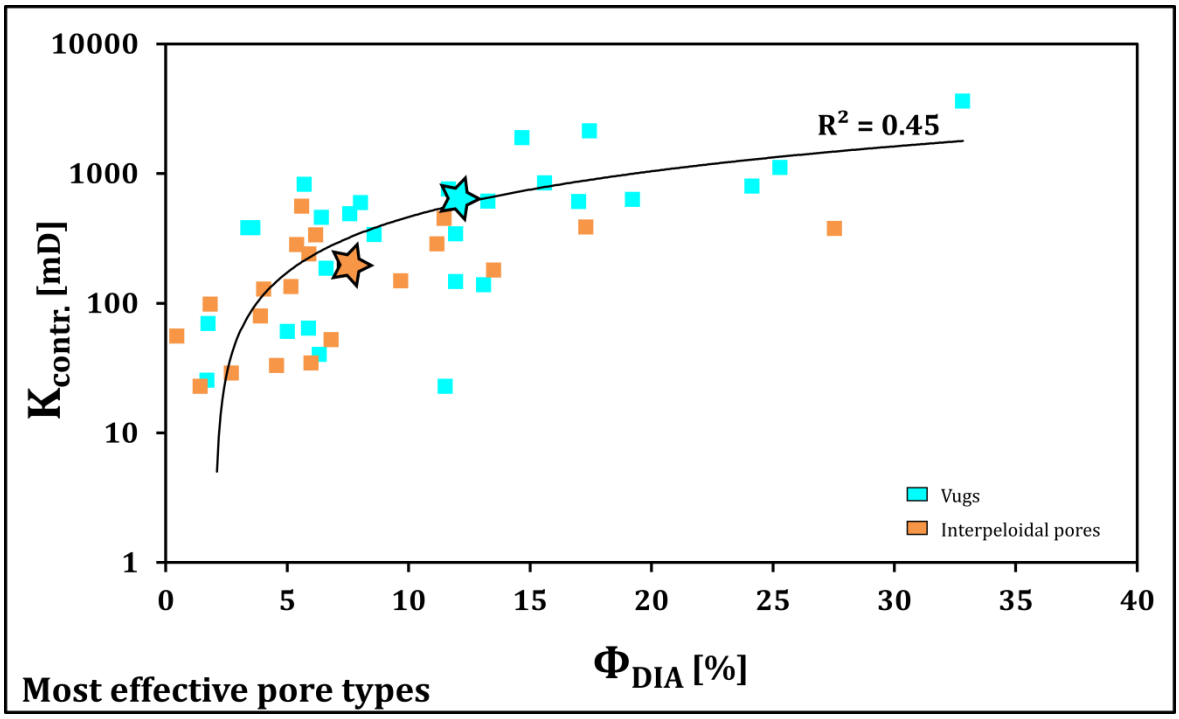

Figure 7.2. Porosity-permeability relationship in the Nördlinger Ries marginal lacustrine carbonates II. Porosity produced by each pore type (Φ_{DIA}) versus pore-type-specific permeability contribution ($K_{contr.}$) of the two most effective pore types identified (i.e.., vugs and interpeloidal pores).

By integrating the third most effective pore type (i.e., skeletal molds) into the plot, the correlation coefficient slightly increases to $R^2 = 0.46$ (Figure 7.3). This improved correlation coefficients in respect to correlation of porosity and total permeability (see Figure 7.1) is relatively high when compared to the usually "data-cloud"-like distributions (sensu Dernaika & Sinclair, 2017) in other carbonate reservoirs. This is also in agreement with the studies of Melim et al. (2001) and Zhang et al. (2017) who demonstrated that the high variation in permeability for given porosity in carbonates are reduced and correlation between both parameters increases if only "connected" (sensu Melim et al., 2001; Zhang et al., 2017) pore types are used for porosity quantification. The increase in correlation is also in accordance with the results of previous studies which also use pore geometry parameters for an improved prediction of permeability (Weger, 2006; Weger et al., 2008). The addition of the remaining ineffective pore types (i.e., intraskeletal pores and filament molds) into the plot of Figure 7.3, both individually and combined, results in a decrease of correlation to $R^2 = 0.44$.

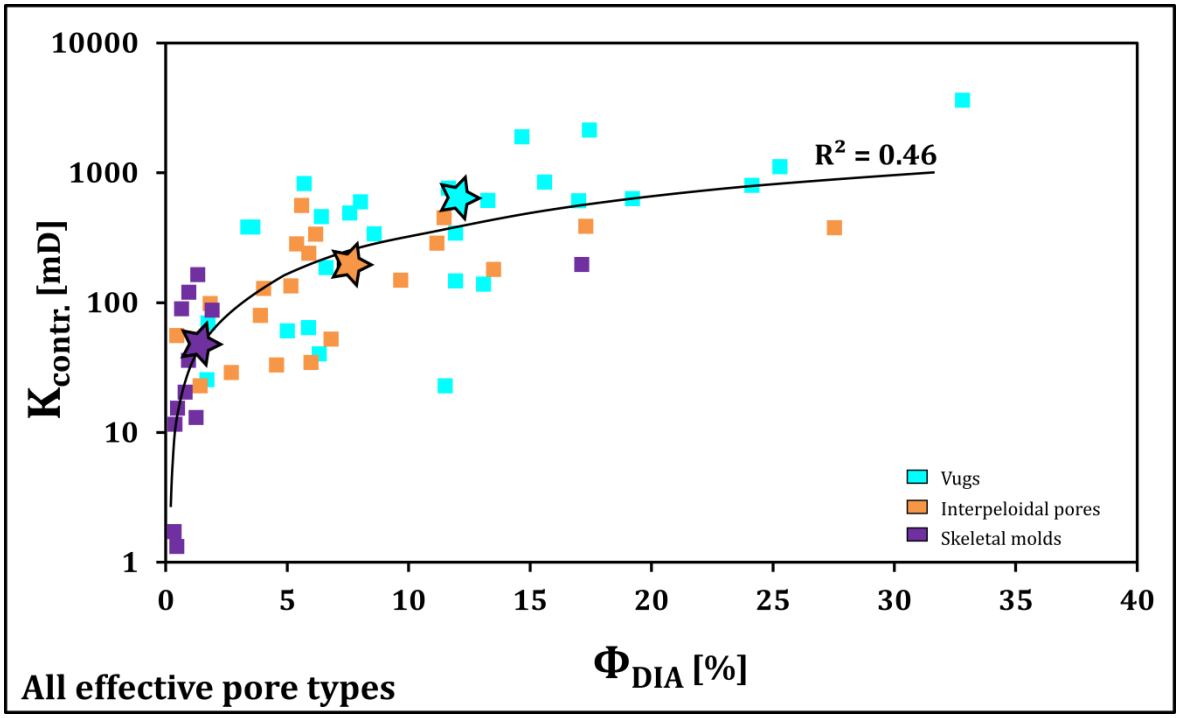

Figure 7.3. Porosity-permeability relationship in the Nördlinger Ries marginal lacustrine carbonates III. Φ_{DIA} versus $K_{contr.}$ for each effective pore type identified (i.e., vugs, interpeloidal pores and skeletal molds). Note the increased correlation between porosity and permeability. Average values for all effective pore types are indicated by stars.

7.3 Discussion of Chapter

Similar increased correlation coefficients for porosity and permeability in carbonate rocks have been achieved by relating porosity and permeability values to the rock fabric, where similar fabrics from different locations yield identical permeability trends (Dernaika & Sinclair, 2017; Zhang et al., 2017). This is mainly due to the fact that fabric-selective pore types (sensu Choquette & Pray, 1970) in carbonate pore systems are confined by the rock fabric type which also encompass its composition, sedimentary structures and textural parameters (Rezaee et al., 2006, and references therein; Dernaika & Sinclair, 2017; Zhang et al., 2017), and individual pore types and their assemblages are distinct for a specific sedimentary facies (Mazzullo, 2004). Therefore, differential postdepositional modification of these facies-dependent pore types and pore type assemblages are the main factor causing the variable and inhomogeneous porosity-permeability relationship in carbonates (Mazzullo, 2004; Zhang et al., 2017). Consequently, as implied from the method presented in this thesis, the individual analysis of each pore type contributing to effective porosity and therefore permeability is key to understand how the examined facies-dependent pore system generates porosity and permeability (Zhang et al., 2017). Consequently, the correlation between both petrophysical parameters is enhanced by using effective porosity, as demonstrated in this chapter (see Figure 7.3). The high effectiveness of specific pore types is also the cause of an increased permeability in some rather low porosity carbonate reservoirs

worldwide (Ehrenberg & Nadeau, 2005), where for instance highly effective fractures provide the most effective pore network. The extraction of the effective pore network is also applied in fluid flow simulations and permeability modelling, for example on 3D models based on two-dimensional CT images (e.g., Knackstedt et al., 2004; Arns et al., 2005; Kayser et al., 2006; Youssef et al., 2007; Iassonov et al., 2009; Knackstedt et al. 2009; Matrecano, 2011; Wildenschild & Sheppard, 2013; Anovitz & Cole, 2015; Hemes et al., 2015; Ranachowski et al., 2015; Kaufhold et al., 2016; Mukunoki et al., 2016; Andriamihaja et al., 2016; Xiong et al., 2016; Kang et al., 2017; Sun et al., 2017).

One further important aspect in understanding porosity and permeability generation is the analysis of pore throats, especially their size and shape. Mazzullo (2004) emphasized that pore throats, which are the most important factor governing pore interconnectivity and thus permeability, are determined by the particle size of the sedimentary fabric and the distribution of pore-filling cement. Since the size, shape and arrangement of pores and their throats are the main factor controlling fluid flow properties (McCreesh et al., 1991), mercury injection has classically been used to determine pore size distributions and pore-type-controlled generation of permeability in pore systems (Pittman, 1992; Rezaee et al., 2006, and references therein). As demonstrated in this thesis, digital images analysis (DIA) offers an alternative petrographic tool to characterize the geometry of pores and consequently to quantitatively describe the size and shape of pore throats. This is crucial since under given porosity, permeability can vary depending on variable pore throat sizes and variations in the number of interconnected pores via throats (He et al., 2014; Zhang et al., 2017). He et al. (2014) further noted, that the complex relationship between porosity and permeability in carbonates is mainly caused by the co-occurrence of ineffective (or isolated) and effective (or interconnected) pores, which in turn results in differential pore system textures with variable interconnections of pores via throats within one facies type. This is in full agreement with the implications of this thesis.

7.4 Conclusions

In numerous studies (e.g., Melim et al., 2001; Mazzullo 2004; Ehrenberg & Nadeau, 2005; Hollis et al., 2010; He et al., 2014; Rashid et al., 2015; Dernaika & Sinclair, 2017; Zhang et al., 2017), it has been shown that the dominant factors controlling the porosity-permeability distribution in carbonates are the rock fabric and its specific pore types as well as pore throat sizes and shapes which determines interconnection of pores, and therefore generating either ineffective or effective porosity. Additionally, carbonate-typical multimodal pore systems can be highly influenced by postdepositional modifications acting at various scales, which are the main processes causing the inhomogeneity of pore system and leading to the often complex and variable porosity-permeability relationship in carbonates. Deviations from a high correlation between porosity and permeability within one rock fabric can be assigned to either varying pore-type-specific geometries, such as touching vugs versus separate vugs (sensu Lucia, 1983), or by differential postdepositional modification through compaction, cementation and dissolution (Mazzullo, 2004; Ehrenberg & Nadeau, 2005; Dernaika & Sinclair, 2017).

All these aspects which potentially lead to a weak porosity-permeability relationship in carbonates are taken into account by using the DIA-based methodology of pore system analysis presented in this thesis: both the rock fabric and the effectiveness of each pore type in generating porosity and permeability over pore throats have been considered when analyzing the geometry of facies-dependent pore type assemblages. In order to evaluate pore type effectiveness, pore shape complexity has been used as a proxy parameter for analyzing the interconnectivity of pores (see Chapter Three and Four). Additionally, the effect of cementation on pore system properties has been quantified which further refines the prediction of porosity and permeability (see Chapter Five). Finally, by extracting effective pore types and associated pore network, isolated ineffective pores are excluded and permeability shows an enhanced correlation of R^2 = 0.46 towards porosity in the analyzed pore systems. This leads to an improved understanding of how porosity and permeability is generated and distributed throughout the marginal lacustrine succession of the Nördlinger Ries.

CHAPTER EIGHT

SYNTHESIS

8.1 Pore Shape Complexity and Effective Porosity

The main concept of this thesis was to utilize pore shape complexity as a proxy parameter for pore (type) effectiveness, since complex-contoured, tortuous and branching pores with high shape complexity values tend to interconnect with adjacent pores more easily as compared to isolated pores with a simple pore contour (Anselmetti et al., 1998; Weger, 2006; Weger et al., 2009). The method presented in Chapter Three and applied in Chapter Four of this thesis builds on the previous work of Anselmetti et al. (1998), Weger (2006) and Weger et al. (2009) which utilize pore shape complexity as a parameter to predict permeability. The strong relationship between both parameters has been also validated with artificial neural networks (ANN) in Chapter Three. With the hereby presented workflow, a quantitative petrographic method is provided which helps to detect one of the most important parameter in pore system analysis: effective porosity. Although carbonate pore systems are often composed of complex assemblages of genetically different primary and secondary pore types which can experience several stages of diagenetic modifications after their formation (e.g., Mazzullo, 2004; Dernaika & Sinclair, 2017), they can be clearly differentiated by their pore-type-specific geometry. This specific geometry determines whether a pore type is effective due to its high shape complexity and resulting high interconnectivity with adjacent pores to form an open pore network, or it is ineffective due to its simple shape which prevents pores to interconnect with other pores. Consequently, they remain as isolated pores in the pore system with little contribution to total permeability.

Since effective porosity is the main factor generating permeability in sedimentary rocks (Koponen et al., 1997, and references therein; Melim et al., 2001; Zhang et al., 2017), it is essential to understand the occurrence, abundance and distribution of effective pore types in the pore systems analyzed. Since the size of pores and - most important - the tortuosity of pore throats are fundamental factors for governing pore interconnectivity and creating effective porosity (McCreesh et al., 1991; Mowers & Budd, 1996; Mazzullo, 2004; Rezaee et al., 2006; He et al., 2014), a combination of both geometrical parameters pore width and pore shape factor γ (sensu Anselmetti et al., 1998) proves to be ideal for precisely evaluating pore (type) effectiveness. Zhang et al. (2017) noted that “pore geometry confines the space that is available for fluid flow” (cited from Melim et al., 2001). Consequently, permeability in carbonates is mainly a function of the type of pore, the pore size and the degree of pore interconnection (Melim et al., 2001; Zhang et al., 2017). Although textural parameters such as mud content can play an important role in producing variable permeability for identical porosity values (Zhang et al., 2017), the type, abundance and distribution of effective pores are the main factors controlling their contribution to permeability (e.g., Lucia, 1983; 1995; Melim et al., 2001; Loucks et al., 2002). Zhang et al. (2017) further pointed out that although information about “connected” porosity is important to improve porosity-permeability

correlations and predictions, such data are usually rare and only total porosity values, which also encompass ineffective porosity, are provided. With the method presented, effective porosity values for each pore type and the entire pore system can be directly calculated from thin section images by quantifying pore shape factor γ (sensu Anselmetti et al., 1998). As a result, ineffective pores can be separated from the effective pore network and obtained effectiveness data can be used to improve permeability predictions.

Additionally, the workflow provides a tool which allows for precisely categorizing different (carbonate) facies types based on their rock fabric and resulting pore structure within a sedimentary petrographic context. This highly complements rock-typing which is commonly used to predict petrophysical properties in a sedimentary succession by relating the rock fabric and its pore structure to the petrophysical response (Giot et al., 2000; Javaux et al., 2000; Porras & Campos, 2001; Granier, 2003; Rushing et al., 2008; Venkitadri et al., 2005; Hollis et al. 2010; Vahrenkamp & Creusen, 2010; Fournier et al., 2013; Rahimpour-Bonab & Aliakbardoust, 2014; Skalinski & Kenter, 2014). As a consequence, more detailed and quantitative rock-typing results in even more precise information about porosity and permeability distribution in a potential reservoir succession. By linking γ to total measured permeability which results in a permeability contribution value for each individual pore type, identical magnitudes of an improved porosity-permeability correlation have been achieved as compared to previous studies which have used different pore geometry parameters such as dominant pore size and perimeter over area (Weger, 2006; Weger et al. 2008). This consequently leads to an enhanced understanding of how carbonate pore systems work and is also of high importance for reservoir characterization studies, since pore systems of two different samples which produce identical permeabilites can have different recovery efficiencies depending on their pore geometry (Hollis et al., 2010). Finally, it has been confirmed that the scale-independent pore shape factor γ is an ideal proxy parameter to quantify the effectiveness of each individual pore type and to detect effective porosity within the pore system.

8.2. Comprehensive Pore System Analysis of the Ries Lake Carbonates

In this thesis, the pore systems of carbonates from the Middle Miocene Nördlinger Ries crater lake have been analyzed in order to understand the heterogeneous porosity and permeability distribution in this marginal lacustrine succession. Carbonates tend to have multimodal pore systems (e.g., Mazzullo, 2004; Hollis et al., 2010; Dernaika & Sinclair, 2017), usually composed of assemblages of primary and secondary pore types. This results in the co-occurrence of both isolated and thus ineffective pores as well as interconnected and thus effective pore types (Melim et al., 2001; Mazzullo, 2004; Ehrenberg & Nadeau, 2005; He et al., 2014; Rashid et al., 2015; Dernaika & Sinclair, 2017; Zhang et al., 2017), as it has been also observed in the studied lacustrine carbonates. The aim of this thesis was therefore to establish a method for identifying all occurring effective pore types and extract effective porosity. This has been realized by using digital image analysis (DIA) performed on 2D thin section images which allows for segmenting the pore system from the surrounding sedimentary fabric, classifying the detected pore system into individual pore types and finally quantifying pore type geometry (see Chapter Three and

Four). The visualization and quantification of pore system in a pore width versus γ plot deliver all information needed to comprehensively describe a pore system and to assign a petrophysical facies to each occurring pore type. As described in Chapter Three, pore width and γ are utilized to characterize the size and shape complexity of individual pores. The efficiency of one pore type (which is the ratio between numbers of pores and porosity produced by these pores) yields additional data about the relationship between size and abundance of pores, and the resulting porosity production. Moreover, the classification into pore types delivers information about the origin and evolution of each pore system analyzed. Pore width and pore shape factor γ were then used as proxy parameters to calculate porosity (Φ_{DIA}) and permeability contribution ($K_{contr.}$). By calibrating γ with the pore-type-specific proportion, the potential contribution of each pore type to total permeability measured with routine injection methods has been quantified and the most effective pore types have been detected. As seen in Table 3 (see Chapter Four), each of the final seven key parameters show distinct mean values and value ranges for each pore type. As presented in Chapter Four, the effectiveness of each pore type assemblage can then be evaluated by establishing the petrophysical facies for each individual type of pore.

On the base of this petrophysical facies, the most effective pore type(s) in the studied marginal lacustrine carbonates could be identified: Secondary and non-fabric-selective vugs are most effective due to their generally big size and complex shape, leading to a high interconnectivity between vugs and adjacent pores. They occur together with the second most effective pore type (i.e., interpeloidal pores) as a distinct assemblage (i.e., PTA 1) in the peloidal grainstone facies. Therefore, this sedimentary facies type and its associated pore system generate highest effective porosity values and have therefore highest pore system properties in the Ries lake carbonates (see Chapter Four). This is also in accordance with previous studies (Lucia, 1983; 1995; Melim et al., 2001; Zhang et al., 2017) which generally consider pore systems dominated by touching vugs and intercrystalline or interparticle pores as the most effective pore systems in generating permeability, whereas moldic pores such as filament molds and isolated intraparticle pores are regarded as less effective even when they dominate the pore system. In Chapter Five, the method has been modified to quantify the impact of cementation on pore system properties, yielding values of decrease caused by cementation for pore width and γ as well as for porosity and permeability. These cementation reduction values can then be used to correct predictions of porosity and permeability, and assign certain threshold values of potential under- or overestimation caused by extensive local and patchy cementation for each relevant parameter. A first approach of quantifying the volume of cement and evaluating its effect on pore system properties with DIA has been presented by Mowers & Budd (1996). The authors calculated porosity and permeability reduction by cementation for the entire pore system. They further suggest integrating analysis of each individual pore type into their method, especially for complex multimodal pore systems in order to enhance precision of their approach, and emphasized the possibility to analyze different stages of postdepositional modification of pore system. By analyzing each different stage of pore system evolution and of each individual pore type with the method presented in Chapter Five, their study has been further improved.

8.3 Fluid Flow Simulation on 2D Thin Section Images

In order to evaluate the workflow presented and its concept of using pore shape factor γ as a proxy parameter for pore effectiveness, the results of Chapter Four have been tested by integrating the dataset into an independent method (i.e., fluid flow simulation). By using DIA, the amount of low, intermediate and high fluid flow has been quantified, representing effective porosity produced by each pore type as derived from fluid flow simulation (see Chapter Six). A comparison between the results of both methods shows an upper methodological threshold in the dataset which points to a relationship between both approaches and the resulting parameters (i.e., effective porosity and pore shape complexity). This threshold is present in the high pore shape complexity regime, indicating that both methods work best in pore systems which contain an open, well-interconnected and highly porous pore space, and deviations mainly originate from pore systems with rather low porosity-permeability properties. Moreover, it has been observed that all data plot in two distinct classes: an upper effective and a lower ineffective pore type class. Vugs, skeletal molds and interpeloidal pores plot in the effective class and thus are the most effective pore types. This has been previously also evaluated with the methodological workflow presented in Chapter Three and Four, and was then confirmed by fluid flow simulation. Accordingly, both methods also identify intraskeletal pores and filament molds as ineffective pore types.

In the lower pore shape complexity regime, the dataset shows an increased scatter of values. These deviations in the dataset towards lower γ in respect to the effective porosity values as derived from fluid flow simulation in the effective porosity field can first be attributed to partial cementation of some pores. By applying the cementation reduction value previously calculated in Chapter Five to the γ value of these partially cemented pore systems, the cause of this deviation has been detected: Although complex pores such as vugs have lost their interconnection with adjacent pores due to partial cementation and occlusion of throats by cement, which is also reflected in a drop in shape complexity values, their general big size still allows for generating unrealistically high fluid flow within these pores in the simulation. In the lower ineffective class, few intraskeletal pores also show deviations towards higher fluid flow values as compared to their pore shape complexity previously calculated. This is caused by the fact that the relatively big but simple-contoured intragastropodal pores also produce a high percentage of effective porosity when analyzed with fluid flow simulation at a thin section scale. However, due to their simple and isolated nature, which is also expressed in a low γ value, they do not interconnect with adjacent pores at larger scales. Thus, both aforementioned deviations clearly indicate the problem of (up-) scaling pore system information. If pore systems which are dominated by big but isolated intragastropodal pores or by partially cemented vugs are analyzed at a different scale (i.e., larger scale; e.g., core scale), fluid flow simulation would yield much lower and therefore realistic values as it is also indicated by their low γ value.

A third deviation in the upper effective porosity class can be assigned to the general problem of analyzing a three-dimensional object in 2D. Pores which are very complex in 3D can appear much simpler in shape in 2D depending on the orientation of the thin section. This 2D/3D effect affects mostly vugs and interpeloidal pores, since both pore types generally show amplified pore shape complexity values as

opposed to ineffective pores when analyzed in 3D. In order to overcome the limitations caused by the 2D/3D effect and the problem of (up-) scaling, the method presented in this thesis must be integrated into the analysis of three-dimensional models which reflect the pore system more realistically. This not only leads to a more precise quantification of pore type geometry by reducing the 2D/3D effect. Moreover, µCT and CT scan images can be acquired at different scales which allows for selecting a scale which is representative for all pore types analyzed. It must be highlighted that pore shape factor γ, which is used in this thesis as a proxy parameter for pore type effectiveness, is scale-independent and is therefore not affected by the problem of (up-) scaling. Therefore, integrating the workflow presented into 3D methods will complement existing methods of analyzing pore systems three-dimensionally.

This is in consensus with recent studies which use effective (or interconnected) porosity to obtain 3D fluid flow models based on CT scan images to better understand permeability generation (e.g., Knackstedt et al., 2009; Iassonov et al., 2009; Matrecano, 2011, and references therein; Wildenschild & Sheppard, 2013; Anovitz & Cole, 2015; Hemes et al., 2015; Ranachowski et al., 2015; Kaufhold et al., 2016; Mukunoki et al., 2016; Andriamihaja et al., 2016; Xiong et al., 2016; Kang et al., 2017; Sun et al., 2017; Buckman et al., 2018). However, these 3D models often lack detailed pore type classifications as well as realistic representation of the pore-hosting sedimentary fabric. Furthermore, the amount of analyzed samples for one study is usually very low due to the more expensive and time-consuming acquisition of the CT images needed to establish the model and associated processing with a 3D image analysis software (see number of samples examined in Knackstedt et al., 2009; Iassonov et al., 2009; Matrecano, 2011; Wildenschild & Sheppard, 2013; Anovitz & Cole, 2015; Hemes et al., 2015; Kaufhold et al., 2016; Mukunoki et al., 2016; Andriamihaja et al., 2016; Xiong et al., 2016; Kang et al., 2017; Sun et al., 2017; Buckman et al., 2018). This is problematic if a large number of samples derived from several outcrop sections or subsurface cores needs to be processed to comprehensively analyze the petrophysical properties of one entire succession and generate a detailed petrophysical model.

In contrast, the 2D method presented in this thesis allows not only for extracting effective porosity by using pore geometry (i.e., pore shape complexity) from each thin section analyzed, but provides a first approach of performing fluid flow simulation directly on thin section images. This extraction of effective porosity from a large number of images also leads to an increased understanding of how porosity and permeability are generated and distributed, and the quantitative results can be directly transferred to models at larger scales. Therefore, an integration of both two-dimensional DIA-based methods of analyzing effective porosity (i.e., pore shape complexity and fluid flow simulation) combined with few 3D models of pore system not only will help to improve potential methodological limitations, but will highly enhance the quality of pore system analysis throughout an entire succession in general. As previously discussed, the quantitative petrographic method presented in this thesis can be further used to improve precision of rock-typing techniques for petrophysical reservoir characterization. Interestingly, some studies even indicate that precise rock-typing is necessary for upscaling thin section information successively to larger scales (e.g., Chautru et al., 2005; Creusen et al., 2007; Gomes et al., 2008; Vahrenkamp & Creusen, 2010; Skalinski et al., 2012; Rebelle & Lalanne, 2014, Chandra et al., 2015;

Kadkhodaie & Kadkhodaie-Ilkhchi, 2018), for example by categorizing microscale rock types into rock type associations which are then transferred into mini-models of rock fabric scale until full (reservoir-) scale models are achieved (e.g., Creusen et al., 2007; Vahrenkamp & Creusen, 2010).

8.4 Porosity-Permeability Relationship

Melim et al. (2001) and Zhang et al. (2017) showed that the correlation between permeability and porosity can be further increased by using "connected" macroporosity. The authors point out that the generation of permeability by effective pore types highly depends on the different types of pores which interconnect (Melim et al., 2001). Therefore, a subdivision of effective porosity into different effective pore types is highly recommended. By extracting only effective pores from the pore system and excluding isolated pores which also encompass micropores (< 10 µm) in the studied carbonates, it has been confirmed that the correlation between porosity and permeability increases (see Chapter Seven). This observation is in accordance with previous studies which noted that the multimodal nature of pore systems which experienced differential small-scale modifications by diagenesis causing a heterogeneous distribution of both ineffective and effective pores is the main factor leading to the often low porosity-permeability relationship in carbonates (e.g., Mazzullo, 2004; Rezaee et al., 2006; Dernaika & Sinclair, 2017; Zhang et al., 2017). Consequently, by extracting effective porosity and excluding ineffective pores, the main factor controlling permeability generation can be detected and the correlation of permeability for given porosity increases. This not only leads to a better understanding of how porosity and permeability are distributed in a succession, but further improves prediction of both fundamental petrophysical parameters by integrating obtained quantitative data into outcrop and reservoir petrophysical models.

Haines et al. (2015) demonstrated that DIA works most accurately on BSE images from lithofacies types which contain pore systems dominated by meso- and macropores with < 5 % of "matrix porosity" (i.e., microporosity) as it is true for the samples examined for this thesis, because if a pore system is dominated by meso- and macropores, most of the permeability will be produced by these pores (Hamon, 2003). This is also in accordance with Baechle et al. (2004) who noted that the correlation between porosity and permeability can be improved by using DIA-derived meso- and macroporosity excluding microporosity instead of total measured porosity, if meso- and macropores (> 10 µm) are the main constituents of the effective pore network. However, as previously noted, micropores can play a dominant role in creating a highly effective pore network. Then, it is one of the most important parameters for prediction of total permeability (e.g., Anselmetti et al., 1998). This also applies to nanoscale pore systems, for example in shale gas reservoirs (Milner et al., 2010; Sondergeld et al., 2010; Loucks et al., 2012; Slatt & O´Brian, 2013; Pang et al., 2017). In order to analyze such micro- and nanopore-dominated systems, the DIA method presented in this thesis provides an ideal tool and can be easily applied on appropriate SEM-derived BSE images.

CHAPTER NINE

SUMMARY

In this thesis, digital image analysis (DIA) has been used as the main petrographic tool for various applications, with the purpose of comprehensively analyzing carbonate pore systems. At first, pore width and pore shape factor γ (sensu Anselmetti et al., 1998) are quantified, which both precisely describe pore size and shape complexity of each pore type analyzed. Since pore-type-specific shape complexity and therefore interconnectivity of pores, here represented by γ, is the main factor determining effective porosity, the potential permeability contribution of each occurring pore type has been calculated by linking γ to total permeability, and pore-type-specific effectiveness was determined. By combining all obtained pore parameters, a petrophysical facies has been established, which then allows for detecting the most effective type of pore system and its corresponding sedimentary facies type. In the case of the marginal lacustrine succession of the Nördlinger Ries crater lake, vugs and interpeloidal pores, which both build up the pore system of the non-skeletal grainstone facies, show highest effective porosity values. The detection of effective pore types is one key element to understand the relationship between porosity and permeability in the usually multimodal pore systems of carbonates which are composed of a co-occurrence of effective and ineffective pore types. The pore-type-specific quantification of pore geometry as presented in this thesis is an improvement in respect to previous studies which focus on analyzing the geometry of the entire pore system or the most dominant pore type, solely.

A further key element in understanding the heterogeneous distribution of porosity and permeability in carbonates is the detection of cemented pore space and the quantification of the impact of cementation on both important petrophysical parameters. Therefore, in a second application of the DIA method, the differential diagenetic modification of pore system by vug-forming dissolution and following cementation has been examined throughout each stage of pore system evolution. The influence of these diagenetic modifications has been quantified with DIA in order to obtain a measure for each relevant parameter describing the increase in pore system properties by dissolution, and a cementation reduction value which quantitatively describes the effect of cementation on pore system properties. These values can then be used to assigned error bars and threshold values to avoid potential over- and underestimation of properties caused by local and patchy cementation.

DIA was then used in a third application to evaluate the results of fluid flow simulation performed on the same dataset and results were compared to discuss the concept of this thesis. Comparison between both independent approaches confirms the previous predictions based on pore shape complexity that vugs and interpeloidal pores of the peloidal grainstone facies build up the most effective pore system in this marginal lacustrine succession. Additionally, the comparison reveals two of the most fundamental

problems in pore system analysis: the problem of (up-) scaling pore system information to different scales and the problem of analyzing a two-dimensional object in 3D (i.e., 2D/3D effect). In order to improve these limitations, the hereby presented methods must be implemented into three-dimensional analysis of pore system which will then eliminate the 2D/3D effect and simultaneously offers the possibility to analyze a pore system at different scales. Since pore shape factor γ is a scale-independent parameter, it is not affected by the problem of scale and is therefore ideal to upscale pore system information to larger scales. Therefore, the implementation of the method presented will also improve existing 3D analysis of pore system.

By combining all applications of the 2D method presented in this thesis, pore type effectiveness can be directly quantified and fluid flow can be simulated on thin section images, resulting in effective porosity values for each sample analyzed. The possibility to directly cross-check quantitative pore geometry values with the thin section image they derive from ensures that no unrepresentative sample and pore system image have been used for analysis, which is a fundamental advantage of the DIA method as compared to routine petrophysical measurements. The DIA-based workflow presented in this thesis delivers an integrative tool which combines numerical petrophysical data with detailed petrographic thin section analysis. It offers a fast, inexpensive, accurate and precise method to comprehensively analyze a large number of samples for improved pore system analysis and reservoir characterization studies, and provides also a tool to quantitatively perform rock-typing for petrophysical applications. Resulting quantitative data are ideal for further integration into modelling and simulation processes, with the purpose of successively upscale thin section information. As demonstrated in this thesis, the detection and extraction of effective porosity further helps to improve the often low correlation between porosity and permeability in carbonates.

REFERENCES

Al-Habshi, A., A. Rahman Darwish, T. Hamdy, and H. Shebl, 2003, Application of sequence stratigraphy and petrography in preparation of reservoir rock typing scheme in one of Thamama gas reservoirs of onshore Abu Dhabi: SPE 81533, 11 p.

Aliakbardoust, E., and H. **Rahimpour-Bonab**, 2013, Effects of pore geometry and rock properties on water saturation of a carbonate reservoir: Journal of Petroleum Science and Engineering, v. 112, p. 296-309. 10.1016/j.petrol.2013.11.018.

Andriamihaja, S., E. Padmanabhan, and J. Ben-Awuah, 2016, Characterization of pore systems in carbonate using 3D X -ray computed tomography: Petroleum and Coal, v. 58, p. 507-516.

Anovitz, L. M., and D. R. **Cole**, 2015, Characterization and analysis of porosity and pore structures: Reviews in Mineralogy and Geochemistry, v. 80, no. 1, p. 61-164. doi: https://doi.org/10.2138/rmg.2015.80.04

Anselmetti, F. S., and G. P. **Eberli**, 1999, The velocity-deviation log: a tool to predict pore type and permeability trends in carbonate drill holes from sonic and porosity or density logs: AAPG Bulletin, v. 83, p. 450-466.

Anselmetti, F. S., and G. P. **Eberli**, 2001, Sonic velocity in carbonates - a combined product of depositional lithology and diagenetic alterations, *in* R. N. Ginsburg, ed., Subsurface Geology of a Prograding Carbonate Platform Margin, Great Bahama Bank: Results of the Bahamas Drilling Project: SEPM Special Publication v. 70, p. 193-216.

Anselmetti, F. S., M. S. Luthi, and G. P. Eberli, 1998, Quantitative characterization of carbonate pore systems by digital image analysis: AAPG Bulletin, v. 82, p. 1815-1836.

Archilha, N. L., R. M. Missagia, C. Hollis, M. A. R. De Ceia, S. A. McDonald, I. A. Lima Neto, D. S. Eastwood, and P. Lee, Permeability and acoustic velocity controlling factors determined from x-ray tomography images of carbonate rocks: AAPG Bulletin, v. 100, no. 8, p. 1289-1309.

Arns, C. H., F. Bauget, A. Limaye, A. Sakellariou, T. J. Senden, A. P. Sheppard,R. M. Sok, W. V. Pinczewski, S. Bakke, L. I. Berge, P. E. Øren, and M. A. Knackstedt, 2005, Pore-scale characterization of carbonates using X-ray microtomography: SPE Journal, v. 10, p. 475-484.

Arp, G., 1995b, Lacustrine bioherms, spring mounds, and marginal carbonates of the Ries-impact-crater (Miocene, southern Germany): Facies, v. 33, p. 35-90, doi:10.1007/BF02537444.

Arp, G., 2006, Sediments of the Ries crater lake (Miocene, southern Germany): Schriftenreihe der Deutschen Gesellschaft für Geowissenschaften, v. 45, p. 213-236.

Arp, G., M. Blumenberg, B.T. Hansen, D. Jung, C. Kolepka, O. Lenz, N. Nolte, K. Poschlod, A. Reimer, and V. Thiel, 2013, Chemical and ecological evolution of the Miocene Ries impact crater lake, Germany: a re-interpretation based on the Enkingen (SUBO 18) drill core: GSA Bulletin, v. 125, no. 7-8, p. 1125-1145.

Asquith, G. B., and C. **Gibson**, 1982, Basic well log analysis for Geologists, 2nd ed.: AAPG, Tulsa, Oklahoma, 216 p.

Baechle, G. T., R. Weger, G. P. Eberli, and J. L. Massaferro, 2004, The role of macro-porosity and microporosity in constraining uncertainties and in relating velocity to permeability in carbonate rocks: Society of Exploration Geophysicists, Expanded Abstracts, v. 23, p. 1662.

Bayerisches Geologisches Landesamt, ed., 1974, Die Forschungsbohrung Nördlingen 1973: Geologica Bavarica, v. 72, p. 1-98.

Bayerisches Geologisches Landesamt, ed., 1977, Ergebnisse der Ries-Forschungsbohrung 1973: Struktur des Kraters und Entwicklung des Kratersees: Geologica Bavarica, v. 75, p. 1-470.

Beach, D. K., 1995, Controls and effects of subaerial exposure on cementation and development of secondary porosity in the subsurface of Great Bahama Bank, *in* D. A. Budd, A. H. Saller, and P. M. Harris, eds., Unconformities and Porosity in Carbonate Strata: AAPG Memoir, v. 63, p. 1-34.

Bolten, R., 1977, Die karbonatischen Ablagerungen des obermiozänen Kratersees im Nördlinger Ries: Ph.D. Thesis, Ludwig-Maximilian-Universität, München, Germany.

Buckman, J., E.-M. C. Charalampidou, S. Zihms, M. H. Lewis, P. W. M. Corbett, G. D. Couples, Z. Jiang, and T. Huang, 2019, High-resolution large area scanning electron microscopy: an imaging tool for porosity and diagenesis of carbonate rock systems, *in* Carbonate Pore Systems: New Developments and Case Studies: SEPM Special Publications, v. 112, p. 1-18.

Buchner, E., W. H. Schwarz, M. Schmieder, and M. Trieloff, 2010, Establishing a 14.6 ± 0.2 Ma age for the Nördlinger Ries impact (Germany) – a prime example for concordant isotopic ages from various dating materials: Meteoritics and Planetary Science, v. 45, p. 662-674.

Chandra, V. S. S., A. Barnett, P. Corbett, S. Geiger, P. Wright, R. Steele, and P. Milroy, 2015, Effective integration of reservoir rock-typing and simulation using near-wellbore upscaling: Marine and Petroleum Geology, v. 67, p. 307326. doi:10.1016/j.marpetgeo.2015.05.005.

Chautru, J. M., H. Arab, N. Fujita, E. Pluchery, E. Poli, H. Shebl, M. Y. El-Henshiri, and T. Shikama, 2005, An integrated RRT prediction method combining thin sections, sequence stratigraphy and logs: SPE 93563, 11 p

Chernyshenko, S. I., Flow Illustrator, http://www.flowillustrator.com (accessed February 19, 2019)

Choquette, P. W., and L. C. **Pray**, 1970, Geologic nomenclature and classification of porosity in sedimentary carbonates: AAPG Bulletin, v. 54, p. 207-250.

Christ, N., S. Maerz, E. Kutschera, O. Kwiecien, M. Mutti, and N. Sheldon, 2018, Palaeoenvironmental and diagenetic reconstruction of a closed-lacustrine carbonate system – the challenging marginal setting of the Miocene Ries Crater Lake (Germany): Sedimentology, v. 65, p. 235-262. doi:10.1111/sed.12401

Cook, J. E., L. B. Goodwin, and D. F. Boutt, 2011, Systematic diagenetic changes in the grain-scale morphology and permeability of quartz cemented quartz arenite: AAPG Bulletin, v. 95, p. 1067-1088.

Coskun, S. B., and N. C. **Wardlaw**, 1995, Influences of pore geometry, porosity and permeability on initial water saturation – an empirical method for estimating initial water saturation by image analysis: Journal of Petroleum Science and Engineering, v. 12, p. 295-308. 10.1016/0920-4105(94)00051-5.

Creusen, A., K. Maamari, S. Tull, V. Vahrenkamp, A. Mookerjee, and M. van Rijen, 2007, Property modelling small scale heterogeneity of carbonate facies: SPE 111451, 5p.

Dernaika, M. R., and G. G. **Sinclair**, 2017, Resolving the link between porosity and permeability in carbonate pore systems: paper SCA2017-77 presented at the International Symposium of the Society of Core Analysts held in Vienna, Austria, 27-30 August 2017, 9 p.

Dickson, J. A. D., 1965, A modified staining technique for carbonates in thin section, Nature: v. 205 (4971), 587 p.

Dickson, J. A. D., 1966, Carbonate identification and genesis as revealed by staining: Journal of Sedimentary Research, v. 36, no. 2, p. 491-505. doi: https://doi.org/10.1306/74D714F6-2B21-11D7-8648000102C1865D

Dunham, R. J., 1962, Classification of carbonate rocks according to texture, *in* W. E. Ham, ed., Classification of carbonate rocks - a symposium: AAPG Memoir, v. 1, p. 108-121.

Durlofsky, L. J., 2003, Upscaling of Geocellular models for reservoir flow simulation: a review of recent progress: Paper presented at 7th International Forum on Reservoir Simulation, Bühl/Baden-Baden, Germany, June 23-27, 2003, 57 p.

Eberli, G. P., G. T. Baechle, F. S. Anselmetti, and M. L. Incze, 2003, Factors controlling elastic properties in carbonate sediments and rocks: The Leading Edge, v. 22, p. 654–660.

Ehrenberg, S. N., and P.H. **Nadeau**, 2005, Sandstone vs. carbonate petroleum reservoirs: a global perspective on porosity-depth and porosity-permeability relationships: AAPG Bulletin, v. 89, p 435-445. 10.1306/11230404071.

Ehrenberg, S. N., G. P. Eberli, and G. T. Baechle, 2006, Porosity-permeability relationships in Miocene carbonate platforms and slopes seaward of the Great Barrier Reef, Australia (ODP Leg194, Marion Plateau): Sedimentology, v. 53, p. 1289-1318.

Ehrenberg, S. N., 2007, Whole core versus plugs: scale dependence of porosity and permeability measurements in platform carbonates: AAPG Bulletin, v. 91, no. 6, p. 835-846.

Ehrlich, R., S. J. Crabtree, S. K. Kennedy, and R. L. Cannon, 1984, Petrographic image analysis I: analyses of reservoir pore complexes: Journal of Sedimentary Petrology, v. 54, p. 1365-1376.

Ehrlich, R., S. J. Crabtree, K. O. Horkowitz, and J. P. Horkowitz, 1991a, Petrography and reservoir physics I: objective classification of reservoir porosity: AAPG Bulletin, v. 75, p. 1547-1562.

Ehrlich, R., S. J. Crabtree, K. O. Horkowitz, and J. P. Horkowitz, 1991b, Petrography and reservoir physics III: physical models for permeability and formation factor: AAPG Bulletin, v. 75, p. 1579-1592.

Esteban, M., and J. L. **Wilson**, 1993, Introduction to karst systems and paleokarst reservoirs, in R. D. Fritz, J. L. Wilson, and D. A. Yurewicz, eds., Paleokarst related hydrocarbon reservoirs: SEPM Core Workshop 18, p. 1-9.

Evamy, B. D., 1963, The application of a chemical staining technique to a study of de-dolomitisation: Sedimentology, v. 2, p. 164-170. doi:10.1111/j.1365-3091.1963.tb01210.x

Evamy, B. D., 1969, The precipitational environment and correlation of some calcite cements deduced from artificial staining: Journal of Sedimentary Research, v. 39, no. 2, p. 787-793. doi: https://doi.org/10.1306/74D71D1B-2B21-11D7-8648000102C1865D

Fabricius, I. L., 2003, How burial diagenesis of chalk sediments controls sonic velocity and porosity: AAPG Bulletin, v. 87, p. 1755-1778.

Fabricius, I. L., 2007, Chalk: composition, diagenesis and physical properties: Bulletin of the Geological Society of Denmark, v. 55, p. 97-128.

Farmer, C. L., 2002, Upscaling: a review: International Journal for Numerical Methods in Fluids, v. 40, p. 63-78. doi:10.1002/fld.267

Fausett, L.V., 1994, Fundamentals of neural networks: architecture, algorithms, and applications: Prentice-Hall, Englewood Cliffs, New Jersey, 461 p.

Fournier, F., G. Fabre, and C. Aug, 2013, Integrated rock-typing with capillary pressure curve clustering: SPE 164354, 10 p.

Giot, D., J.-M. Dawans, R. King, P. Lehmann, E. Shaw, and F. El Wazeer, 2000, Tracking permeability in a major limestone reservoir from rock observation to 3D modelling: SPE 87233, 16 p.

Gomes, J. S., M. T. Riberio, C. J. Strohmenger, S. Negahban, and M. Z. Kalam, 2008, Carbonate reservoir rock typing—the link between geology and SCAL: SPE 118284, 14 p.

Granier, B., 2003, A new approach in rock-typing, documented by a case study of layer-cake reservoirs in field "A", offshore Abu Dhabi (U.A.E.): Carnets de Geologie, CG2003 (A04), p. 1-13.

Haines, T. J., J. E. Neilson, D. Healy, E. A. H. Michie, and A. C. Aplin, 2015, The impact of carbonate texture on the quantification of total porosity by image analysis: Computers & Geosciences, v. 85, p. 112-125.

Hamon, G., 2000, Field-wide variations in wettability: Paper SPE 63144-MS, presented at SPE Annual Technical Conference and Exhibition, Dallas, Texas, USA, 1.-4. October, 9 p.

He, L., L. Zhao, J. Li, J. Ma, R. Lui, S. Wang, and W. Zhao, 2014, Complex relationship between porosity and permeability of carbonate reservoirs and its controlling factors: a case of platform facies in Pre-Caspian Basin: Petroleum Exploration and Development, v. 41, no. 2, p. 225-234. 10.1016/S1876-3804(14)60026-4.

Hemes, S., G. Desbois, J. Urai, B. Schroeppel, and J.-O. Schwarz, 2015, Multi-scale characterization of porosity in Boom Clay (HADES-level, Mol, Belgium) using a combination of X-ray mu-CT, 2D BIB-SEM and FIB-SEM tomography: Microporous and Mesoporous Materials, v. 208, p. 1-20. 10.1016/j.micromeso.2015.01.022.

Hollis C., V. Vahrenkamp, S. Tull, A. Mookerjee, C. Taberner, and Y. Huang, 2010, Pore system characterisation in heterogeneous carbonates: an alternative approach to widely-used rock-typing methodologies: Marine and Petroleum Geology, v.27, no. 4, p. 772-793.

Honarpou, M. M., N. F. Djabbarah, and K. Sampath, 2003, Whole core analysis – Experience and challenges: Society of Petroleum Engineers Paper 81575, 16 p.

Hüttner, R., and H. **Schmidt-Kaler**, 1999, Die Geologische Karte des Rieses 1:50 000, Erläuterungen zu Erdgeschichte, Bau und Entstehung des Kraters sowie zu den Impaktgesteinen, 2nd ed.: Geologica Bavarica, v. 104, p. 7-76.

Iassonov, P., T. Gebrenegus, and M. Tuller, 2009; Segmentation of X-ray computed tomography images of porous materials: a crucial step for characterization and quantitative analysis of pore structure: Water Resources Research, v. 45, no. W09415, p. 1-12.

Jankowski, B., 1977, Die Postimpact-Sedimente in der Forschungsbohrung Nördlingen 1973: Geologica Bavarica 75, p. 21-36.

Javaux, C., F. Cochet, B. Gautheir, C. Prinet, L. ten Haven, and M. Herriou, 2000, 3D geological model to reservoir simulation of the lower Arab Formation- Abu Al Bukhoosh (ABK) Field, offshore Abu Dhabi: SPE 87235, 9 p.

Johnson, R. W., 2016, Handbook of Fluid Dynamics, 2nd ed.: CRC Press, Boca Raton, Florida, 1560 p.

Kadkhodaie, A., and R. **Kadkhodaie-Ilkhchi**, 2018, A review of reservoir rock typing methods in carbonate reservoirs: relation between geological, seismic, and reservoir rock types: Iranian Journal of Oil & Gas Science and Technology, v. 7, p. 13-35. 10.22050/IJOGST.2019.136243.1461.

Kang, Z., J. Zhao, D. Yang, Y. Zhao, and Y. Hu, 2017, Study of the evolution of micron-scale pore structure in oil shale at different temperatures: Oil Shale, v. 34, no. 1, p. 42-54. 10.3176/oil.2017.1.03.

Kasper, T., P. Francus, T. Haberzettl, L. Zhu, and R. Mäusbacher, 2013, Image analysis in sedimentology as application for high-resolution grain size analysis: a case study of lake sediments from Tangra Yumco (Tibetan Plateau): Himalayan Karakorum Tibet Workshop & International Symposium on Tibetan Plateau 2013, p. 22-24.

Kaufhold, S., G. Grathoff, M. Halisch, M. Plötze, J. Kus, K. Ufer, R. Dohrmann, S. Lafage, and C. Ostertag-Henning, 2016, Comparison of methods for the determination of the pore system of a potential German gas shale: The Clay Minerals Society Workshop Lectures Series, v. 21, p. 163-190.

Kayser, A., M. Knackstedt, and M. Ziauddin, 2006, A closer look at pore geometry: Oilfield Review, v. 18, p. 4-13.

Knackstedt, M. A., C. H. Arns, A. Limaye, A. Sakellariou, T. J. Senden, A. P. Sheppard, R. M. Sok, W. V. Pinczewski, and G. F. Bunn, 2004, Digital core laboratory: reservoir-core properties derived from 3D images: Journal of Petroleum Technology, v. 56, no. 5, p. 66-68.

Knackstedt, M. A., M. Madadi, C. H. Arns, G. T. Baechle, G. P. Eberli, and R. J. Weger, 2009, Carbonate petrophysical parameters derived from 3D images: American Association of Petroleum Geologists Annual Symposium (AAPG 2008), ed. AAPG, USA, 9 p.

Koponen, A., M. Kataja, and J. Timonen, 1997, Permeability and effective porosity of porous media: Physical Review E, v. 56, n. 3, p. 3319-3325.

Lee, J., Y. Park, Y. Jo, J. Jeong, and S. Eom, 2009, A relationship between porosity and permeability of carbonate rock reservoirs: American Geophysical Union Fall Meeting December 2009, 1859 Hydrology/Rocks: physical properties, AGU Abstracts 12 (2009), abstract id. H11A-0789.

Li, H., and L. F. **Durlofsky**, 2015, Upscaling for compositional reservoir simulation: Society of Petroleum Engineers - SPE Reservoir Simulation Symposium 2015. 1. 411-430. 10.2118/173212-PA.

Lønøy, A., 2006, Making sense of carbonate pore systems: AAPG Bulletin, v. 90, no. 9, p. 1381-1405.

Loucks, R. G., 2002, Controls on reservoir quality in platform interior limestones around the Gulf of Mexico: example from the lower cretaceous Pearsall formation in south Texas: Gulf Coast Association of Geological Societies Transactions, v. 52, p. 659-672.

Loucks, R. G., R. M. Reed, S. C. Ruppel, and D. M. Jarvie, 2009, Morphology, genesis, and distribution of nanometer-scale pores in siliceous mudstones of the Mississippian Barnett Shale: Journal of Sedimentary Research, v. 79, no. 12, p. 848-861.

Loucks, R. G., R. M. Reed, S. C. Ruppel, and U. Hammes, 2012, Spectrum of pore types and networks in mudrocks and a descriptive classification for matrix-related mudrock pores: AAPG Bulletin, v. 96, p. 1071-1098.

Lucia, F. J., 1983, Petrophysical parameters estimated from visual descriptions of carbonate rocks: A field classification of carbonate pore space: Journal of Petroleum Technology, v. 35, p. 629-637.

Lucia, F. J., 1995, Rock-fabric/petrophysical classification of carbonate pore space for reservoir characterization: AAPG Bulletin, v. 79, no. 9, p. 1275-1300.

Lucia, F. J., 1999, Carbonate reservoir characterization: Berlin, Springer-Verlag, 226 p.

Ma, L., A.-L. Fauchille, P. J. Dowey, F. F. Pilz, L. Courtois, K. G. Taylor, and P. D. Lee, 2017, Correlative multi-scale imaging of shales: a review and future perspectives, *in* E. H. Rutter, J. Mecklenburgh, and K. G. Taylor, eds., Geomechanical and Petrophysical Properties of Mudrocks: Geological Society, London, Special Publications, 454, first published online May 2, 2017. https://doi.org/10.1144/SP454.11

Maerz, S., 2012, Comparison between sedimentary facies and petrophysical facies using applied petrophysics and digital image analysis - implication for reservoir characterization studies in the Buntsandstein, early Triassic, Central Germany: Diploma thesis, University of Potsdam, Potsdam, Germany, 144 p.

Martin III, W. D., B. J. Putman, and N. B. Kaye, 2013, Using image analysis to measure the porosity distribution of a porous pavement: Construction and Building Materials, v. 48, p. 210-217.

Matrecano, M., 2011, Porous media characterization by micro-tomographic image processing: Ph.D. dissertation thesis, University of Napoli, Naples, Italy, 126 p.

Mazzullo, S. J., 2004, Overview of porosity evolution in carbonate reservoirs: Kansas Geological Society Bulletin, v. 79, p. 20-28.

McCreesh, C. A., R. Ehrlich, and S. J. Crabtree, 1991, Petrography and reservoir physics 2: Relating thin section porosity to capillary pressure: AAPG Bulletin, v. 10, p. 1563-1578.

Melim, L. A., F. S. Anselmetti, and G. P. Eberli, 2001, The importance of pore type on permeability of Neogene Carbonates, Great Bahama Bank: SEPM Special Publication, v. 70, p. 217-238.

Milner, M., R. McLin, and J. Petriello, 2010, Imaging texture and porosity in mudstones and shales: comparison of secondary and ion-milled backscatter SEM methods: Canadian Unconventional Resources and International Petroleum Conference, Calgary, Alberta, Canada, October 19-21, 2010, SPE Paper 138975, 5 p.

Mowers, T. T., and D. A. **Budd**, 1996, Quantification of porosity and permeability reduction due to calcite cementation using computer-assisted petrographic image analysis techniques: AAPG Bulletin, v. 80, p. 309-322.

Mukunoki, T., Y. Miyata, K. Mikami, and E. Shiota, 2016, X-ray CT analysis of pore structure in sand: Solid Earth, v. 7, p. 929-942. https://doi.org/10.5194/se-7-929-2016

Nakayama, Y., and R. F. **Boucher**, 1998, Introduction to Fluid Mechanics, 1st ed.: Butterworth-Heinemann, Oxford, UK, 334 p.

Pang, Y., M. Soliman, H. Deng, and H. Emadi, 2017, Analysis of effective porosity and effective permeability in shale-gas reservoirs with consideration of gas adsorption and stress effects: SPE Journal, v. 22, no. 6, 21 p. 10.2118/180260-PA.

Pemberton, S. G., and M. K. **Gingras**, 2005, Classification and characterizations of biogenically enhanced permeability: AAPG Bulletin, v. 89, p. 1493-1517.

Peng, S., J. Yang, X. Xiao, B. Loucks, S. C. Ruppel, and T. Zhang, 2015, An integrated method for upscaling pore-network characterization and permeability estimation: example from the Mississippian Barnett Shale: Transport in Porous Media, v. 109, no. 2, p. 359-376.

Pittman, E. D., 1992, Relationship of porosity and permeability to various parameters derived from mercury injection-capillary pressure curves for sandstone: AAPG Bulletin, v. 76, no. 2, p. 191-198.

Pohl, J., 1977, Paläomagnetische und gesteinsmagnetische Untersuchungen an den Kernen der Forschungsbohrung Nördlingen 1973: Geologica Bavarica 75, p. 329-348.

Porras, J. C., and O. **Campos**, 2001, Rock typing: a key approach for petrophysical characterization and definition of flow units, Santa Barbara field, Eastern Venezuela Basin: SPE 69458, 6 p.

Pramanik, A. G., V. Singh, R. Vig, A. K. Srivastava, and D. N. Tiwary, 2004, Estimation of effective porosity using geostatistics and multiattribute transforms: a case study: Geophysics, v. 69, no. 2, p. 352-372.

Purser, B. H., 1978, Early diagenesis and the preservation of porosity in Jurassic limestones: Journal of Petroleum Geology, v. 1, p. 83-94.

Qi, D., P. Wong, and K. Liu, 2001, An improved global upscaling approach for reservoir simulation: Petroleum Science and Technology, v. 19, no. 7-8, p. 779-795.

Qi, D., and T. **Hesketh**, 2005, An analysis of upscaling techniques for reservoir simulation: Petroleum Science and Technology, v. 23, no. 7-8, p. 827-842. doi:10.1081/LFT-200033132

Qi, D., and S. **Zhang**, 2009, Major challenges for reservoir upscaling: Petroleum Science and Technology, v. 27, no. 17, p. 1985-1992. doi:10.1080/10916460802608818

Rahimpour-Bonab, H., and E. **Aliakbardoust**, 2014, Pore facies analysis: incorporation of rock properties into pore geometry based classes in a Permo-Triassic carbonate reservoir in the Persian Gulf: Journal of Geophysics and Engineering, v. 11, 20 p.

Ranachowski, Z., D. Jozwiak-Niedzwiedzka, P. Ranachowski, M. Dąbrowski, S. Kudela Jr., and T. Dvorák, 2015, Analysis of pore distribution and connectivity on concrete using X-ray microtomography: International Symposium "Brittle Matrix Composites 11", Warsaw, Poland, September 28-30, 2015, v. 1, p. 203-212.

Rashid, F., P. W. J. Glover, P. Lorinczi, R. Collier, and J. Lawrence, 2015, Porosity and permeability of tight carbonate reservoir rocks in the north of Iraq: Journal of Petroleum Science and Engineering, v. 133, p. 147-161, https://doi.org/10.1016/j.petrol.2015.05.009.

Rebelle, M., and B. **Lalanne**, 2014, Rock-typing in carbonates: a critical review of clustering methods: SPE 171759, 14 p.

Renshaw, R., C., J. P. Robinson, G. A. Dimitrakis, J. R. Bows, and S. W. Kingman, 2016, Characterisation of potato crisp effective porosity using micro-CT, Journal of the science of food and agriculture, v. 96, p. 4440-4448. 10.1002/jsfa.7655.

Rezaee, M. R., A. Jafari, and E. Kazemdzadeh, 2006, Relationships between permeability, porosity and pore throat size in carbonate rocks using regression analysis and neural networks: J. Geophysical Engineering, v. 3, no. 4, p. 370-376. 10.1088/1742-2132/3/4/008.

Rider, M. H., 2002, The geological interpretation of well logs, 2nd ed.: Rider-French Consulting Ltd, 280 p.

Riding, R., 1979, Origin and diagenesis of lacustrine algal bioherms at the margin of the Ries crater, Upper Miocene, southern Germany: Sedimentology, v. 26, p. 645-680.

Roduit, N., JMicroVision: Image analysis toolbox for measuring and quantifying components of high-definition images: Version 1.2.7., http://www.jmicrovision.com (accessed October 28, 2018).

Rushing, J.A., K. E. Newsham, and T. A. Blasingame, 2008, Rock typing: Keys to understanding productivity in tight gas sands: SPE 114164, 31 p.

Saller, A. H., D. A. Budd, and P. M. Harris, 1994a, Unconformities and porosity development in carbonate strata: ideas from a Hedberg conference: AAPG Bulletin, v. 78, p. 857-871.

Saller, A. H., J. A. D. Dickson, and F. Matsuda, 1999, Evolution and distribution of porosity associated with subaerial exposure in upper Paleozoic platform limestones, west Texas: AAPG Bulletin, v. 83, p. 1835-1854.

Skalinski, M., and J. A. M. **Kenter**, 2014, Carbonate petrophysical rock typing: integrating geological attributes and petrophysical properties while linking with dynamic behavior, *in* S. M. Agar and

S. Geiger, eds., Fundamental controls on fluid flow in carbonates: Geological Society, London, Special Publications 2014, v. 406, p. 229-259.

Skalinski M., R. Salazar, G. La Torraca, Z. Yang, and J. Urbach, 2012, Heterogeneous carbonates – integrating plug and whole core data using rock types: SCA201212, 12 p.

Slatt, R. M., and N. R. **O'Brien**, 2013, Microfabrics related to porosity development, sedimentary and diagenetic processes, and composition of unconventional resource shale reservoirs as determined by conventional scanning electron microscopy, *in* W.K. Camp, E. Diaz, and B. Wawak, eds., Electron microscopy of shale hydrocarbon reservoirs: AAPG Memoir, v. 102, p. 37-44.

Sondergeld, C. H., R. J. Ambrose, C. S. Rai, and J. Moncrieff, 2010, Microstructural studies of gas shale: Society of Petroleum Engineers Unconventional Gas Conference, Pittsburgh, Pennsylvania, February 23–25, 2010, SPE Paper 131771, 17 p.

Sun, H., S. Vega, and G. Tao, 2017, Analysis of heterogeneity and permeability anisotropy in carbonate rock samples using digital rock physics: Journal of Petroleum Science and Engineering, v. 156, p. 419-429.

Tiab D., and E. C. **Donaldson**, 2004, Petrophysics, 2nd ed.: Elsevier Science Publishers, Amsterdam, New York, 889 p.

Venkitadri, V. S., H. T. Shebl, T. Shibasaki, C. A. Dabbouk, and S. M. Salman, 2005, Reservoir rock type definition in a giant Cretaceous carbonate: SPE 93477, 16p.

Vahrenkamp, C., and A. **Creusen**, 2010, The role of sedimentary fabric for rock typing and model upscaling in carbonate reservoirs: Search and Discovery Article #50306, 23 p.

Verwer, K., H. Braaksma, and J. A. Kenter, 2008, Acoustic properties of carbonates: effects of rock texture and implications for fluid substitution: Geophysics, v. 73, no 2, p. B51-B65. 10.1190/1.2831935.

Verwer, K., G. P. Eberli, G. T. Baechle, and R. J. Weger, 2010, Effect of carbonate pore structure on dynamic shear moduli: Geophysics, v. 75, no. 1, p. E1-E8.

Verwer, K., G. P. Eberli, and R. J. Weger, 2011, Effect of pore structure on electrical resistivity in carbonates: AAPG Bulletin, v. 95, no. 2, p. 175-190.

Weger R. J., 2006, Quantitative pore/rock type parameters in carbonates and their relationship to velocity deviations: Ph.D. dissertation thesis, University of Miami, RSMAS, Miami, USA, 232 p.

Weger, R. J., G. T. Baechle, J. L. Masaferro, and G. P. Eberli, 2004, Effects of pore structure on sonic velocity in carbonates: Society of Exploration Geophysicists, Expanded Abstracts, v. 23, p. 1774.

Weger, R. J., G. P. Eberli, G. T. Baechle, J. L. Massaferro, and Y.-F. Sun, 2009, Quantification of pore structure and its effect on sonic velocity and permeability in carbonates: AAPG Bulletin, v. 93, no. 10, p. 1297-1317.

Wildenschild, D., and A. P. **Sheppard**, 2013, X-ray imaging and analysis techniques for quantifying pore-scale structure and processes in subsurface porous medium systems: Advances in Water Resources, v. 51, p. 217-246. 10.1016/j.advwatres.2012.07.018.

Xiong, Q., T. G. Baychev, and A. P. Jivkov, 2016, Review of pore network modeling of porous media: experimental characterisations, network constructions and applications to reactive transport: Journal of Contaminant Hydrology, v. 192, p. 101-117.

Youssef, S., E. Rosenberg, N. F. Gland, J. A. Kenter, M. Skalinski, and O. Vizika, 2007, High resolution CT and pore-network models to assess petrophysical properties of homogeneous and heterogeneous carbonates: SPE/EAGE Reservoir Characterization and Simulation Conference, Abu Dhabi, October 28-31, 2007, U.A.E., Society of Petroleum Engineers, SPE Paper 111427, 12 p.

Zhang, S., P. Lu, D. Cantrell, Y. Zarettsky, D. Jobe, and S. M. Agar, 2017, Improved quantification of the porosity-permeability relationship of limestones using petrographical texture: Petroleum Geoscience, v. 24, no. 4, p. 440-448.

APPENDIX

Appendix Chapter Two: ***Total porosity and permeability***

	Sample	Φtotal [%]	Ktotal [mD]	Facies
1	1A1	18.01	2265.00	*Cladophorites* Boundstone
2	1A10	27.37	240.50	*Cladophorites* Boundstone
3	1A11	15.55	20.90	*Cladophorites* Boundstone
4	1A12	28.64	2070.00	*Cladophorites* Boundstone
5	1A14	23.58	240.50	*Cladophorites* Boundstone
6	1A2	19.07	44.50	*Cladophorites* Boundstone
7	1A6	19.05	72.00	*Cladophorites* Boundstone
8	1A8	35.82	2032.00	*Cladophorites* Boundstone
9	1B7	13.85	370.00	*Cladophorites* Boundstone
10	1B9	21.26	111.00	*Cladophorites* Boundstone
11	1C10	12.07	780.00	*Cladophorites* Boundstone
12	1C4	16.23	52.00	*Cladophorites* Boundstone
13	1C5	15.32	782.00	*Cladophorites* Boundstone
14	1D5	24.07	36.50	*Cladophorites* Boundstone
15	1D6	18.85	557.10	*Cladophorites* Boundstone
16	1D9	25.33	204.50	*Cladophorites* Boundstone
17	2A4	11.33	24.50	*Cladophorites* Boundstone
18	2A7	10.15	140.50	*Cladophorites* Boundstone
19	2A9	35.14	7.20	*Cladophorites* Boundstone
20	2B9	11.51	35.45	*Cladophorites* Boundstone
21	2C12	5.64	2.10	*Cladophorites* Boundstone
22	2C2	12.64	637.00	*Cladophorites* Boundstone
23	2C5	9.78	463.80	*Cladophorites* Boundstone
24	2D2	9.11	674.00	*Cladophorites* Boundstone
25	2D8	21.86	9.15	*Cladophorites* Boundstone
26	2D9	23.30	64.00	*Cladophorites* Boundstone
27	3A12	20.67	1215.50	*Cladophorites* Boundstone
28	3A13	27.97	98.50	*Cladophorites* Boundstone
29	3A14	14.70	187.00	*Cladophorites* Boundstone
30	3A7	18.68	26.70	*Cladophorites* Boundstone
31	3A8	13.83	52.00	*Cladophorites* Boundstone
32	3C8	14.85	16.00	*Cladophorites* Boundstone
33	3.13	26.96	177.50	Skeletal Grainstone
34	1E4	19.86	241.00	Skeletal Grainstone
35	1A7	39.22	240.50	Skeletal Grainstone
36	1B10	21.26	976.00	Skeletal Grainstone
37	1B12	16.99	234.00	Skeletal Grainstone
38	1B2	18.30	176.00	Skeletal Grainstone
39	1B4	26.64	34.30	Skeletal Grainstone

Sample		Φtotal [%]	Ktotal [mD]	Facies
40	1B5	11.62	230.50	Skeletal Grainstone
41	1C2	22.69	644.50	Skeletal Grainstone
42	1C3	15.72	237.50	Skeletal Grainstone
43	1C8	16.30	10.00	Skeletal Grainstone
44	1C9	12.60	8.10	Skeletal Grainstone
45	1D2	18.35	359.50	Skeletal Grainstone
46	1D3	6.97	138.00	Skeletal Grainstone
47	1D4	17.18	27.55	Skeletal Grainstone
48	1D8	21.04	12.00	Skeletal Grainstone
49	2A1	11.02	1.32	Skeletal Grainstone
50	2A10	20.98	928.00	Skeletal Grainstone
51	2A13	28.54	1867.00	Skeletal Grainstone
52	2A8	42.26	35.00	Skeletal Grainstone
53	2C7	8.58	10.35	Skeletal Grainstone
54	2D11	13.38	964.00	Skeletal Grainstone
55	3A10	10.40	787.00	Skeletal Grainstone
56	3A16	27.97	788.50	Skeletal Grainstone
57	3B11	30.96	327.00	Skeletal Grainstone
58	3B12	13.63	3.60	Skeletal Grainstone
59	3B13	18.24	193.00	Skeletal Grainstone
60	3B3	28.32	1379.00	Skeletal Grainstone
61	3B6	42.89	971.62	Skeletal Grainstone
62	3C1	21.67	1086.00	Skeletal Grainstone
63	3C10	22.95	139.50	Skeletal Grainstone
64	3C11	15.27	86.00	Skeletal Grainstone
65	3C12	23.97	215.00	Skeletal Grainstone
66	3D7	22.12	1.90	Skeletal Grainstone
67	3.16	26.96	788.05	Non-Skeletal Grainstone
68	3.9	24.27	317.00	Non-Skeletal Grainstone
69	1A3	12.64	565.75	Non-Skeletal Grainstone
70	1A4	19.00	1151.50	Non-Skeletal Grainstone
71	1A9	30.13	45.00	Non-Skeletal Grainstone
72	1B1	17.38	35.00	Non-Skeletal Grainstone
73	1B11	37.23	3543.50	Non-Skeletal Grainstone
74	1B3	15.49	406.50	Non-Skeletal Grainstone
75	1C1	16.51	878.50	Non-Skeletal Grainstone
76	1C11	18.41	875.00	Non-Skeletal Grainstone
77	1C12	20.56	150.00	Non-Skeletal Grainstone
78	1C6	24.27	735.00	Non-Skeletal Grainstone
79	1D10	40.39	16.00	Non-Skeletal Grainstone
80	2A5	19.78	9.80	Non-Skeletal Grainstone
81	2A6	16.90	875.50	Non-Skeletal Grainstone
82	2B1	12.86	849.50	Non-Skeletal Grainstone
83	2B10	20.09	328.50	Non-Skeletal Grainstone
84	2B11	19.69	41.50	Non-Skeletal Grainstone

Sample		Φtotal [%]	Ktotal [mD]	Facies
85	2B13	15.70	258.50	Non-Skeletal Grainstone
86	2B14	19.65	221.50	Non-Skeletal Grainstone
87	2B3	11.13	4.60	Non-Skeletal Grainstone
88	2B4	16.71	1.40	Non-Skeletal Grainstone
89	2B5	23.10	73.50	Non-Skeletal Grainstone
90	2B6	18.81	185.00	Non-Skeletal Grainstone
91	2B7	10.96	172.35	Non-Skeletal Grainstone
92	2B8	9.66	2.05	Non-Skeletal Grainstone
93	2C10	3.88	4.60	Non-Skeletal Grainstone
94	2C4	29.37	385.00	Non-Skeletal Grainstone
95	2C9	8.46	1.20	Non-Skeletal Grainstone
96	2D10	8.45	15.90	Non-Skeletal Grainstone
97	3A1	11.42	2.20	Non-Skeletal Grainstone
98	3A11	19.06	83.40	Non-Skeletal Grainstone
99	3A5	17.18	356.00	Non-Skeletal Grainstone
100	3B1	35.67	401.00	Non-Skeletal Grainstone
101	3B10	14.70	3.60	Non-Skeletal Grainstone
102	3B2	25.41	2400.00	Non-Skeletal Grainstone
103	3B4	36.95	55.50	Non-Skeletal Grainstone
104	3B5	38.70	2911.00	Non-Skeletal Grainstone
105	3B8	17.75	17.00	Non-Skeletal Grainstone
106	3B9	17.69	19.30	Non-Skeletal Grainstone
107	3C1	21.68	1086.00	Non-Skeletal Grainstone
108	3C2	13.50	69.87	Non-Skeletal Grainstone
109	3C3	7.35	13.45	Non-Skeletal Grainstone
110	3C4	16.54	55.45	Non-Skeletal Grainstone
111	3C5	16.84	161.00	Non-Skeletal Grainstone
112	3D1	25.15	743.00	Non-Skeletal Grainstone
113	3D2	21.35	62.25	Non-Skeletal Grainstone
114	3D4	18.56	181.00	Non-Skeletal Grainstone
115	3D9	17.47	126.00	Non-Skeletal Grainstone
116	1E2	17.21	33.35	Palustine Breccia
117	1E3	19.84	655.00	Palustine Breccia
118	1A13	23.58	113.00	Palustine Breccia
119	2A12	20.25	98.50	Palustine Breccia
120	2C13	12.72	492.50	Palustine Breccia
121	2D7	26.27	19.50	Palustine Breccia
122	3D5	46.03	1.60	Palustine Breccia

Appendix Chapter 3: ***ANN data***

	Thin Section Image	Φ_{total}	K_{total}	Φ_{DIA_total}	Pore width	γ	ED	PoA
		[%]	[mD]	[%]	[µm]	[-]	[µm]	[µm]
1	1A10_2	18.01	2265.00	23.94	13.40	1.51	15.93	17.09
2	1A14_3	23.58	240.50	23.13	27.23	1.44	21.19	28.47
3	1A8_5	35.82	2032.00	16.00	16.50	1.79	18.72	31.72
4	1B10_2	21.26	976.00	37.01	41.79	3.38	40.74	22.47
5	1B11_5	37.23	3543.50	34.65	36.65	3.61	39.21	39.15
6	1B2_2	18.30	176.00	16.91	24.26	3.32	25.86	14.31
7	1B7_8	13.85	370.00	9.77	59.40	1.70	66.37	40.07
8	1C1_11	18.41	875.00	13.42	14.54	1.86	17.26	15.71
9	1C6_8	24.27	735.00	13.48	19.57	2.11	22.41	19.35
10	1D2_15	18.35	359.50	16.34	31.87	2.29	37.93	19.39
11	1E4_7	19.86	241.00	17.33	16.69	1.74	20.85	24.75
12	2A6_5	16.90	875.50	19.64	22.44	2.65	23.67	17.17
13	2C4_6	29.37	385.00	17.30	20.76	1.65	23.04	12.70
14	2C5_18	9.78	463.80	4.06	20.46	1.56	24.81	31.74
15	2D11_8	13.38	964.00	6.63	39.18	1.44	46.47	23.50
16	3.13_3	26.96	177.50	18.41	21.03	1.78	23.72	12.82
17	3.16_1	26.96	788.05	28.91	25.73	2.65	26.85	19.30
18	3A10_8	10.40	788.50	12.80	17.62	1.93	19.57	10.79
19	3A12_13	20.67	1215.50	28.04	54.33	1.79	61.14	48.84
20	3A13_6	27.97	98.50	6.70	16.30	1.23	20.37	15.50
21	3A14_13	14.70	187.00	4.05	6.69	1.23	25.86	16.32
22	3A5_9	17.18	356.00	12.92	10.83	1.92	12.44	3.86
23	3A7_4	18.68	26.70	14.43	35.16	1.54	40.09	29.39
24	3A8_2	13.83	52.00	9.62	24.53	1.71	28.33	16.13
25	3B1_13	35.67	401.00	29.24	40.33	2.66	40.31	14.39
26	3B3_4	28.32	1379.00	27.31	14.62	2.58	15.39	13.71
27	3B5_9	38.70	2911.00	23.77	15.87	1.97	18.50	16.75
28	3B6_9	42.89	971.62	32.89	29.50	2.06	33.25	26.41
29	3C1_3	21.67	1086.00	9.40	11.57	1.51	15.43	25.12
30	3C12_3	23.97	215.00	25.72	36.83	1.78	40.84	36.63
31	3D1_6	25.15	743.00	18.43	8.08	2.53	9.94	13.41
32	3D4_8	18.56	181.00	13.50	24.93	1.82	27.90	15.16

Appendix Chapter 3 and 4: ***Pore type properties***

	Thin Section Image	PTA	Pore Type	Φ_{DIA_total} [%]	K_{total} [mD]	Pore width [µm]	γ [-]
1	1A10_2	2	Vuggy	23.94	240.5	164.29	1.85
2	1A14_3	2	Vuggy	23.13	565.70	141.35	1.72
3	3A7_4	2	Vuggy	14.43	26.70	308.42	1.66
4	3A8_2	2	Vuggy	9.62	52.00	186.92	2.01
5	1B7_8	2	Vuggy	9.77	370.00	339.59	1.76
6	1A8_5	2	Vuggy	16.00	2032.00	186.19	1.85
7	2C5_18	2	Vuggy	4.06	463.80	218.26	1.55
8	3A12_13	2	Vuggy	28.04	1215.50	408.26	1.85
9	1C6_8	1	Vuggy	13.48	735.00	298.70	2.52
10	3.16_1	1	Vuggy	28.91	788.05	386.89	3.23
11	3B5_9	1	Vuggy	23.77	2911.00	210.38	2.03
12	1B10_2	3	Vuggy	37.01	976.00	667.26	3.38
13	1C1_11	1	Vuggy	13.42	878.50	197.84	2.10
14	3B3_4	3	Vuggy	27.31	1379.00	385.46	3.39
15	1D2_15	3	Vuggy	16.34	359.50	484.33	2.93
16	3B1_13	1	Vuggy	29.24	401.00	355.25	2.88
17	3A5_9	1	Vuggy	12.92	356.00	481.77	2.77
18	3B6_9	3	Vuggy	32.89	971.62	260.31	2.46
19	3C1_3	3	Vuggy	9.40	1086.00	294.20	1.40
20	1B11_5	1	Vuggy	34.65	3543.50	333.94	3.43
21	2D11_8	3	Vuggy	6.63	964.00	134.81	1.44
22	2A6_5	1	Vuggy	19.64	875.50	238.95	2.77
23	3A10_8	3	Vuggy	12.80	788.50	240.33	1.85
24	3D1_6	1	Vuggy	18.43	743.00	355.44	2.88
25	3.13_3	3	Vuggy	23.06	177.50	148.50	1.87
26	1E4_7	3	Vuggy	17.33	241.00	206.14	1.51
27	3C12_3	3	Vuggy	25.72	215.00	663.66	2.32
28	3B5_9	1	Skel. Moldic	23.77	2911.00	20.46	2.84
29	1B10_2	3	Skel. Moldic	37.01	976.00	22.06	3.96
30	3B3_4	3	Skel. Moldic	27.31	1379.00	31.27	2.72
31	1D2_15	3	Skel. Moldic	16.34	359.50	38.19	2.87
32	3B6_9	3	Skel. Moldic	32.89	971.62	17.14	2.08
33	3C1_3	3	Skel. Moldic	9.40	1086.00	7.42	1.66
34	2D11_8	3	Skel. Moldic	6.63	964.00	20.16	2.23
35	3A10_8	3	Skel. Moldic	12.80	788.50	27.97	1.93
36	3.13_3	3	Skel. Moldic	23.06	177.50	10.67	2.43
37	1E4_7	3	Skel. Moldic	17.33	241.00	20.27	2.26
38	3C12_3	3	Skel. Moldic	25.72	215.00	14.30	2.16
39	1B2_2	3	Skel. Moldic	16.91	176.00	24.26	2.25
40	1B10_2	3	Intraskeletal	37.01	976.00	51.34	2.08

	Thin Section Image	PTA	Pore Type	Φ_{DIA_total}	K_{total}	Pore width	γ
				[%]	[mD]	[µm]	[-]
41	3B3_4	3	Intraskeletal	27.31	1379.00	103.99	1.62
42	1D2_15	3	Intraskeletal	16.34	359.50	468.19	1.90
43	3B6_9	3	Intraskeletal	32.89	971.62	94.77	1.67
44	3C1_3	3	Intraskeletal	9.40	1086.00	294.20	1.56
45	1E4_7	3	Intraskeletal	17.33	241.00	310.54	1.96
46	3C12_3	3	Intraskeletal	25.72	215.00	349.61	1.60
47	3.13_3	3	Intraskeletal	23.06	177.50	312.58	1.55
48	1C6_8	1	Interpeloidal	13.48	735.00	15.70	1.59
49	3.16_1	1	Interpeloidal	28.91	788.05	17.72	1.56
50	3B5_9	1	Interpeloidal	23.77	2911.00	9.94	1.66
51	1B10_2	3	Interpeloidal	37.01	976.00	29.31	2.27
52	1C1_11	1	Interpeloidal	13.42	878.50	10.98	1.48
53	3B3_4	3	Interpeloidal	27.31	1379.00	10.48	2.04
54	1D2_15	3	Interpeloidal	16.34	359.50	25.02	1.53
55	3B1_13	1	Interpeloidal	29.24	401.00	39.91	2.64
56	3A5_9	1	Interpeloidal	12.92	356.00	10.64	1.78
57	3B6_9	3	Interpeloidal	32.89	971.62	14.25	1.41
58	1B11_5	1	Interpeloidal	34.65	3543.50	13.15	1.67
59	2D11_8	3	Interpeloidal	6.63	964.00	17.71	1.30
60	2A6_5	1	Interpeloidal	19.64	875.50	15.05	2.74
61	3A10_8	3	Interpeloidal	12.80	788.50	14.98	1.24
62	3D1_6	1	Interpeloidal	18.43	743.00	6.69	1.63
63	3.13_3	3	Interpeloidal	23.06	177.50	24.64	1.28
64	1E4_7	3	Interpeloidal	17.33	241.00	10.09	1.33
65	3C12_3	3	Interpeloidal	25.72	215.00	25.21	1.64
66	2C4_6	1	Interpeloidal	17.30	385.00	20.76	1.65
67	3D4_8	1	Interpeloidal	13.50	181.00	24.93	1.82
68	3A14_13	2	Filament mold	4.05	187.00	16.30	1.23
69	3A13_6	2	Filament mold	6.70	98.50	24.11	1.23
70	1A10_2	2	Filament mold	23.94	240.5	11.02	1.18
71	1A14_3	2	Filament mold	23.13	565.70	15.65	1.12
72	3A7_4	2	Filament mold	14.43	26.70	24.00	1.11
73	3A8_2	2	Filament mold	9.62	52.00	18.61	1.15
74	1B7_8	2	Filament mold	9.77	370.00	26.44	1.21
75	1A8_5	2	Filament mold	16.00	2032.00	7.84	1.17
76	2C5_18	2	Filament mold	4.06	463.80	11.50	1.51
77	3A12_13	2	Filament mold	28.04	1215.50	22.70	1.24

	Thin Section Image	PTA	Pore Type	Φ_{DIA_PT}	$K_{contr.}$	Abund.	Effic.
				[%]	[mD]	#	[-]
1	1A10_2	2	Vuggy	11.93	146.44	34	35.09
2	1A14_3	2	Vuggy	13.72	341.22	28	49.00
3	3A7_4	2	Vuggy	11.51	22.79	12	95.92
4	3A8_2	2	Vuggy	6.33	40.20	18	35.17
5	1B7_8	2	Vuggy	8.58	336.87	8	107.25
6	1A8_5	2	Vuggy	14.68	1880.88	28	52.43
7	2C5_18	2	Vuggy	3.38	380.01	6	56.41
8	3A12_13	2	Vuggy	25.30	1114.69	16	158.13
9	1C6_8	1	Vuggy	7.58	488.19	9	84.22
10	3.16_1	1	Vuggy	19.23	631.85	21	91.57
11	3B5_9	1	Vuggy	17.45	2129.62	40	43.63
12	1B10_2	3	Vuggy	24.14	798.70	9	268.22
13	1C1_11	1	Vuggy	8.02	596.49	18	44.56
14	3B3_4	3	Vuggy	11.64	760.04	15	77.60
15	1D2_15	3	Vuggy	6.61	185.02	4	165.25
16	3B1_13	1	Vuggy	1.70	25.38	1	170.00
17	3A5_9	1	Vuggy	1.75	69.50	1	175.00
18	3B6_9	3	Vuggy	17.01	605.63	35	48.60
19	3C1_3	3	Vuggy	3.59	380.78	3	119.67
20	1B11_5	1	Vuggy	32.82	3605.10	15	218.80
21	2D11_8	3	Vuggy	5.71	824.74	24	23.79
22	2A6_5	1	Vuggy	15.60	846.38	23	67.83
23	3A10_8	3	Vuggy	6.42	458.66	13	49.38
24	3D1_6	1	Vuggy	13.27	610.42	11	120.64
25	3.13_3	3	Vuggy	13.09	138.50	57	22.96
26	1E4_7	3	Vuggy	5.01	60.49	11	45.55
27	3C12_3	3	Vuggy	5.88	64.00	2	294.00
28	3B5_9	1	Skel. Moldic	0.72	122.78	53	1.36
29	1B10_2	3	Skel. Moldic	0.51	15.52	22	2.32
30	3B3_4	3	Skel. Moldic	0.85	44.48	35	2.43
31	1D2_15	3	Skel. Moldic	1.84	87.58	43	4.28
32	3B6_9	3	Skel. Moldic	0.71	21.39	59	1.20
33	3C1_3	3	Skel. Moldic	1.29	162.92	53	2.43
34	2D11_8	3	Skel. Moldic	0.46	103.17	27	1.70
35	3A10_8	3	Skel. Moldic	0.20	12.58	8	2.50
36	3.13_3	3	Skel. Moldic	0.08	1.10	11	0.73
37	1E4_7	3	Skel. Moldic	0.81	14.65	47	1.72
38	3C12_3	3	Skel. Moldic	0.12	1.22	12	1.00
39	1B2_2	3	Skel. Moldic	16.91	176.10	23	73.52
40	1B10_2	3	Intraskeletal	10.94	191.87	44	24.86

	Thin Section Image	PTA	Pore Type	Φ_{DIA_PT}	$K_{contr.}$	Abund.	Effic.
				[%]	[mD]	#	[-]
41	3B3_4	3	Intraskeletal	3.35	104.63	18	18.61
42	1D2_15	3	Intraskeletal	1.90	50.54	1	190.00
43	3B6_9	3	Intraskeletal	11.27	271.97	51	22.10
44	3C1_3	3	Intraskeletal	4.52	535.65	14	32.29
45	1E4_7	3	Intraskeletal	8.80	138.03	7	125.71
46	3C12_3	3	Intraskeletal	12.90	96.77	8	161.25
47	3.13_3	3	Intraskeletal	5.32	97.54	25	21.28
48	1C6_8	1	Interpeloidal	5.90	239.69	649	0.91
49	3.16_1	1	Interpeloidal	9.68	153.62	946	1.02
50	3B5_9	1	Interpeloidal	5.60	560.32	1353	0.41
51	1B10_2	3	Interpeloidal	1.42	22.81	31	4.58
52	1C1_11	1	Interpeloidal	5.40	283.00	1011	0.53
53	3B3_4	3	Interpeloidal	11.47	449.75	1873	0.61
54	1D2_15	3	Interpeloidal	5.99	34.56	368	1.63
55	3B1_13	1	Interpeloidal	27.54	377.13	748	3.68
56	3A5_9	1	Interpeloidal	11.17	285.67	2445	0.46
57	3B6_9	3	Interpeloidal	3.91	79.76	538	0.73
58	1B11_5	1	Interpeloidal	1.83	98.23	258	0.71
59	2D11_8	3	Interpeloidal	0.46	55.51	83	0.55
60	2A6_5	1	Interpeloidal	4.04	128.36	617	0.65
61	3A10_8	3	Interpeloidal	6.18	334.64	1108	0.56
62	3D1_6	1	Interpeloidal	5.16	134.01	2750	0.19
63	3.13_3	3	Interpeloidal	4.57	33.10	373	1.23
64	1E4_7	3	Interpeloidal	2.71	28.82	652	0.42
65	3C12_3	3	Interpeloidal	6.82	52.36	300	2.27
66	2C4_6	1	Interpeloidal	17.30	385.14	1287	1.34
67	3D4_8	1	Interpeloidal	13.50	179.88	685	1.97
68	3A14_13	2	Filament mold	4.05	82.24	78	5.19
69	3A13_6	2	Filament mold	6.70	40.32	83	8.07
70	1A10_2	2	Filament mold	12.01	93.89	383	3.14
71	1A14_3	2	Filament mold	9.41	219.04	2150	0.44
72	3A7_4	2	Filament mold	2.92	3.86	294	0.99
73	3A8_2	2	Filament mold	3.29	11.95	494	0.67
74	1B7_8	2	Filament mold	1.19	32.08	68	1.75
75	1A8_5	2	Filament mold	1.32	106.84	549	0.24
76	2C5_18	2	Filament mold	0.68	73.34	132	0.52
77	3A12_13	2	Filament mold	2.74	80.99	179	1.53

Appendix Chapter 5: ***Cementation and pore system evolution***

	Thin Section Image	Φ_{DIA} (1)	Φ_{DIA} (2)	Φ_{DIA} (3)	γ (1)	γ (2)	γ (3)
		[%]	[%]	[%]	[-]	[-]	[-]
1	1_75	1.31	16.48	15.41	1.31	2.29	1.33
2	1_105_1	3.85	15.93	11.98	1.44	1.69	1.54
3	1_105_2	2.32	7.75	5.34	1.46	1.87	1.60
4	1_105_3	3.05	8.23	6.78	1.52	1.88	1.85
5	1_115_1	2.83	9.56	8.24	1.59	2.84	1.37
6	1_115_2	1.06	27.57	10.58	1.32	2.78	1.52
7	1A10_1	1.54	14.33	7.24	1.40	2.39	1.72
8	1A10_4	7.19	15.02	9.92	1.37	1.89	1.89
9	2_45	3.32	7.47	6.81	1.53	1.90	1.74
10	2A1_1	0.83	8.29	2.97	1.43	1.96	1.82
11	2A1_2	0.22	14.12	8.66	1.15	2.31	1.32
12	2A1_3	0.49	17.05	6.69	1.16	1.76	1.58
13	3_49_1	2.46	18.29	15.58	1.36	2.10	1.44
14	3_49_2	0.84	26.86	26.15	1.38	2.22	1.63
15	3_60_1	8.29	12.10	2.84	1.24	1.46	1.53
16	3_60_2	3.88	16.86	3.60	1.27	2.28	1.50
17	3_60_3	5.31	20.86	11.78	1.22	2.17	1.63
18	3_243	0.48	21.72	7.34	1.78	3.16	1.76
19	3A4_1	0.49	10.59	6.89	1.32	2.77	1.97
20	3A4_2	0.15	11.29	9.65	1.25	2.74	1.41
21	4_40_1	1.20	26.35	23.20	1.31	2.23	1.55
22	4_40_2	2.01	11.01	4.67	1.44	1.92	1.77
23	4_158_1	4.68	18.76	9.47	1.34	1.94	1.52
24	4_158_2	5.33	17.13	14.78	1.25	1.88	1.62
25	4_158_3	1.35	10.22	4.20	1.35	2.65	1.56
26	4_158_4	1.41	10.58	1.67	1.21	3.16	1.52
27	4_178_1	1.60	10.63	8.31	1.26	1.69	1.49
28	4_178_2	0.66	15.93	11.98	1.32	2.11	1.51
29	4_178_3	0.59	3.82	1.03	1.43	1.97	1.85
30	3A13_1	0.32	8.54	7.64	1.36	1.90	1.65
31	3A13_3	0.82	18.91	13.05	1.78	3.50	1.67
32	3A13_4	1.42	31.05	19.75	1.69	2.73	1.93
33	8_3_1	1.66	7.62	6.37	1.67	2.82	1.68
34	8_3_2	3.13	8.54	5.64	1.44	2.15	1.63
35	2C1_2	0.56	21.74	1.99	2.09	3.50	2.17
36	2C1_3	1.41	8.77	1.32	1.94	3.03	1.84
37	2C1_4	0.69	7.35	2.11	2.01	4.63	1.51
38	2D10	0.55	10.35	7.35	1.32	2.63	1.71
39	3A8_1	0.69	8.86	6.08	1.22	2.15	1.34
40	3A8_3	1.46	4.97	4.14	1.25	1.77	1.57

	Thin Section Image	Φ_{DIA} (1)	Φ_{DIA} (2)	Φ_{DIA} (3)	γ (1)	γ (2)	γ (3)
		[%]	[%]	[%]	[-]	[-]	[-]
41	3A8_4	1.73	10.77	5.83	1.29	2.16	1.56
42	3A10_1	1.28	13.59	12.51	1.42	2.25	1.72
43	3A10_2	0.32	8.66	6.05	1.44	1.81	1.45
44	3A10_3	1.74	13.89	5.14	1.47	2.67	1.64
45	3A10_4	2.19	10.12	7.05	1.51	1.66	1.53
46	4A13_1	2.36	18.44	16.59	1.48	2.78	1.61
47	4A13_2	1.65	10.38	9.30	1.49	2.09	1.56
48	4A13_3	4.18	9.74	5.00	1.72	1.75	1.57
49	2B9	0.99	20.75	2.29	1.44	3.69	1.79
50	2A8_1	0.81	37.66	6.62	1.81	2.56	1.86
51	2A8_2	0.67	20.35	13.18	2.02	3.29	1.55
52	2A8_3	0.45	13.79	10.27	1.53	2.96	1.64

	Thin Section Image	Pore width (1) [µm]	Pore width (2) [µm]	Pore width (3) [µm]	Kcontr. (1) [mD]	Kcontr. (2) [mD]	Kcontr. (3) [mD]
1	1_75	11.39	23.62	36.10	124.25	217.20	126.15
2	1_105_1	18.29	24.24	34.42	136.58	160.29	146.07
3	1_105_2	18.46	19.39	29.77	138.48	177.37	151.76
4	1_105_3	22.14	23.87	38.69	144.17	178.31	175.47
5	1_115_1	23.58	16.17	22.63	150.81	269.37	129.94
6	1_115_2	30.65	14.31	56.67	125.20	263.68	144.17
7	1A10_1	31.26	25.13	24.91	132.79	226.69	163.14
8	1A10_4	26.01	28.48	33.45	129.94	179.26	179.26
9	2_45	25.08	24.58	25.99	145.12	180.21	165.04
10	2A1_1	26.52	31.68	30.47	135.63	185.90	172.62
11	2A1_2	21.35	28.60	29.71	109.08	219.10	125.20
12	2A1_3	33.10	35.44	37.41	110.02	166.93	149.86
13	3_49_1	23.10	18.21	28.90	128.99	199.18	136.58
14	3_49_2	22.31	28.60	35.58	130.89	210.56	154.60
15	3_60_1	44.22	45.98	38.97	117.61	138.48	145.12
16	3_60_2	41.45	49.30	42.66	120.46	216.25	142.27
17	3_60_3	49.53	30.63	35.16	115.71	205.82	154.60
18	3_243	13.52	20.03	29.69	168.83	299.72	166.93
19	3A4_1	23.14	22.69	25.67	125.20	262.73	186.85
20	3A4_2	20.45	28.81	54.28	118.56	259.88	133.74
21	4_40_1	28.60	26.20	32.99	124.25	211.51	147.01
22	4_40_2	32.27	14.86	34.09	136.58	182.11	167.88
23	4_158_1	29.10	15.34	36.12	127.10	184.01	144.17
24	4_158_2	17.28	17.79	32.10	118.56	178.31	153.65
25	4_158_3	29.23	16.80	38.43	128.04	251.35	147.96
26	4_158_4	26.38	18.32	31.12	114.77	299.72	144.17
27	4_178_1	36.23	20.61	26.47	119.51	160.29	141.32
28	4_178_2	19.74	26.59	59.58	125.20	200.13	143.22
29	4_178_3	15.79	22.83	19.03	135.63	186.85	175.47
30	3A13_1	8.61	19.60	49.32	128.99	180.21	156.50
31	3A13_3	14.75	17.15	26.32	168.83	331.97	158.40
32	3A13_4	16.36	18.15	40.14	160.29	258.94	183.06
33	8_3_1	11.51	27.09	34.74	158.40	267.47	159.34
34	8_3_2	10.94	28.77	36.66	136.58	203.92	154.60
35	2C1_2	12.68	22.43	27.77	198.23	331.97	205.82
36	2C1_3	10.98	16.37	25.23	184.01	287.39	174.52
37	2C1_4	12.76	18.49	21.84	190.64	439.15	143.22
38	2D10	15.79	18.85	20.31	125.20	249.45	162.19
39	3A8_1	17.00	25.87	33.19	115.71	203.92	127.10
40	3A8_3	12.20	26.80	29.19	118.56	167.88	148.91

	Thin Section Image	Pore width (1) [µm]	Pore width (2) [µm]	Pore width (3) [µm]	Kcontr. (1) [mD]	Kcontr. (2) [mD]	Kcontr. (3) [mD]
41	3A8_4	18.94	29.00	28.35	122.35	204.87	147.96
42	3A10_1	10.11	23.91	26.32	134.68	213.41	163.14
43	3A10_2	12.24	18.20	18.72	136.58	171.67	137.53
44	3A10_3	14.01	19.68	18.70	139.43	253.24	155.55
45	3A10_4	18.11	23.40	23.85	143.22	157.45	145.12
46	4A13_1	20.02	31.25	41.78	140.38	263.68	152.71
47	4A13_2	22.43	29.89	29.22	141.32	198.23	147.96
48	4A13_3	12.90	26.74	36.31	163.14	165.98	148.91
49	2B9	7.86	16.17	33.96	136.58	349.99	169.78
50	2A8_1	15.04	21.93	22.91	171.67	242.81	176.42
51	2A8_2	8.50	17.81	66.93	191.59	312.05	147.01
52	2A8_3	5.91	15.55	67.47	145.12	280.75	155.55

Appendix Chapter 6: *Fluid flow simulation*

	Thin Section Image	Pore Type	γ	Effective Porosity
			[-]	[%]
1	1.10_1	Vuggy	3.21	99.20
2	1.13_2	Vuggy	2.57	87.01
3	1.4_6	Vuggy	1.82	36.78
4	1A10_2	Vuggy	1.85	86.64
5	1B10_2	Vuggy	3.38	96.61
6	2A1_2	Vuggy	2.64	73.93
7	2A3_7	Vuggy	2.33	50.77
8	2A6_5	Vuggy	2.77	94.8
9	2A7_8	Vuggy	2.94	86.77
10	2B1_2	Vuggy	1.34	70.75
11	3.16_1	Vuggy	3.23	89.09
12	3A10_8	Vuggy	1.85	90.46
13	3A7_4	Vuggy	1.66	98.67
14	3B1_16	Vuggy	2.81	94.2
15	3B6_9	Vuggy	2.46	97.74
16	3C10_3	Vuggy	1.32	68.75
17	3C13_11	Vuggy	1.87	59.37
18	3C13_3	Vuggy	3.02	97.94
19	3D1_6	Vuggy	2.88	94.19
20	3D10_5	Vuggy	2.6	92.83
21	3D10_6	Vuggy	3.1	93.04
22	1B10_2	Skeletal moldic	3.96	96.8
23	1C13_6	Skeletal moldic	2.42	83.33
24	2B13_7	Skeletal moldic	2.76	88.87
25	2C9_13	Skeletal moldic	2.32	73.17
26	2D11_8	Skeletal moldic	2.23	90.43
27	3B2_4	Skeletal moldic	2.68	88.51
28	3B6_9	Skeletal moldic	2.08	92.16
29	3C10_3	Skeletal moldic	2.97	83.41
30	3C13_11	Skeletal moldic	2.42	28.57
31	3C5_5	Skeletal moldic	1.9	31.98
32	3D10_5	Skeletal moldic	2.72	98.02
33	1B10_2	Intraskeletal	2.08	10.42
34	1C13_6	Intraskeletal	1.81	36.09
35	2B1_2	Intraskeletal	1.39	16.28
36	2B9_1	Intraskeletal	1.45	31.34
37	3B2_4	Intraskeletal	2.2	14.36
38	3B6_9	Intraskeletal	1.67	41.09
39	3C10_3	Intraskeletal	2.23	20.25
40	3C5_5	Intraskeletal	1.43	22.66

	Thin Section Image	Pore Type	γ	Effective Porosity
			[-]	[%]
41	1.10_1	Interpeloidal	2.51	80.31
42	1.13_2	Interpeloidal	2.61	98.71
43	1B10_2	Interpeloidal	2.27	99.86
44	1C13_6	Interpeloidal	1.19	66.01
45	2A3_7	Interpeloidal	1.38	57.12
46	2A6_5	Interpeloidal	2.74	74.89
47	2B13_7	Interpeloidal	2.17	81.58
48	2B9_1	Interpeloidal	1.89	72.43
49	2B9_11	Interpeloidal	1.98	84.09
50	2C4_6	Interpeloidal	1.65	13.93
51	2C9_13	Interpeloidal	2.02	65.42
52	2D11_8	Interpeloidal	1.3	90.11
53	3.16_1	Interpeloidal	1.56	60.45
54	3A10_8	Interpeloidal	1.24	74.75
55	3B1_16	Interpeloidal	2.64	96.38
56	3B2_4	Interpeloidal	2.36	82.77
57	3B6_9	Interpeloidal	1.41	82.44
58	3C13_11	Interpeloidal	1.28	14.81
59	3C13_3	Interpeloidal	2.43	89.09
60	3C5_5	Interpeloidal	2.19	28.64
61	3C5_6	Interpeloidal	2.1	74.07
62	3D1_6	Interpeloidal	1.63	88.51
63	3D10_5	Interpeloidal	2.58	92.81
64	3D2_9	Interpeloidal	1.85	60.82
65	1.4_6	Filament moldic	1.33	6.73
66	1A10_2	Filament moldic	1.18	38.78
67	2A1_2	Filament moldic	1.31	7.94
68	3A7_4	Filament moldic	1.11	9.95
69	3C13_11	Filament moldic	1.23	0.00

Appendix Chapter 6: ***Non-dimensionalized Navier-Stokes equation and Reynolds number (Re)***

Non-dimensionalized Navier-Stokes equation

The Navier-Stokes equation is based on Newton´s second law which can be expressed as

$$\frac{\rho \delta v}{\delta t} = -\nabla p + \mu \Delta v$$

v: fluid velocity [m/s]

p: pressure [Pa]

ρ: density [kg/m^3]

t: time [s]

μ: dynamic viscosity [kg/m*s]

This equation is now non-dimensionalized by selecting the characteristic scales U (= velocity) and L (= length):

$$v = \frac{v}{U}$$

$$t = \frac{t}{L/U}$$

$$p = \frac{p}{\rho U^2}$$

and the coordinate vector x

$$x = \frac{x}{L}$$

resulting in the non-dimensionalized Navier-Stokes equation

$$\frac{\delta v}{\delta t} = -\nabla p + \left(\frac{1}{Re}\right) \Delta v$$

including the Reynolds number

$$Re = \frac{\rho v L}{\mu}$$

Transforming this formula to describe fluid motion in the Euler regime results in

$$\frac{\delta v}{\delta t} = -v\nabla v - \nabla p + \left(\frac{1}{Re}\right)\Delta v$$

This formula describes that at a fixed point in space, the velocity changes with time with the rate $\frac{\delta v}{\delta t}$ depending on the velocity of the fluid particle and the difference in velocity of a previous particle at the same point so that the velocity at that point is changing with the rate $-v\nabla v$. Pressure on one side of the fluid volume is greater than the pressure on the other side of the fluid volume, so that the fluid will accelerate and the corresponding rate of the velocity change is described as $-\nabla p$. The diffusion of velocity due to friction is expressed by $\left(\frac{1}{Re}\right)\Delta v$.

Reynolds number (Re)

The dimensionless Reynolds number (Re) describes the ratio of inertial forces to viscous friction forces within a fluid, and depends on the fluid velocity, the kinematic viscosity of the fluid and the characteristic dimension. It is defined as

$$\mathrm{Re} = \frac{\rho v L}{\mu} = \frac{v\,L}{\nu}$$

ρ: density of the fluid [kg/m^3]

v: velocity of the fluid with respect to the object [m/s]

L: characteristic linear dimension [m]

μ: dynamic viscosity of the fluid [kg/m*s]

ν: kinematic viscosity of the fluid [m^2/s]

At low Reynolds numbers, a flow shows a laminar behavior. After exceeding a critical value of Re, flow behavior transitions into turbulent.

Appendix Chapter 7: ***Porosity-permeability relationship***

Thin Section Image		PTA	TOTAL		VUGS		INTERPELOIDAL	
			Φ_{DIA}	Ktotal	Φ_{DIA}	$K_{contr.}$	Φ_{DIA}	$K_{contr.}$
			[%]	[mD]	[%]	[mD]	[%]	[mD]
1	1A10_2	2	23.94	240.5	11.93	146.44		
2	1A14_3	2	23.13	565.70	13.72	341.22		
3	1A8_5	2	16.00	2032.00	14.68	1880.88		
4	1B10_2	3	37.01	976.00	24.14	798.70	1.42	22.81
5	1B11_5	1	34.65	3543.50	32.82	3605.10	1.83	98.23
6	1B2_2	3	16.91	176.00				
7	1B7_8	2	9.77	370.00	8.58	336.87		
8	1C1_11	1	13.42	878.50	8.02	596.49	5.40	283.00
9	1C6_8	1	13.48	735.00	7.58	488.19	5.90	239.69
10	1D2_15	3	16.34	359.50	6.61	185.02	5.99	34.56
11	1E4_7	3	17.33	241.00	5.01	60.49	2.71	28.82
12	2A6_5	1	19.64	875.50	15.60	846.38	4.04	128.36
13	2C4_6	1	17.30	385.00			17.30	385.14
14	2C5_18	2	4.06	463.80	3.38	380.01		
15	2D11_8	3	6.63	964.00	5.71	824.74	0.46	55.51
16	3.13_3	3	23.06	177.50	13.09	138.50	4.57	33.1
17	3.16_1	1	28.91	788.05	19.23	631.85	9.68	153.62
18	3A10_8	3	12.80	788.50	6.42	458.66	6.18	334.64
19	3A12_13	2	28.04	1215.50	25.30	1114.69		
20	3A13_6	2	6.70	98.50				
21	3A14_13	2	4.05	187.00				
22	3A5_9	1	12.92	356.00	1.75	69.50	11.17	285.67
23	3A7_4	2	14.43	26.70	11.51	22.79		
24	3A8_2	2	9.62	52.00	6.33	40.20		
25	3B1_13	1	29.24	401.00	1.70	25.38	27.54	377.13
26	3B3_4	3	27.31	1379.00	11.64	760.04	11.47	449.75
27	3B5_9	1	23.77	2911.00	17.45	2129.62	5.60	560.32
28	3B6_9	3	32.89	971.62	17.01	605.63	3.91	79.76
29	3C1_3	3	9.40	1086.00	3.59	380.78		
30	3C12_3	3	25.72	215.00	5.88	64.00	6.82	52.36
31	3D1_6	1	18.43	743.00	13.27	610.42	5.16	134.01
32	3D4_8	1	13.50	181.00			13.50	179.88

Thin Section Image		PTA	SKELETAL MOLDS		FILAMENT MOLDS		INTRASKELETAL	
			Φ_{DIA} [%]	Kcontr. [mD]	Φ_{DIA} [%]	Kcontr. [mD]	Φ_{DIA} [%]	Kcontr. [mD]
1	1A10_2	2			12.01	93.89		
2	1A14_3	2			9.41	219.04		
3	1A8_5	2			1.32	106.84		
4	1B10_2	3	0.51	15.52			10.94	191.87
5	1B11_5	1						
6	1B2_2	3	16.91	176.10				
7	1B7_8	2			1.19	32.08		
8	1C1_11	1						
9	1C6_8	1						
10	1D2_15	3	1.84	87.58			1.90	50.54
11	1E4_7	3	0.81	14.65			8.80	138.03
12	2A6_5	1						
13	2C4_6	1						
14	2C5_18	2			0.68	73.34		
15	2D11_8	3	0.46	103.17				
16	3.13_3	3	0.08	1.10			5.32	97.54
17	3.16_1	1						
18	3A10_8	3	0.20	12.58				
19	3A12_13	2			2.74	80.99		
20	3A13_6	2			6.70	40.32		
21	3A14_13	2			4.05	82.24		
22	3A5_9	1						
23	3A7_4	2			2.92	3.86		
24	3A8_2	2			3.29	11.95		
25	3B1_13	1						
26	3B3_4	3	0.85	44.48			3.35	104.63
27	3B5_9	1	0.72	122.78				
28	3B6_9	3	0.71	21.39			11.27	271.97
29	3C1_3	3	1.29	162.92			4.52	535.65
30	3C12_3	3	0.12	1.22			12.90	96.77
31	3D1_6	1						
32	3D4_8	1						

ACKNOWLEDGMENTS

I would like to thank Maria Mutti for her support, guidance and thrust over the last decade.

This thesis was funded by Eni SpA Upstream and Technical Services and was part of an Eni R&D project on Continental Carbonates. Therefore, I would like to thank Alfredo Frixa, Paola Ronchi, Emilio Tebaldi, Maurizio Orlando and the Eni management.

Many thanks to Christina Günter for assistance at the SEM, Christine Fischer for preparation of high-quality thin sections, Antje Musiol for lab maintenance, and Ines Münch for computer and software support.

I would also like to thank my dear colleagues Sara Tomás, Gerd Winterleitner, Gianluca Frijia, Michael Szurlies and Heiko Pingel for fruitful discussion which helped to improve this thesis, as well as Tanja Karius, Richard Arndt and Eddy Kutschera for helping with lab and field work, and all members of the Institute of Geoscience at University of Potsdam.

Most of all, I would like to thank my beloved family for always being there for me, and I dedicate this thesis to my mother and my father.

PUBLICATIONS & PRESENTATIONS

Results gained in this thesis have previously been presented at the following conferences:

ECSM (Early Career Sedimentologist Meeting) at Leibniz University Hannover, in Hannover, Germany, 2018. **Talk**

AAPG/SEG International Conference and Exhibition, London, United Kingdom, 2017. **Talk**

EAGE First Workshop on Evaluation and Drilling of Carbonate Reservoirs, Potsdam, Germany, 2017. **Talk**

Dolomieu Conference on Carbonate Platforms and Dolomite, Selva di Val Gardena, Italy, 2016. **Talk**

Results gained during my PhD but not part of this thesis have previously been published in the following publications:

Christ, N., S. Maerz, E. Kutschera, O. Kwiecien, M. Mutti, and N. Sheldon, 2018, Palaeoenvironmental and diagenetic reconstruction of a closed-lacustrine carbonate system – the challenging marginal setting of the Miocene Ries Crater Lake (Germany): Sedimentology, v. 65, p. 235-262. doi:10.1111/sed.12401

STATUTORY DECLARATION

Declaration:

I hereby declare that I wrote the present dissertation with the topic

ANALYZING PORE SYSTEMS THROUGH COMPREHENSIVE DIGITAL IMAGE ANALYSIS (DIA):

QUANTIFYING PORE TYPE GEOMETRY, DETECTING EFFECTIVE POROSITY AND RECONSTRUCTING PORE SYSTEM EVOLUTION

independently and used no other aids than those cited. In each individual case, I have clearly identified the source of the passages that are taken word for word or paraphrased from other works.

I further hereby declare that I have not submitted this thesis to any other university but the University of Potsdam.

I also hereby declare that I have carried out my scientific work according to the principles of good scientific practice in accordance with the current "Proposals for Safeguarding Good Scientific Practice" of the Deutsche Forschungsgemeinschaft (DFG).

Potsdam, September 2019

Sven Maerz